SPECTROSCOPIC STUDIES OF FIELD-INDUCED ELECTRON EMISSION FROM ISOLATED MICROSTRUCTURES

Anthony David Archer, BSc

Doctor of Philosophy

THE UNIVERSITY OF ASTON IN BIRMINGHAM

October 1992

THE UNIVERSITY OF ASTON IN BIRMINGHAM

SPECTROSCOPIC STUDIES OF FIELD-INDUCED ELECTRON EMISSION FROM ISOLATED MICROSTRUCTURES

Anthony David Archer, BSc.

A thesis submitted for the degree of Doctor of Philosophy

1992

SUMMARY

A detailed investigation has been undertaken into the field induced electron emission (FIEE) mechanism that occurs at microscopically localised 'sites' on uncoated and dielectric coated metallic electrodes. These processes have been investigated using two dedicated experimental systems that were developed for this study. The first is a novel combined photo/field emission microscope, which employs a UV source to stimulate photo-electrons from the sample surface in order to generate a topographical image. This system utilises an electrostatic lens column to provide identical optical properties under the different operating conditions required for purely topographical and combined photo/field imaging. The system has been demonstrated to have a resolution approaching 1µm. Emission images have been obtained from carbon emission sites using this system to reveal that emission may occur from the edge triple junction or from the bulk of the carbon particle. An existing UHV electron spectrometer has been extensively rebuilt to incorporate a computer control and data acquisition system, improved sample handling and manipulation and a specimen heating stage. Details are given of a comprehensive study into the effects of sample heating on the emission process under conditions of both bulk and transient heating. Similar studies were also performed under conditions of both zero and high applied field. These show that the properties of emission sites are strongly temperature and field dependent thus indicating that the emission process is 'non-metallic' in nature. The results have been shown to be consistent with an existing hot electron emission model.

Key words: field electron emission, electron spectroscopy, high voltage vacuum insulation, hot electrons, photo-electron microscopy.

DEDICATED TO MY MOTHER AND FATHER

.

ACKNOWLEDGEMENT

CONTENTS

Page

CHAPTER 3 : ELECTRON ENERGY ANALYSER 57

CHAPTER 4: EXPERIMENTAL STUDIES OF LOCALISED FIEE PROCESSES 82

LIST OF FIGURE CAPTIONS

13

LIST OF TABLES

CHAPTER 1 - INTRODUCTION

1.1 Limitations of vacuum insulation

A vacuum would be expected to prove an excellent insulating medium owing to the absence of any material capable of providing free charge carriers. In practice, however, it is found to be of limited effectiveness as an insulating medium. From a technological point of view this is a major problem since the use of vacuum insulation is crucial for a wide range of device applications, such as RF cavities, power vacuum switching devices, electron microscopes, and more recently, to the insulation of power supplies in space.

It is found that at high field levels, typically in excess of $10MVm^{-1}$, there is a possibility of arcing, or sparking, occuring between vacuum insulated electrodes, when the gap resistance effectively falls to zero. Such an event, known as breakdown, can result in serious damage to the device concerned, and almost invariably causes a reduction in the field strength the electrode gap may subsequently sustain [1]. In many cases it is possible to protect against the occurence of breakdown, but such procedures are often expensive [1]. The limitation of breakdown is of particular importance to space-power systems owing to the difficulties and expense of making repairs. Due to the great technological importance of suppressing this process, much research effort has been expended to determine the fundamental mechanisms involved [1].

For the case of broad area electrodes having a gap separation of <5mm in the field range $10-30MVm^{-1}$ and insulated by an ultra-high vacuum (UHV), the onset of breakdown is thought to be associated with the same physical process that is responsible for the prebreakdown currents that flow between the electrodes [1,2]. These currents arise from microscopically localised electron emission processes, and it is with a fundamental study of the physical nature of this process that this thesis is primarily concerned.

1.2 Field-induced cold cathode emission processes

The phenomenon of field emission, the emission of electrons from metallic electrodes under the application of intense electric fields, was first observed during the latter part of the Nineteenth Century, with much of the early understanding being developed by Millikan during the 1920's [3]. In 1928, Fowler and Nordheim [4] developed a theoretical model to explain the process which was based on the quantum mechanical tunnelling of electrons through the surface barrier of the metal electrode. This process typically requires a field strength of some 3×10^9 Vm^{-1}. The theory has been well verified by experiment, and has for many years been used to explain the occurence of prebreakdown currents [1], since the I-V characteristics of electrode gaps follow the theory to give a straightline on an FN plot; that is, a plot

of $\ln(I/V^2)$ vs $1/V$.

In practical devices, the field strengths experienced rarely come within even two orders of magnitude of the 3×10^9 Vm^{-1} limit required by the FN theory. However, from observations of the localised nature of the emission, it was assumed that metallic micro-protrusions, or whiskers, were present on the elctrode surface and that these produced the necessary field enhancement, termed the ß-factor, to cause 'metallic' field emission to occur [1].

Serious problems do exist with this theory however, principally the difficulty of finding whiskers [5], and, at a technological level, the inability of electrode polishing techniques to improve device performance. Unrealistically high ß-factors of the order of 100-1000 are also required in order to achieve the necessary field enhancements. Over the last few decades, there has been a growing body of work which has tended to contradict the micro-protrusion hypothesis of metallic field emission in favour of a non-metallic emission process. Thus, *in situ* point anode scanning techniques have failed to observe the necessary micro-protrusions, and have, instead, indicated that the emission is associated with impurity micro-structures of 0.1-10μm in size that are attached to, but electrically insulated from the electrode material [5,6]. Such structures have been found to have a varied elemental composition, including foreign metallic elements, oxides, sulphides, carbon and sulphur [7]. Electron spectroscopy studies have further shown that the energy distribution of the emitted electrons is shifted below the metal Fermi level, and that both the spectral shift and halfwidth (FWHM) are strongly field dependent [6]. These factors have thus tended to support models based on a non-metallic emission process.

Various models have been proposed to explain these characteristics. Some have been based on purely geometrical effects, while others depend upon the electronic properties of the micro-structures: however, none of these have fully explained all the experimental observations. The field induced hot electron emission model describing a metal-insulator (MI) system [8], provides the best quantitative description of the experimental observations, although it is not complete. There is however, much evidence to indicate that other emission regimes exist to which this model does not apply. Of particular significance is work by Bajic and Latham [9] who investigated the characteristics of artificial micro-emitters consisting of conducting particles embedded in a resin matrix. Details of possible emission regimes and models are considered more fully in Chapter 2.

1.3 Instrumental systems

An electron energy analyser system has been of great importance to the fundamental study and understanding of the emission process [10]. This system, based around a high resolution electron energy spectrometer, has been radically upgraded during the course of the present experimental programme. Thus, a new

experimental chamber incorporating a pre-chamber/load-lock assembly and step-motor controlled specimen manipulation system has been designed. Furthermore, a dedicated computer control and data acquisition and analysis system has been designed in order to improve the flexibility of the experimental system and the speed and accuracy of data analysis and presentation. This instrumental work is described fully in Chapter 3.

This advanced system enables a variety of observations on the emission process to be undertaken [10]. Emission site distributions on a cathode may be mapped, overall electrode gap characteristics measured, and subsequently the properties of individual emission sites can be studied, including both energy spectra from one point and electronic energy selective images of sites. The specimen sample holder incorporates a heater stage capable of heating a sample electrode to 600°C, thus enabling the study of thermal effects on the emission process to be undertaken. Experimental measurements showing the various capabilities of this system are presented in Chapter 4.

As stated above, electron emission has been shown to be associated with impurity microstructures of between 0.1 - 10μm in size, however, it remains to be clarified which of several different proposed models is appropriate for explaining the process. To resolve this issue, a high resolution imaging system is required which is capable of imaging both the surface topography in the vicinity of an emission site and also the field emitted electrons from that site. In order to achieve both these requirements, a high resolution instrument based around the principles of a photo-electron microscope has been designed and developed, and this system is described, together with experimental results, in Chapter 5.

1.4 Experimental programme

The experimental programme consisted of several major investigations aimed at improving the understanding of the fundamental processes involved. The work also indicated possible technological applications in the fields of both suppression of the emission process and its application to electron sources. The experimental programme is summarised below:

i) In order to investigate the fundamental nature of the emission mechanism, simulated metal-insulator structures have been employed to study the MI regime. This study utilised Langmuir-Blodgett multilayers [11] to coat broad-area cathodes with dielectric layers of omega-tricocenoic acid to well defined thicknesses (in the range 90 - 750Å). Results are presented showing the spectral characteristics of these devices in Chapter 4.

ii) Studies on the effects of thermal processing on the emission process have been of great importance, not only to the fundamental understanding of the emission mechanism, but also at the technological level. For example, Niedermann *et al* [12]

have shown that on heating niobium cathodes to temperatures of up to 800°C the formation of new emission sites is stimulated, with a consequent increase in electrode emissivity. However, heating within the range 1200-2000°C results in a suppression of emission. Indeed, this result has been applied to an electrode conditioning treatment by Padamsee [13] with some success. In a further study of these effects, Chapter 4 presents an investigation of the effects of thermal loading on the emission process. These include measurements of how the emission site distribution, I-V characteristics and spectra vary with temperature. Comparison is also made between the effects of bulk heating under conditions of both zero- and high-applied field in the temperature range from ambient to 600°C.

iii) In addition, an investigation is described which assesses the effects of pulsed thermal surface loading as a possible technological treatment to suppress emission. The experiment was based around a NdYAG laser with the capability of delivering various thermal loadings up to levels sufficient to cause surface vaporisation. Results detailing the observed effects on emission site populations, electrode emissivity and spectral characteristics are presented in Chapter 4 and compared with those for the case of bulk heating.

iv) In order to further advance our fundamental understanding of the basic emission process, a combined photo/field emission imaging system, capable of displaying superimposed images of both the sample surface topography and field emission sites, was designed and developed. An initial study of simulated sites created by the introduction of contaminant carbon particles to the surface of OFHC Cu electrodes was undertaken using this system. The purpose of this study was to investigate the relationship between the particle and the position of the electron emission centre. The results of this study, together with the experimental system design, are presented in Chapter 5

CHAPTER 2 : FIELD-INDUCED ELECTRON EMISSION

2.1 Historical development

Electrical breakdown in vacuum was first observed around the turn of the century, when Millikan and co-workers [3,14] undertook much of the early work in the development of this field of study. These early investigations established that a pre-breakdown current flowed across a vacuum gap at field levels of $\sim 10^8 Vm^{-1}$, which increased rapidly with applied voltage until breakdown occured. It was shown by this group during the 1920's, that the noisy, reversible pre-breakdown currents were electronic in nature and originated from a cold emission process on the cathode. Furthermore, from observations of complementary fluorescent spots on the anode, the emission was shown to be localised in nature. Such emission sites were assumed to result from either field enhancing micro-protrusions associated with the intrinsic roughness of the electrodes, or a local reduction in the work function due to isolated chemical impurities.

The development by Fowler and Nordheim [4], in 1928, of their theory explaining field emission in terms of quantum mechanical tunnelling through the surface barrier was of great importance to the modelling of the emission process. According to this theory, a surface field of $\geq 3 \times 10^9$ Vm^{-1} reduced the width of the surface barrier sufficiently to enable electrons to tunnel through. It was predicted that a plot of $\ln(I/F^2)$ vs $1/F$ (known as an F-N plot), where I is the current flowing and F the applied field, would yield a straight line. For non-planar surfaces, the local field strength is given by $F=\beta(V/d)$ where β is the microscopic field enhancement factor, V the applied gap voltage and d the gap spacing. By substituting the above expression for F in the Fowler-Nordheim relation, it turns out that β is inversely proportional to the gradient of an F-N plot and may thus be determined directly, whilst the emitting area, A_e, may be determined from the intercept of the plot and is given by $\ln(A_e\beta^2)$. The F-N theory, in combination with the localised nature of the emission led to an explanation of the pre-breakdown emission process in terms of metallic micro-protrusions existing on the electrode surface where a sufficiently high field enhancement existed for tunnelling to occur [1].

Good agreement was apparently observed between theory and experiment, particularly for field emission microtips. Work by Boyle et al [15] using a crossed wire geometry in UHV found good straight-line fits for their F-N plots, but somewhat unexpectedly β was found to vary with wire spacing. In general though, their experimental findings were broadly consistent with an explanation based on the existence of small metallic protrusions on the cathode surface. Further evidence to support the micro-protrusion model was obtained by Little and Smith [16], and

Tomasche and Alpert [17], who used a TEM to observe the electrode surface profile directly. After use, cathodes made from a variety of electrode materials including tungsten, stainless steel, kovar, nickel, silver and copper were examined in a TEM and found to have whiskers which were assumed to give ß-factors high enough for F-N emission to occur [16,17]. Significantly, however, no such features were observed before the application of an electric field [1]. Emission was also found to be independent of temperature up to 1000°C, and of illumination with visible light, thus supporting the assumption that it did not occur from areas of low work function.

2.2 Metallic 'cold' electron emission

2.2.1 Field emission of electrons from an atomically clean metal surface by quantum mechanical tunnelling

As mentioned in the previous section, Fowler and Nordheim [4] were the first to apply quantum mechanics to explain the field emission of electrons from atomically clean metal surfaces. For an infinite metal surface, as shown in Fig. 2.1, the application of an electric field results in a Schottky modified surface potential barrier [18] of a triangular shape. When the field strength is sufficiently high, $\sim 3 \times 10^9 \text{Vm}^{-1}$, the width of the surface potential barrier is reduced to approximately the wavelength of electrons within the metal, and they then satisfy the criteria required to tunnel through this barrier. By assuming that the 'free electron' theory holds within the metal and that there is an external vacuum, a relation between the emission current density, J, and applied electric field, F, may be derived.
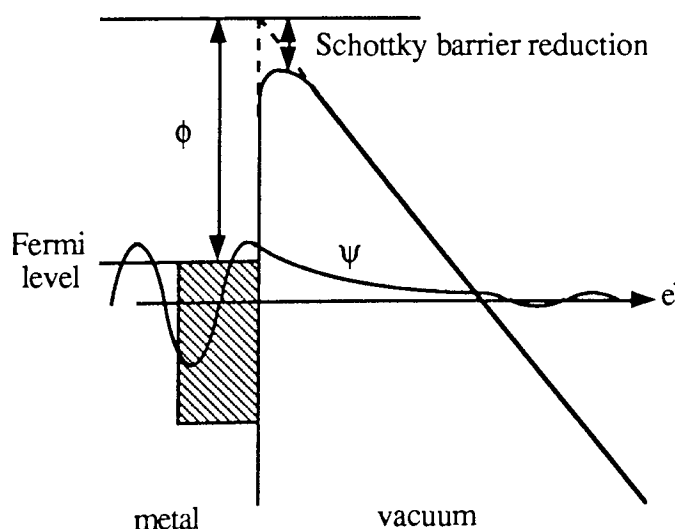
Figure 2.1 Schematic illustration of the tunnelling of an electron through the surface potential barrier due to the application of a strong electric field.

The current density depends solely upon two factors: the flux of electrons incident on the surface and the probability of these electrons tunnelling through the surface barrier. By the application of Fermi-Dirac statistics, the electron supply function $N(W_x)dW_x$, which is the flux of electrons incident normal on the surface with normal energy components between W_x and W_x+dW_x, may be determined. Secondly, the transmission coefficient $D(W_x)$, representing the probability of electrons in that energy range being transmitted through the barrier is obtained by solving the Schrœdinger equation using the WKB approximation [18]. The emitted current density, J, is then obtained by summing over all possible electron energies according to the equation

$$J = e \int_{all\ E} D(W_x)N(W_x)dW_x \qquad\qquad 2.1$$

For temperatures <300K, this equation yields the following result

$$J = \frac{1.54 \times 10^{-6} F^2}{\phi\ t^2(y)} \exp\left[\frac{-6.83 \times 10^9 \phi^{1.5} v(y)}{F}\right] \qquad\qquad 2.2$$

where F is the surface electric field and ϕ the emitting surface work function. $t(y)$ and $v(y)$ are tabulated dimensionless elliptic functions [19,20] of the variable $y = 3.79 \times 10^{-5} F^{1.5}/\phi$. Within the field range for stable emission currents, viz $1 \times 10^9 < F < 6 \times 10^9$ Vm^{-1}, these functions have values $t(y) \approx 1$ and $v(y) = 0.956 - 1.062y^2$. Substituting these approximations into equation 2.2 and rearranging gives the most useful form of the F-N equation

$$J = 1.54 \times 10^{-6} \left[\frac{10^{4.54\phi}}{\phi}\right]^{-1/2} F^2 \exp\left[\frac{-6.83 \times 10^9 \phi^{1.5}}{F}\right] \qquad\qquad 2.3$$

In the case of a practical emission regime, particularly that of a broad area electrode, the surface field, F_{mic}, over some emitting area A_e may be locally enhanced above the macroscopic field, F_{mac}, by a factor ß where

$$ß = \frac{F_{mic}}{F_{mac}} \qquad\qquad 2.4$$

The emission current, I, is related to the current density by the equation $I = JA_e$ and thus the F-N law may be expressed as

$$I = A_e\ 1.54 \times 10^{-6} \left[\frac{10^{4.54\phi}}{\phi}\right]^{-1/2} \frac{(ßV)^2}{d^2} \exp\left[\frac{-6.83 \times 10^9 \phi^{1.5} d}{V}\right] \qquad\qquad 2.5$$

where d is the electrode spacing and V the applied gap voltage. Plotting the current-voltage characteristic of a gap with a single emitter in the form of $\ln(I/V^2)$ vs $(1/V)$ would then result in a straight line of slope

$$m = -6.53 \times 10^9 \phi^{1.5} (d/\beta)$$ 2.6

and intercept

$$c = \ln \left[1.54 \times 10^{-6} \left[\frac{10^{4.54\phi} A_e \beta^2}{\phi d^2} \right]^{-1/2} \right]$$ 2.7

Since d is known and ϕ may be assumed from the bulk metal value, the slope of an F-N plot yields the ß-factor of an emitter, and by substitution into equation 2.7, the emitting area A_e may then be calculated.

2.2.2 Energy distribution of field emitted electrons from a clean surface

In practice, observations of field emitted electron spectra reveal that the electron supply function depends on the total energy and not the normal energy distribution [21]. This effect has been studied theoretically by Young [22] using the free electron theory and two new parameters defined as:

i) $N(W,E)dWdE$ = number of electrons incident upon the surface per unit area per second with a total energy in the range E to E+dE and having an x-component normal to the surface in the energy range W to W+dW.
ii) $P(W,E)dWdE = N(W,E)D(W)dWdE$ which is the number of electrons in the given energy ranges transmitted through the energy barrier.

The total energy distribution is then given by the relation

$$P(E)dE = \int P(W,E)dWdE$$ 2.8

which was shown by Young [22] to be given by

$$P(E)dE = \frac{4\pi m Dp}{h^3} \exp(-c) \frac{\exp(E-E_f/Dp)dE}{1+\exp(E-E_f/K_bT)}$$ 2.9

where

$$c = \frac{4e^{1/2}(2m\phi^3)^{1/2}}{3hF} v(y)$$ 2.10

28

$$D_p = \frac{he^{1/2}F}{2(2m\phi)^{1/2}} \cdot \frac{1}{t(y)}$$ 2.11

with $E_f = -\phi$ and the other parameters as previously defined. Fig. 2.2(a) shows the close agreement between the experimentally measured energy distribution and the total energy theory, while Fig. 2.2(b) shows the effect of temperature on the theoretical normal and total energy distributions.

Figure 2.2. Graphs showing a) the predicted theoretical energy distributions using the normal and total energy distributions compared with experimental result and b) the predicted variation of the emission energy distribution with temperature (from [22]).

Furthermore it should be noted that the Free-Electron model does not always apply, since the band structure can modify the electron energy distribution. The interested reader is referred to the work of Modinos [23] for a treatment of these effects, as they are beyond the scope of this thesis.

2.2.3 Temperature dependence of emission current

The basic Fowler-Nordheim theory is calculated for a temperature of 0K, but is valid for temperatures up to ~300K. Above this temperature however, many electrons begin to occupy states above the Fermi level, as shown by the high temperature electron energy distribution in Fig. 2.2(b). Electrons at these higher energies clearly see a much narrower barrier than those at the Fermi level and will therefore have a higher tunnelling probability. Therefore, there is an increase in the emission current owing to an increased population of electrons with a high tunnelling probability. This effect has been considered by several authors [24,25], and for T<1500K, Murphy and Good showed that the temperature assisted field emission current density, J_T, can be accurately described by the equation [24]

$$J_T = J \frac{\pi p}{\sin(\pi p)} \qquad 2.12$$

where J is the low temperature F-N current density, and p is a dimensionless temperature and field dependent parameter given by

$$p \approx 9.3 \times 10^5 \phi^{1/2} T/E \qquad 2.13$$

At higher temperatures, when p>2/3, the approximations leading to the above expression become invalid and tabulated data of the more recent analyses by Christov [25] should be used.

2.2.4 Resonant tunnelling

The Fowler-Nordheim model [4] developed above applies to atomically clean metallic surfaces. The addition of surface adsorbates can result in a significant alteration of the field emission current from metallic surfaces [21]. These effects could not be adequately explained by models describing a change in work function, or polarisation effects arising from the adsorbates [21]. For example, Ermich [26] found that molecular nitrogen adsorbed on the <100> plane of tungsten resulted in an increase in the field emission current of between 10^2 - 10^4 associated with an increase in the work function as derived from an F-N plot. According to the F-N model, these effects are contradictory.
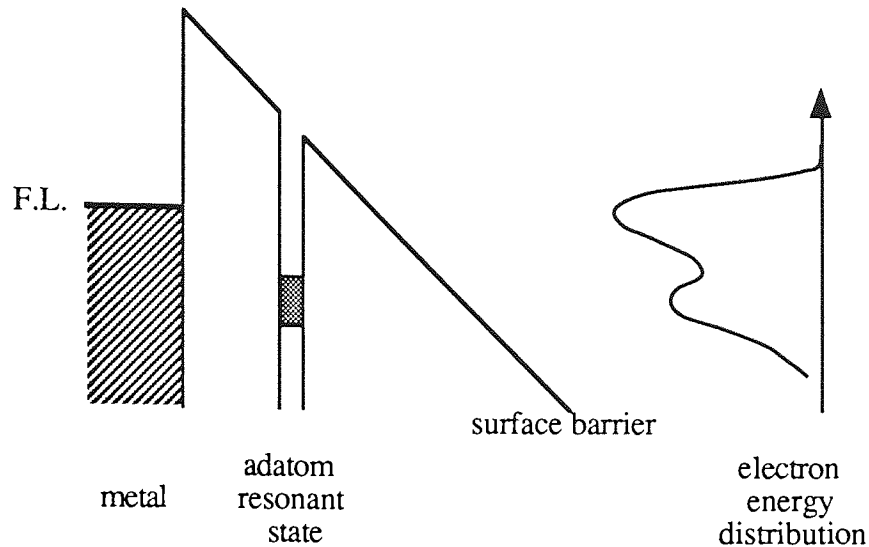
Figure 2.3 Schematic diagram illustrating the potential barrier due to a resonant tunnelling state and the effect such a state has upon the field emitted energy distribution.

Duke and Alferieff [27] developed a model that explained these results by considering quantum mechanical tunnelling via virtual excited states of the adsorbed atoms or molecules, as illustrated in Fig. 2.3. The addition of these states can modify the surface barrier and therefore the probability of tunnelling through that barrier. According to the model, should an adatom have a virtual energy level at or near the sample Fermi level, then electrons may tunnel either directly into vacuum or via the resonant state. The resonant state will have a narrower barrier width and therefore a higher tunnelling probability [27] resulting in an increase in the current density at that particular energy. In practice, the electron wavefunctions of the metal overlap those of the adatom and thus tend to broaden the width of the virtual states [27].

For experimental purposes, this effect can be used to probe the energy levels of adatoms and molecules [21], and is quantified by comparing the measured energy distribution of an atomically clean surface, $j(\varepsilon)$, with that due to the metal surface and adsorbates, $j'(\varepsilon)$, to calculate an enhancement factor, $R(\varepsilon)$, according to the equation

$$R(\varepsilon) = j'(\varepsilon)/j(\varepsilon) \qquad\qquad 2.14$$

A typical example is shown in Fig. 2.4 for the case of Ba atoms adsorbed on <110> molybdenum [28]. These results show relatively low enhancement factors of <2. According to the theory, the maximum enhancement would occur for a resonant state at the centre of the barrier [27], however an adatom is typically at a distance of ~0.2nm compared with a barrier width of ~3nm thus resulting in such low values of $R(\varepsilon)$.

31

Figure 2.4 R(ϵ) due to barium atoms adsorbed on the <110> crystal plane of molybdenum (from [28]).

2.3 Non-metallic electron emission processes

2.3.1 Evidence indicating alternative field emission processes on broad area cathodes

Although the micro-protrusion model was for many years believed to provide sufficient explanation for the existence of pre-breakdown currents, the hypothesis has been contradicted by an increasing body of evidence that has been derived from advances in experimental techniques since the 1960's. Such evidence includes: F-N plots that are both curved and variable, switch-on phenomena, noisy and unstable pre-breakdown currents and microdischarges.

During the 1960's Cox and Hurley were the first to present evidence contradicting the micro-protrusion hypothesis. Cox [29] made a large number of tests on 14mm diameter copper-chromium alloy vacuum switches with a plane-parallel gap spacing of 6mm at a pressure of 2×10^{-10} mBar. In about 1% of the tests he found an unstable emission with an irreversible hysteresis-like I-V characteristic. Hurley, working on OFHC copper using a point anode probe [30], showed the existence of two types of site which he termed 'a' and 'b' sites, which had different emission properties. 'a' sites generally gave straight-line F-N plots and went to breakdown at currents $> 5 \times 10^{-5}$A with resulting site destruction. However, 'b' sites were characterised by an I-V characteristic having a negative resistance profile as shown in Fig. 2.5. Furthermore, 'b' site breakdown occured randomly in the current range 10^{-5} to 10^{-3}A, but without the destruction of the site.

Further strong evidence against the micro-protrusion model was provided

by Cox *et al* [5,31] in a later series of experiments by the use of an anode probe hole technique for locating emission sites on broad area cathodes. By scanning the cathode relative to the anode probe hole emission sites could be located to an accuracy of 0.1mm in the initial attempt [31], and to within 10μm using a refined technique housed in an SEM [5].
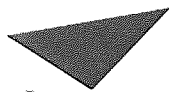
Aston University

Content has been removed for copyright reasons

Figure 2.5 Graph showing 'b' site negative resistance profile (from [30]).

An early application of the technique above utilised a tungsten tip embedded in a planar copper cathode to simulate an emission site [31]. The emission was found to originate not from this artificial micro-protrusion, but from a close, though definitely separate, location. In a refined experimental system, housed in an upgraded SEM, the important technological finding emerged that emission could occur from superficially adhering dust particles. Furthermore, it was shown that this could largely be prevented by ultrasonic cleaning followed by limited handling in a clean-room environment. Emission sites were then found to be located at cracks and grain boundaries, as shown in Fig. 2.6, or at the specimen edge, even after attempts at profiling to prevent a field enhancement in this region [5]. Of more importance, the study failed to locate any surface micro-features or particles that could result in the necessary field enhancement as predicted from the F-N plots.

This work was further developed by Latham and co-workers using a scanning micropoint anode mounted in an SEM [32,33]. By the use of gradually finer anode tips, the resolution of the system could be improved to the order of 3-4μm. Furthermore, the system was capable of revealing the topographical and chemical nature of the emitting particles by use of a built-in X-ray spectroscopy

facility. When viewed under the SEM, the particles typically appeared bright, as shown by Fig. 2.7, thus indicating that they are either insulated from the metal substrate or that they are of an insulating nature themselves. A range of elements, including Al, Au and Ag were identified as being associated with these structures, although it was not possible to determine their chemical composition accurately since the spectrometer could not detect elements below neon. Again, no evidence was found to support the micro-protrusion hypothesis, and, in fact, a control experiment found that emission occured from surface contaminant particles in preference to deliberately created metallic asperities [32].
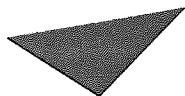
Aston University

Content has been removed for copyright reasons

Figure 2.6 a) Surface in region of emission site as viewed in the SEM and b) emission current distribution for above site (from [5]).

More recent work by Niedermann *et al* [7,34] on emission from broad area niobium cathodes using the same technique, but incorporating improved analytical facilities, has yielded further interesting results. Firstly, they have conclusively confirmed that emission is associated with impurity particles, or inclusions, on the cathode surface. Secondly, by the use of a high resolution Auger electron spectrometer, they have identified a range of chemical elements to be present in emitting particles, particularly carbon and oxygen which could not be detected by Athwal and Latham [32]. Thirdly, by the use of an UHV prep-chamber, studies could also be performed into the effects of bulk heating. These found that after

Figure 2.7 SEM image showing that an emission site is associated with a particle which appears bright (from [33]).

annealing at temperatures up to 800°C, the number of emission sites was increased, with sites (i.e. particles) appearing where previously there had been no particles present. On extending the annealing to the higher temperature range of 1200-2000°C, it was found possible to suppress most of the emission sites. These results are believed to be explained by migration of impurities present in the bulk of the material to the surface, or back into the bulk. Indeed, performing high temperature heat treatment on niobium cathodes with intentionally introduced emitting carbon particles showed them to disappear co-incidently with the suppression of the emission [12]. In general, the new sites that appeared were composed of carbon, and up to 20% of 'natural' sites were also found to be composed of carbon.

Figure 2.8 Image of cathode spots. Note that flares (arrowed) are also visible from the cathode (from [35]).

35

Further evidence of the non-metallic nature of the emission process has been demonstrated by Hurley and Dooley [35,36]. They investigated the spots of light which could appear on the cathode when a pre-breakdown current flowed (see Fig. 2.8). First noted by Klyarfell and Pokrovskya-Soboleva [37], they investigated the optical spectrum obtained from a cathode spot, shown in Fig. 2.9. They attributed the photo-emission to electro-luminescence produced by the action of the electric field on insulating or semi-conducting surface inclusions. To verify this assumption they investigated the variation of the emitted light intensity with the applied voltage, and showed it to follow the Alfrey-Taylor law which is characteristic of the behaviour of electro-luminescent cells [38]. In a later experiment, Hurley [39] directly demonstrated that electron emitting sites on copper were sources of electro-luminescence.

Figure 2.9 Optical spectrum of cathode spots (from [36]).

A comprehensive series of electron spectroscopy studies, undertaken by Latham and co-workers [8,32,33,40], have greatly improved the state of knowledge about the emission process. Perhaps the most important result, shown in Fig. 2.10, was the comparison of the energy spectrum from an artificial metallic tip with that originating from a natural emission site [32]. This clearly revealed that the electrons emitted from an emission site have energies well below the Fermi level. Furthermore, the width (FWHM) is considerably broader than for metallic emission and lacks the sharp high energy edge. The FWHM and shift of the spectral peak below the substrate Fermi level have also been shown to be strongly dependent upon the applied gap field [32], as indicated in Fig. 2.11. Often, it is also observed that the spectra exhibit a multi-peaked structure [33]. These

Figure 2.10 Comparison of the emission spectra from a) an artificial micro-protrusion and b) a 'natural' emission site (from [32]).

Figure 2.11 Graph indicating the variation in the spectral shift and FWHM with applied gap voltage (from [8]).

experimental results strongly indicate a non-metallic emission mechanism in contradiction to the micro-protrusion hypothesis.

In more recent experiments, Bayliss and Latham [8,41,42] showed that an emission site is often composed of discrete emission sources, or sub-sites (as shown in Fig. 2.12), each of which exhibits a single-peaked spectrum similar to that of Fig. 2.10 (b). Plots of the I-V characteristics of sub-sites also revealed a contact-bulk current limited transition. These findings led to the development of the quantitative band model described in Section 2.4.2, which involved the concept of a hot electron emission mechanism occuring in a metal-insulator-vacuum (MIV) micro-regime to explain the experimental observations.

Aston University

Content has been removed for copyright reasons

Figure 2.12 a) typical image of an emission site showing several sub-sites and b) individual spectra from each of these sub-sites (from [41]).

2.3.2 Broad area electrode emission regimes

Much of the work described in the previous section supports emission occuring through metal-insulator (MI) systems, however more recent work indicates that a variety of different regimes may be involved. Bayliss [42] found, whilst experimenting on intentionally oxidized samples, that a flashover resulted in the formation of many more emission centres. This effect is illustrated by the high resolution maps of Fig. 2.13, which were recorded at currents of 4μA and 40μA respectively for the same gap voltage of 6kV. On the basis of Auger analysis, these were determined to be 'splashed' particles of anode material deposited on the thick oxide layer, and the emission was therefore assumed to result from a metal-insulator-metal (MIM) emission regime.
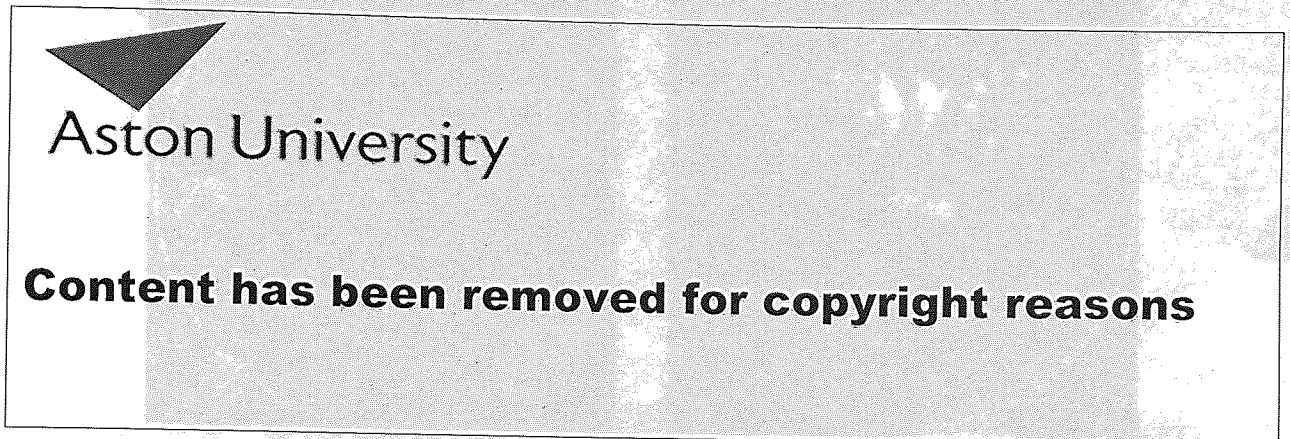
Figure 2.13 Site maps of a 14mm diameter sample showing the site distribution a) before and b) after a flashover (from [42]).

Figure 2.14 Emission site distribution due to 9 carbon particles placed on an electrode in a triangular array showing each has become an emission centre (from [34]).

Much further work has been carried out to investigate artificial sites created by the deposition of carbon particles onto the electrode surface. Such sites were first reported by Athwal *et al* [43], who showed that the deposition of a small 'dot' of pencil lead, or drop of colloidal graphite (aquadag), onto a cathode could promote field emission at gap fields as low as $4MVm^{-1}$. Typical electron energy spectra show the characteristic energy shift and FWHM of 'natural' sites, often in multi-peaked structures. The above findings were confirmed by Noer *et al* [44], who deposited graphitic particles onto the surface of an electrode that had been heat treated to be emission free up to fields of $100MVm^{-1}$. As shown in Fig. 2.14, they were able to demonstrate that all the particles became emitters at an average field of $30\ MVm^{-1}$. Similar results have also been obtained on anodized samples, with oxide thicknesses of up to 1300Å [42]. High emissivity can also be obtained from cathodes coated in resin-particle composite films [45] including iron, silicon, silicon carbide and, particularly, carbon: these structures consist of particles embedded in a resin film and thus have a metal-insulator-metal-insulator layering, yet they can give very high emission currents of tens of micro-amps at field levels of only a few MVm^{-1}.

2.4 Non-metallic field induced electron emission processes

This section describes the principal theoretical models that have been developed thus far to explain the physical origin of pre-breakdown emission currents. They are generally based on 'non-metallic' emission processes, and it will be shown how they are better able to explain the principal experimental observations than the traditional F-N model.

2.4.1 The filamentary model

This model was developed by Hurley [46] in an attempt to give a qualitative explanation of his cathode electro-luminescence observations [39]. In fact, the filamentary model is based on the well-known Ovshinsky 'switching' phenomenon [47] observed in thin metal-insulator/semiconductor-metal devices. As discussed by Dearnaley *et al* [48] and Adler *et al* [49], such devices switch from an 'off' to an 'on' state at an applied field in the range $10\text{-}100MVm^{-1}$ with a conductivity increase of up to a factor of 10^8. This process is explained by the authors in terms of the formation of conducting filaments through the insulating layer. Furthermore, these filaments can be electroformed if the current is applied over a time scale >1ms, such that fundamental changes result in the structure of the dielectric in the region of the filament. Hurley assumed that the same process could occur in the ambient oxide layer of metallic electrodes at field strengths of $>10MVm^{-1}$ and could provide
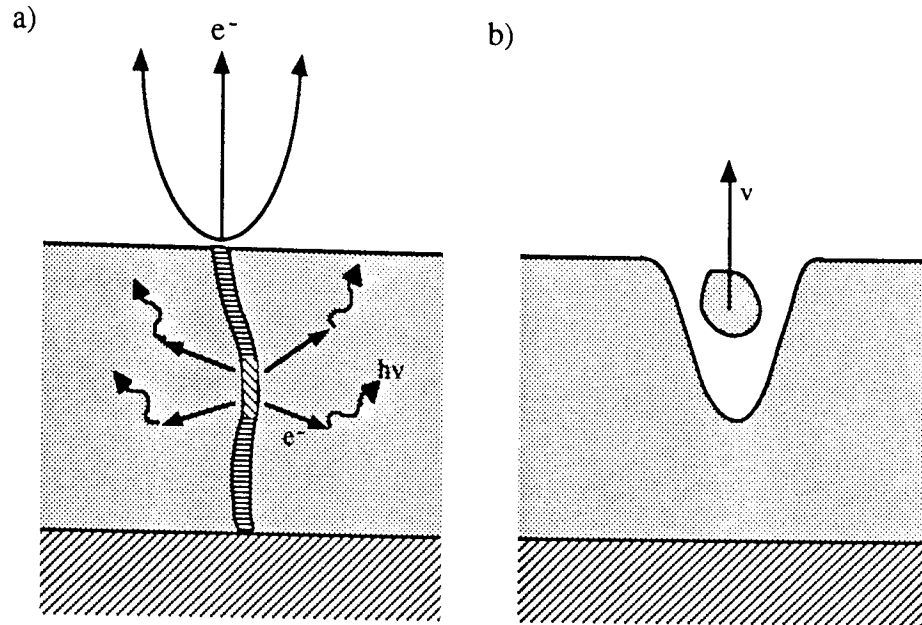
Figure 2.15 Schematic of the filament model emission process showing a) steady state emission with scattering of electrons from high resistance regions producing electro-luminescence and b) breakdown induced by heating and vaporisation of a region of the filament.

an explanation of his observed emission and electro-luminescence results.

Hurley reasoned that a conducting filament through the ambient oxide layer would experience a field enhancement at the tip of sufficient magnitude to enable F-N emission to occur (see Fig. 2.15). Electro-luminescence could then be explained by the scattering of electrons accelerated across high resistance sections of the filament into the bulk of the oxide where impact ionisation events and recombination processes, as described by Hickmott [50], would be experienced. Furthermore, the metal-insulator interface conditions could be used to explain the negative resistance behaviour of 'b' sites observed in their I-V characteristics. It would be expected that under certain conditions, sections of the filament could become so heated that vaporisation would occur and thus explain the occurence of micro-discharges.

2.4.2 The dynamic field emission model

Halbritter [51] has described a model which explains emission in terms of a dynamic process through low density hydrocarbon surface impurities. By assuming a continuous population of electron traps in the impurity bandgap, an applied field of $\sim 10 \text{MVm}^{-1}$ could cause electron emission from these traps by stochastic processes. Such electrons would then be heated by acceleration due to the penetrating electric field to energies between 1-10eV. Collisions of these electrons with atoms would then result in excited atomic states that could decay by a variety of emission processes: photon, electron or atom (gas desorption). A

41

positive charge distribution would result in the impurity leading to a local field enhancement which in turn causes a tunnelling current to flow from the metal. Successive impact ionisations then lead to an avalanche, i.e. a high conductivity channel would be formed. Such avalanche events have been observed to occur non-destructively in SiO_2 [52]. Only the high energy electrons, after acceleration across the impurity, would have the necessary energy to escape owing to the positive charge distribution. The rest would be slowed by collisions and neutralise the positive charge, thus leading to pulsed emission occuring under dc field conditions.

According to the calculations of Halbritter [51], these pulsations would occur on a timescale of nanoseconds for 100Å thick impurity structures. In order for an avalanche to occur, the mean free path for electrons, λ_e, must be large compared to the thickness of the impurity hence the postulation of low density irregular hydrocarbon impurities, which can have λ_e as great as 200Å. There is limited experimental evidence to support this hypothesis, since, for example, in only very few cases did Niedermann *et al* [12] find any traces of hydrocarbons at emission sites. The mechanism also implies that emission could be triggered externally by visible photons, which is not observed experimentally.

2.4.3 The antenna model

Consideration of the emission regime for deposited carbon [43], or breakdown induced emission sites from 'splashes' of anode material deposited on the cathode [42], suggests a model based on conducting particles insulated from the substrate as shown in Fig. 2.16. Graphitic carbon would be likely to occur in the shape of thin flakes, and is essentially conducting at the low current densities found at field emission sites. Such a particle, insulated from the substrate, would then behave as an antenna probing the electric potential at some distance h above the electrode surface. As a conducting particle has the same potential at all points, this would result in the probed potential being developed across the insulator at the point of contact of the particle to the surface.

Although a conducting particle would cause a modification of the field near the surface, an estimate of the effect may be made by assuming an homogenous field. For a particle of height h, the order of field enhancement is ß = h/d, where d is the thickness of the insulator. Such a locally high field then causes electrons to tunnel into the insulator where they acquire sufficient kinetic energy to be transmitted through the flake. However, not all of these electrons would escape: some will inevitably lose energy by collision and thus be captured by the flake. Others could cause secondary electrons to be emitted into the vacuum. Such processes would therefore affect the total charge on the flake which would alter the

potential across the insulator and hence the tunnelling current. This charging process could thus potentially explain the observation of site switching and emission current instability [33].
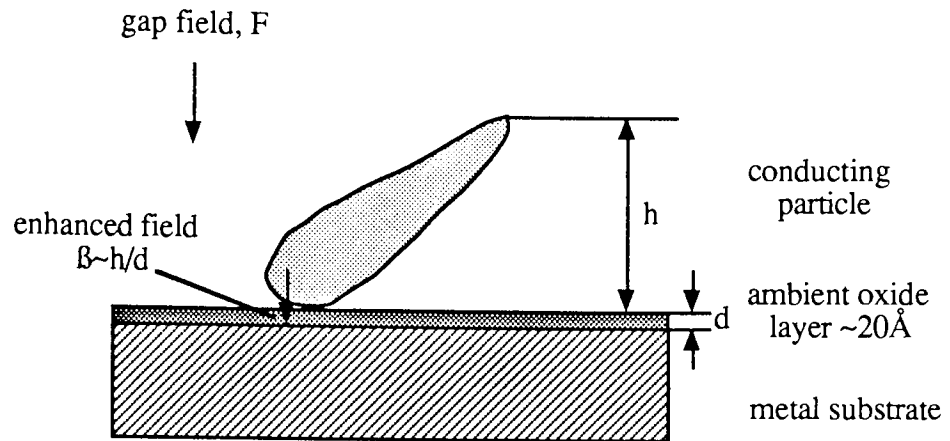
Figure 2.16 Schematic illustrating how the antenna effect could promote FIEE.

Some support for this model is found by the observation of diffraction like emission images [53] from some natural sites, and from artifical graphite particles. Alterations in the charge state however, would result in the emission not following the F-N law, although such deviations are sometimes observed experimentally.

2.4.4 The hot electron emission model

Developed by Latham and co-workers [8,54,55], this model is based on electron conduction through a dielectric, with subsequent emission of field heated electrons into the vacuum. The model arose from observations of a wide range of experimental measurements, particularly the energy distribution of electrons emitted from sites on broad area cathodes. As shown in Fig. 2.17, the emission regime is assumed to be some form of 'foreign' dielectric-like surface inclusion, or anomalously thick oxide aggregation, of between 0.1-10μm thick in the direction of the applied field F.

Such a structure would therefore support a potential drop of 2-3V for an applied field of 10-20MVm^{-1}. This assumption is directly supported by observations performed in SEM's using point anode probe techniques [7,32], which have shown emitting particles to have such dimensions. Furthermore, as discussed by Halbritter [57], it is assumed that the surface inclusions are only partly crystalline and certainly impure, so that there will be a resulting distribution of both trapping states and donor centres within the inclusion. It is then required that the metal-insulator interface forms a blocking contact under low field conditions (Fig. 2.18(a)). At certain microscopic locations on this interface however, it is assumed that a contact favourable to tunnelling exists; this could be

43

due, for example, to marked band bending arising from local concentrations of impurity atoms in the insulator which provide the necessary donor centres.
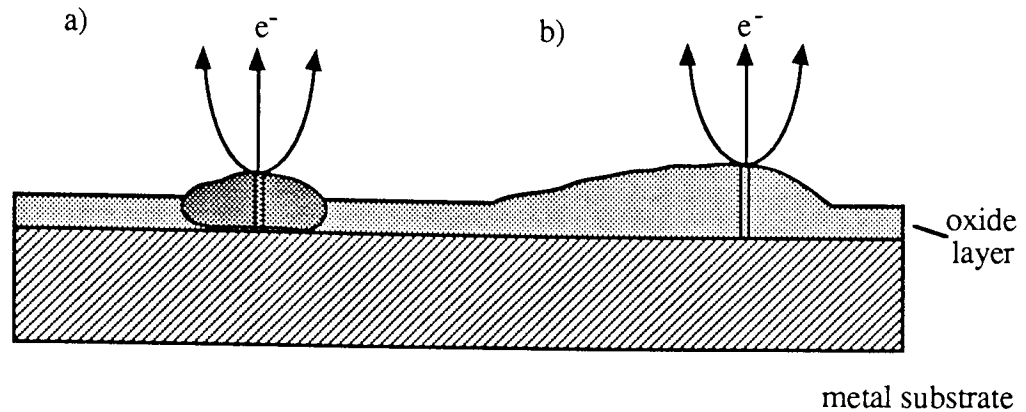
Figure 2.17 Schematic illustrating the metal-insulator emission regime caused by either a) a dielectric particle or b) thick region of the surface oxide layer.

2.4.4.1 The switch-on mechanism

Under zero-field conditions, the energy band diagram of such a localised region, shown in Fig. 2.18(a), is characterised by a high internal field at the metal-insulator interface and a depletion layer just within the insulator. On application of an external field, penetration through the dielectric will result in a reinforcement of the internal field at the MI contact, and, once a certain threshold value of applied field is exceeded, the tunnelling of electrons from the metal substrate into the insulator (Fig. 2.18(b)). Eventually, these electrons will fill any empty traps within the insulator thus shifting the Fermi level progressively closer to the conduction band edge due to the increased electron density within the insulator. As the field is increased further, more electrons will tunnel into the insulator, but since the traps are now full, these electrons will accumulate at the insulator-vacuum interface to fill the surface states and create a degenerate pool of cold electrons in the conduction band. This surface charge will thus screen the external field from the insulator and so remove the conditions for tunnelling to lead to the state shown in Fig. 2.18(c). As the field is further increased however, the situation can become as shown by Fig. 2.18(d), with electron tunnelling again occuring. In this state, an electron tunnelling into the conduction band will be rapidly accelerated towards the vacuum interface region where the effective temperature, T_e, of electrons stored near this interface will be increased by scattering processes. If T_e is high enough, then electrons may be emitted thermionically over the reduced Schottky surface barrier.

As continuous emission is established, a transition takes place to leave the system in the state shown by Fig. 2.18(e). Electrons at the surface of the insulator are preferentially emitted resulting in an increase of the surface field relative to the bulk field and thus causing a charge redistribution to give the highest electron

Figure 2.18 The band state of the insulator with applied field. a) is the initial state with no applied field. (b), (c) and (d) illustrate the changes with increasing applied field until stable emission is initiated in state (e) (from [8]).

density a short way into the insulator [58]. The most important feature of this switch-on mechanism is that no permanent structural changes occur to the emission channel region, but that the channel path is essentially 'memorized' by the surface charge distribution. An energy band configuration similar to that of Fig. 2.18(d) results immediately after re-application of a field. Thus, should the applied field be reduced to zero for a short time, a switch-on process would be unlikely to recur. Furthermore, it would be expected that emission would continue even if the applied field is reduced to below the switch-on value.

Figure 2.19 shows the field distribution associated with an emitting conduction channel (i.e. in the state of Fig. 2.18(e)). Two field enhancement factors may then be defined: β_1, the ratio of the vacuum field immediately above the conducting channel, F_{tip}, to the macroscopic electrode gap field, F_0; and β_2, the ratio of the average field within the filament, F_{fil}, to the insulator field well away from the channel, F_{ins}. Thus

$$\beta_1 = F_{tip}/F_0 \qquad \text{and} \qquad \beta_2 = F_{fil}/F_{ins}$$

Since $F_{ins} = F_0/\varepsilon_r$,

$$\frac{F_{tip}}{F_{fil}} = \varepsilon_r \frac{\beta_1}{\beta_2} \qquad\qquad 2.15$$
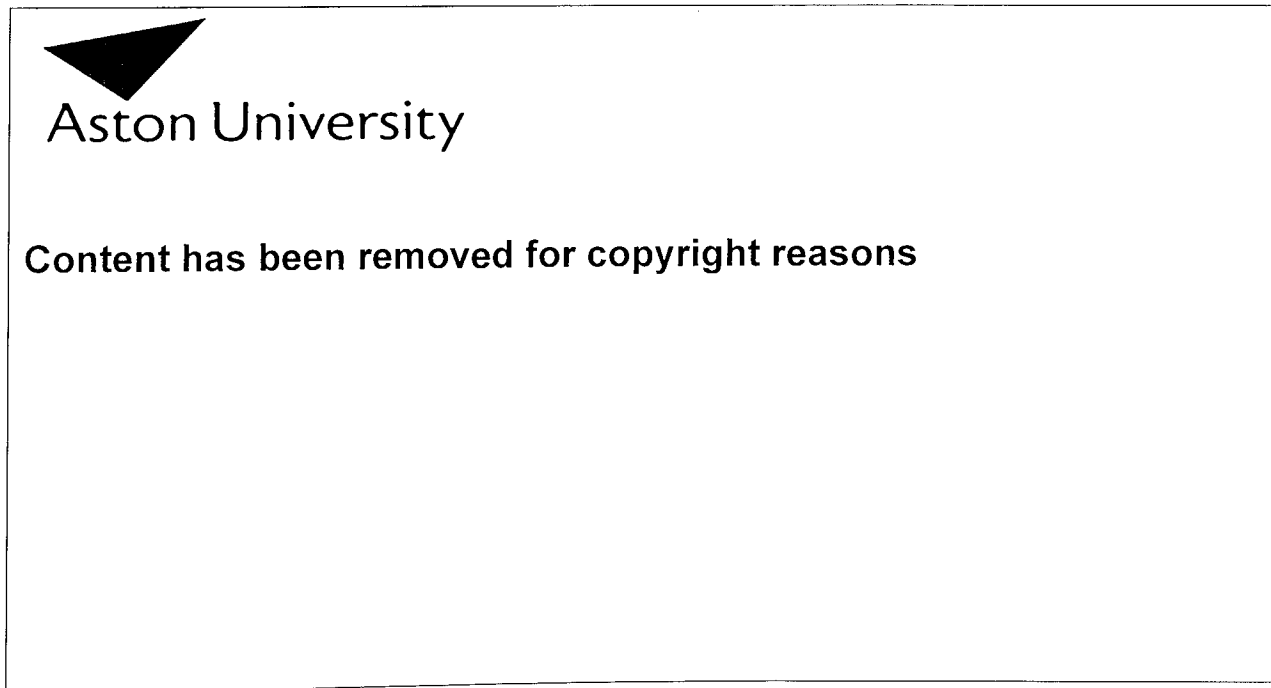
Figure 2.19 The field intensity distribution within a conducting filament (from [8])

Figure 2.18 Detailed emission site band diagram in the 'on' state (from [8]).

The 'switch-on' model is not completely consistent with experimental observation. Under conditions of good vacuum it is found that once a site is switched on then it does not exhibit another 'switch-on' process no matter how long it is left under zero-field conditions; i.e. it is difficult to see how the proposed switching process could memorize the channel path for a long time [59], although it is possible that a forming process may occur whereby the properties of the dielectric are permanently altered in the vicinity of the emission site c.f. the filamentary model [46]. Furthermore, even if the memorizing effect holds at room temperature, some electron traps and surface states would be expected to relax back to the initial pre-switch-on state with sample heating to 600°C. Such effects have not, however, been observed during thermal stimulation studies [61], although it is

possible that permanent changes occur to the dielectric in the region of the filament during conduction [46]. Even if the memory effect held during heating, neutralisation of charge would be expected to occur both at the surface and within the insulator-vacuum interface region implying the likely necessity of another switch-on process occuring. However, ion beam bombardment studies [41,61] have not shown this.

2.4.4.2 The emission current density

From a detailed study of the energy band diagram for the 'on' state, as shown in Fig. 2.20, it may be seen that the surface region of the insulator contains a dense accumulation of the stored electron gas. It would therefore be expected that this region would have similar electronic properties to a metal. This situation, as the high field limit of thermionic emission, has been considered by Murphy and Good [24], who derived the following equation to give the current density

$$J = \frac{4\pi me}{h^3} \cdot \frac{\pi/N}{\sin(\pi/N)} K_b^2 T_e^2 \exp\left[\cdot \frac{-(\phi - b(F/a))^{1/2}}{K_b T_e} \right] \qquad 2.16$$

where N is defined as

$$N = \frac{K_b T_e}{b} \left[\frac{F}{a} \right]^{-3/4} \qquad 2.17$$

and is a factor determining the shape of the energy spectrum, typically having a value of less than 1.6 [8,42].

Both the electronic properties of the metal-insulator contact junction and the bulk material of the insulator will influence the current density. As discussed by Simmons [62], this will be manifested as a transition from contact-limited to bulk-limited conduction. In the contact-limited region, the J-V characteristic will be given by [62]

$$J_t = \frac{5.56 \times 10^{-14}}{\epsilon^* \phi} N_D(V_c + \phi_m - \phi_i) \cdot \exp\left[-3.6 \times 10^{13} \left(\frac{\phi^3}{N_D(V_c + \phi_m - \phi_i)} \right)^{1/2} \right] \qquad 2.18$$

where ϕ_m and ϕ_i are the metal and insulator work functions respectively, ϕ is the contact barrier height, ϵ^* the high frequency dielectric constant of the insulator, N_D the donor density and V_c the potential across the contact junction due to the applied field. This equation predicts a sharply rising current with applied voltage, and hence a rapidly falling contact resistance that is essentially independent of temperature.

For low fields, the current density for the bulk-limited region follows the equation [59]

$$J_0 = e\mu \frac{V_b}{d} N_c \left[\frac{N_D}{N_T}\right]^{1/2} \exp\left[-\frac{E_D + E_T}{2K_b T_e}\right] \qquad 2.19$$

where N_C is the effective density of states in the insulator, N_D the donor density, N_T the trap density, E_D and E_T the donor and trap energy levels respectively, μ the electron mobility and V_b the potential across the bulk due to the applied field. This equation applies for the case of $E_T > F_L > E_D$, where F_L is the Fermi level, and when all the energy levels are beneath the insulator conduction band and virtually all the electron traps are filled. For the high field case, where the Poole-Frenkel effect must be considered (the field assisted thermal ionisation of donors and traps), the bulk conductivity becomes field dependent, and the J-V relationship is expressed as

$$J = J_0 \exp\left[\frac{e}{K_b T_e} \left[\frac{eV_b}{\pi\varepsilon_r\varepsilon_0 d}\right]^{1/2}\right] \qquad 2.20$$

or

$$J = J_0 \exp\left[\frac{e}{2K_b T_e} \left[\frac{eV_b}{\pi\varepsilon_r\varepsilon_0 d}\right]^{1/2}\right] \qquad 2.21$$

depending upon the nature and position of the traps [62].

Should the insulator contain a high donor density ($N_D > 10^{24} m^{-3}$) and a high trap density ($N_T > 10^{25} m^{-3}$), then the depletion layer will be very thin and its bulk conductivity will be low despite the high donor density. Under such conditions, a contact-limited to bulk-limited transition may be observed in the current voltage characteristic [62]. Bulk-limited conduction becomes dependent on the Poole-Frenkel effect, and may be illustrated by plotting $\ln(I)$ vs $V^{1/2}$ to separate the bulk and contact-limited regions. The slope of the bulk-limited region is then inversely proportional to $d^{1/2}$, where d is the insulator thickness. This interpretation gives a generally satisfactory explanation of experimental results. From equations 2.20 and 2.21, it may be seen that the bulk region has a finite conductivity independent of applied field i.e. suggesting that the emission current will not become saturated. Experimentally however, it has been shown by Mousa and Latham [63], using a simulated regime, that the emission current does reach a saturation point. This observation suggests that mechanisms other than the Poole-Frenkel effect may be operating in the bulk region.

2.4.4.3 The energy distribution of emitted electrons

Murphy and Good [24] also considered the energy distribution for the high-field limit of thermionic emission, which is applicable to the emission regime as discussed in the previous section [8,42]. As has already been considered, the energy spectra correspond to the total energy distribution P(E) rather than the normal energy distribution P(W). Unfortunately, Murphy and Good developed their analysis in terms of this latter quantity. However, their transmission coefficient, D(W), remains valid, and may therefore be used in conjunction with the total energy supply function, N(W,E)dWdE as developed by Young [22] in order to derive the required emitted electron energy distribution, viz

$$P(E)dE = \int_{W=-\infty}^{W=E} D(W)N(W,E)dWdE \qquad 2.22$$

Substitution from Murphy and Good [24] then gives

$$D(W) = \frac{1}{1+\exp\{-\pi(F/a)^{-1/4}[1+(W/b)(F/a)^{-1/2}]\}} \qquad 2.23$$

and from Young [22]

$$N(W,E)dEdW = \frac{4\pi m}{h^3} \cdot \frac{dWdE}{1+\exp[(E-E_f)/K_bT_e]} \qquad 2.24$$

Integrating Eq. 2.23 then leads to

$$P(E)dE = \frac{4mb}{h^3}\left[\frac{F}{a}\right]^{3/4}\frac{Ln\{1+\exp\{\pi(F/a)^{-1/4}[1+(E/b)(F/a)^{-1/2}]\}}{1+\exp[(E-E_f)/K_bT_e]} dE \qquad 2.25$$

where F corresponds to the microscopically enhanced surface field at the top of the emitting channel, E_f is the Fermi level, T_e the temperature of the hot electron population behind the surface barrier and a and b are constants given as

$$a = \frac{m^2e^2}{h^4(4\pi\varepsilon_0)^3} = 5.15 \times 10^{11} \text{Vm}^{-1} \qquad 2.26$$

and

$$b = \frac{me^4}{h^2(4\pi\varepsilon_0)^2} = 27.2 \text{ eV} \qquad 2.27$$

Further, the Fermi energy will itself be equal to $-\phi$, the barrier height at the insulator-vacuum interface.

A further theoretical development of this model [8,42] leads to the important spectral parameters

$$E_p = AK_bT_e - b\left[\frac{F}{a}\right]^{1/2} \qquad\qquad 2.28$$

and

$$f = \frac{K_bT_e[2.328\pi K_bT_e - 1.303b(F/a)^{3/4}]}{\pi K_bT_e - b(F/a)^{3/4}} \qquad\qquad 2.29$$

where E_p is the postion of the spectral peak relative to the substrate cathode Fermi level, while f is the full width half maximum. The second equation indicates that f has the interesting property that it may either increase or decrease with increasing applied field depending on the relative rate of increase of T_e and F.

2.4.4.4 Hot electron temperature

From Fig. 2.18, the insulator surface potential at a conducting channel may be seen to be

$$\frac{d\beta_2}{D\epsilon} V_0 + \phi_m - \phi_i - V^* \qquad\qquad 2.30$$

where D is the electrode gap width, V_0 the voltage applied across the gap, and V^* represents the effect of the stored negative charge, which may be assumed to be constant for moderate changes in the applied field. These negative charges are assumed to be trapped throughout the bulk of the insulator, in the vacuum surface states, and also at the bottom of the conduction band where the barrier is too wide for tunnelling to occur [8,42]. By geometry, the difference between the conduction band edge at the vacuum surface and the metal Fermi level, ΔV (in electron volts) is

$$\Delta V = \frac{d\beta_2}{D\epsilon} V_0 + \chi - \phi_i - V^* \qquad\qquad 2.31$$

where χ is the insulator's electron affinity. In traversing the insulator contact and bulk regions, most electrons lose an energy S (in eV), where S is the measured displacement of the spectral peak from the metal Fermi level. Therefore the energy available to generate hot electrons near the vacuum surface will be

$$\Delta E = \Delta V - S \qquad\qquad 2.32$$

where ΔE is measured from the bottom of the conduction band at the vacuum interface [8,42]. Much of this energy is, however, dissipated by electron interactions with the insulator lattice thermalising to the lattice temperature, T_0. Assuming the hot electron temperature varies linearly with ΔE, then

$$(K_b/e)(T_e - T_0) = \alpha \Delta E \qquad 2.33$$

with α being a constant of unknown value. By substitution of 2.31

$$K_b T_e/e = [(d\beta_2/D\epsilon)V_0 - S + \chi - \phi_i - V^*] + K_b T_0/e \qquad 2.34$$

This derivation is based upon the assumption by Latham [56] that the hot electron temperature is a linear function of ΔE. Although this gives a good fit to the experimental results, it is only a good approximation in the case where the potential drop is over the electron mean free path. For the insulator-vacuum interface conditions assumed by the model however, the potential drop is over ~50nm, which is several electron mean free paths. The electrons would then tend to lose virtually all their energy through lattice scattering processes. This has been taken into account by the model with the addition of a 'loss factor' α in equation 2.33. However, this does not provide a clear physical picture of the electron heating and energy loss processes, which questions the existence of hot electrons under the field conditions assumed by the model [64].

2.4.5 Coherent scattering of electrons by MIM structures

2.4.5.1 Emission images from MIM structures

Athwal *et al* [43] made the first investigation into field induced electron emission (FIEE) arising from intentionally deposited carbon particles on broad area electrodes. In this study, techniques were developed for depositing graphite particles at specific locations on broad area electrodes. SEM micrographs revealed that typical carbon deposits consisted of a random distribution of carbon particles insulated from the substrate electrode with dimensions ranging from sub-micron to 10 microns. Emission measurements under UHV conditions revealed a direct correlation between the spatial location of a deposit and the 'switch-on' of sites at anomalously low applied fields, typically $\leq 8 MVm^{-1}$.

Figure 2.21 gives a typical example of the I-V characteristics and associated F-N plot obtained from a single carbon emission site. These plots illustrate both the extremely emissive nature of such sites and that the F-N plot may be divided into two linear regions. Here the low field region is characterised by β values in the

range 300-1000, whilst the high field region shows ß > 1000. From measurements of the emitted electron energy spectra, Athwal *et al* [43] showed that the emission mechanism was non-metallic in nature, i.e. similar to that occuring for 'natural' sites as described in section 2.3.1.
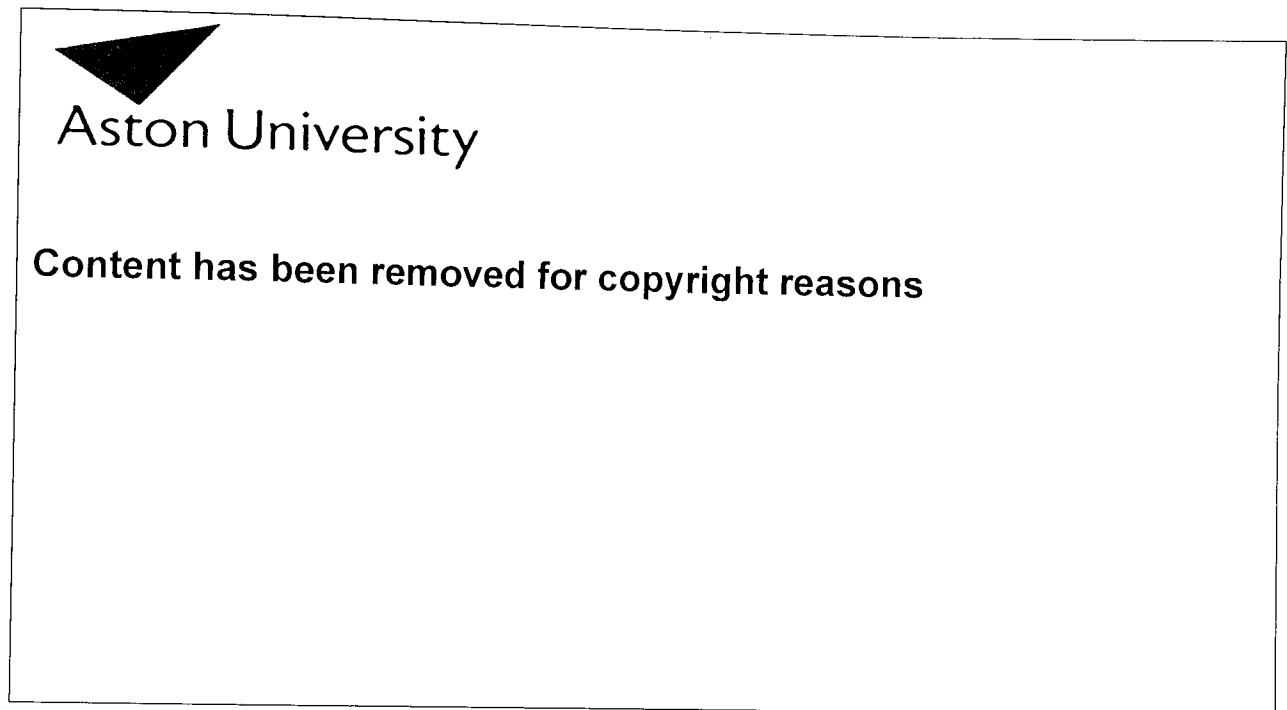
Figure 2.21 Graph showing typical I-V characteristics for a carbon MIM emitter (from [43]).

Further work by Xu and Latham [53] on artificial MIM structures made by the deposition of graphite particles on copper electrodes has improved understanding of this emission process. Studies have found the emission site image, as shown in Fig. 2.22, to consist of arc-like segments. Furthermore, spectroscopic measurements have revealed that arcs of greater radius are of higher energy (Fig. 2.23), and that the radius increases with increasing applied field.

a)   b)   c)
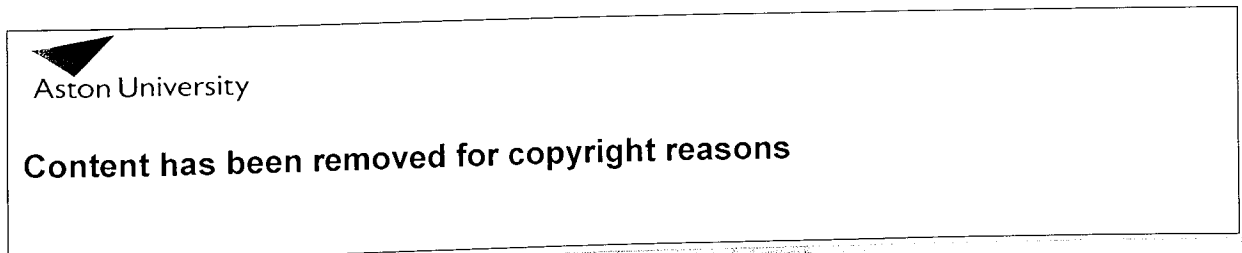
Figure 2.22 Emission site images from MIM emitters showing arc like segments, either a) with diffuse regions such as observed in normal sites, b) singly or c) multiply (from [53])

Similar observations have been made of electron emission occuring from purpose fabricated broad area metal-insulator-metal structures by various authors,

notably Verderber *et al* [65] and Simmons *et al* [66,67]. In particular, Simmons *et al* [67] imaged electrons ejected from the top metal electrode as bright arcs of the same radii superimposed on a faint background. As shown in Fig. 2.24, these arcs all appeared to subtend an angle of <180°. An electron diffraction model in which electrons generated in the insulating medium impinge normally upon the upper metal electrode and undergo a coherent scattering process before being emitted into vacuum was proposed by Simmons *et al* [67] in order to explain his observations.

Aston University

Content has been removed for copyright reasons

Figure 2.23 Energy selective images of an arc showing a) typical energy spectrum and b) total energy image, c) high energy image and d) low energy image (from [53]).

Aston University

Content has been removed for copyright reasons

Figure 2.24 Images of the electron emission from purpose fabricated MIM structures consisting of 1000Å thick alumina dielectric layers on an Al substrate. The voltages indicate the potential drop, v_b, across the insulating layer and the associated exposure times required for each image thus showing the rapid increase in current density with v_b (from [67]).

2.4.5.2 Model of coherent electron scattering from MIM structures

First proposed by Simmons *et al* [67], this model was developed to explain the observation of arc-like emission electron images from artificial MIM structures. These MIM structures consisted of an Al substrate separated from a top Au electrode by a thin insulating layer. Electrons are assumed to be injected into the conduction band of the insulator by a tunnel-hopping process via discrete levels provided by injected ions. Acceleration towards the top Au electrode follows, with a fraction arriving with little loss in energy: i.e. with an energy of $v_b+\eta$, where v_b is the bias voltage across the sandwich and η is the Fermi energy of the top metal electrode. The transverse energy of the electrons will only be of the order of K_bT so the electrons will be incident normally on the top metal electrode.

By Braggs law, coherent scattering occurs through an angle of 2θ, where θ is given by $\sin\theta=\lambda/2d(hkl)$, and the electron wavelength is $\lambda=12.27/(v_b+\eta)^{1/2}$. Thus, for example, the separation of the Au (111) plane is $d_{111} = 2.35\text{Å}$ giving $\theta = 40.5°$ for $v_b=10V$ and therefore a scattering angle of $2\theta=81°$. The electrons would therefore be diffracted almost into the plane of the electrode.

Furthermore, in order to escape from the metal, the electron requires sufficient energy to overcome the work function energy barrier. By consideration of the electron velocity components perpendicular, $v_\perp$ and parallel, $v_{\parallel}$ to the metal surface for all angles, it may be shown that only those electrons satisfying the condition [67]

$$v_\perp\cos\theta > [(\phi+\eta)2/m]^{1/2} \qquad\qquad 2.35$$

may emerge from the surface. Thus, with reference to Fig. 2.25(a), only those electrons diffracted through an angle less than θ normal to the surface will be able to escape, with the rest being internally reflected.

Following a more detailed study of electron emission from artificial sites, Xu and Latham [53] proposed a model based on coherent scattering in the graphite flake, i.e. as shown in Fig. 2.25. As discussed by Athwal *et al* [43], the antenna effect of the graphite flake is responsible for initiating an MIM switching process in the critical insulator region. Electrons are then injected from the substrate into the conduction band of the insulator where, according to the hot electron emission model of Bayliss and Latham [8], they are heated by acceleration towards the graphite flake. Subsequently, coherent scattering occurs in the graphite flake where only those electrons with sufficient energy will be able to escape, as developed in the previous discussion. Xu and Latham [53] further proposed that the high energy electrons would give rise to the well defined outer edge shown by Fig. 2.23(b), whilst the diffuse inner edge results from both incoherent scattering and thermionic

emission of hot electrons. This hypothesis was confirmed initially by preliminary electron spectroscopy measurements [68], and then by the use of a more advanced energy-selective electronic imaging technique [69]. A more detailed account of FIEE from artificial carbon sites, including the effects of photo- and thermal-stimulation, has been given by Xu [61].

a)

b)

$$v_e = \sqrt{\left(\frac{\phi}{2em}\right)}$$

c)

conducting particle

substrate
surface
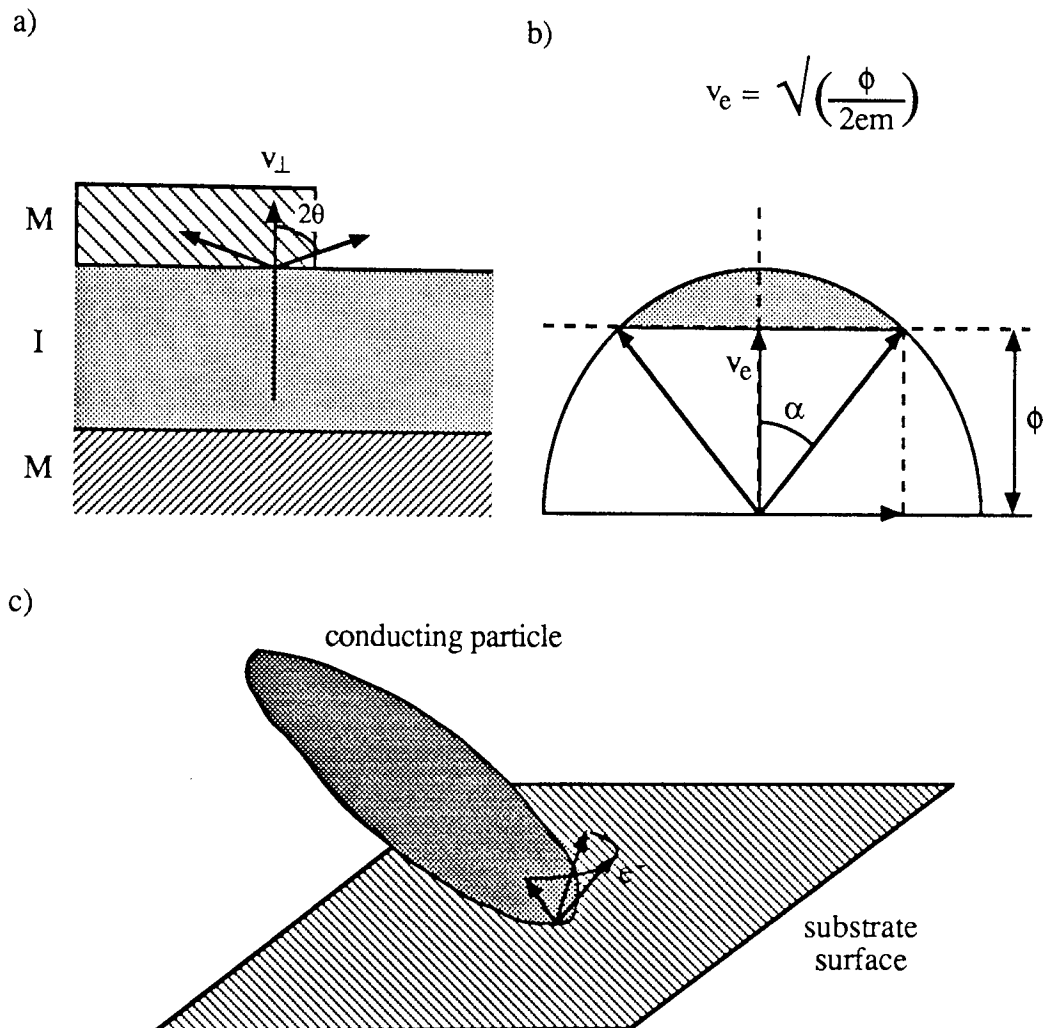
Figure 2.25 a) Schematic structure of an MIM emission site indicating the field enhancement across the insulator by the antenna effect and b) the electron emission process where the shaded region represents those electrons that may be emitted. c) Illustrates the topography of the emission site and indicates how the arc-like images are produced.

CHAPTER 3 : ELECTRON ENERGY ANALYSER

3.1 Introduction

This chapter describes the principal analytical facility employed for the research programme; namely a hemispherical electron energy analyser used for the detection of electron emission sites and their subsequent characterisation. As described elsewhere [61], a 'manual' version of this facility has been used for earlier studies but suffered from some limitations. These were principally: i) the requirement of opening the UHV chamber to air and removing the entire sample manipulation system in order to change samples; and ii) that site distributions and energy spectra had to be recorded photographically from a storage oscilloscope display. Accordingly, the present project included a major commitment to upgrade all elements of this analytical facility.

During the first half of the research programme, much effort was therefore devoted to the redesign of the entire system including the vacuum chamber, sample manipulation and treatment facilities, and the acquisition, storage and analysis of data. In order to maximise flexibility and ease of use, as many operational functions as possible were placed under computer control. To complement this, data acquisition and analysis were computerised in order to increase the rate of data throughput and accuracy of data analysis.

The following sections provide detailed accounts of the operating principles of the spectrometer, the design and implementation of the computer interface circuitry and the incidental software development in greater detail.

3.2 Hemispherical energy analyser

3.2.1 Principle of operation of the hemispherical energy analyser

First discussed by Purcell [70], this type of spectrometer employs an energy dispersive element in order to directly generate an electron energy spectrum. Referring to Fig. 3.1, it may be seen that the hemispheric type of analyser employs a pair of concentric hemispheres with a potential difference ΔV between them such that electrons within the specific energy range of (E-ΔE) to (E+ΔE) entering at slit B traverse the hemisphere and emerge at slit C. Electrons outside these bounds collide with the hemispheres and are either captured or emerge diffusely at C. In order to achieve high energy resolution, a low electron pass energy is required, as discussed in section 3.2.2. Consequently, an interfacing lens assembly, AB, becomes necessary to both decelerate the field emitted electrons (by an accelerating voltage of severAl kV), and to focus them onto the input aperture of the
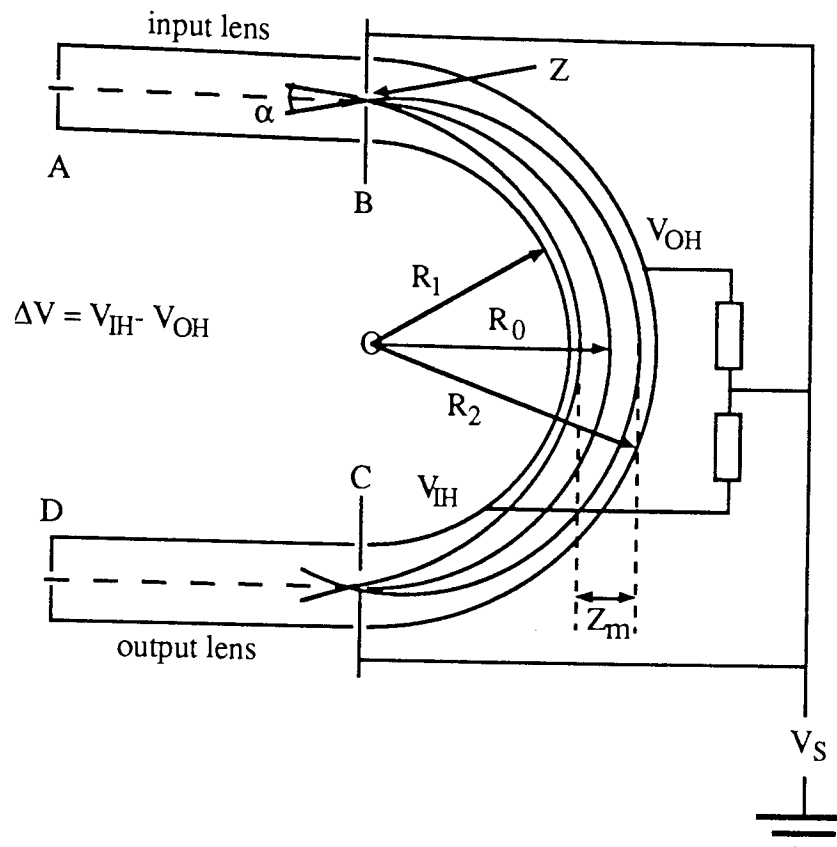
Figure 3.1 Illustration of the principle of operation of a hemispherical analyser.

hemispheres. At the output of the hemispheres a further lens assembly, CD, is required to accelerate the emerging electrons for detection by an electron multiplier and to prevent detection of any scattered electrons emerging at slit C.

The first working example of a hemispherical energy analyser was demonstrated by Kuyatt and Plummer [71] in 1967, utilising a 135° hemispherical element on a 25mm radius giving an energy resolution of 20meV. Braun et al [69] developed an instrument with a full 180° deflection angle and a 50mm radius having an energy resolution of ~25meV. The present Aston instrument has been based on this design, but includes further interfacing lens design modifications by Latham and co-workers [40,42,61] in order to convert the instrument for use with broad area cathodes rather than field emission tips.

3.2.2 Design features of the hemispherical analyser element

The full design equations for a hemispherical analyser were developed by Kuyatt and Plummer [71] , but may be summarised as follows.

Firstly, it may be shown that an electron will follow a path in the mid-sphere between two hemispheres at different potentials according to the equation

$$mv^2 = eF_0R_0 \qquad\qquad 3.1$$

where e, m and v are the electron charge, mass and velocity respectively, and F_0 the electric field strength at radius R_0. For a given electron pass energy, E, this equation of motion may then be satisfied by the application of potentials of V_1 to the inner hemisphere (of radius R_1) and V_2 to the outer hemisphere (of radius R_2) as defined by the equations

$$V_1 = \frac{E}{e}\left[\frac{R_2}{R_1} - 1\right]$$
  3.2

$$V_2 = \frac{E}{e}\left[\frac{R_1}{R_2} - 1\right]$$
  3.3

Thus ΔV, the potential applied across the elements will be

$$\Delta V = \frac{E}{e}\left[\frac{R_2}{R_1} - \frac{R_1}{R_2}\right]$$
  3.4

For an analysing system with input and output slits to the hemispheres of width Z, and an angular beam spread of α, the energy resolution is calculated to be

$$\frac{\Delta E}{E} = \frac{Z}{2R_0} + \frac{\alpha^2}{2}$$
  3.5

In order to minimise the broadening of the transmission function (i.e. the analyser FWHM), the input lens is designed to have the property that

$$\alpha^2 = Z/4R_0$$
  3.6

which substituted into Eq. 3.5 leads to

$$\frac{\Delta E}{E} = \frac{Z}{8R_0}$$
  3.7

Finally, the minimum deviation, Z_m, of the beam from the central radial path between the hemispheres may be shown to be

$$\frac{Z_m}{R_0} = \frac{\Delta E}{E} + \left[\alpha^2 + \left[\frac{Z}{R_0} + \frac{\Delta E}{E}\right]\right]$$
  3.8

These equations show that in order to obtain the best resolution it is necessary that $\Delta E/E$ should be as small as possible thus requiring E, Z and α to be as small as

possible, and R_0 to be as large as possible. However, at very low energies electrons become difficult to control owing to the effects of stray magnetic fields and hemisphere surface patch effects [70], whilst decreasing the aperture size results in a reduction in the total electron transmission through the analyser with a consequent reduction in the signal to noise ratio for a given detector sensitivity. By consideration of all these factors, the Aston instrument was designed to have the parameters shown in Table 3.1 [72].

$E = 2eV$	Energy Resolution ~ 25meV	
$Z = 1mm$	$Z_m = 5mm$	
$R_0 = 50mm$	$R_1 = 40mm$	$R_2 = 60mm$
$\Delta V = 1.67V$	$V_1 = 1.0V$	$V_2 = -0.67V$

Table 3.1 Hemispherical energy analyser design parameters.

In order to minimise the effects of the Earth's magnetic field, a mu-metal shield was fitted over the whole analyser. Subsequently, Bayliss [42] showed that further screening of the Earth's magnetic fields by using Helmholtz coils had no effect on the resolution of the spectrometer.

3.2.3 Analyser input and output lenses

Since the Aston analyser was designed for the study of field emitted electrons, it incorporates an input lens assembly that has to perform several important functions. The first requirement is that the first lens element must double as the anode and be capable of running at a potential of several kilo-volts with respect to the cathode. Secondly, the input lens is required to decelerate the field emitted electrons as the pass energy of the analyser is only 2eV. These requirements are met by a four-stage electron lens assembly, designed by Heddle [73], that both decelerates the incoming electrons and focusses them onto the input aperture of the hemispherical energy analysis element. Furthermore, a pair of x-y deflector plates were incorporated in the second stage of the input lens to enable fine steering of the electron beam.

The output lenses, consisting of three stages (and including two further pairs of x-y deflector plates), re-accelerate the emerging electrons to approximately 200eV, and focusses them onto the input of the electron multiplier. They also serve the function of filtering out any electrons that have been scattered in the hemispheres, but emerged at slit C, so that they do not produce a spurious signal. The layout of these lens assemblies and the analyser system is shown schematically in Fig. 3.2.

phosphor screen

x-y deflection plates

V4

probe hole ~0.5mm

V1 V2 V3

V_{IH}

V_{OH}

channeltron electron multiplier

V7 V6 V5
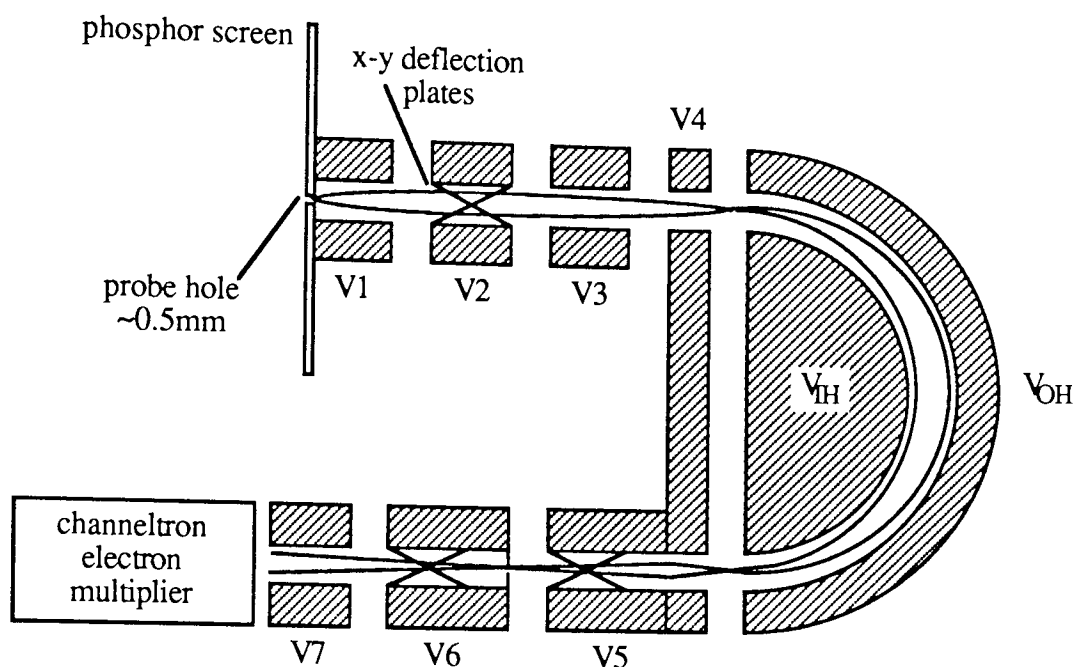
Figure 3.2 Schematic diagram indicating the arrangement of lens electrodes in the input and output lenses to the hemispherical energy analyser.

3.2.4 Broad area cathode interfacing lens

The original input lens to the analyser was designed to work up to potentials of ~3kV [72] which were sufficient to stimulate field emission from tips. In order to stimulate emission from broad area cathodes however, although far lower fields are required they must be uniform over the area of the cathode and may not be generated using the geometrical field enhancement that occurs at an emission tip. As discussed in chapter 2, fields in the range of 10-30MVm^{-1} [2] are typically required to stimulate emission from broad area cathodes, which is a condition that may be satisfied by the application of a p.d. of 15kV across an electrode gap of 0.5mm. Thus, the original lens system could not provide the necessary field conditions to stimulate emission from broad area cathodes and therefore an additional interfacing lens was required for the hemispherical analyser in order to study this regime. Furthermore, the addition of another lens stage enabled the use of the original input lens as a screen by coating it with a phosphor. This development enabled images of emission sites to be viewed and regions of the site to be aligned with the input aperture (original input lens) of the hemispherical analyser in order to make spectroscopic measurements.

The design of this interfacing lens has been much modified by Latham and co-workers [42,61], but the overall principle of operation has not been significantly altered. The lens consists of two electrodes, the first (anode) is planar, of 50mm diameter and with a 0.5mm central aperture. The second element is a section of tube, 8mm in diameter and 15mm long. As used in the spectrometer system, this

electrode arrangement behaves as a diverging lens, as indicated schematically in Fig. 3.3. This electron-optical behaviour results in a magnified image of an emission site being projected onto the screen that is both real and erect.

The magnification varies with alteration of the various parameters e.g. anode voltage, lens voltage and screen voltage, but typically has a value between 28 and 81 within the usual instrument operating range [61]. Furthermore, there is very little alteration in the magnification as the anode voltage is varied. However, since there is a field intensification at an emission site due to either charging and/or geometrical effects, field lines converge at the emission site. The field emitted electrons emerge at low energy though, and they therefore tend to be accelerated along the field lines which thus results in an additional magnification of the site image. Therefore, the quoted magnification of the lens only applies to a spatial translation of the emission site at the lens input, and not the overall magnification of the emission site image. A treatment of the electron-optical behaviour of a similar lens assembly, and the local field enhancement effects associated with surface emission sites is given in section 5.2, although greater detail may be found in Grivet [74].

cathode

anode   lens electrode

phosphor screen/
analyser input
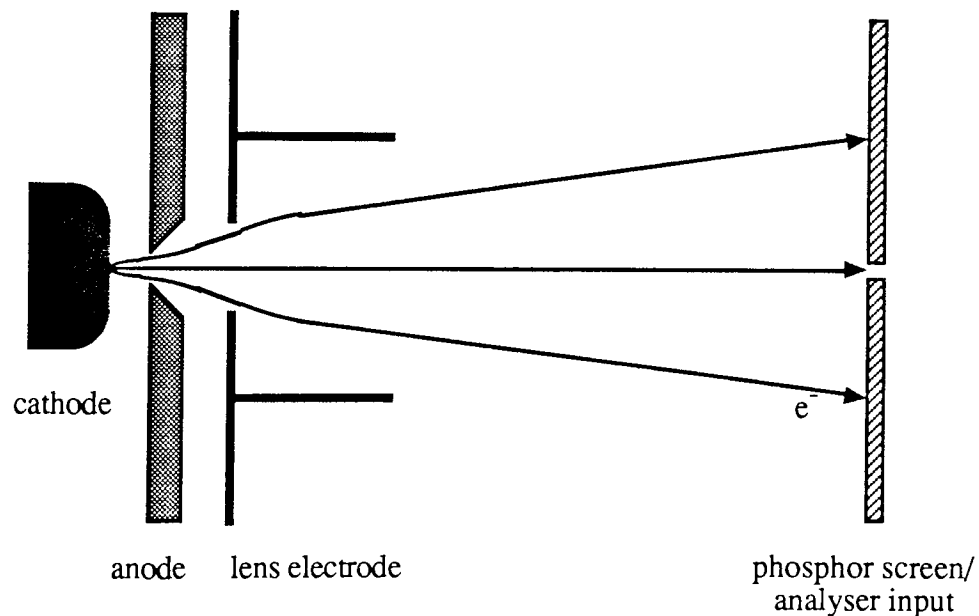
Figure 3.3 Schematic showing the optical behaviour of the interfacing lens designed for operation of the analyser with broad area electrodes.

3.2.5 Spectrometer energy selection drive system

The voltages for the input and output lenses are all derived from a single EHT supply which drives a resistor chain, as shown in Fig. 3.4 [75]. This maintains a constant voltage ratio between the various lens elements, and hence constant lens optical properties [74], as the voltage on the input to the entire lens assembly is adjusted. The hemisphere potentials are maintained from a floating stabilised power

supply with the hemisphere mid-potential rail tied to the energy selection potential, V_4. In order to scan the pass energy of the analyser it is then only necessary to vary V_4, which is driven by a DAC from the computer in the up-graded system. This method of scanning, in which the voltage across the hemispheres remains fixed, maintains the resolution of the analyser at a constant value. Furthermore, this approach has a negligible effect upon the lens focussing properties.

Figure 3.4. Power supply chain to drive the spectrometer lenses and perform electron energy scans (from [75]).

3.2.6 Calibration of the analyser

By defining an electron at the Fermi level of a metal to have zero potential energy, it follows that an electron just at rest outside the metal will have an energy equivalent to the work function, ϕ. In the case of the spectrometer system, since the experimental samples employed are metals, and the analyser and cathode are electrically connected, the Fermi levels of the sample and analyser hemispheres will be the same. By taking the energy scale to have its zero at the Fermi level, the expression for the kinetic energy of an electron traversing the hemispheres becomes

$$E = eV_4 - \phi \qquad\qquad 3.9$$

where V_4 is the mid-potential of the hemispheres, ϕ the work function of the analyser hemispheres and E the kinetic energy of a transmitted electron, typically 2eV for this system.

It is therefore possible to calibrate the analyser using a field emitter that has a known Fermi level position in its energy distribution, since E and V_4 have known values. By comparison of the measured energy distribution with the known distribution, the value of V_4 for an electron emitted from the sample Fermi level may be determined and thus the value of E for an electron emitted from any sample's Fermi level is known.

Young [22] has shown that for a clean tungsten emitter at ~300K, the Fermi level occurs 73% up the high energy slope of the energy distribution. Braun *et al* [72] used this information to determine ϕ for this instrument as 4.26±0.03 eV and hence, for a value of E=2eV, a mid-potential voltage of $V_4 = 6.26$V corresponds to the Fermi level of any field emitter.

3.2.7 Resolution of the analyser

Young and Kuyatt [76] established a technique for the determination of the resolution of an electron energy analyser from a field emission energy distribution. They assumed a Gaussian transmission function for an energy analyser of the form

$$G(E) = \frac{0.939438}{\Delta E_{1/2}} \exp\left[\frac{2.772588}{(\Delta E_{1/2})^2} E^2\right] \qquad\qquad 3.10$$

where $\Delta E_{1/2}$ is the full width half maximum of the transmission function and G(E) is normalised. The effect of this transmission function on the field emitted energy distribution, P(E)dE, is then given by the convolution

$$J(E) = \int P(E')G(E'-E)dE \qquad\qquad 3.11$$

where J(E) is the measured electron energy distribution. The leading edge of the measured energy distribution will suffer the greatest distortion due to the analyser as it is the most rapidly changing feature of the spectrum. The resolution is therefore defined as the difference in energy, ΔJ(E), between the 10% and 90% levels of the leading edge of the energy distribution. Fig. 3.5 shows the variation of ΔJ(E) with FWHM, which clearly shows that low temperature field emitters are required to obtain meaningful results. Furthermore, these data assume an atomically clean micropoint.

Aston University

Content has been removed for copyright reasons

Figure 3.5 Spectrometer resolution vs field emitter leading edge width (10%-90%) showing the dependence upon sample temperature (from [76]).

Braun *et al* [72] showed this edge value to be very dependent on the degree of surface contamination, and that it is not possible to obtain a measurement close to the theoretical value until the sample is thoroughly cleaned. After cleaning by the technique of field desorbtion [77], they then obtained a value of 0.11eV for ΔJ(E), close to the theoretical value of 0.10eV which implied an analyser FWHM of 50meV. A rather large peak displacement from the expected value indicated that the emitter was still not thoroughly clean. By comparison with results of Young and Muller [78] they concluded that the analyser width was <30meV.

3.3 Experimental chamber

3.3.1 UHV chamber

The experimental chamber was completely redesigned to give improved visibility and porting access to the sample (as shown in Fig. 3.6). Thus, the new

design, which was built by VG Special Systems, incorporated a pre-chamber/loadlock assembly enabling improved sample turn around times. This improvement allows specimens to be changed whilst maintaining the main chamber under vacuum. The design also provides the flexibility to perform a wide variety of sample surface treatments under vacuo in the pre-chamber without the need to expose the sample to atmosphere or the main experimental chamber to possible sources of contamination.
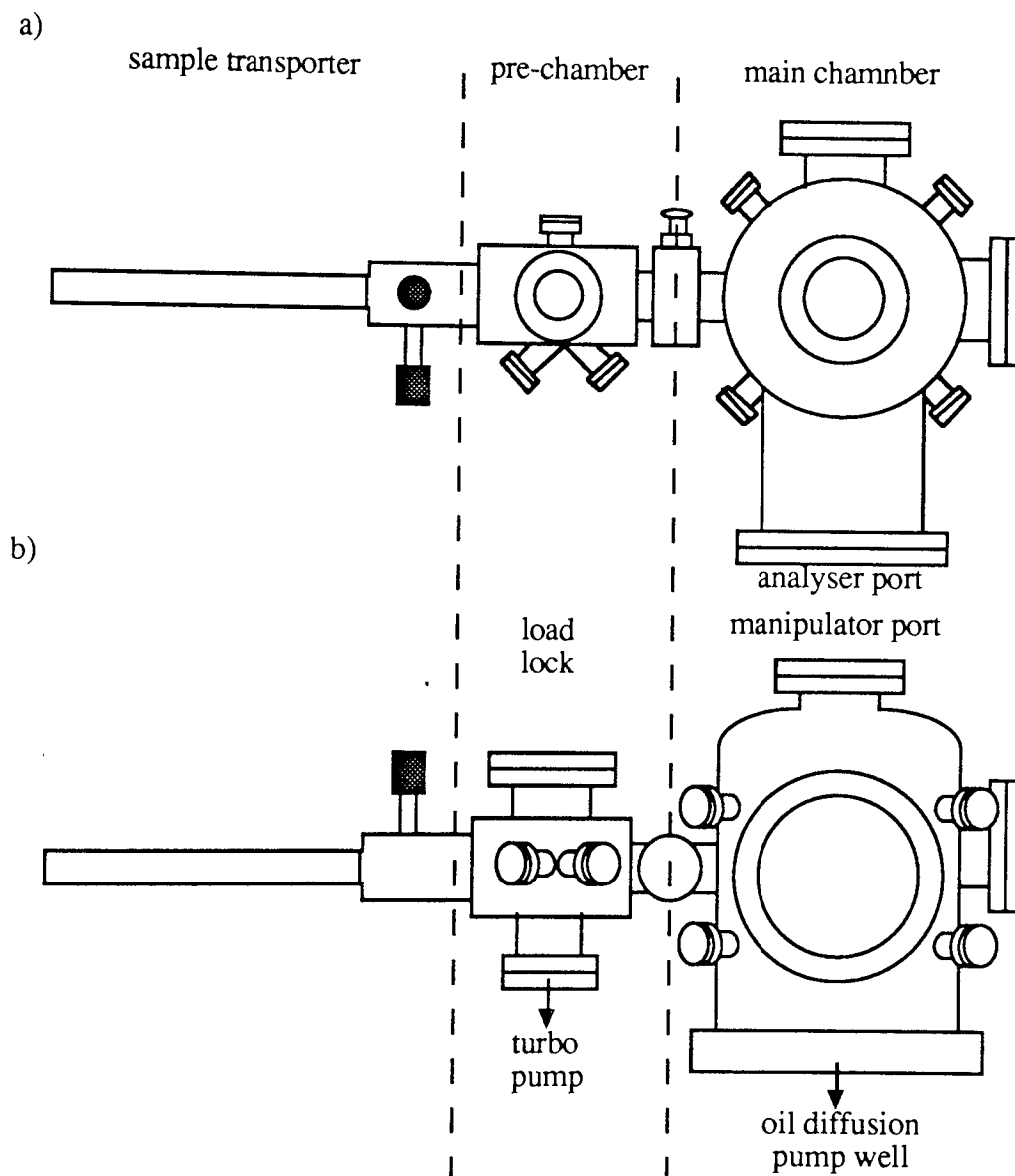
Figure 3.6 Schematic of the UHV chamber layout indicating the porting, pre-chamber and sample transporter.

Pumping of the main chamber is performed through a pumping well incorporating a titanium sublimation pump and an isolation valve to a 24 hour cold-trap and an Edwards E04 oil-diffusion pump backed by an E2M8 rotary pump. An ultimate pressure of better than 10^{-10} mBar may be attained within the main chamber after baking. The pre-chamber/loadlock assembly is pumped by a Balzers

turbo pump backed by an Edwards E2M1.5 rotary pump, and can be pumped down to a pressure of 5×10^{-7} mBar within an hour of sample loading ready for sample transfer to the main experimental chamber.

Thus, the main chamber incorporates the hemispherical analyser assembly with the associated electrical feedthroughs, and the sample manipulation system. A schematic indicating the overall experimental layout is shown in Fig. 3.7. Figures 3.8 and 3.9 show photographs of the entire experimental facility, including the laser for sample surface treatment (see section 3.6).
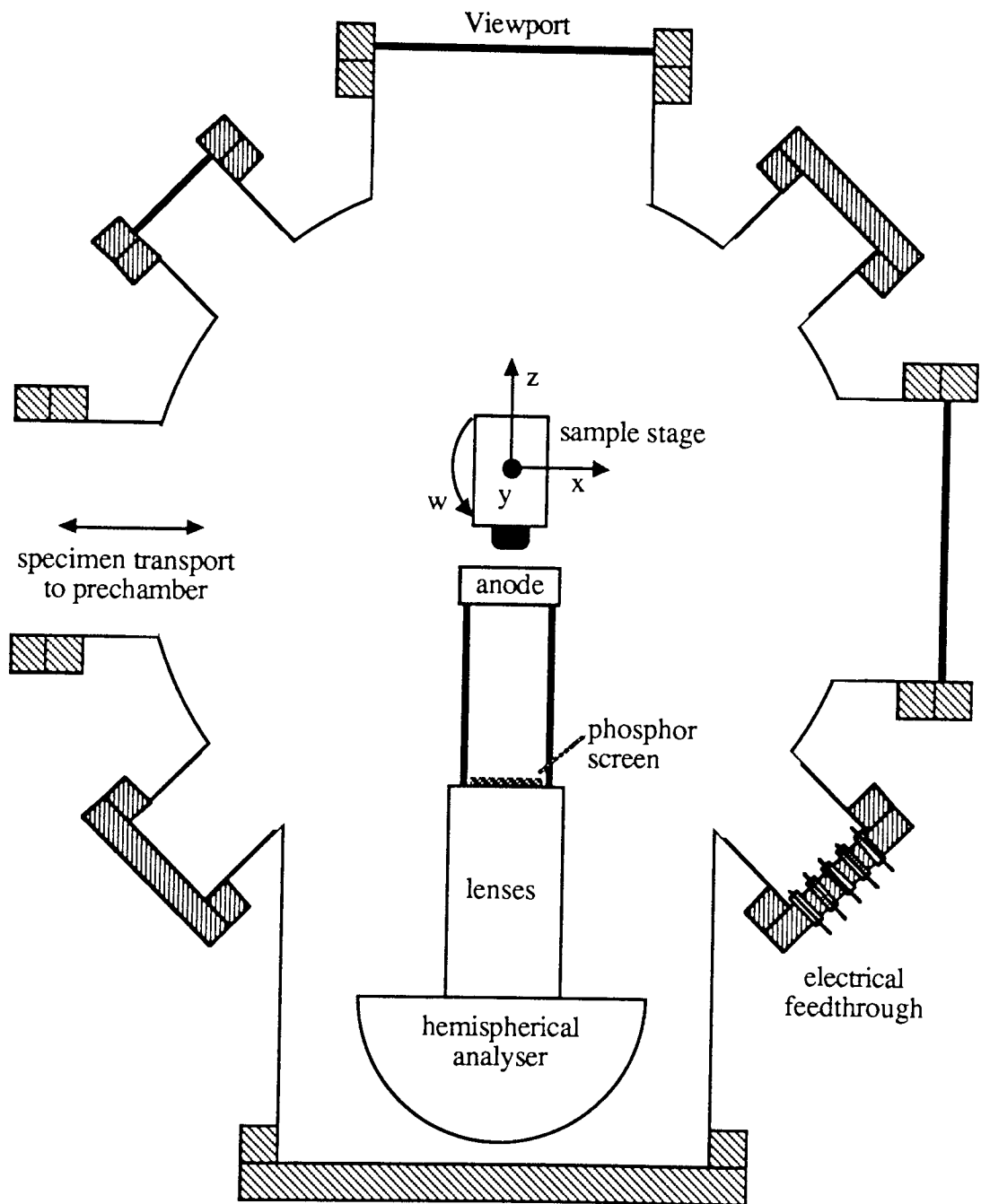
Figure 3.7 Internal layout of the main experimental chamber showing the position of hemispherical analyser, electrical feedthroughs, sample transfer lock and viewports.
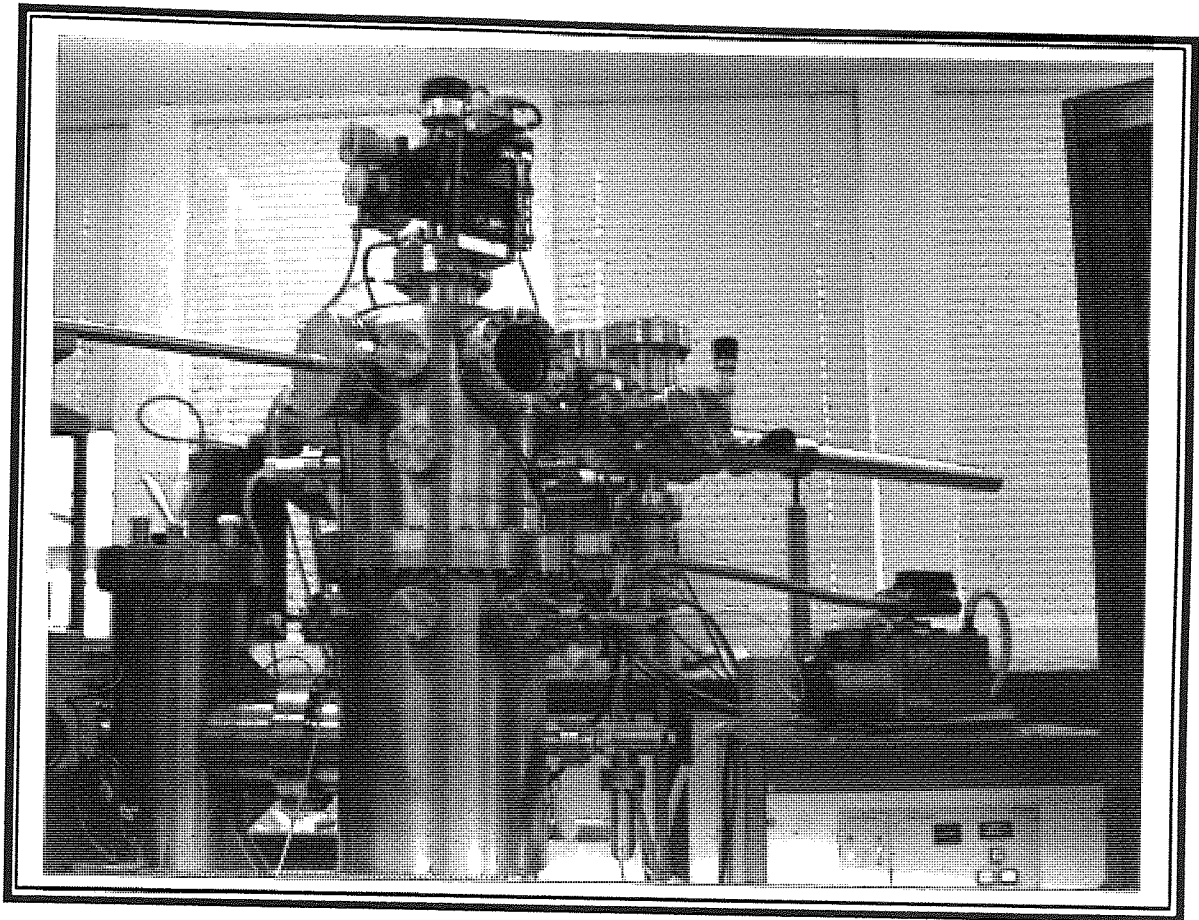
Figure 3.8 View of main chamber (left), pre-chamber and sample transport (right) and manipulation systems (top centre).
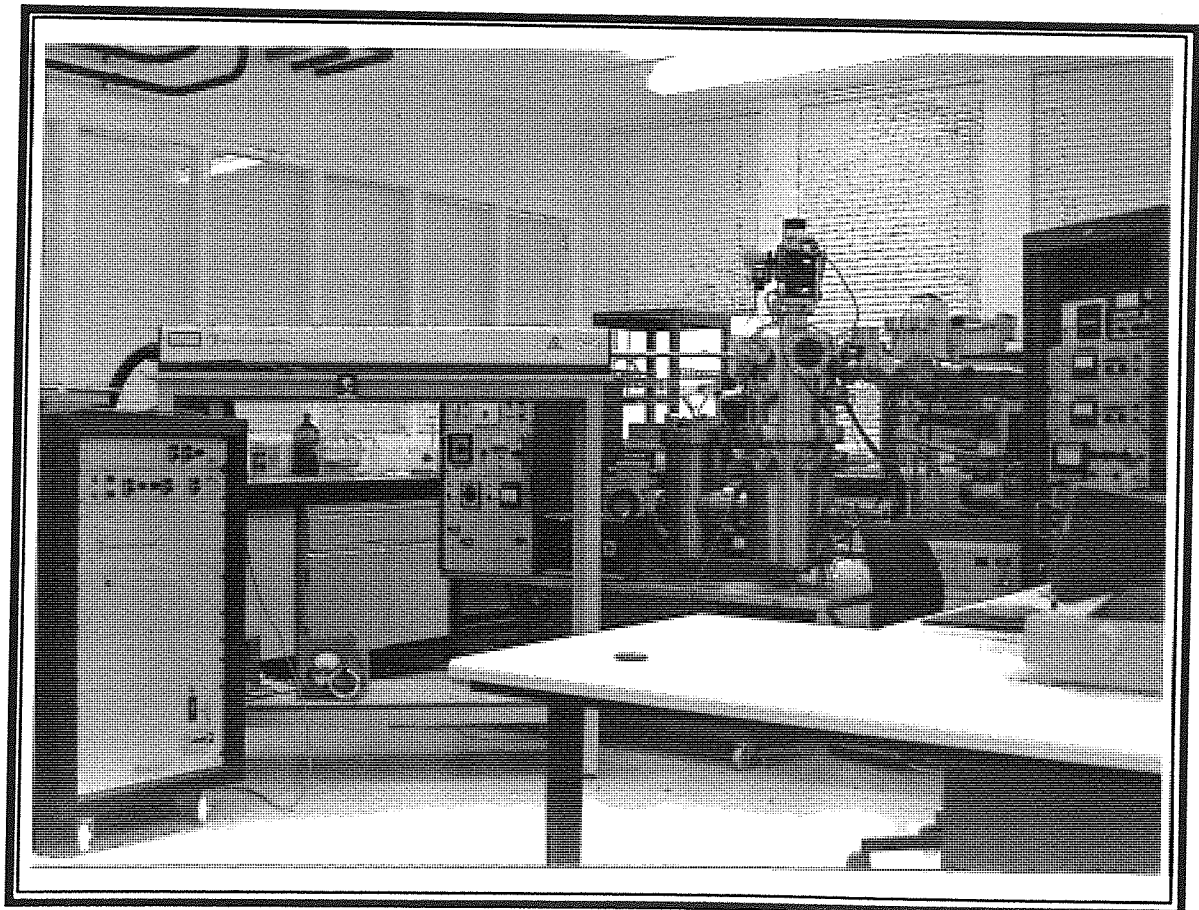
Figure 3.9 View of main chamber (centre) and laser surface treatment facility (left).

3.3.2 Sample handling and manipulation

The sample handling and manipulation is based around a new VG specimen pod system. A schematic showing the sample holder, which comprises a sample holder with a built in heating element and spring clips to hold a sample mounting stub, is illustrated in Fig. 3.10. The sample pod has a bayonet mounting system for attachment to the specimen manipulator, and there is a mechanical sample transporter to facilitate sample changeover.
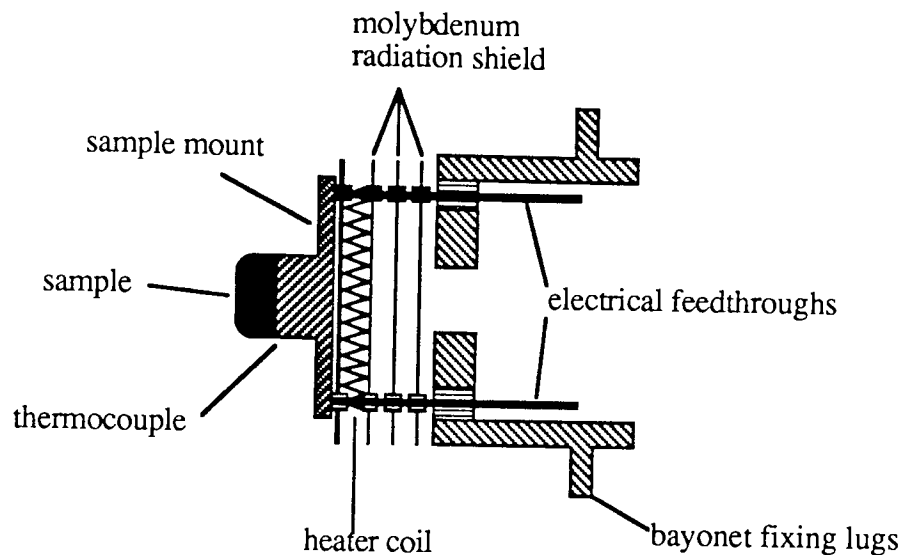
Figure 3.10 Cross-section of the sample holder indicating the heating system and mounting points for attachment to the manipulator and sample transporter.

The heater is capable of attaining temperatures up to 900°C, but is limited in practice to a sample surface temperature of ≤600°C to avoid evaporation effects. The controller (Tactical 310) can maintain the set temperature to within ±2°C over a temperature range of -200° to 1200°C, however, since the sample stage is not fitted with a cooling attachment only temperatures above ambient are attainable. The controller employs a K-type thermocouple to measure the sample temperature, of which two are provided on the sample pod. A further feature of this unit is that the cathode is electrically isolated from the heater and the chamber earth, so that the emission current drawn from the cathode may be measured directly.

The sample manipulator, a VG HPLT, has stepper motor driven x,y and z motions, and a manually controlled primary rotary motion. The x and y axes have a movement range of ±12.5mm vectorially with a step resolution of 2.5μm and a repeatability of 1.0μm, while the z axis has a 50mm travel. The whole manipulation system is controlled via an intelligent stepper motor control system (VG SMPC4) which may be driven from either a handset or, as in our case, from a computer via an RS232 serial interface.

3.4 Computer interfacing hardware

The computer control and data acquisition function was implemented using a mixture of commercially available interface cards and custom built circuitry. The system is based around an Acorn Archimedes 440 computer with the Acorn I/O, Wild Vision ADC-1208 and Intelligent Interfaces IEEE-488 interface cards (known as 'podules'). The Acorn I/O podule implements the BBC computer 1MHz Bus (giving 8 I/O and 8 address lines) which was used to access the custom built interface circuitry.

The measurement functions to be implemented are detailed below, whilst Fig. 3.11 shows the overall design of the control and data acquisition/analysis system. The Wild Vision ADC-1208 is a 12-bit multiplexed 8 channel analogue-to-digital converter capable of performing up to 166 000 conversions per second with a +5V to -5V full scale input range. This is used to record all the measurement inputs. The custom circuitry was developed to interface between the outputs of measuring equipment and to drive the hemispherical analyser, since appropriate commercial units were not available, and these are described fully in section 3.4.2.

3.4.1 Computer measurement and control functions

i) Electrode gap characteristics

The gap voltage is measured directly by using a potential divider chain between the EHT supply at the anode and earth which has a divider ratio of 1:3000 and a total resistance of 150MΩ thus giving an output of 5V for 15kV applied to the anode. This output is then measured directly by an ADC input on the computer. The divider draws a current of 0.1mA which is well within the 5mA supply limit of the EHT power supply used (Brandenburg). The gap current is measured directly from the cathode using a Keithley 440 electrometer. The voltage output available from this electrometer is then fed directly to an ADC input on the computer. These measurement circuits are shown in more detail in Figure 3.10.

ii) Mapping of emission sites

Several techniques are available to locate emission sites. Generally, an anode probe-hole scanning technique [5] is used such that when an emission site is located over the anode probe-hole the emission current may be detected on the second electrode by the application of a small positive bias voltage of typically 20V (Fig. 3.12). The resolution of this technique is approximately the diameter of the anode probe hole, which is 0.5mm. Thus, the sample may be stepped at fairly large

70
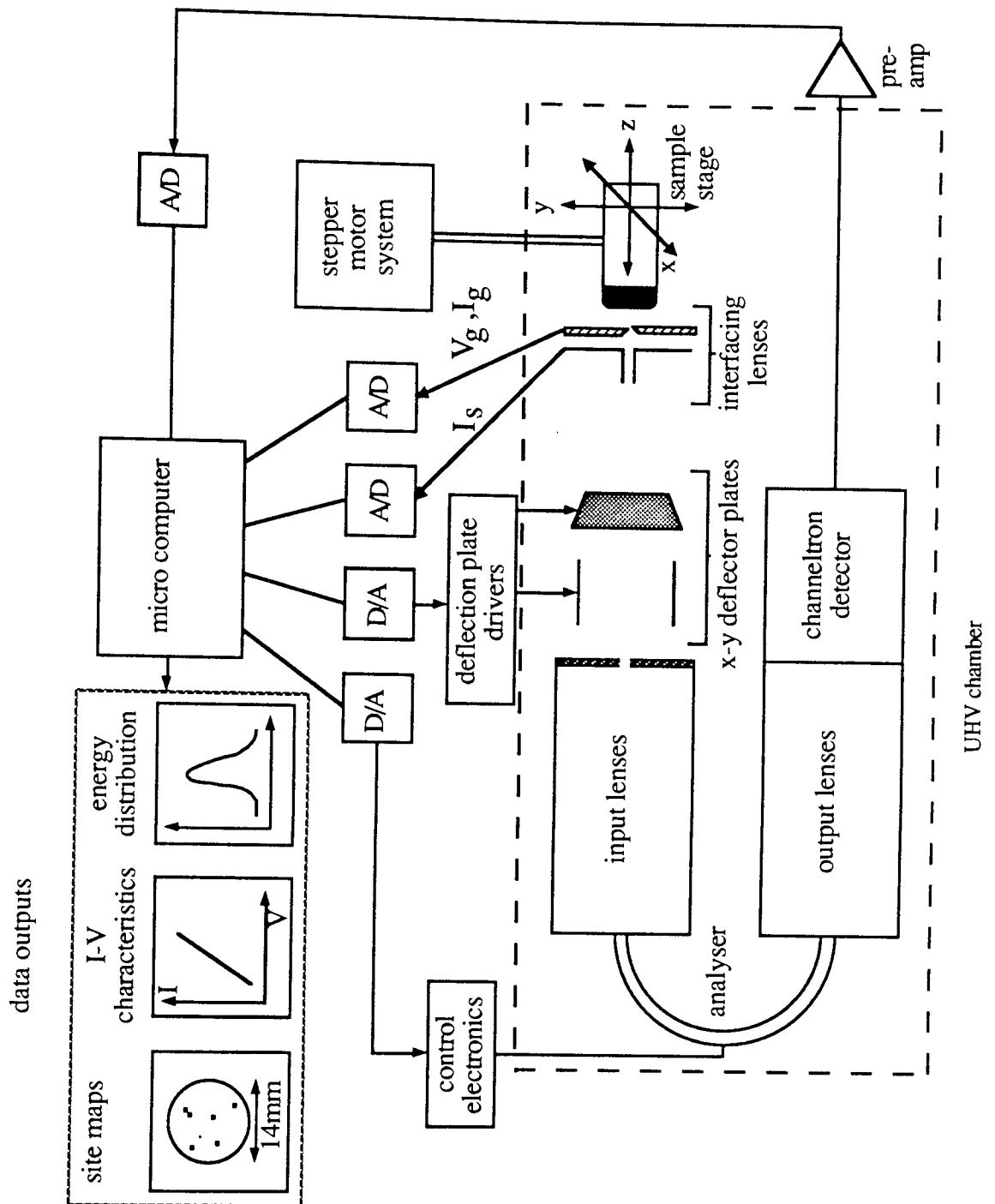
Figure 3.11 Schematic showing an overview of the computer control and data acquisition system.

intervals (typically 150μm) while still enabling the emission sites to be located and mapped in terms of the stepper motor co-ordinates. A Keithley 610 electrometer is used to detect this current resulting in a detection threshold of $\sim 10^{-8}$A. Again, the ouput from the electrometer is input to the computer using the ADC card.

A higher resolution scanning technique may be employed where the spectrometer itself is used as the detection element. This gives a greater sensitivity than the anode probe hole technique owing to the electron multiplier employed at the output of the analyser. Whilst this method has the advantage of greater

71

sensitivity and spatial resolution, it suffers from the serious limitation of requiring a long time to generate a site map (ca. 2-3 hours). Therefore, the anode probe-hole technique is generally employed.
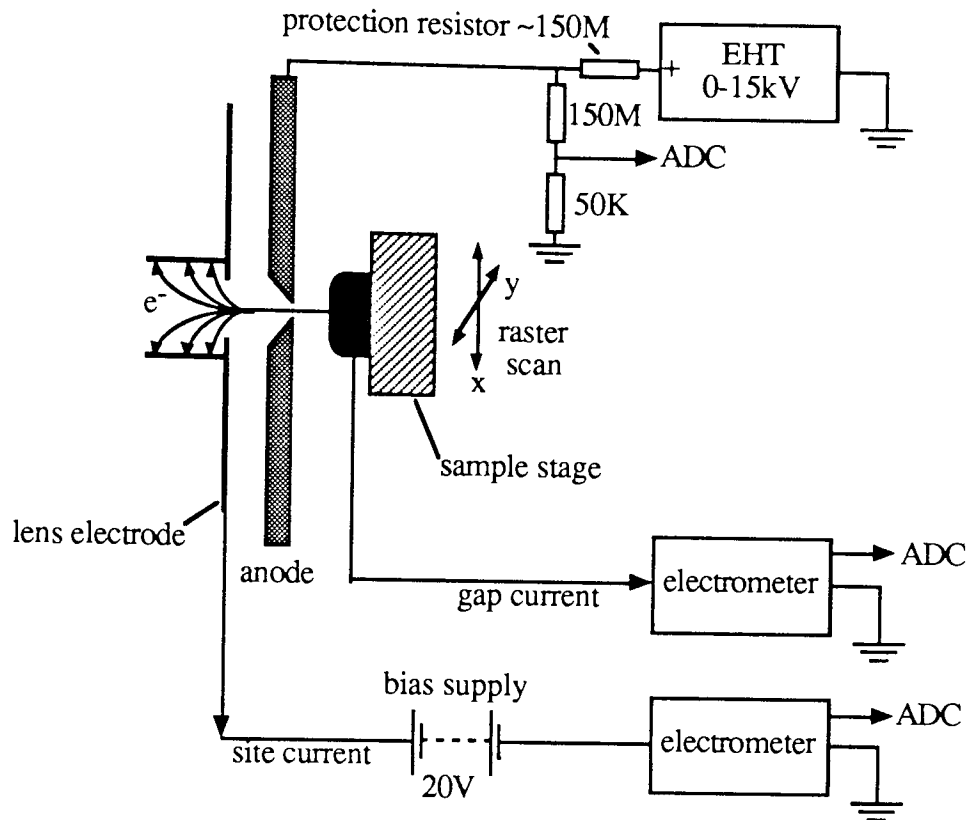
Figure 3.12 Circuit diagram illustrating the measurement of the gap I-V characteristics and location of emission sites by an anode probe hole technique.

iii) Electron energy spectra

Spectra are referenced to the sample Fermi level and recorded by scanning the pass energy of the hemispherical analyser whilst measuring the analyser multiplier output through a Brandenburg isolation/pre-amplifier and NE1310 ratemeter. The procedure is controlled from the computer via a digital-to-analogue converter (DAC) which drives a custom built op-amp with a designed output range of ±20V. The circuit is described in greater detail in section 3.4.2.

iv) Energy selective emission site imaging

This is a technique enabling the intensity distribution of emitted electrons at a particular energy from a site to be mapped spatially. The function is implemented by setting the spectrometer to a specific pass energy and then deflecting the site image across the analyser input aperture in a raster scan pattern using a pair of x-y deflection plates. By recording the signal at each position in the raster scan, a map

of the intensity distribution across the site for electrons of that particular energy may then be generated. The x-y deflector plates are driven from the computer via a pair of latched 8bit output ports driving a DAC that drives the HV amplifier which generates the deflection voltage across the plates. The interfacing drive circuits are described in section 3.4.3.

3.4.2 Computer control interfacing circuit

The computer control interfacing circuitry was driven from the 1MHz Bus podule on the Archimedes computer. This podule provides equivalent interfacing facilities to those provided on the BBC computer range, namely a user port providing eight input/output lines, and a bus with eight address lines and eight bi-directional data lines. The interfacing circuitry was attached to the bus, using the two lowest address lines, A0 and A1, to select the DAC, and A2 and A3 to address the two eight bit latches used to implement the deflection plate driver circuitry. The control line FC is used as an enable when a valid address for the interface board is present on the address lines. The whole circuit is clocked at 2MHz (this is twice the clock frequency of the original interface as available on the BBC computers, but makes no material difference to the circuit operation).

The circuit diagram is shown in detail in Figure 3.13. The address, data and control lines from the computer are firstly buffered by IC's 1, 2 and 9. Subsequently, IC's 3, 4, 5 and 6 perform the address decoding. IC 10 is the DAC, and IC's 11 and 12 are op-amps which convert the current output of this chip to a voltage and set the signal scaling. IC 13 is a precision voltage reference and IC's 7 and 8 are the eight bit latches.

$\overline{WR}$	$\overline{CS}$	A1	A0	FUNCTION
X	1	X	X	Device not selected
1	X	X	X	No data transfer
0	0	0	0	DAC loaded directly from the data bus
0	0	0	1	Most significant input register loaded from data bus
0	0	1	0	Least significant input register loaded from data bus
0	0	1	1	DAC internal register loaded from input registers

Table 3.2 Truth table for loading data into the DAC chip.

Figure 3.13 Circuit diagram of the interface connected to the 1MHz bus.

74

When the data line FC goes low, a valid address for the board is present on the address lines, so each of these is ANDed with the inverted FC signal to obtain the chip select logic signals. Furthermore, from system timing charts, valid data will be present on the data lines when the clock is high, so the chip selects must be ANDed with the clock, which is implemented by IC's 4 and 6 (IC6 is actually a NAND gate since the WRITE select uses inverse logic on the DAC chip; the truth table for the DAC chip write cycle is shown in Table 3.2). Pin 1 is the chip enable, and must be held low for the DAC to operate. Furthermore, it is necessary to transfer the data to the DAC in two steps since it requires a 14 bit word, whereas the data bus is only 8 bits wide. This is achieved using two WRITE cycles to load internal registers in the DAC, and then by an appropriate address code (see Table 3.2), the data may then be converted to a voltage output. The two eight bit latches are implemented using 74LS373's, the data on the inputs is switched to the outputs when pin 11 is high. These data levels are held on the outputs when pin 11 goes low, whatever the subsequent status of the data inputs.

The digital to analogue converter is an Analogue Devices 1408. This is a 14 bit device thus giving a possible 16384 output steps. Over the required measurement range of ±20V, only 1600 steps (equivalent to 12 bit conversion) are required at the analyser resolution, and therefore the step resolution of the DAC is well within that of the analyser and will not affect the measured spectra. The DAC gives a current rather than voltage output, so a scaling/buffering circuit (based around IC's 11 and 12 which are OP-07 low noise instrumentation op-amps) is required. This circuit is given in the device data sheet, and gives a bipolar output of $\pm V_{ref}$, the reference voltage derived from IC13, for the extremes of the conversion values.

The following circuit, based on transistors T1 to T8, is a discrete component op-amp (similar to a 351) [79] which is used to provide the final voltage output amplification. This is scaled such that a maximum output swing of ±20V is available for ramping the spectrometer. A discrete component device was employed since no commercial ic's were readily available.

3.4.3 Deflection plate driver circuit

The deflection plates and associated driver circuit were designed by Xu [61] to enable the image of an electron emission site to be scanned over the entrance aperture to the spectrometer. By this process it is then possible to generate a map of the spatial intensity distribution of electrons emitted at a specific energy across the emission site.

The deflection plate design required that the plate dimensions should be such
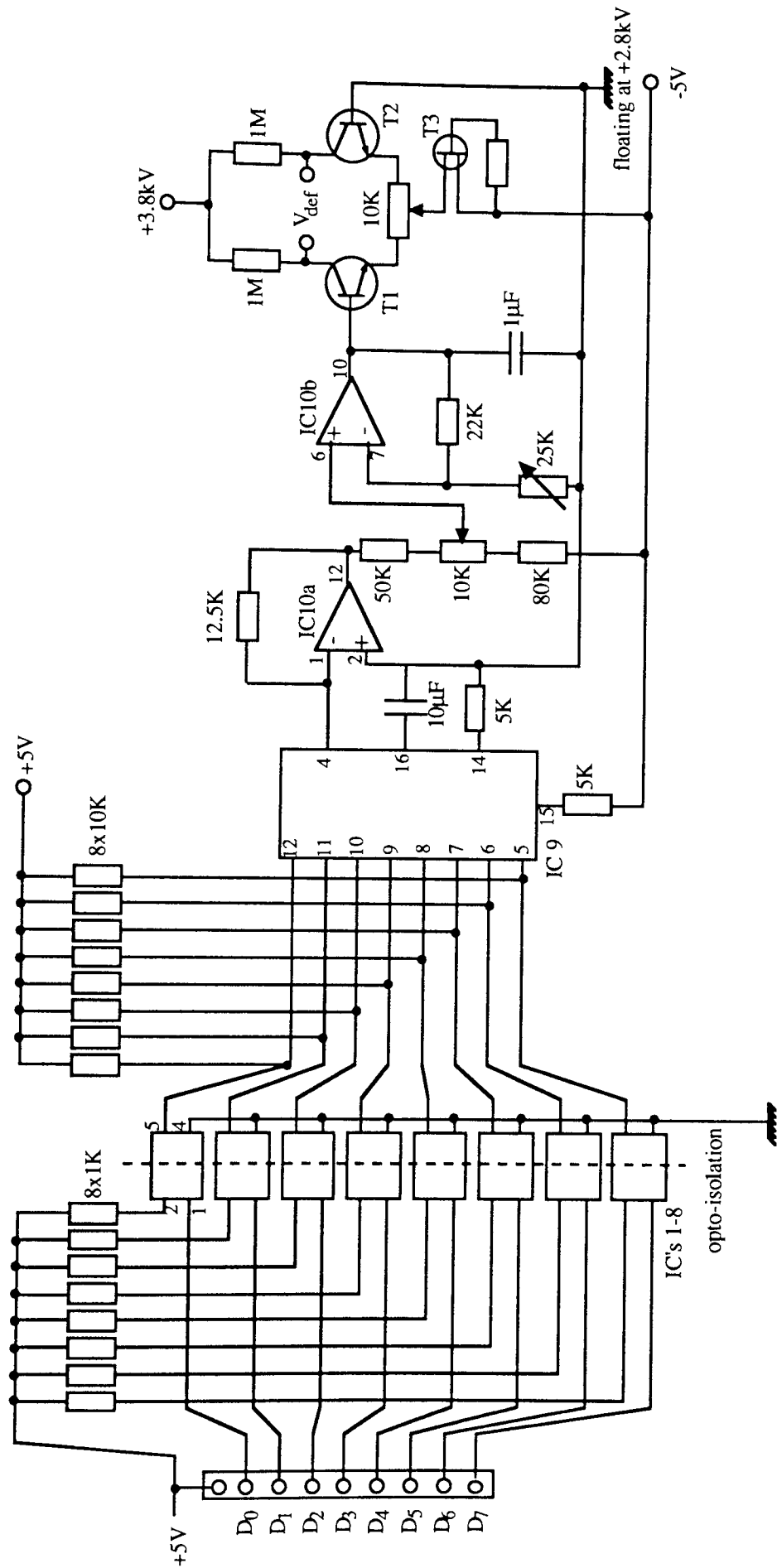
Figure 3.14 Deflection plate driver circuit.

that they did not disturb the existing electron-optical performance of the projection lens system. Furthermore, the plate separation had to be such that there was no physical clipping of the field of view onto the phosphor screen at the input to the spectrometer system. The system was therefore designed with the deflector plates floating at the same potential as the phosphor screen so as to minimise the disturbance to the optical behaviour of the projection lens system. Generation of a differential voltage between the plates then deflects the electron beam.

Only minor modifications to the circuit developed by Xu [61] were required to implement the computer control function. Shown in Fig. 3.14, the circuit is required to float at the analyser input potential of 2.8kV, so the board must be isolated from the address decoding logic to protect the computer and other circuitry. This is achieved using opto-isolators (IC's 1-8) between the 8 bit latches described in section 3.4.2 and the DAC on the deflector plate drive board. RS 307-979 opto-isolators were used, which are capable of isolating a potential difference of up to 4kV. The 8 bit data is then fed to a DAC0800 8 bit DAC to generate the control voltage which drives a long tailed pair, based around transitors Tr1 and 2, to give the required voltage differential between a pair of deflection plates.

3.5 Experimental and analysis software

All the software was written in BASIC 5, the native language of the Archimedes computer, although some system calls were required to support the 1MHz Bus interface. All the measurement and control functions detailed above (see section 3.4.1) are available from the main program, with the various analysis and data presentation functions being implemented by several smaller programs.

The experimental control and data acquisition program runs from a central menu calling each of the individual functions, as indicated schematically in Fig. 3.15. An initialisation routine is required to set up the control of the stepper motor system: the current motor co-ordinates must be input by the user as there is no way to automatically read them in. In each of the functions initial default parameters (e.g. cathode scan diameter and scan step spacing) may be amended prior to performing the measurement.

Several data analysis programs were developed, dedicated to processing the recorded data from the different measurement functions. The first, IVSVSOLVE, enables the study of I-V characteristics using a Fowler-Nordheim plot. A standard straight-line least squares fit is employed to obtain the ß-factor and emitting area. Spurious points may be removed and a screen dump utility allows graphical data output on the printer.
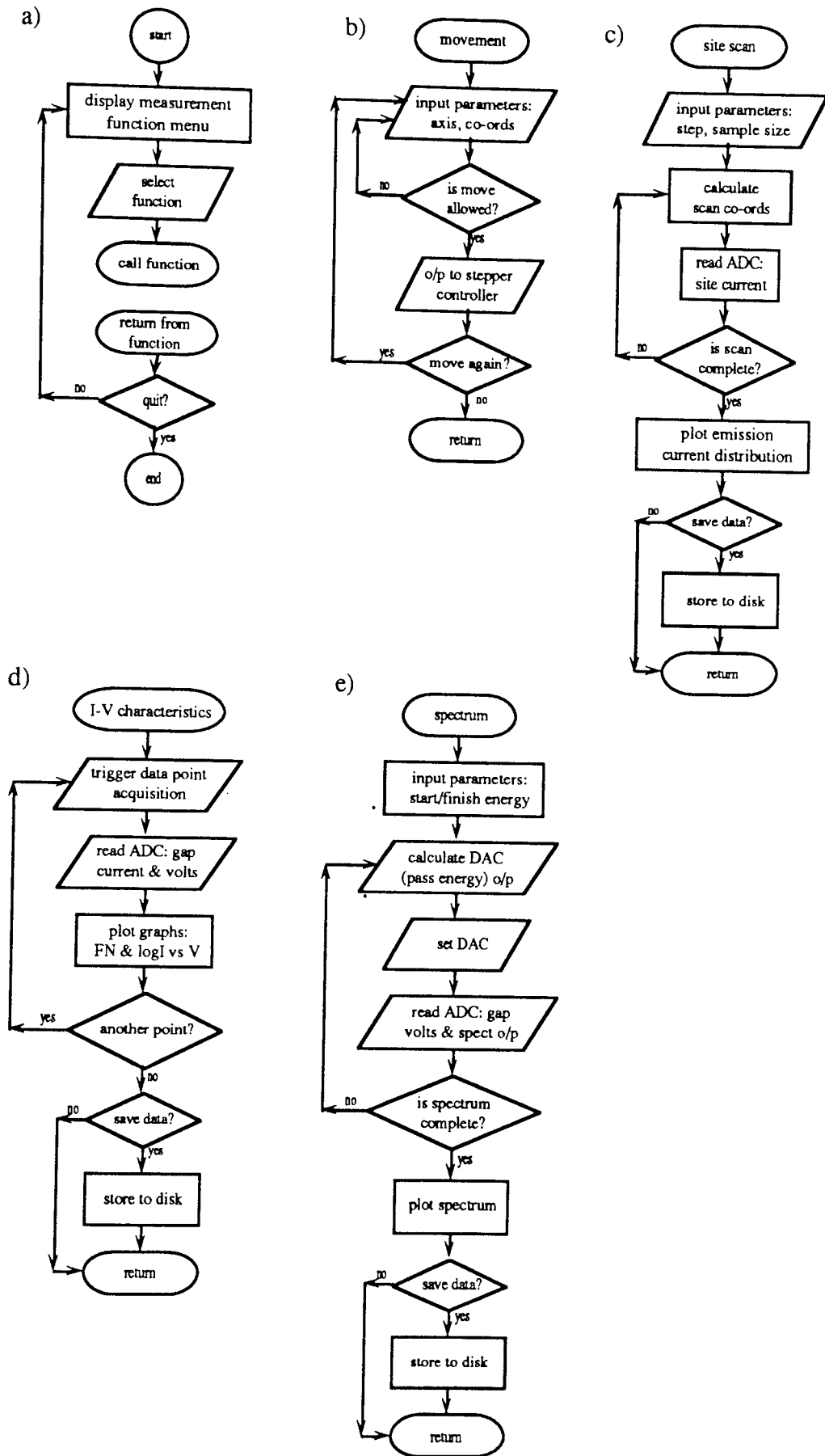
Figure 3.15 Flow charts indicating the operation of the control and data acquisition software. a) main menu, b) movement control, c) site scan, d) I-V characteristic measurement and e) spectrum acquisition.

The program SPANALYSIS analyses the spectral data to obtain the peak position and hence shift from the Fermi level, the FWHM and the area under the curve. Based on an algorithm described by A. Savitzky and M.J.E Golay [80], the program performs a least squares fit of a quadratic function to the peak region using an integer method, in order to determine the peak centre and height. Data may also be smoothed prior to analysis. An estimate of the peak position must be input, and the program is only capable of analysing single peak spectra at present. Multiple plots may be overlaid in order to view the effect of altering the gap field on the emission process. The spectral and I-V data shown in this thesis have been derived using these analysis programs.

3.6 Electrode transient surface heating system

To provide increased experimental flexibility, a further sample heating system utilising a NdYAG pulsed laser has also been implemented in the main experimental chamber. This system extends the sample heating range to enable the study of transient surface heating effects on planar broad area electrodes. Owing to the constraints of the experimental system, it was not possible to irradiate the sample while applying an electric field. This system is described more fully in the following sections.

3.6.1 Optical design

The experiment was based around a NdYAG pulsed laser, manufactured by Spectron Laser Systems, which has an output energy of 40mJ per pulse in the TEM_{00} mode at a maximum pulse rate of ~50Hz. In order to obtain the minimum possible focal spot size, it was necessary to take several different factors into account. A laser beam may not be focussed to an infinitely small spot size, but to a waist that is limited both by diffraction effects and the fundamental optical properties of lenses.

The diameter of the first minimum [81], w_D, due to diffraction is given by the equation

$$w_D = l \operatorname{Tan}\left(\frac{1.22\lambda}{D}\right)$$

3.12

where λ is the wavelength, l is the distance separating the aperture from the electrode surface and D the diameter of the aperture.

Fundamental optical effects defined by Gaussian optics also limit the spot size. For a spherical beam profile with a gaussian energy distribution, as is produced by a laser in the TEM_{00} mode, the beam cannot be focussed to a point but is focussed

to a waist which thus defines the spot size (as indicated by Fig. 3.16). Higher order laser modes produce energy distribution patterns that contain multiple maxima and minima rather than a single maximum having a gaussian intensity profile, and therefore may not be focussed to as small a spot size [81]. Neglecting diffraction effects, the beam is focussed to a waist diameter, ω_0' [82], limited by beam half angle of divergence in the far field, θ_{FF}, the wavelength, λ, the focal length of the lens, f, and the separation of the beam source from the lens, s, according to the equation

$$\omega_0' = \frac{\lambda/\pi\theta_{FF}}{[(1\text{-}s/f)^2 + (\lambda/\pi f\theta_{FF}2)^2]^{1/2}} \qquad 3.13$$

In order to obtain the best compromise in performance between diffraction and Gaussian optical spot sizes, a short focal length lens is required and therefore it was necessary to mount the focussing lens within the vacuum chamber. An achromatic lens of focal length 50mm and diameter 20mm was employed as this type of lens has low aberrations [81].
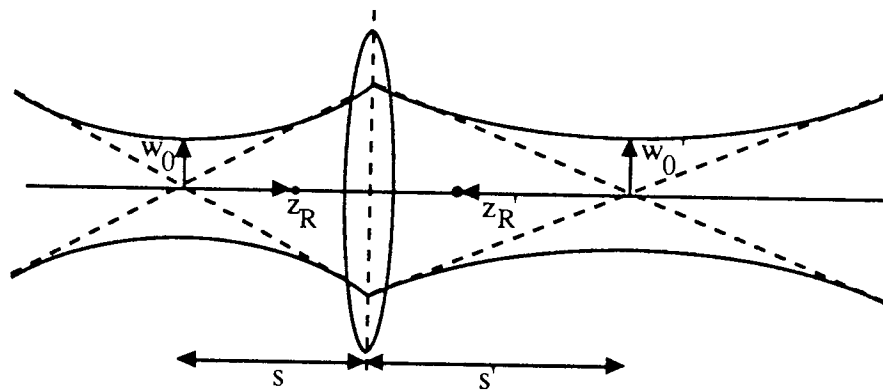
Figure 3.16 Illustration of gaussian focussing by lenses, and the important parameters for determining minimum beam waist size.

3.6.2 Experimental laser chamber layout

The experimental optical arrangement is shown in Fig. 3.17, and a minimum theoretical spot size of 10µm may be calculated from equation 3.13 for these optical parameters. Diffraction through this aperture will produce the first minimum at a diameter of ~1µm, which is much smaller than the limit due to the focussing properties of gaussian beams. Since these two effects influence each other, the gaussian intensity profile of the laser beam will then be modulated by the intensity variation of the single aperture diffraction pattern [81]. Aberrations of the lens will

80

also affect the calculated spot size, tending to shift the best focus from the paraxial focal point towards the lens and increasing the size of the spot. The effects of various types of aberration are described briefly in chapter 5 for the case of electron optics, although the geometrical aberrations apply equally for light optics. However, an achromatic lens has low aberrations and should therefore have little effect on the minimum spot size.

Owing to the hazards associated with laser radiation it was also necessary to consider the safety aspects of operating this system. Protection was provided by incorporating light-tight covers over all the viewports on the experimental chamber which actuated the safety interlocks provided on the laser itself through micro-switches. These safety features are also indicated in Fig. 3.17.
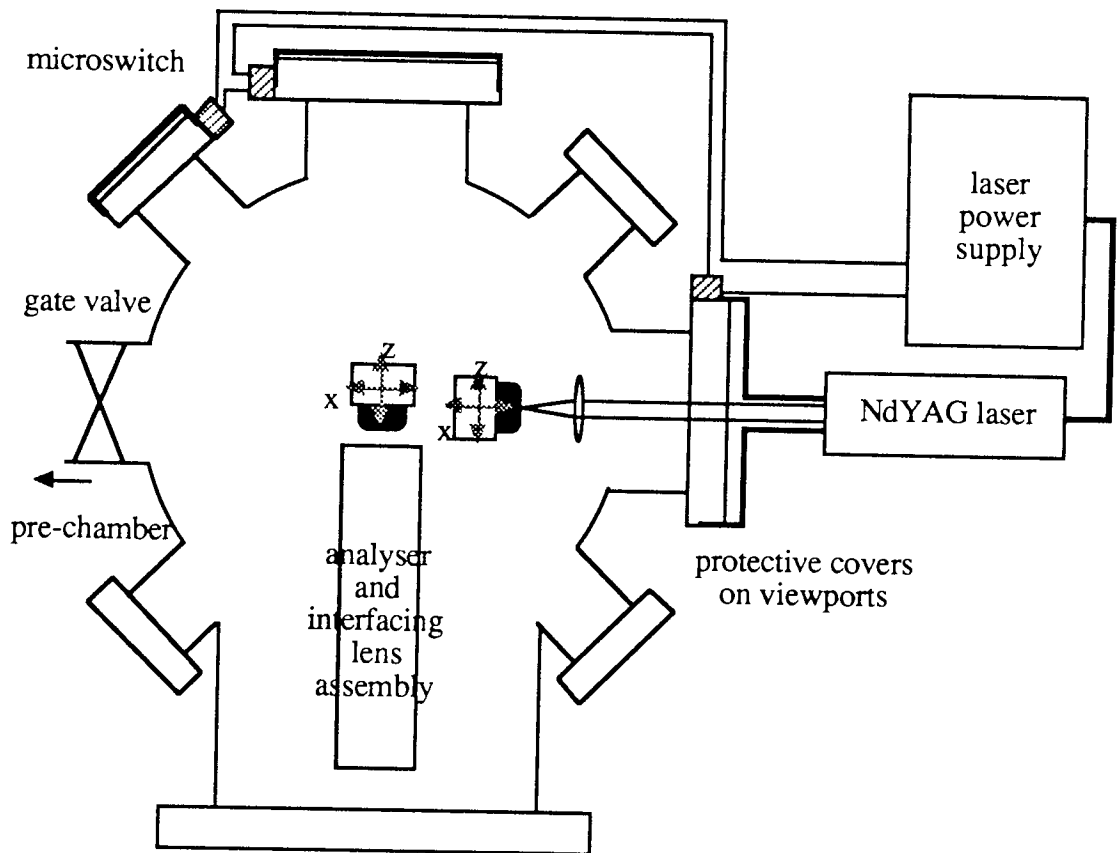
Figure 3.17 Experimental chamber layout for performing surface heating experiments by pulsed laser. The laser safety features are also indicated schematically.

CHAPTER 4: EXPERIMENTAL STUDIES OF LOCALISED FIEE PROCESSES

The experimental studies described in this chapter were performed using the electron energy spectrometer described in the previous chapter.

4.1 Introduction

The performance of vacuum as an insulating medium is of great importance in a wide variety of device applications such as: power switches, RF cavities etc. The unpredictable onset of breakdown events, where the effective resistance of the electrode gap falls to zero, limits the application of vacuum insulation technology. An important source of such breakdowns is thought to be the electron emission currents which are known to flow from localised 'sites' when sufficiently high fields, in the region of 10-100 MVm^{-1}, are applied to electrodes [1]. For many years the emission was modelled in terms of surface micro-protrusions, where the field enhancement at a protrusion raised the local field to a level sufficient to enable electrons to tunnel through the surface potential barrier. As discussed in Chapter 2, a growing body of evidence collected over the previous two decades has tended to suggest an alternative explanation whereby the emission results from impurity micro-structures on the electrode surface. The precise emission mechanism is unclear, although the hot electron model of Bayliss and Latham [8] currently provides the best explanation.

In order to improve our understanding of the fundamental emission mechanism operating in metal-insulator micro-structures, a study has been undertaken using a simulated MI regime. Thus, by the use of a Langmuir-Blodgett coating technique, high quality, well controlled dielectric films were deposited on broad area planar electrodes to produce the required micro-structure [83]. In section 4.2, results will be presented from a study of a range of such MI structures of varying thickness, including data on the overall electrode and individual site I-V characteristics, and the electron energy spectra obtained from individual emission sites.

Owing to the technological importance of the occurence of HV electrical breakdown in vacuum insulated devices, much effort has been devoted at a technological level into the suppression of the effect. A variety of techniques have been developed to 'condition' electrodes in order to enable them to function at higher field strengths. Four main methods of electrode conditioning have been concentrated on by previous researchers in the field: spark conditioning, glow discharge conditioning, current conditioning and gas conditioning [1].

Recent research however, has indicated that it may also be possible to use thermal treatments of electrodes as a conditioning technique. For example, work by

Niedermann et al [12,44] has indicated that thermal processing can have a significant effect upon both the emissivity and the distribution of sites on electrodes. Indeed, Padamsee [13] has developed a thermal treatment technique to improve the performance of superconducting niobium RF cavities. In order to further probe the fundamental nature of the emission process, and also to investigate possible technological applications of thermal processing for electrode conditioning, a programme of research has been undertaken utilising the sample heating stage of the spectrometer system.

Thus, the effects of bulk heating on the emission site population, electrode I-V characteristics, spectral properties and emission site I-V characteristics have been investigated over the temperature range of 25-600°C. Such measurements have been undertaken both for the cases of zero and high applied fields. This experimental study is described in section 4.3. Further to this study, an investigation was also made into the effects of localised heating on the emission process, which is described in section 4.4. This investigation studied the transient heating of the electrode surface by the use of a high power pulsed laser under conditions of zero applied field and ambient bulk temperature.

4.2 Simulated M-I regime using LB films

As discussed in Chapter 2, there is much experimental evidence [6,34,42] indicating that impurity micro-structures on an electrode surface are responsible for field induced electron emission. Emission from such impurity structures was explained by Latham and co-workers [8,42,61] in terms of a field induced hot electron emission model. This model assumes an insulating impurity micro-structure of sub-micron dimensions on the metal electrode surface that gives rise to a metal-insulator emission regime.

Simulation studies [63,84] of this emission regime were initially performed using etched tungsten micro-point tips coated with a thin layer of epoxylite resin of thickness ≤ 0.5μm. These showed the characteristic 'switch-on' phenomena associated with the formation of electroformed conducting filaments through the dielectric layer. It was further established that such coatings also resulted in an enhancement of emission [63].

It was therefore decided to investigate the effects of submicron dielectric coatings on planar broad area electrodes, both from the technological perspective of potential applications to electron sources and also to further the understanding of the fundamental emission mechanism. For these studies, Langmuir-Blodgett (LB) films were used to produce the dielectric medium since they may be deposited with a high degree of reproducibility and with a low concentration of defects [83]. The film thickness may also be controlled to within the ångstrom scale range [86].

The experimental programme investigated the HV insulating properties of coated electrodes in order to provide an insight into the switching, electrical conduction and electron emission phenomena associated with MI structures. The study was performed on a collaborative basis with the GEC Hirst Research Centre [11,85].

4.2.1 Langmuir-Blodgett coating technique

The LB coating technique relies on the use of organic molecules containing both hydrophilic ('water loving') and hydrophobic ('water hating') functional groups. At an air/water interface, such molecules will align themselves so that the hydrophilic group is towards the water and the hydrophobic group towards the air. By the application of pressure parallel to the interface it is then possible to compact the molecules into a layer one molecule thick which may then be transferred to a surface by using a dipping process to create a highly ordered, although non-crystalline LB film (see Fig. 4.1). Such films may be produced accurately to a well defined thickness controlled by adjusting both the number of layers deposited and the size of the molecule.
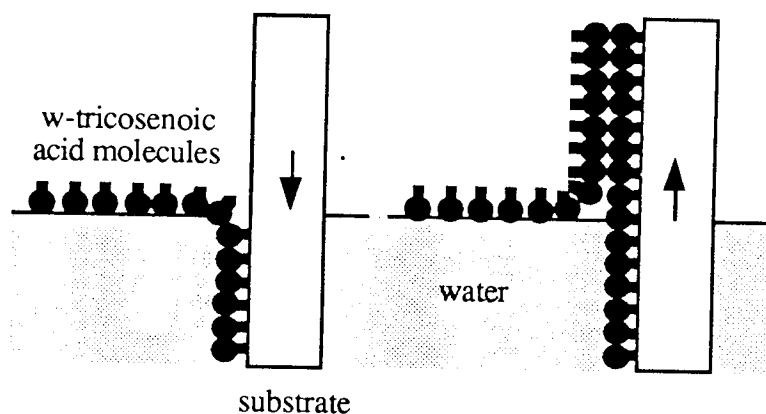
Figure 4.1 Schematic illustrating the Langmuir-Blodgett coating technique.

For this study, ω-tricosenoic acid ($H_2C=CH(CH_2)_{20}CO_2H$) was used to produce films of thickness in the range 90-470Å (a monolayer thickness is 30Å [86]) on Cu electrodes precoated with 1000Å metal substrates. Three substrate metals were used: gold, silver and tungsten. The ω-tricosenoic acid was prepared by the GEC Hirst Research Centre [87] and the substrates dipped using the technique due to Peterson [88]. The ω-tricosenoic acid was prepared as a 10^{-3}M solution in 1,1,1-trichloroethane which was dissolved onto a pure water sub-phase (Eglastat spectrum) and compressed using a surface pressure of 35mNm^{-2}. Layers were applied to the substrates at the rate of 0.1mms^{-1} lowering into solution, and 0.05mms^{-1} raising.

4.2.2 Experimental observations of LB coated broad area electrodes

The experimental studies to be described in the following section represent a follow-up study to that performed by S.Bajic, which is described more fully in his PhD thesis [45]. He investigated the distribution and stability of emission sites and the overall electrode emission characteristics, and a summary of his main experimental findings is presented in this section to provide a background for the experimental investigation to be described below.

Firstly, electrodes showed a characteristic 'switch-on' process. Thus, when initially increasing the applied gap voltage, no emission was observed until the switch-on voltage was reached. At this point the gap current rapidly increased as emission sites became active. During the first cycling of the applied field, the I-V curve showed a hysteretic behaviour which became a reversible characteristic after several cycles i.e. as is shown in Fig. 4.2. 'Switch-on' typically occured at field strengths of $E_{SW} \sim 20MVm^{-1}$ giving ≤ 30 sites at $30MVm^{-1}$. No correlation between E_{SW} and the film thickness or substrate material could be identified. Significantly, if a film was maintained under vacuum, or even exposed to various gas atmospheres, no new 'switch-on' process was observed, i.e. the site populations were permanent once established.

Aston University

Content has been removed for copyright reasons

Figure 4.2 Illustration of the reversible I-V characteristics of three LB coated electrodes of a) 510Å, b) 270Å and c) 90Å. The initial hysteretic behaviour is shown for c) (from [85]).

Overall site emissivity showed an exponential rise with applied field giving a linear F-N plot with ß-factors in the range 1000-5000. This compares with ß of 200-500 for the control electrodes. Emission currents of ~100μA could be obtained from these coated electrodes, at which point saturation of the emission current became evident. A greater number of emission sites (up to 30), were obtained on the coated electrodes compared to the controls (see Fig. 4.3). These sites were also significantly more stable, with the overall electrode current showing fluctuations in emission current of ≤2% at 1μA.

<div style="text-align:center">(a)   (b)   (c)</div>

Figure 4.3 Site distributions recorded at an emission current of ~10^{-4} A on a) a control, and b) and c) on LB coated electrodes with a film thickness of d (from [45]).

After exposure of the electrodes to gases at 1bar, no new 'switch-on' process was observed and the original site population remained virtually unchanged. Such exposure did, however, result in a slight destabilisation of the emission current with time. Similar results were observed for electrodes after removal from the vacuum system and storage in a vacuum dessicator. These results imply that some form of ageing takes place. Furthermore, a poor vacuum environment was shown to degrade the stability of the emission current, although the helium conditioning effect [89] was not observed to occur.

4.2.3 New experimental findings

The LB film coated cathodes were stored in a vacuum dessicator for at least 24 hours prior to insertion into the spectrometer system. In order to minimise the risk of external contamination from the anode, this was ultrasonically cleaned before use. Measurements were performed at a pressure in the 10^{-10}mbar range using a gap spacing of 0.5mm which enabled dc fields in the range 0-30 MVm^{-1} to be applied to the cathode.

4.2.3.1 Individual site I-V characteristics

These measurements were performed using the spectrometer system described

in Chapter 3. Initially, a site distribution map was recorded after switching on the emission sites. By employing the focussing electrode behind the anode to collect all the electrons transmitted through the anode probe-hole, it was possible to record the I-V characteristics of an individual site when it was positioned over the anode probe-hole (see Fig. 3.12). A typical result is shown in Fig. 4.4 for the I-V characteristic of a site formed in a 210Å thick LB film. These studies revealed ß-factors for sites that were generally of several hundred. However, no relationship was found between the thickness of the LB film and either the measured site ß-factors or the overall electrode emissivity.

a)
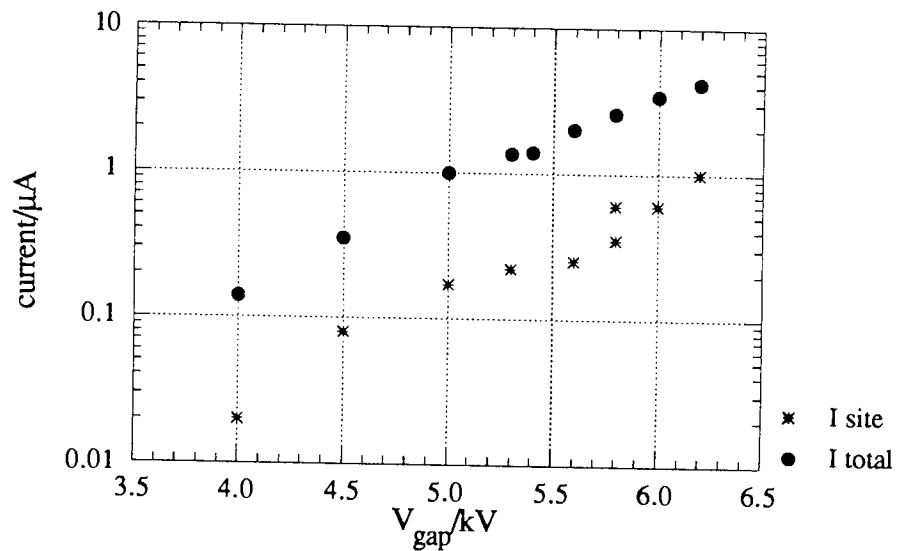
b)
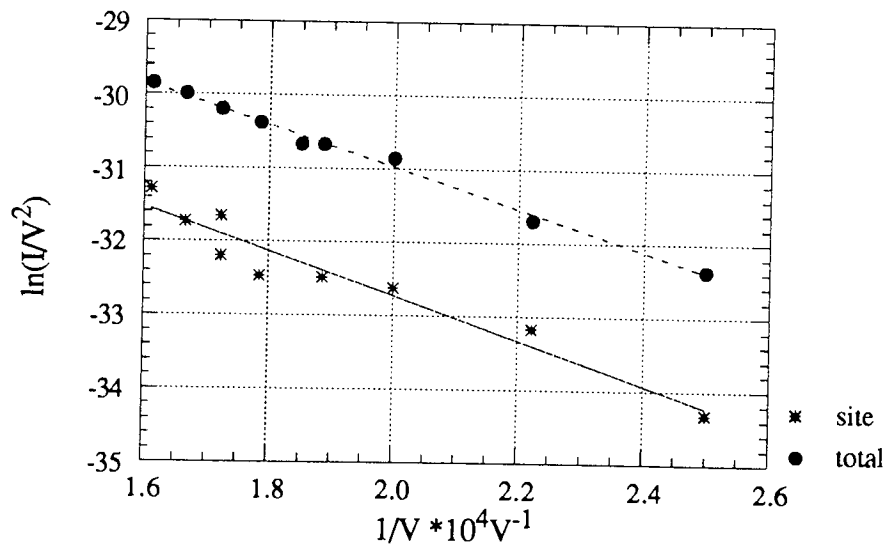
Figure 4.4 a) Individual emission site and total electrode I-V characteristics and b) FN plot for the above data from a 210Å thick LB film on a W substrate.

It was also possible to project an entire image of an emission site onto the phosphor screen within the system. However, owing to the recent introduction of new deflection plates to the analytical system, it was not possible to photographically record such an emission site image. Typically, the image was extensive and consisted of both diffuse spots (sub-sites) and sharp arc-like structures similar to those observed from some MIM structures as discussed in chapter 2 (c.f. Fig. 2.22 (b)).

4.2.3.2 Electron energy spectra of emission sites on LB films

Once a particular emission site had been located, an individual sub-site could then be positioned over the entrance probe-hole to the electron energy analyser. Emission spectra from this sub-site were then obtained over a range of gap fields, typically between 5-10MVm^{-1}, using an energy scan width of 10eV. These measurements indicated that a sub-site generally gave rise to a single-peaked spectrum, as shown in Fig. 4.5, although in a small percentage of cases ($\leq$5%), multiple peak spectra were observed [42,54].
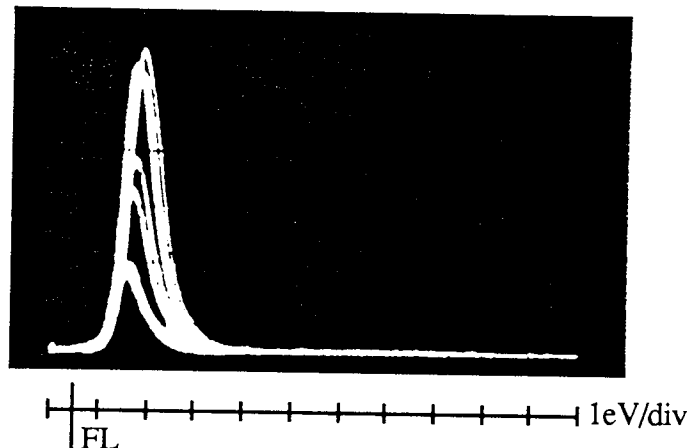
Figure 4.5 Typical spectral sequence obtained from an LB site (210Å thick LB film on Ag substrate measured over the field range 4.6-5.8 MVm^{-1}).

Figure 4.5 shows the type of spectral sequence typically obtained from an LB emission site (in this case it was from an Ag substrate specimen coated with a 210Å film). The spectra were recorded over a field range of 4.6-5.8 MVm^{-1} in 0.2MVm^{-1} steps and show features typical of a non-metallic emission process, namely: i) a peak shift, ΔE_S, below the substrate Fermi level ($\geq$1eV), ii) a broad peak FWHM, $\Delta E_{1/2}$, of $\geq$0.5eV, and iii) a high degree of peak symmetry. Furthermore, closer inspection shows that, in common with 'natural' emission sites on HV electrodes
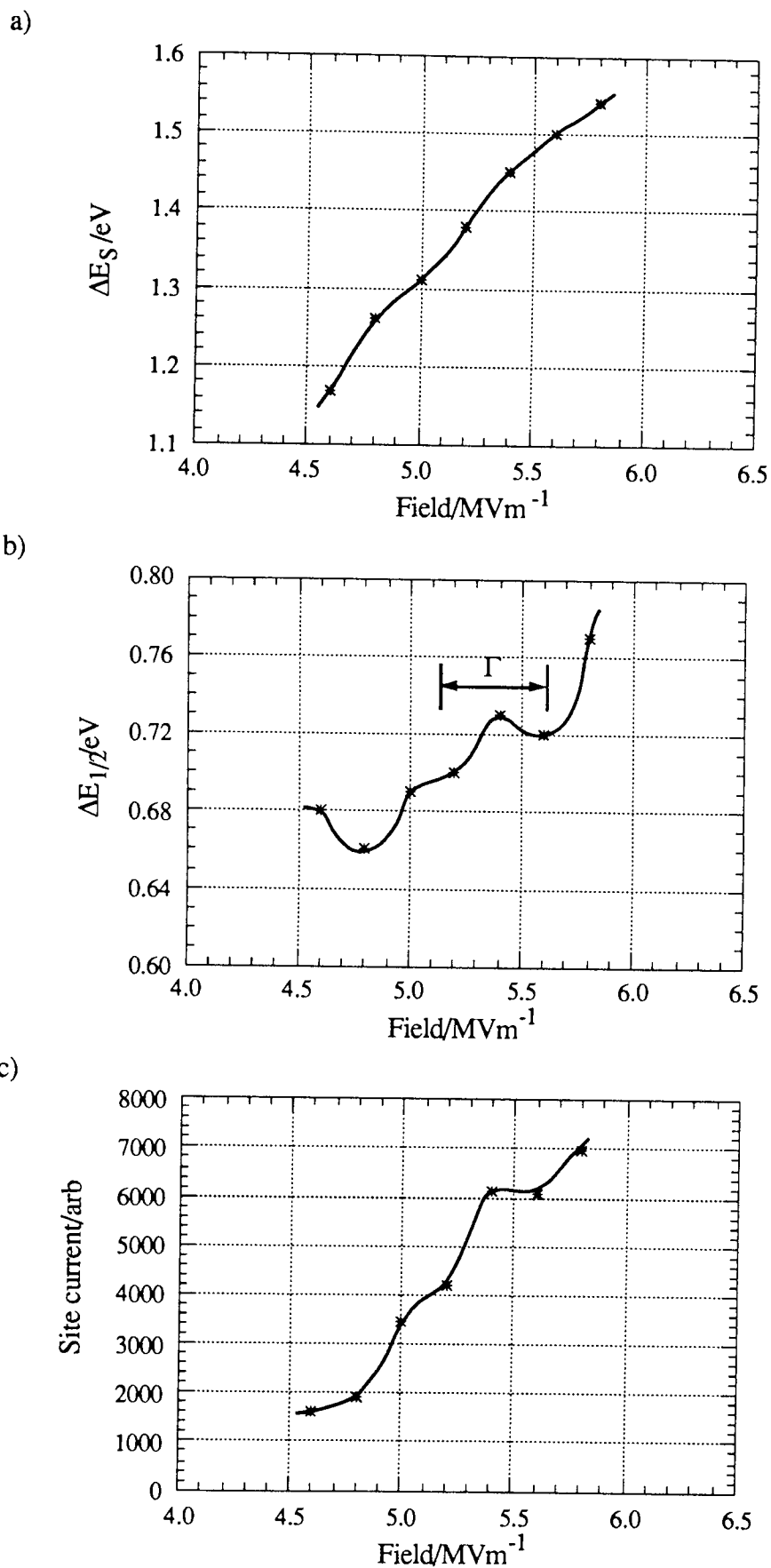
Figure 4.6 Spectral data for site on 210Å LB coated electrode showing a) ΔE_S, b) $\Delta E_{1/2}$ and c) sub-site current (arbitrary units) vs applied field.

a)

b)

c)
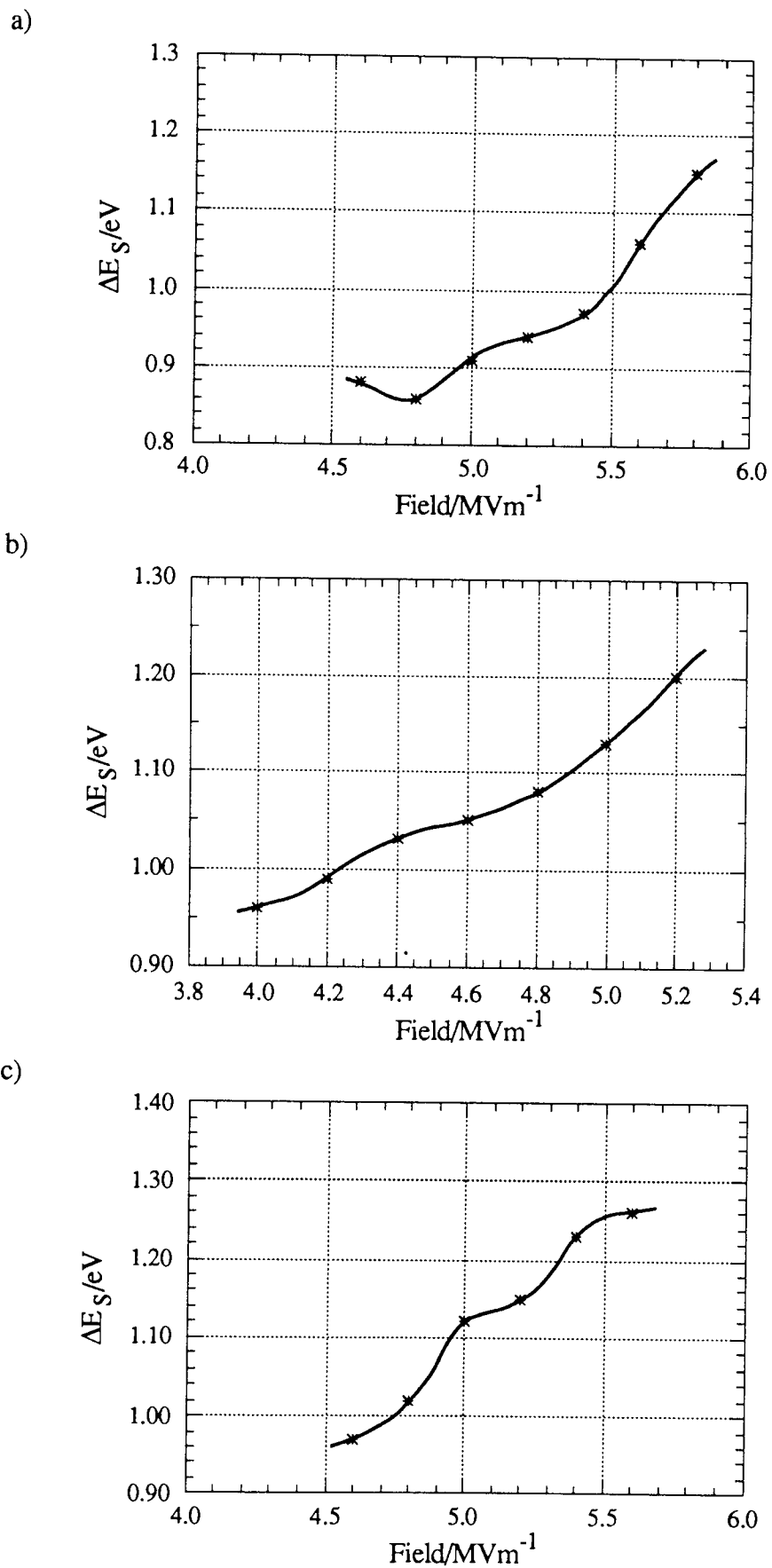
Figure 4.7 Comparison of ΔE_S of sites on electrodes coated with LB films of thickness a) 210Å, b) 330Å and c) 450Å.

a)

b)

c)
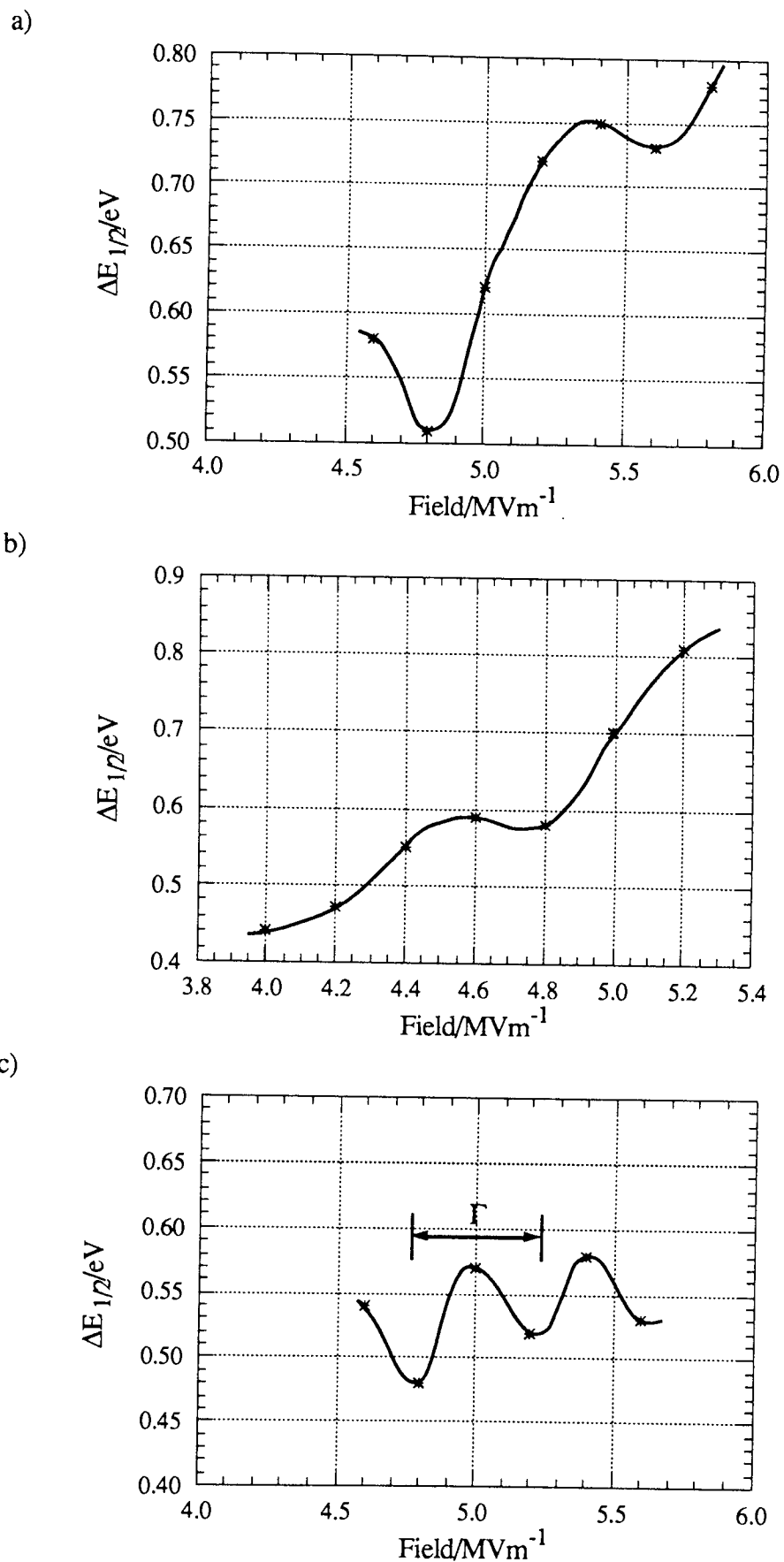
Figure 4.8 Comparison of $\Delta E_{1/2}$ of sites on electrodes coated with LB films of thickness a) 210Å, b) 330Å and c) 450Å.
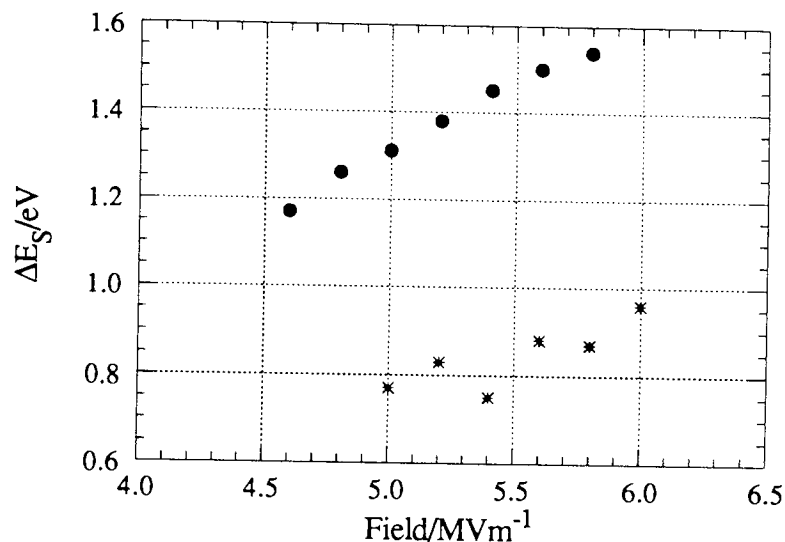
Figure 4.9 Illustration of ΔE_S for two sub-sites of an emission site on an LB coated electrode showing the wide variation in their spectral characteristics.

[40,41], the spectra show strong variations with increasing applied field. To illustrate this, Fig. 4.6 shows the typical field dependence of ΔE_S and $\Delta E_{1/2}$ for the series of spectra in Fig. 4.5. Also plotted is the field dependence of the site current, which is determined from the area under the spectral peak. By comparison with 'natural' HV electrode site behaviour (c.f. Fig 2.11), it will be seen that the LB films gave rise to significantly greater shifts ($\geq 1 eV$) and FWHM's ($\geq 0.5 eV$). No correlation was observed between the spectral shift or FWHM and the coating thickness.

Contrary to the behaviour of 'natural' sites, however, is the observation of an apparent oscillatory variation in the spectral characteristics of a significant proportion of the sub-sites (~50%) observed on the LB films. This phenomenon is significant within the data acquisition uncertainty of ±0.02eV. The oscillation is most marked in the behaviour of the spectral width, where the mean value is generally found to be virtually constant, but sinusoidally modulated with field (Fig. 4.6(b)). Furthermore, it is clear that the oscillations of the three spectral parameters show the same phase and frequency relationship with a constant period, Γ, of ~0.6 MVm^{-1}. Individual sub-site I-V characteristics may also be determined and these are typically of the form shown in Fig. 4.6(c). Sub-site ß-factors may not be calculated since the currents are determined by integration of the spectral peak. The I-V characteristics also reveal the oscillatory behaviour observed in the other spectral parameters.

Comparative studies have been performed on samples having different coating thicknesses. Figures 4.7 and 4.8 show the spectral shift and width respectively for Ag substrate electrodes with LB multilayers of: a) 210Å, b) 330Å and c) 450Å. In

92

general, these studies have shown that there is no correlation between the coating thickness and the spectral shift or FWHM. Similarly, those sub-sites that display an oscillatory behaviour have the same period, and therefore there does not appear to be any correlation of Γ with either the film thickness or gap field. In fact, there is as wide a variation in the spectral parameters between the individual sites of an electrode as there are between sites on electrodes of different coating thickness, as may be seen from Fig. 4.9.

4.2.5 Discussion of the emission properties of LB coated electrodes

The findings presented in the previous section have shown that the coating of an electrode with a thin dielectric film (of thickness 100-1000Å) results in a marked change in electrode emission properties. Compared to 'natural' uncoated electrodes, there is an increase in the number of emission sites and hence overall emission current at a given applied field. Emission may also be stimulated at anomalously low field strengths of <10MVm^{-1} and high currents, up to 10μA per site may be obtained. The characteristic site 'switch-on' process, and the forming of a permanent site distribution will now be discussed in terms of the filamentary and hot electron models.

Further consideration will also be given to the electron emission spectra, particularly the observations of anomalous oscillatory behaviour in the spectral shifts, widths and site current with increasing applied field. Such behaviour has been noted in independent studies of oxide coated cathodes [42], which have a strikingly similar emission regime consisting of thick (≥50Å) oxide layers coating OFHC copper substrates. No precise quantitative explanation of these phenomena exists at present, although it is possible to consider certain potential mechanisms.

4.2.5.1 Idealised filamentary model

Firstly, the idealised filamentary model as developed by Dearnaley et al [48] and Adler et al [49], will be considered. This model, described in section 2.4.1, considers dielectric switching in MIM devices to create conducting channels or filaments that are permanently formed. If such channels were assumed to be formed in the LB dielectric layer between the metal substrate and vacuum interface, they would provide a conduction path for electrons and therefore explain the steady state emission properties of the LB films. The formation of such channels is assumed to occur randomly at positions on the MI interface where suitable conditions exist for the injection of electrons from the metal into the conduction band of the dielectric. At the vacuum interface electrons are then emitted either through, or over, the

vacuum barrier. This has generally been assumed to occur through the generation of hot electrons by heating in the electric field. However in this case, the dielectric material is known to have a negative electron affinity [86] and thus electrons in the conduction band are already above the vacuum barrier [90].
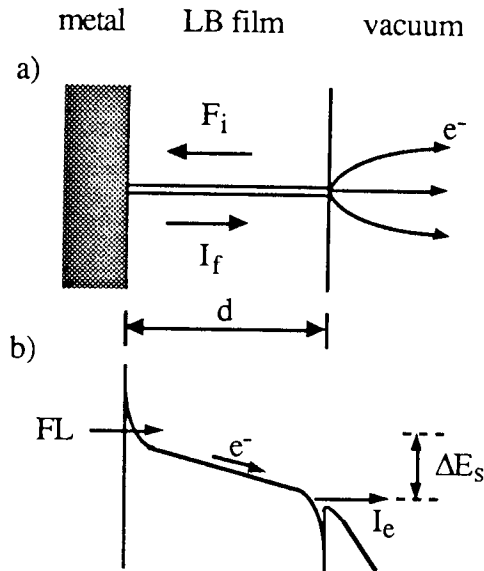
Figure 4.10 Schematic showing a) an idealised filament formed through the dielectric LB film and b) the associated band diagram.

Assuming the dielectric properties are constant in the vicinity of a conducting filament, i.e. that the current is low, then the shift in the spectral peak, ΔE_s, will be related to the potential drop due to the internal field as indicated in Fig. 4.10. Thus, for a film of thickness d, the implied internal field is given by

$$F_i = \Delta E_s / d \qquad\qquad 4.1$$

However, this indicates a value of $\sim 100 MVm^{-1}$, an enhancement of some ten times greater than the internal field calculated from electrostatics, which is approximately $F = \varepsilon_r F_g$ where F_g is the gap field and ε_r the relative permittivity of value ~ 2 [86]. However, a metallic conducting filament would experience a field enhancement at its tip, of approximate value

$$\text{ß} = 2 + h/r \qquad\qquad 4.2$$

where h is the filament height and r its radius. At a current density of 10^7 Acm^{-2} (the current density threshold for the electro-migration of metallic atoms into the dielectric [91]) and a site current of 5µA, the diameter of a channel would be $\sim 2 \times 10^{-7}$cm thus resulting in a field enhancement of $\sim 15x$ for a 500Å LB film.

94

Alternatively, other factors could affect the measured spectral shift should the filament not be metallic in nature. These could include both effects due to surface charge screening in the dielectric layer and resistive transport losses through the filament. These effects may be characterised by the equation

$$\Delta E_s - V_{int} = k_1 F_g d/\varepsilon_r + i_f R_f \qquad 4.3$$

where k_1 represents a constant to compensate for the field reduction due to surface charging, V_{int} represents the potential drop across the interface between the substrate and filament, and i_f and R_f correspond to the filament current and resistance respectively. For the system under consideration k_1 is assumed to be ~1 owing to the negative electron affinity which would be expected to prevent charge accumulation. If a large number of traps or surface states exist, then the value of k_1 could be altered significantly, although it is not possible to quantify these factors at present. It would be expected that a metallic filament would have a negligible potential drop at the interface and therefore V_{int} ~0. Thus, using the data from Fig. 4.7(a), a filament resistance of R_f ~ 0.1 MΩ is implied by a filament current of 5μA.

Previous experiments have shown that LB [91,92] and oxynitride [93] MIM structures show similar conductivities. Particularly in the case of the LB structures [91], both high conductivity (few tens mΩ) and low conductivity (1MΩ) states have been observed. It is unclear whether the filaments are metallic in nature, although in the case of the low conductivity state [91] a conducting behaviour of $I \propto V^2$ is exhibited, characteristic of Poole-Frenkel conduction [94] or Schottky emission [95] which are both non-metallic processes. In the case of these LB coated emitters however, it is not possible to determine which conduction mechanism may be operating since the I-V characteristics of the bulk dielectric may not be measured directly. As discussed in detail in section 4.3.3.1, the voltage drop across the entire dielectric region is the sum of the potentials across the M-I interface region and the dielectric bulk. Thus it is not possible to determine the nature of the filamentary conduction mechanism, although the creation of metallic filaments may be possible by electromigration of substrate material [91], which occurs under high current densities of >$10^7 Acm^{-2}$. The observed field enhancement is also consistent with a metallic filament at such current densities.

A further point to consider is that these films are very thin, of the order of 7-15 molecules in thickness (30Å per layer), which may result in an incomplete band structure i.e. the conduction band may consist of discrete levels rather than a continuum of states [96]. Thus, as the applied field is increased consequently increasing the M-I interface field, it will become possible for electrons to tunnel into higher states in the conduction band of the dielectric. However, this would happen in discrete jumps owing to such a non-continuous band structure thereby resulting in discrete jumps in conductivity. Such a mechanism may therefore account for the observed oscillatory behaviour of the spectral characteristics.

Additional support for this model is provided by the observation that the helium conditioning effect does not appear to be operative on these emitters. As discussed by Bajic [45,96,97], the addition of helium gas at low pressures ($<10^{-5}$ torr) into the electrode gap results in the suppression of emission occuring from 'natural' sites on Cu electrodes. The model he developed explains this effect by considering the implantation of high energy helium ions into the critical interface region between the metal and insulator. It is assumed that these implanted ions reduce the band bending and thereby suppress the tunnelling of electrons into the insulator, which is an important aspect of the hot electron model [8]. Under the gap voltage range (5-15kV) at which helium conditioning is observed [45,96], helium ions have a range of ~1μm which corresponds to the typical thickness of an impurity particle. The LB films are very much thinner than this and therefore this mechanism would not be expected to influence emission from such sites, in accordance with the experimental observations.

The filamentary model therefore provides a fairly good explanation of the steady state emission characteristics. It does not, however, provide an explanation for the initiation of emission. As already stated, ω-tricosenoic acid has a negative electron affinity, and therefore the conduction band in the dielectric is raised well above the Fermi level of the substrate metal. Under these conditions, it is very difficult to see how electrons could be injected into the conduction band of the LB film. The following sections discussing particulate contamination and charging effects consider potential regimes that would enable initiation of the emission process.

4.2.5.2 Field induced hot electron model

Although it was stated that the hot electron model would be unlikely to be applicable to this regime since the dielectric has a negative electron affinity [86], the findings of the anomalous oscillatory behaviour in the spectral characteristics may be explained in terms of this model.

The energy levels of the dielectric would be altered by any degree of charge accumulation in the conduction band, due to, for example, traps or surface states. Should such charging result in a raising of the vacuum barrier so that the electron affinity becomes positive, electrons would then require heating in order to be emitted and thus the hot electron model would become applicable. A shifting of the conduction band closer to the Fermi level, resulting from charge accumulation, would have the additional property of increasing the probability of electron tunnelling between the metal and dielectric occuring.

From reference to equation 2.29, deriving the width, $\Delta E_{1/2}$ in the hot electron model it may be seen that $\Delta E_{1/2}$ depends on the relative change of the electron

temperature T_e with applied field at the I-V interface. As discussed by Bayliss and Latham [8] and Xu [61], the hot electron temperature will depend on a number of factors, in particular the local field at the interface region and the electron energy loss processes in this region due to electron-phonon interactions [99].

According to the hot electron model, the total energy available for the generation of hot electrons is given by

$$\Delta E = V_o \frac{d\beta 2}{D\varepsilon_o} + \chi - \phi_i - S - V*$$ (4.4)

where $V*$ represents the screening effect of stored charge at the I-V interface (see Fig. 2.20). Thus, the available energy for generating hot electrons is dependent on the surface charge and it may therefore be possible that the fluctuations in $\Delta E_{1/2}$ could be associated with fluctuations in the stored charge as the field is increased. Fluctuations in the stored charge would also affect the surface field enhancement, and therefore the shift ΔE_s.

Alternatively, if the assumption of Bayliss and Latham [8] that the hot electron temperature is a linear function of ΔE is applied, then

$$k(T_e - T_o) = \alpha e \Delta E$$ (4.5)

where α is a factor representing the energy loss to lattice phonons. Thus, $\Delta E_{1/2}$ would be expected to increase with ΔE assuming that $\Delta E_{1/2}$ is independent of T_e. The complex large molecular structure of ω-tricosenoic acid may well give rise to a wide spectrum of phonon loss modes for conduction band electrons which could alter non-linearly with ΔE. Furthermore, since the material is non-crystalline, there may exist characteristic phonon modes that alter spatially between film layers. Consequently, the oscillatory nature of certain spectra may be related to particular frequencies and harmonics of the multilayer film structure.

From equations 4.4 and 4.5, it may be seen that both the energy loss mechanisms and the field at the surface of an emitting channel are important to the measured spectral properties, although at this time it is not possible to give a more quantitative explanation of these phenomena.

4.2.5.3 Contaminant particles

Observations of 'natural' emitters have shown them to be associated with impurity particles of size $\leq 1\mu m$ [8]. Under laboratory conditions such contaminants are found in densities of up to $10^7 cm^{-2}$ [7] and such contamination levels would therefore be expected on the LB substrates, and could be responsible for the initiation of the emission process. As indicated from Fig. 4.11, three main types of

particulate contamination would be expected: on the substrate surface (either an insulating inclusion, or a conducting particle separated from the substrate by the ambient surface oxide layer), within the dielectric film, or on the surface of the LB film. Also indicated by this figure are the potential emission mechanisms.
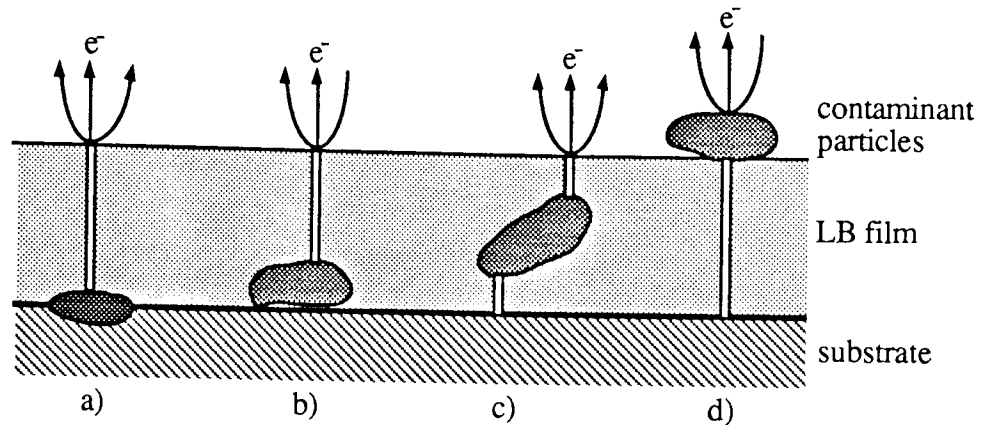
Figure 4.11 Possible types of particulate contamination in LB films and their role in the emission process. These contaminants may be a) an insulating surface inclusion, b) a conducting particulate separated from the substrate by the ambient surface oxide layer, c) a conducting particle embedded within the film or d) a conducting particle on the surface.

For the case of a contaminant particle present on the substrate surface, shown by Figs. 4.11(a) or (b), several mechanisms may be important. Firstly, the LB film may modify the surface properties, such as the work function, of the underlying particle. This effect is employed in the use of caesium and caesium oxide coatings on thermionic and photo-emitters in order to increase their efficiency [100], and results from the overlap of the substrate and coating wavefunctions. Thus, a coating of only a few molecules of the dielectric may well reduce the barrier height at the I-V interface and thereby decrease the field at which an existing dielectric particle on the sample surface would become an emitter. Alternatively, it is possible that in coating over a large contaminant particle there will exist defects in the dielectric film creating areas of the particle that are not insulated from the vacuum but can emit electrons direct without transport through the dielectric. For such a case though, it is difficult to explain why this effect would increase the number of particles that emit at a given field, or lower the field at which site 'switch-on' occurs, although pinhole defects could enhance the substrate surface field [5].

A second potential emission regime exists (Fig. 4.11(c)) for a particle embedded in the LB film. In this case, as described by Bajic [9,45], an initial antenna effect could result in the formation of a conducting filament between the substrate and the particle. Should this occur, the potential of the particle would fall rapidly to that of the substrate resulting in a field enhancement at the upper surface.

This in turn could then stimulate the formation of a secondary conducting channel through the dielectric layer between the particle and the vacuum.

For the case of a contaminant particle on the film surface (Fig. 4.11(d)), the dielectric film of thickness 100-500Å would be expected to provide a good blocking contact. As discussed in chapter 2, a conducting particle separated from the substrate in such an MIM regime is believed to initiate a dielectric switching event resulting in emission. For example, a particle of size ~1μm on a dielectric of 500Å thickness and $\varepsilon_r=2$, would experience a field enhancement of $\beta = 1/(2*0.05)$ ~10, similar in value to that derived from the spectral data. Furthermore, in the case of 'natural' emitters, such contaminant particles are separated by a thin oxide layer of 20-50Å thickness which may not always provide a sufficiently good blocking contact. In this case, a particle would charge, resulting in a reduction of the field enhancement and therefore a diminished probability of the creation of an emission centre. This could explain the increased number of emission sites observed on the LB coated samples compared to uncoated emitters. Additionally, contamination at the interface could produce impurity levels that would enable resonant tunnelling between the metal substrate and LB film layer (c.f. Poole-Frenkel conduction [94]) and thereby provide a mechanism by which electrons could enter the conduction band of the dielectric. Site 'switch-on' is, however, observed to occur at far lower fields with LB coated samples than for 'natural' emitters, but the thickness of the dielectric layer is an order of magnitude greater, which of itself would be expected to result in an increase in the applied field required to initiate tunnelling from the metal substrate, or to induce breakdown of the dielectric.

The validity of a contaminant particle model, particularly that of the MIM case of Fig. 4.11(d), is further supported by the observation of arc-like segments in the emission images similar to those of artificial MIM structures [53]. Such images are thought to be due to diffraction of hot electrons at the IM interface. Furthermore, such a model could also provide an explanation of the existence of multiple sub-sites at each emission centre: images typically consist of large diffuse areas overlapped by arc-like segments which are characteristic of diffraction. This may be explained in terms of both diffraction occuring at the interface of the contaminant particle and also emission from field enhancing features on the particle itself. Alternatively, diffraction of electrons at the vacuum interface of the LB film may be responsible for these arc-like features in the cases of Figs. 4.11(a)-(c).

Diffraction effects may also occur during electron transport though the LB film. The observed oscillatory behaviour of the spectral characteristics (Figures 4.7 and 4.8) appears to be both of constant period, Γ~0.1eV, and independent of total film thickness [85]. Thus, it would appear that this behaviour may be an intrinsic property of the films themselves, where the most obvious parameter is the spacing between the individual monolayers of the structure. Such periodic behaviour is

characteristic of Bragg diffraction effects, which could influence the emission process and hence the spectral characteristics.

Considering a one dimensional Bragg diffraction model for the electrons transported within the LB film, the first and second order diffraction maxima are given by

$$n\lambda_1 = 2D \qquad\qquad (n+1)\lambda_2 = 2D$$

where λ_1 and λ_2 are the de Broglie wavelengths associated with electrons of energy E according to the equation $\lambda(\text{Å}) = 12.2/E^2$ for E in eV. Thus, the difference in wavelength $\Delta\lambda = \lambda_1 - \lambda_2$ will equal the lattice spacing ($\sim$30Å) for n=1. This then implies an energy difference of $\Delta E = 0.2\text{eV}$ between the first and second maxima. These fluctuations are of the same order as the periodic variation of the spectral parameters ($\sim$0.1eV). Thus, it is possible that as the electrons approach the I-V interface they are progressively heated above the ground state energy and so acquire sufficient energy to satisfy the above condition to enhance their escape probability.

A further feature that should be considered is the requirement for electrons to be injected into the conduction band of the LB film. This mechanism is considered in the hot electron model [8], and is assumed to require a high concentration of donors and traps in order to generate a thin depletion region and hence a likely tunnelling contact. Such a condition results from a high concentration of impurities, however the LB films used in this study are of high quality with a low concentration of impurities [86], and therefore marked band-bending at the MI interface is unlikely. Band-bending may result from polarisation of the dielectric film, which would be particularly applicable to the case of surface contamination on the LB film (Fig. 4.11(d)).

The observation that the helium conditioning effect does not occur in these films does not support hot electron emission by particulate contamination, particularly on the substrate surface. For particles contaminating the surface of the LB film however, ions are not likely to affect the emission, particularly if the antenna effect of the surface particle initiated filament formation.

4.2.5.4 Surface charging effects

Field enhancement effects are not limited solely to geometrical factors but may also be initiated by free charges. Thus, for the LB film emission regime the internal field is given by the external applied field, E, and the opposing polarisation field, P, generated within the dielectric by the aligned dipole charges as expressed in the equation: $D = \varepsilon_0 E + P$. Field enhancements could be caused by additional free positive charges on the sample surface. For example, a single positive charge

would generate a field of $30MVm^{-1}$ at a distance of 50Å falling to $0.3MVm^{-1}$ at 500Å. Alternatively, charge migration to asperities [101] on impurity particles on the film surface could result in sufficient field enhancement to promote electron emission. Indeed, some models [8] have invoked charge migration effects at the MI and I-V interfaces within the emission mechanism. These were based, however, on the assumption of the migration of electron-hole pairs generated by impact ionisation events within the insulator bulk. Such events are highly unlikely to be involved in the current emission regime since the generation of such an electron-hole pair typically requires ~1.5x the bandgap energy [102], which is some 10eV for the dielectric used in the current study.

Further charging mechanisms within the dielectric overlayer could influence the emission process, such as the ionisation of interband impurity levels or exoemission from shallow traps within the insulator bulk. If it is assumed that the widths of the electron energy spectra, typically $\geq 0.5eV$, indicate the average energy available in collision processes within the conduction band, then it would be probable that ionisation of shallow interband impurities would occur i.e. those less than 0.5eV below the bottom of the conduction band. Contaminant particles, typically known to contain foreign elements such as S or C [34] could provide the source of such impurities. Alternatively, exoemission [103,104] from shallow traps could enhance an initial charging mechanism and hence initiate emission. Thus, electron flow from the metal to insulator is not necessarily required in order to stimulate emission (as in the hot electron emission model of section 2.4.4, or the idealised filamentary model).

The memorising of 'formed' emission sites, even over long periods of time (several weeks) in ambient atmospheres does not contradict a mechanism involving surface charging. Although it is likely that exposed charges would be neutralised over such a time period, such charging could well be the mechanism that initiates emission after which permanent changes in the dielectric then produce a formed filament. Alternatively, either MI interface charging [8] or filament formation, whether of a metallic or non-metallic nature, would also provide a basis for the creation of 'permanent' sites.

4.3 Effect on the emission process of bulk heating under conditions of zero and high applied fields

Thermal stimulation has proved to be a powerful diagnostic technique for fundamental investigations of the microscopically localised prebreakdown electron emission process. Studies by Bayliss and Latham [41], and later Xu and Latham [105] have shown that as a result of the bulk heating of an electrode in the presence of an applied electric field, profound changes occur in the spectral characteristics of

an emission site. Thus, as the temperature is increased, the peak shifts towards the Fermi level and the FWHM increases; furthermore, the peak shape is also affected and becomes more symmetrical. Investigations by Niedermann *et al* [12,34] have shown that the overall distribution of sites is also affected by thermal processing, where heating of niobium electrodes up to 800°C stimulated the formation of emission sites, but heating in the range 1200-2000°C resulted in a suppression of the emission [12]. However, similar thermal treatments of aluminium electrodes [106] consistently had little effect upon either the emissivity or site distribution.

Thus, it was decided to investigate the effects of bulk thermal heating on copper electrodes using the spectrometer system. By employing an integral sample-heater stage, the effects of bulk temperature cycling over the range 25-600°C were studied under both zero- and continuous-applied field conditions. Measurements were made on the overall distribution of emission sites, the I-V characteristics of both the electrode and individual emission sites, and electron energy spectra at both ambient and elevated temperatures.

4.3.1 Zero-field temperature cycling

Bulk heating under zero-field conditions was performed by cycling the electrode to progressively higher temperatures and then cooling to ambient before measuring the emission characteristics. The temperature was cycled to progressively higher temperatures in 100°C steps up to a maximum of 570°C, with care being taken to ensure that the temperature was raised slowly in order to prevent the chamber pressure exceeding 10^{-6} mBar as the sample outgassed. All emission site measurements were performed at a chamber pressure of better than 10^{-9} mBar.

a)   b)
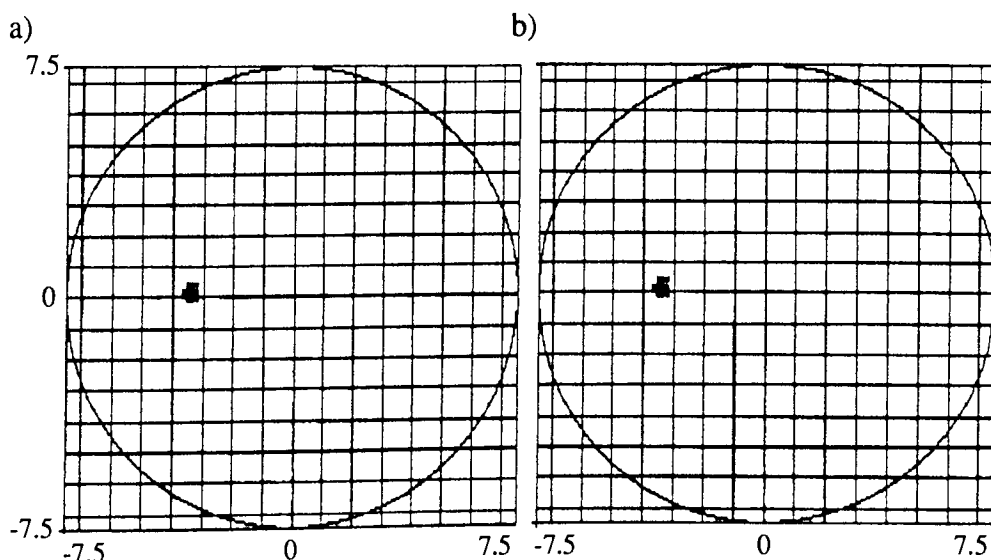
Figure 4.12. Plot showing that there was no variation in site distribution as the electrode was cycled to different bulk temperatures with a hold for several hours before cooling. a) initial distribution and b) after heating to 500°C.

102

a)
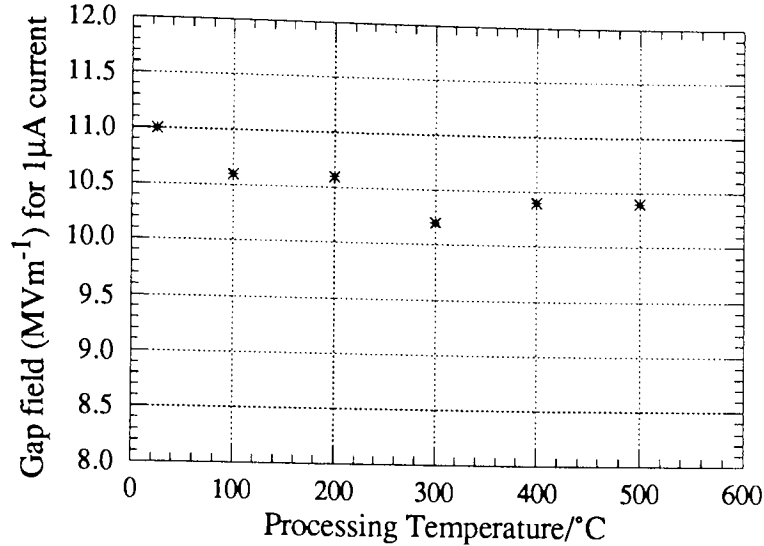
b)
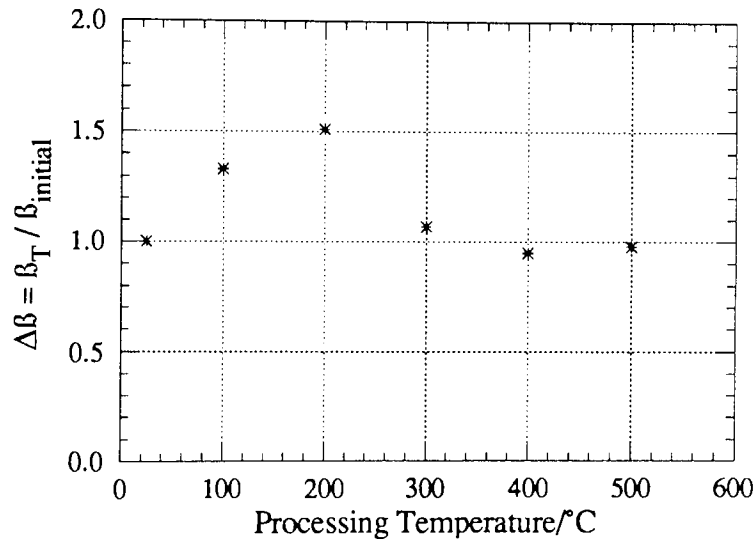
Figure 4.13 I-V characteristics of electrodes during zero-field bulk heat treatment. a) variation in the gap field required to draw 1μA and b) ratio of electrode post heat treatment, β_T, and initial, $\beta_{initial}$, β-factors.

Over the range of temperature that the sample could be heated through, little variation in electrode properties was observed. In general the site distribution was unaltered, as may be seen from the site maps of sample CH6 shown in Fig. 4.12, which compare the initial site distribution with that observed after heating to 500°C. The overall sample emissivity was also unaffected, showing only random fluctuations, although such fluctuations varied in degree with different samples. Fig. 4.13(a) shows the typical variation in gap field required to draw a current of 1μA, while Fig. 4.13(b) indicates the fluctuations in the ratio of the β-factors during the treatment procedure. It was occasionally observed that a sample did exhibit alteration to the emission site distribution during heat treatment, however the resulting site distributions were generally stable after further heating treatments to the same temperature, and this effect is illustrated for the case of a site distribution

a)

b)

c)
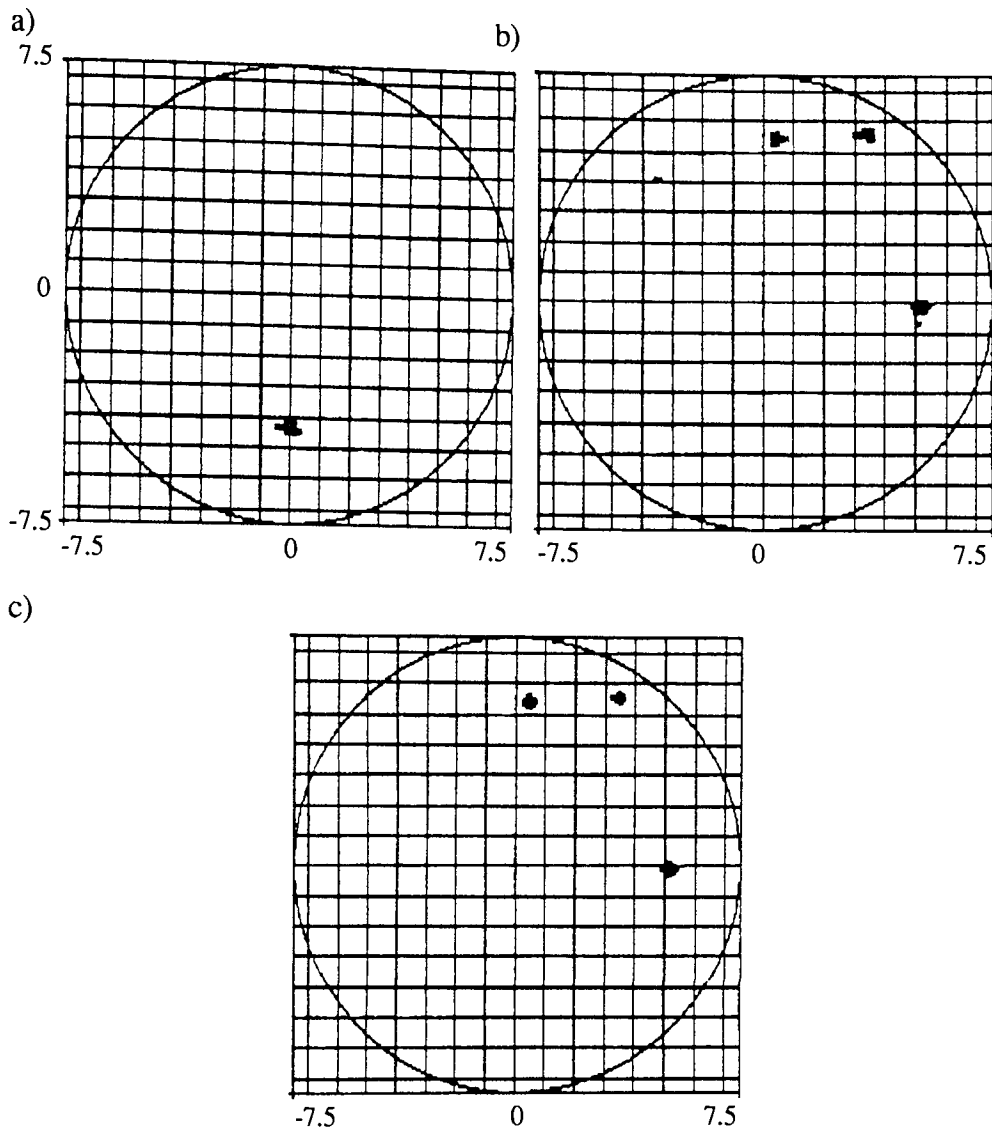
Figure 4.14 Switch in site distribution a) before and b) after heating of one electrode to 500°C, and c) permanency of new site distribution after further heat treatment to 570°C.
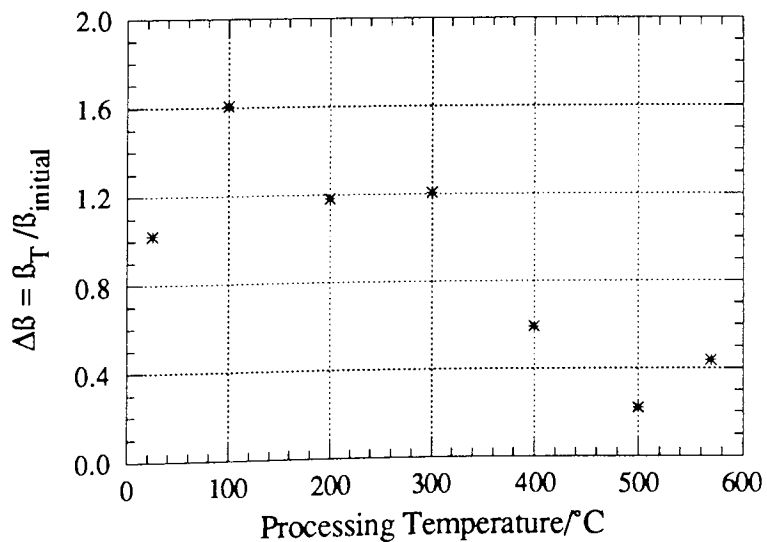
Figure 4.15 Change in electrode emissivity associated with the alteration in emission site distribution after heating to 500°C under zero-field conditions.

104

alteration after treating a sample at 500°C, shown by the series of site maps of Fig. 4.14. The electrode I-V characteristics also showed a change when the site distribution altered, but were stable after further treatments at this temperature, as indicated in Fig. 4.15. It is therefore concluded that this alteration in the emission site distribution represented a random switching of the emission site population as is occasionally observed [56].

In general, the emission spectra showed little variation with the temperature cycling treatment, as may be seen from the spectral parameters for a site after heating at 500°C and then 570°C (see Fig. 4.16). Spectra were typically of the form observed for 'natural' emission sites, where Fig. 4.17 presents a typical series of spectral curves for a site, recorded over the gap field range 7.06-8.40 MVm^{-1}.

a)

b)
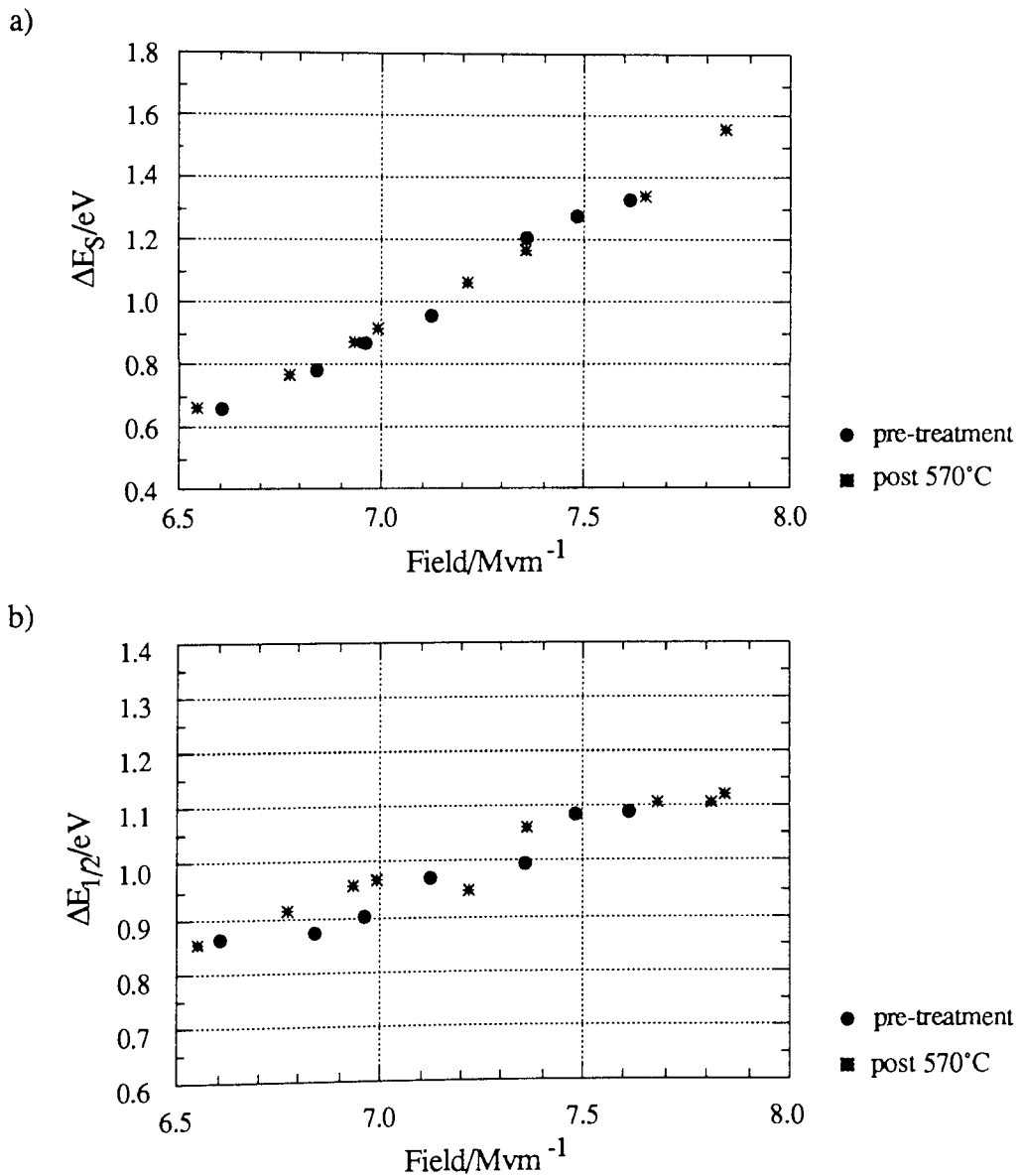
Figure 4.16 a) ΔE_S and b) $\Delta E_{1/2}$ for a typical site under zero-field heat treatment showing that the spectral parameters were generally unchanged by such treatment.
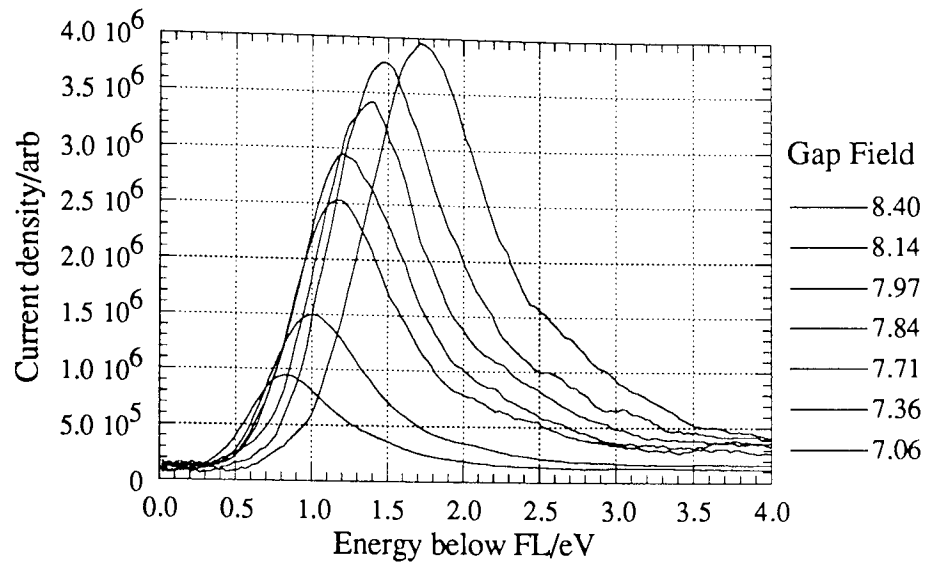
Figure 4.17 A typical series of emission spectra recorded over a gap field range of 7.06-8.40 MVm^{-1} (smallest to largest curve consecutively).

a)

b)
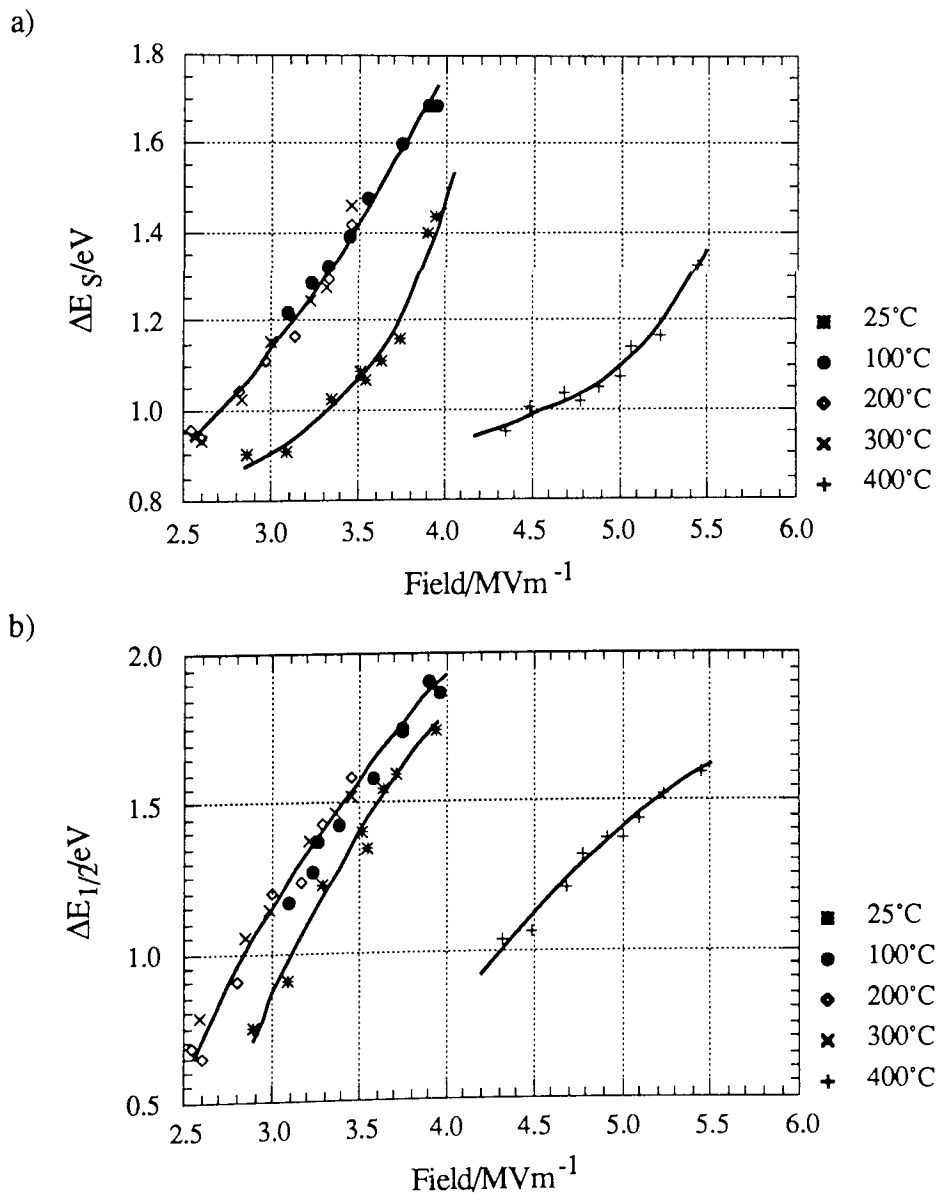
Figure 4.18 Spectral characteristics of the emission site that ceased to emit after 500°C zero field heat treatment showing a) ΔE_S and b) $\Delta E_{1/2}$.

No trend was observed in the spectral properties of the emission site which 'switched-off' until it was heated to a temperature of 400°C. On the subsequent heating cycle the site 'switched-off' and curves showing the peak shift, ΔE_s, and FWHM, $\Delta E_{1/2}$, for the as 'switched-on' state and after cycling at increasing temperatures, in 100°C steps, up to 400°C are plotted in Figs 4.18(a) and (b) respectively. On the subsequent treatment at 500°C the site switched off and therefore spectral data could not be recorded. It should also be noted that this site displays a slight change in both the spectral properties and the overall electrode emissivity after the first heat treatment, which is probably attributable to outgassing effects.

4.3.2 High-field bulk heating

Observations were also made for the case of continuous heating of the sample under high applied field conditions up to a maximum temperature of 500°C, with measurements being recorded at 100°C intervals. An important aspect of the experimental procedure is that the sample temperature was raised slowly in order to prevent the chamber pressure going above 10^{-6}mBar with the consequent risk of a breakdown event occuring. In fact it was necessary for the sample to be held at the set temperature for several hours to enable the chamber pressure to recover to better than 10^{-9}mBar. Effects on the electrode gap resulting from thermal expansion of the sample stage were monitored, and compensated for, by the capacitive technique due to Xu [61].
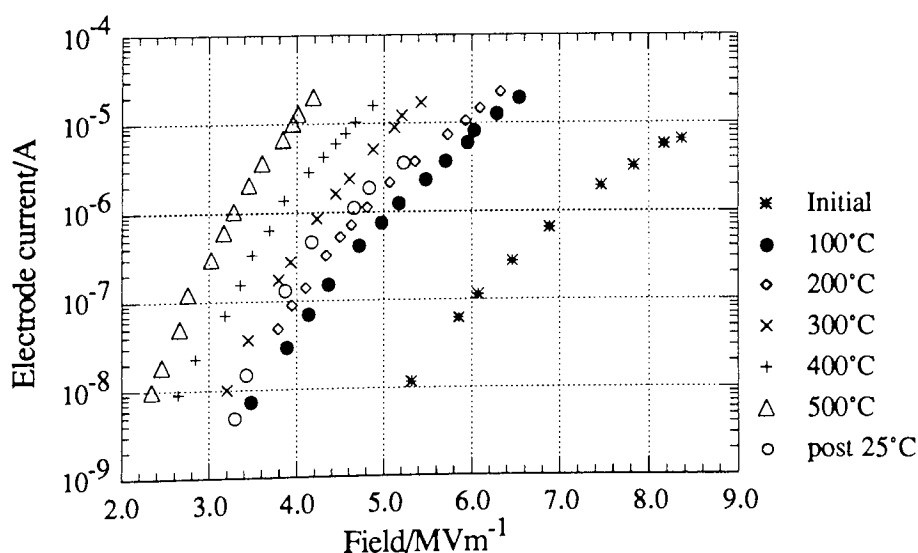
Figure 4.19 Variation of the total electrode I-V characteristics with temperature during bulk heating with a high applied field.

i) I-V characteristics.

As is shown by the series of I-V curves of Fig. 4.19, the total electrode I-V characteristics were strongly influenced by heating. Thus, even a relatively modest temperature rise to 100°C, resulted in a dramatic increase in electrode emissivity, which became more pronounced with increasing temperature. Significantly, after cooling back to ambient temperature the electrode emissivity was still enhanced compared to the case of zero-field heating, with a typical increase in the electrode ß-factor of between 1.5-2 times.
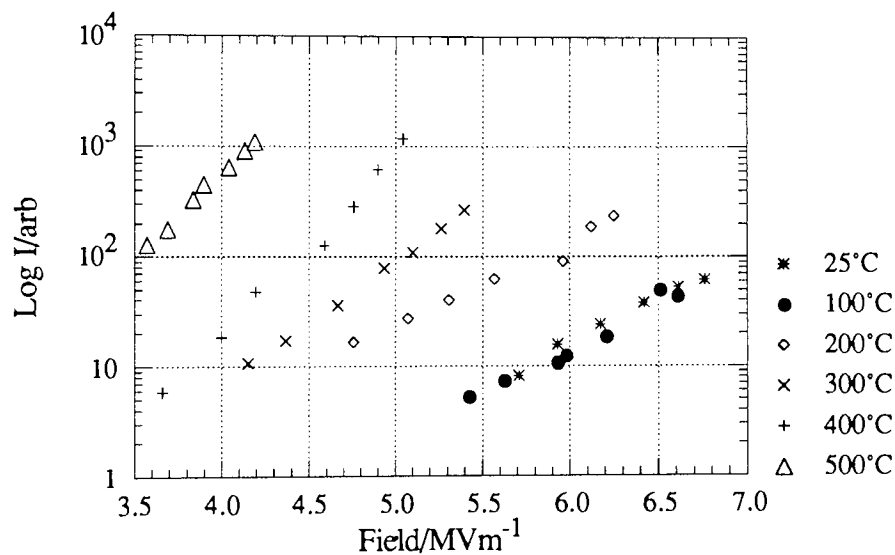
Figure 4.20 Graph showing the variation in sub-site emission current with temperature during bulk heating with a high applied field.
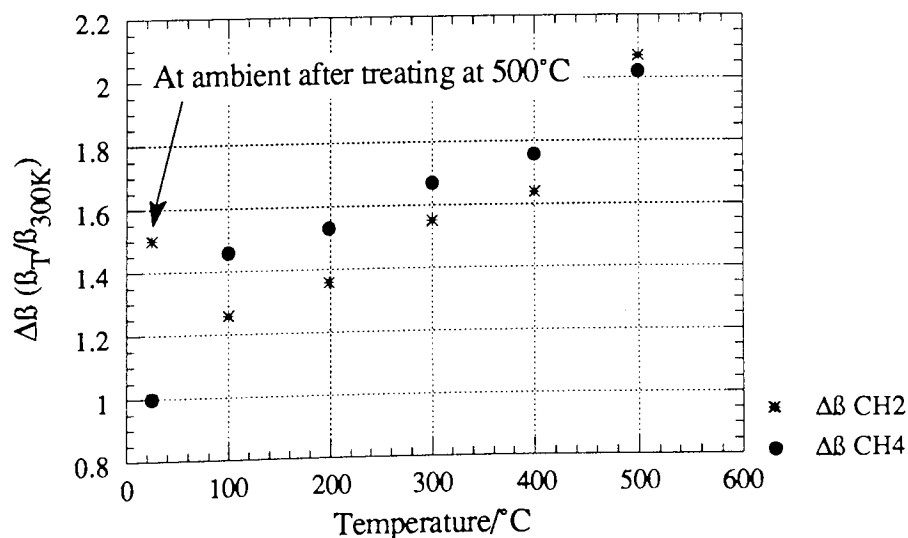
Figure 4.21 Alteration in electrode ß-factor with temperature during bulk heating with a field applied for two different electrodes, CH2 and CH4.

108
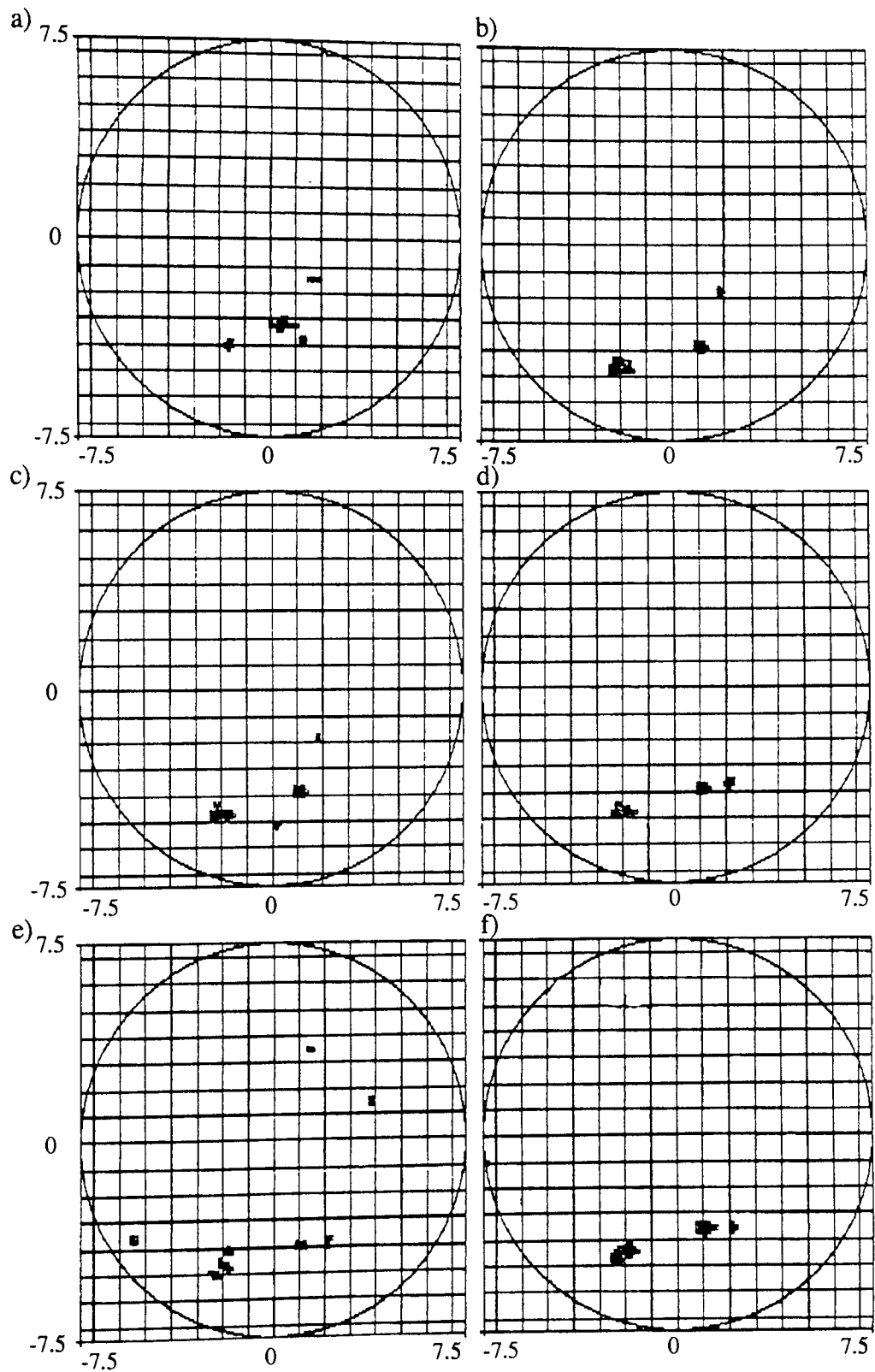
Figure 4.22 Distribution of emission sites with temperature during bulk heating under conditions of high applied field showing site distributions a) initially, b) at 200°C, c) at 300°C, d) at 400°C, e) at 500°C and f) after cooling back to ambient.

Studies on the emission characteristics of individual emission sites by measurement of the spectral area (Fig. 4.20) showed a general increase in emissivity with increasing temperature, i.e. similar to that observed for the total electrode behaviour described above. These measurements were determined from the area under the spectral peak and are therefore not quantitative, although they do enable a comparison of the 'before' and 'after' emission site ß-factors to be made, which show a clear trend to an increasing ß-factor as the temperature is raised (Fig. 4.21).

ii) emission site distribution.

There was little observed effect upon the emission site distribution until a temperature of 300°C was attained, at which point the formation of new sites was stimulated. However, some of the original emission sites were also extinguished during this process as may be seen from the sequence of site maps shown in Fig. 4.22. On cooling back to ambient temperature, some of these new emission sites were still evident, explaining the increase in overall electrode emissivity, and indicating that their 'switch-on' was an effect related to the application of an electric field during bulk heating, rather than being due to a purely thermal effect. Furthermore, some of the initial sites that 'switched-off' at elevated temperatures were found to start emitting again once the electrode was cooled back to ambient.

iii) spectral characteristics

The spectra observed were typical of those from 'natural' emission sites on broad area OFHC copper electrodes, with a peak shifted below the substrate Fermi level by $\Delta E_s \geq 0.5eV$ and FWHM of $\Delta E_{1/2} \geq 0.5eV$. Such spectra are characteristic of a non-metallic emission process as shown by the typical spectral sequence of Fig. 4.23(a) for the variation of the emission spectrum with field at ambient temperature.

However, as the bulk temperature was raised, significant changes were observed in the spectral characteristics as illustrated in Fig. 4.23(b). These changes consisted of alterations in both the peak shift and FWHM with field. The peak shift (Fig. 4.24(a)), ΔE_s, was seen to be reduced slightly with increasing sample temperature, although owing to the increase in emissivity lower field ranges were used for each increasing temperature measurement. Of more interest, it may also be seen that the gradient of the increase in ΔE_s with field shows a marked reduction (in the case of Fig. 4.24(a) from $1.0eV/MVm^{-1}$ to $0.2eV/MVm^{-1}$) as the bulk temperature is raised. The FWHM shows a very strong trend towards increasing

a)

b)
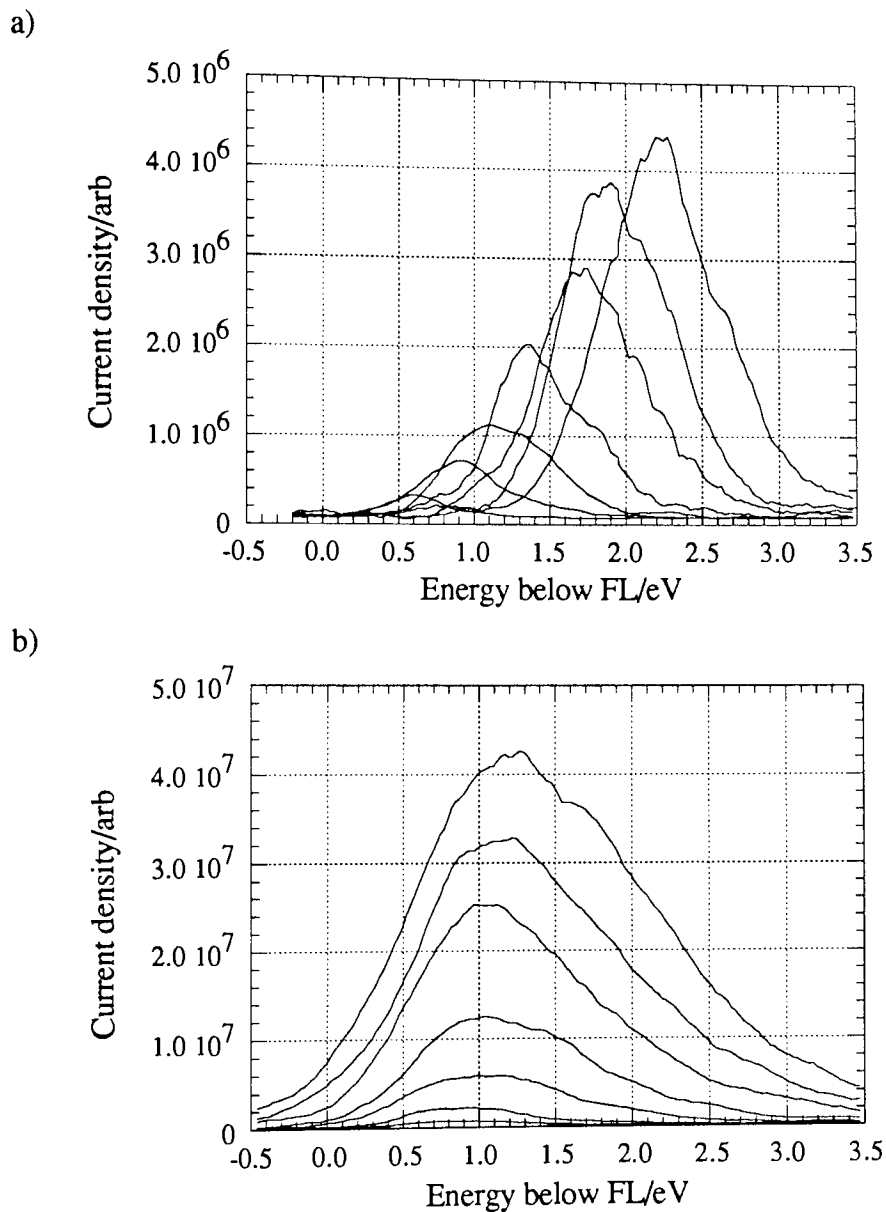
Figure 4.23 Series of spectral curves recorded at a) 25°C between 6.85-8.11 MVm⁻¹ and b) at 500°C between 3.33-5.13 MVm⁻¹.

width with temperature, as illustrated by Fig. 4.24(b). The gradient of this parameter is also seen to increase for higher bulk temperatures.

4.3.3 Discussion of bulk heating effects

The variation of the effects of bulk heating on the emission process shows distinct differences between the applied- and zero-field cases. It is not possible to explain all of these results completely, but qualitative agreement with the hot electron model of Bayliss and Latham [8] may be demonstrated by consideration of the physical processes occuring during bulk sample heating. In this context it is first necessary to consider the effects of bulk heating on the physical properties of

a)

b)
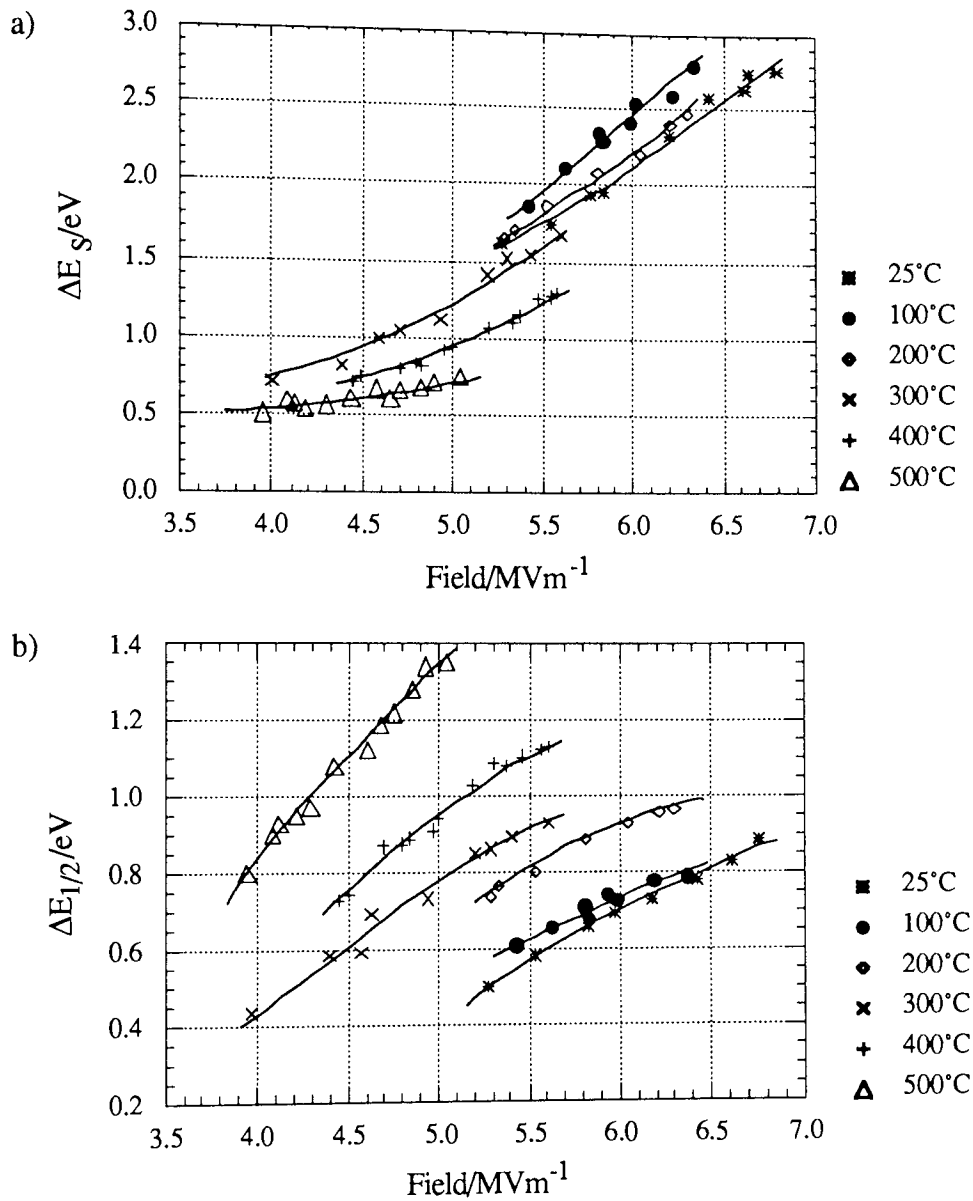
Figure 4.24 Graphs showing the variation in spectral parameters with temperature during bulk heating under high applied field conditions for a) ΔE_S and b) $\Delta E_{1/2}$.

the insulator and metal in order to provide the theoretical framework within which to discuss the various observations.

4.3.3.1 Variation in physical properties with temperature

The hot electron model [8] assumes certain electronic conditions for emission to occur, viz that an impure insulating particle is present on the surface with a favourable tunnelling contact between the insulator and the substrate metal. This contact must behave as a blocking contact, or the insulator would charge up as a field was applied thus screening the M-I interface. It is therefore necessary to assume that the insulator contains donor centres, due to impurities, which then produce a thin depletion layer at the metal-insulator interface and thus marked band bending.

For such a system, bulk heating will affect the populations of electrons within the donor and trapping states markedly by their thermal promotion to the conduction band, where such effects would be expected to influence the charge distribution and band shape within the insulator.

The electron distribution within the metal will also be affected by bulk heating with an increase in the high energy electron population above the Fermi level. This will result in a slight decrease in the degree of band bending required to initiate the conditions for tunnelling across the M-I interface. By Fermi-Dirac statistics, the probability of electron occupation of an energy state at energy E follows the equation

$$P(E) = \frac{1}{1+\exp((E-E_f)/k_bT)} \qquad 4.6$$

Bulk heating will also have an effect upon the conductivity of the insulator, which varies exponentially with temperature according to the equation [65,66,67]

$$J = e\mu \frac{V_b}{d} N_c \left[\frac{N_D}{N_T}\right]^{1/2} \exp\left[-\frac{E_D+E_T}{2k_bT}\right] \qquad 4.7$$

where N_c is the effective density of states in the insulator, N_D is the donor density, N_T the trap density, E_T and E_D are the electron trap and donor energies respectively, F_L is the Fermi level position, μ is the electron mobility, d the insulator thickness, V_b is the voltage across the bulk of the insulator and J the current density. From this equation it will be seen that as the temperature is increased the voltage across the bulk of the insulator, V_b, will decrease for the same current density. Therefore, the insulator will be able to conduct the same current at a lower applied field across the insulator, and hence, at a smaller gap field. This equation may not be entirely valid at elevated temperatures however, as it applies under conditions where $E_T>F_L>E_D$ with all energy levels just under the conduction band and when nearly all the electron traps are full. It is this latter condition that may breakdown at higher temperatures as thermal excitation of the traps may result in a significantly lowered occupation probability. For example, the thermal energy associated with a temperature of 500°C is ~0.07eV.

A further effect that should be considered is the tunnelling current across the M-I interface. This is given by the equation [65,66,67]

$$J = \frac{5.56 \times 10^{-14}}{\epsilon^*\phi_0} N_D(V_c+\phi_m-\phi_i) \exp\left[-3.6 \times 10^{13}\left[\frac{\phi_0^3\epsilon^*}{N_D(V_c+\phi_m-\phi_i)}\right]^{1/2}\right] \qquad 4.8$$

which is seen to be essentially independent of temperature since the principal criteria affecting the tunnelling current are the area of the contact and the potential

across this contact, V_c. Therefore the current density across the I-V interface, while not directly dependent upon the bulk temperature, will be affected by the surface field and band structure at the M-I interface through the term V_c. These factors are themselves determined by the charge density in that region which is influenced by the bulk sample temperature.

4.3.3.2 Emission site distribution

It is clear from the results shown by the two different bulk heating regimes that the stimulation of new emission centres under heating is not solely a thermal effect but may also require the application of an electric field. Studies by Niedermann *et al* [12,44,106] have shown that the effects of bulk thermal heating on the emission site distribution under zero applied field conditions are very materials dependent. It was found that Nb electrodes showed an increase in the number of emission sites with bulk heating up to 800°C followed by a suppression of emission after heating to higher temperatures. On the other hand, the emission from Al electrodes was found to be unaffected by thermal treatment [106]. These results were explained in terms of a diffusion model where impurities were assumed to diffuse into the bulk when suppression of emission occurred and from the bulk to the surface to stimulate emission sites [12,44]. From the current work, it is clear that further processes may also be important to the stimulation/suppression of emission during thermal treatment.

It is also clear from the results that four types of site switching processes are associated with bulk heating, namely: i) permanent 'switch-on' of sites by heating, ii) permanent 'switch-off' of sites, iii) temporary 'switch-on' at elevated temperatures, and iv) temporary suppression of emission by heating. The four different site stimulation/suppression effects observed may be explained by a consideration of the different electronic states within the insulator, and the variation of electron populations with temperature as discussed in the previous section. However, the hot electron model of Bayliss and Latham [8] will be shown to be broadly consistent with the observed emission site distributions for the case of bulk heating under an applied field.

i) Site 'switch-on' at elevated temperature:

Bulk heating will affect the population of electrons in both the trapping and donor states in the bulk of the insulator. These states are assumed to be described by a band model where the trapping states are above and the donor states below the Fermi level. Thus, as the applied field is raised, electron tunnelling is first established between the metal and insulator as the bottom edge of the conduction band falls below the metal Fermi level; however, it is then suppressed as the traps

114

in the bulk of the insulator become filled and screen the M-I interface from the applied field. When this occurs the conduction band is raised above the metal Fermi level and a further rise in the applied field is necessary to re-establish a tunnelling contact. Site 'switch-on' does not occur until all the traps and insulator surface states have been filled.

However, bulk heating would be expected to result in an emptying of some of the shallow traps thus resulting in a greater potential drop across the M-I interface. For a potential site in the pre-emission stage with the traps and surface states mainly filled, the promotion of charge from the traps into the conduction band may well result in the 'switch-on' of the site. Thus, the electrons promoted to the conduction band will be swept towards the I-V interface by the penetrating field to accumulate at the surface region. Furthermore, increased numbers of donor states will also be excited to result in a decrease of the depletion layer width as more positive charge will be present in the interface region. This effect will also result in a reduction in the total negative charge stored in the bulk of the insulator and thus increase the interface potential relative to the bulk to pull the conduction band edge down towards the metal Fermi level. Once the charge accumulation is sufficient to create the necessary field intensification at the interface region, significant electron heating and electron emission may then result. Such electron heating coupled with the increase in the M-I interface field due to the reduction of the stored negative charge could then result in a sudden pulse of electrons being injected into the insulator conduction band thus switching the site on. It would also be expected that this process will be influenced by the increase in conductivity of the bulk insulator region, since a lower bulk potential drop would be necessary for stable emission thus making the switch to an emitting state more favourable.

Thus, depending on the specific electronic configuration of the impurity, it may be possible to stimulate emission thermally through several different, and possibly complimentary, processes when an electric field is applied. These processes will not, however, occur in the case of bulk heating with no applied field as the site is not in a conducting state and it is not possible for electrons to tunnel between the metal and insulator. It would therefore be expected that under the earlier zero-field temperature cycling regime, the alterations to the charge state within the insulator during heating will relax back to the initial state after cooling hence preserving the original electronic charge state unaltered.

ii) Site 'switch-off' at elevated temperature:

The 'switch-off' of certain sites during thermal treatment is more difficult to explain, since once emission has been established, a current flow may be sustained for a far lower field than that required to initiate the emission, since several dynamical processes tend to reinforce the switch to an emitting state [8]. However,

should the trap and donor states be at relatively low energies, thermal stimulation may well not cause significant alterations to the charge distribution within the insulator bulk, or the electron populations in the trap and donor levels. In this case, the only effects occuring to promote emission as the temperature is raised will be slight changes to the bulk conductivity and the stored surface charge.

During the course of the experiment, the applied field was adjusted to maintain the emission current within the range 10-20μA to avoid the risk of breakdown events occuring. As may be seen from the experimental data, the overall field is reduced by approximately one half at 500°C. Therefore, the extinguishing of certain sites may occur because the applied field may have become too low to maintain electron emission. The fact that they remained off after cooling back to ambient may also be explained by this argument, since the results show an increase in the overall electrode emissivity due to additional sites being stimulated. This effect would also be reinforced as the bulk conductivity would be reduced after cooling thus tending to oppose the re-establishment of emission from such sites. However, as discussed in the following section, the emissivity of a site tends to be increased by bulk heating owing to an increase in the conductivity of the insulator.

iii) Effects of cooling on thermally stimulated emission sites:

Of more interest is the permanence of emission sites established during bulk heating under applied field conditions once the sample has been cooled again. Several processes will be occuring in these sites that would tend to reduce their emissivity. These processes will include the reduction in bulk conductivity as discussed above, and the relaxation of charge back into the traps and donors.

The reduction in the bulk conductivity will result in an increase in the voltage that must be applied across the insulator bulk for a given current density. Thus, a dynamical balance will be attained whereby a reduced current density will flow such that the bulk and surface voltage drops are compatible. Furthermore, thermally emptied traps will be re-occupied resulting in a greater degree of shielding of the interface region. Thus, the overall potential drop between the insulator surface and metal will also be reduced, thereby further decreasing the current density. There will also be an alteration to the stored charge at the I-V interface as discussed in following sections. This charge is assumed to increase with temperature resulting in an intensification of the insulator surface field which further reinforces emission at elevated temperatures.

It should also be noted that the width of the depletion layer will be affected by temperature. In the discussion above, the switch-on of sites at elevated temperatures was also related to the ionisation of donor states which had the effect of decreasing the width of the depletion region and thus stimulating emission. On

116

cooling, these sites will be re-occupied and thus the depletion zone will increase in width.

The overall effect of these factors must vary from site to site depending upon their particular electronic structure such that some will 'switch-on' at elevated temperatures but switch off again when cooled to ambient temperature whilst others will become permanent emitters.

iv) Effects of cooling on thermally suppressed emitters:

Those sites that 'switched-off' at elevated temperature, but 'switched-on' after cooling back to ambient present a serious problem to understand; the case for those sites which were pemanently 'switched-off' by heating has been discussed in section (ii), however, certain ideas will be applicable to this section. For these sites it must be speculated that the principal effect of heating was to alter the charge distribution within the dielectric such that the width of the M-I interface barrier was increased, either by affecting the width of the depletion layer, or by increasing the amount of charge stored at the I-V interface, and thus reducing the tunnelling current and hence resulting in the 'switch-off' of the site. Should the charge distribution be able to relax back to the initial state as cooling occurs, then it is possible that the M-I interface width would be reduced so enabling the site to 'swicth-on' again.

v) Summary of thermal effects on emission site distributions:

Clearly, there are several factors have an important influence on the behaviour of sites during bulk heating with a field applied. It is tentatively proposed that it is the specific impurity levels and donor/trap densities coupled with the effects on the insulator conductivity and electron distributions that determine the specific behaviour with temperature of an emission site. Since it is assumed that all the emission sites have a suitable M-I junction for a tunnelling contact to exist, it would be expected that emission would be observed from each site at room temperature upon the application of a sufficiently large field.

4.3.3.3 Individual site I-V characteristics

The emission current from an individual site shows a rapid increase with bulk temperature such that at a temperature of 500°C, a constant emission current will flow with the field reduced by almost half (see Fig. 4.19). Furthermore, the gradient of the I-V characteristic also alters from 0.4MVm^{-1} to 1.8MVm^{-1} per decade of current from the plot of log I vs F_{gap}. It is not possible to discuss this variation in the emission site current quantitatively as the current could only be

measured in arbitrary units from the area of the spectral curves. However, because of the small size of the analyser entrance aperture compared to the emission site image coupled with the low dependence of the site magnification on the gap field (see section 3.2.4), it is reasonable to assume that the measured data are proportional to the emission current density and are therefore independent of any potential variations in the area of the emission site. A variation in either the stored charge or the area of the site, and hence field intensification at the I-V interface could alter the measured values. This effect would, however, tend to reduce the measured current density as the magnification of the site image would increase since the field lines would be diverged to a greater extent at the surface, as indicated schematically in Fig. 4.25.
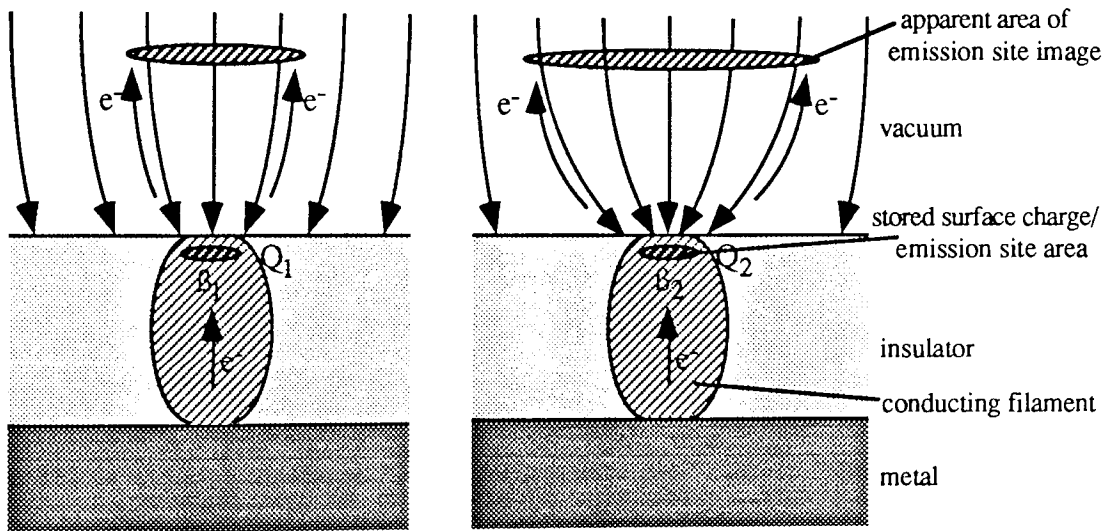
Figure 4.25 Effect of surface charge, and hence ß-factor, on the magnification of an emission site image, where $Q_2 > Q_1$ and $ß_2 > ß_1$.

The emission site current density is given by the equation derived by Murphy and Good [24]

$$J = \frac{4\pi m e}{h^3}\left[\frac{\pi/N}{\sin(\pi/N)}\right]k_b{}^2 T_e{}^2 \exp\left[\frac{-(\phi - b(F/a)^{1/2})}{k_b T_e}\right] \qquad 4.9$$

where the terms have the meanings defined in section 2.4.4.2. The lnJ vs F_g plots (Fig. 4.20) show essentially straight line behaviour over the range studied, although the gradient of the curves becomes less at lower applied fields. Taking logs of the above equation gives

$$\ln(J) = \ln\left[\frac{4\pi m e}{h^3}\left[\frac{\pi/N}{\sin(\pi/N)}\right]k_b{}^2\right] + 2\ln(T_e) - \frac{\phi}{k_b T_e} + \frac{b(F/a)^{1/2}}{k_b T_e} \qquad 4.10$$

Plotting this function at constant N (Fig. 4.26) indicates that for high surface field

118

values (approaching the region of $10^9 MVm^{-1}$) the variation of ln(J) becomes approximately linear with field.
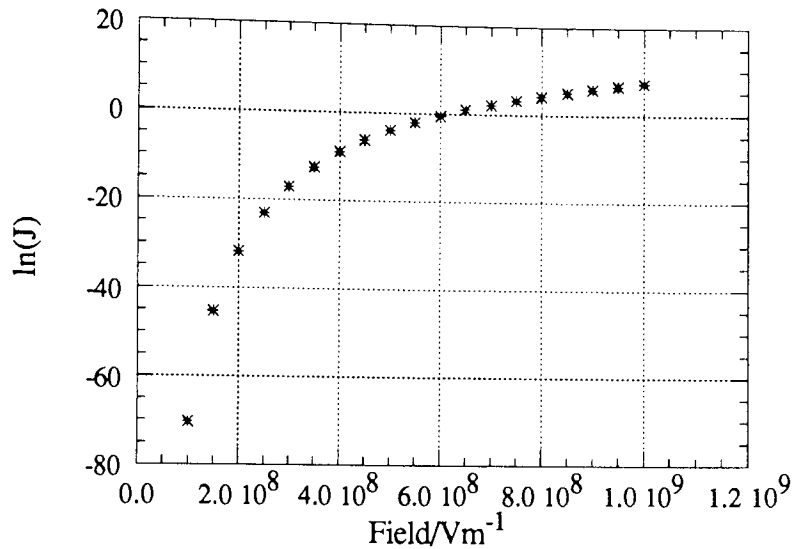
Figure 4.26 Theoretical variation of ln(J) with the surface field for N=1.3.

The observation that the same site current density is measured for a lower applied field at higher bulk temperatures indicates that either the field intensification factor, and hence surface field F, is increasing as the bulk temperature is increased; or that the hot electron temperature is increasing relative to the surface field. The latter factor would result in a change in the spectral shape since N would be altered. This is not observed to occur, however, as may be seen in the plot of Fig. 4.27, where spectra from a sub-site measured at the same *site emission current density* while at room temperature and 500°C are overlaid (with appropriate corrections to account for the difference in spectral shift). Thus, for a given site *current density*, the surface field and hot electron temperature are in the same ratio (i.e. the hot electron temperature depends upon the accelerating field F, not the bulk temperature); but, the current density increases with bulk temperature since F has a higher value for a given applied gap field. Furthermore, an increase in the ß-factor would also result in an increase in the gradient of site current with gap field as is observed (Fig. 4.20). An increase in the ß-factor with temperature would imply that either: i) an increase in the charge stored at the vacuum interface was occuring as the bulk temperature was increased; or ii) that the extent of the stored charge i.e. the emitting area was decreasing. It is not possible at this stage to determine which of these effects is occuring, for, although the overall emission current increases, the number of emission sites is also increased by heating. An increase in the stored charge may be explained by consideration of Fermi-Dirac statistics, which would imply a higher probability of electron occupation of states just above the Fermi level. By consideration of the band model shown in Fig. 2.18, it may be seen that in the region where the conduction band edge has risen above the Fermi level, an

increase in the probability of state occupation will lead to an increase in the charge present. For the case where the Fermi level is well above the conduction band edge, the total electron population will remain constant with just a shift in the distribution.
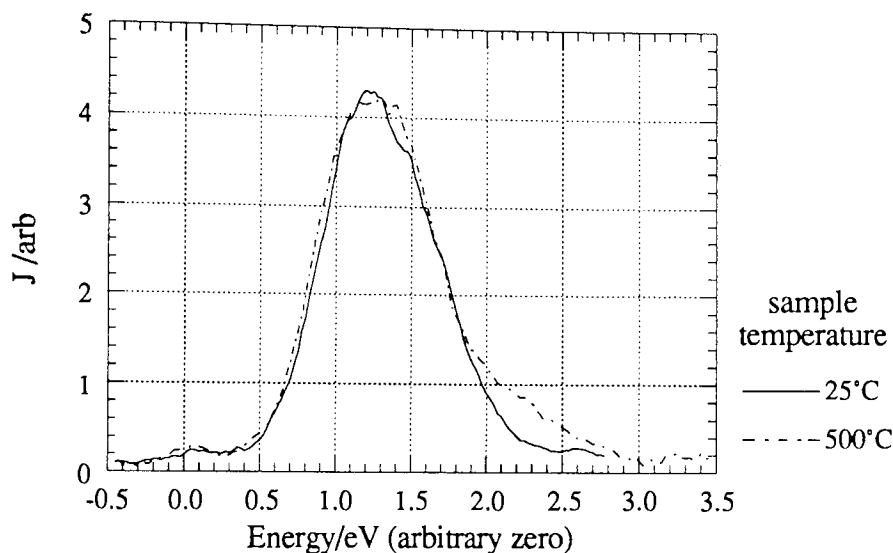
Figure 4.27 Spectra recorded at 25°C and 500°C at the same emission current indicating that the spectral shape is independent of bulk temperature for a given emission current (N.B. the energy axes for these two curves are different and have been shifted for purposes of the shape comparison).

It has been shown, however, that this charge distribution may be affected by bulk heating to cause an increase in the surface field intensification, and thus an increase in the emissivity. These factors thus reveal that an increase in temperature should result in a reduction of the applied gap field for the same emission current density, and also an increased rate of current change with gap field.

4.3.3.4 Total electrode I-V characteristics

In general it was observed that bulk heating under zero-field conditions did not result in any significant change in the overall I-V characteristics of an emission site. However, it was often observed that there was a jump in the emissivity after the first heat treatment of samples. Similarly, there was a large increase in the emissivity in the case of bulk heating under conditions of a high applied field in the first 100°C of heating compared with the effects of further heating. Such alterations are probably due to the outgassing of the sample that occurs as the bulk temperature is raised. Indeed, surface adatoms have been shown to have a significant effect upon metallic field emission sites since they can modify the surface barrier and work function [28]. It would be expected that they could therefore also influence the emission from surface impurities by a similar process of modification of the surface barrier. Such effects must be of small magnitude since additional structure in the electron energy distributions from emission sites characteristic of virtual states due to an adatom providing a resonant tunnelling route through the surface

barrier are not visible [28].

The strong increase in the total electrode I-V characteristics with temperature may be readily explained in terms of two processes. Firstly, the increase in the number of emission sites and secondly, an increase in the emission current density, and hence the emission current from each site. It is not certain that individual site emission currents increase at higher bulk temperatures since a decrease in the emission area would counteract the increase in the current density. The increase in emissivity after cooling back to ambient temperature compared to the initial emissivity before heat treatment probably results from the increased number of emission sites. Since there is generally no effect on the emission site population or upon the emissivity of individual sites during bulk heating under zero-field conditions, the overall electrode I-V characteristics would not be expected to alter, as is indeed observed experimentally.

4.3.3.5 Spectral properties

The spectral data show several features which may be summarised as follows: i) the peak is shifted below the metal Fermi level by an energy, ΔE_s, which decreases as the bulk temperature is increased, ii) the FWHM, $\Delta E_{1/2}$, has an initial value of $\geq 0.5 eV$ which increases with sample temperature, iii) the gradient of ΔE_s with applied field decreases as the bulk temperature is increased; and iv) the gradient of $\Delta E_{1/2}$ with field increases with bulk temperature. These results may be explained qualitatively by consideration of the fundamental physical principles that underly the hot electron model of Bayliss and Latham [8]. Thus, as an increase in the bulk temperature will affect both the conductivity of the bulk insulator (as discussed above) and the energy distribution of the electrons at the I-V interface region. The occupation of states at the surface will also be affected, however it is not possible to give a quantitative discription of this owing to the lack of knowledge of the precise electronic system giving rise to the emission.

According to the hot electron model, the FWHM is given by the equation [8]

$$\Delta E_{1/2} = \left[\frac{2.328N^2 - 1.303N}{N-1}\right] \frac{b}{\pi} \left[\frac{F}{a}\right]^{3/4} \qquad 4.11$$

which predicts that a plot of $\Delta E_{1/2}$ vs $F_g^{3/4}$ should give a straight line of gradient number x $\beta_1^{3/4}$ since $F=\beta_1 F_g$. In fact this is confirmed by the experimental plots presented in Fig. 4.28 of the spectral data. The increase in gradient can therefore be seen to be explained by an increase in the surface field intensification, β_1; however, the plots also indicate that the fitted lines do not pass through the origin, but have a significant intercept of negative value between 1 and 2 eV. The β values indicated by this data are also shown in Table 4.1. β_1 values of the order of 700 are within

121

the range expected from previous findings [42], however, the higher temperature values of several thousand are somewhat larger than would be expected.
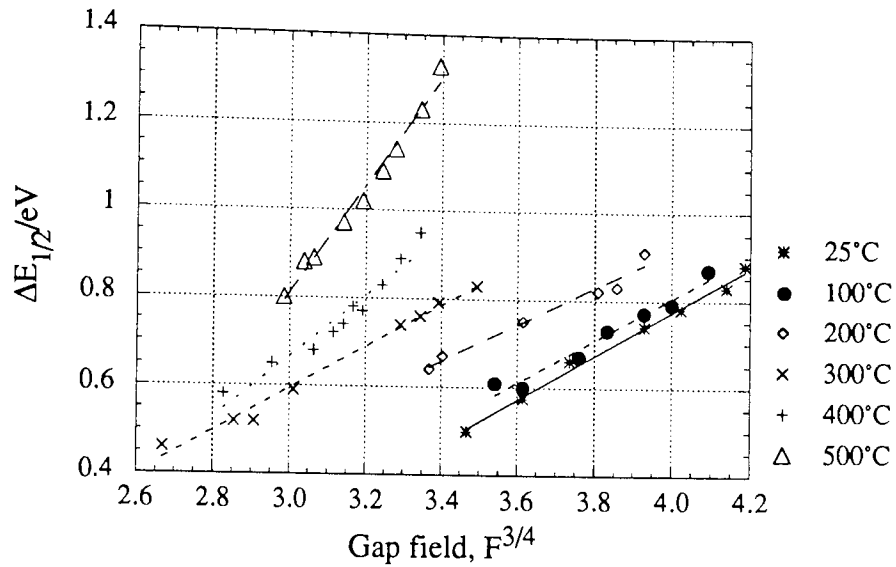
Figure 4.28 Experimental plots of $\Delta E_{1/2}$ vs $F_g^{3/4}$ with increasing bulk temperature for an emission site.

Temperature/°C	Gradient	Intercept/eV	R	ß-factor
25	0.50	-1.20	0.992	773
100	0.49	-1.10	0.982	752
200	0.43	-0.78	0.985	634
300	0.48	-0.85	0.994	732
400	0.69	-1.41	0.968	1186
500	1.23	-2.88	0.993	2557

Table 4.1 Tabulated results for $\Delta E_{1/2}$ vs $F_g^{3/4}$ indicating ß values with bulk temperature.

A consideration of the band diagram for the emitting state, shown in Fig. 2.18, reveals that the spectral shift, ΔE_s is given by [8]

$$\Delta E_s = E_p + \frac{\beta_2 d}{\varepsilon_r} F_g + \phi_M - \phi_I - V^*$$
    4.12

where

$$E_p = AkT - b(F/a)^{1/2}$$
    4.13

These equations show that a decrease in shift with increasing temperature is consistent with the argument developed above, from the current density data, that

the stored charge is also increasing thus leading to an increase in β_1. As the spectral shape does not alter with bulk temperature, the relationship between F and T_e remains constant, and hence the peak position relative to the vacuum barrier will be the same for spectral peaks of the same area (and presumably emission current density). Thus, as the spectral shift is observed to decrease at a given applied field when the bulk temperature is increased, it follows that either β_2 or the stored charge must be responsible for this effect. An increase in the stored charge would also be expected to influence β_2 through the associated effect of reducing the potential across the insulator bulk at a given applied field.

A further factor that may be calculated from the spectral data is the energy loss experienced by the electrons during transport within the bulk insulator. According to the hot electron model, it is assumed that the hot electron temperature is a linear function of the energy available for accelerating the electrons [8]. From this assumption, the hot electron temperature is then given by the equation

$$\frac{k_b T_e}{e} = \alpha \left[\left[\frac{d\beta_2}{D\varepsilon_r} \right] V_0 - S + \chi - \phi_I - V^* \right] + \frac{k_b T_0}{e} \qquad 4.14$$

where α is the energy loss factor due to electron-phonon interactions that tend to thermalise the electrons to the bottom of the conduction band. From this equation, it would be expected that the degree of heating required by the electrons to be emitted is reduced as the bulk temperature increases. Such a factor is therefore broadly consistent with the observation that the same hot electron temperature and surface field may be observed at a reduced gap field during the bulk heating experiments.

For the case of bulk heating under zero-applied field conditions, the spectral characteristics of individual emission sites did not generally show any significant alterations after treatment at different temperatures. Since all spectral measurements for these sites were performed at ambient temperature, any differences would represent a change in the electronic structure of the emission site itself. Thus, the slight variation observed in the characteristics after the initial heat treatment (Fig.4.18) may be attributed to outgassing effects. For the case of the site which 'switched-off' after a high temperature heat treatment, it was observed that there was little variation in the spectra until a treatment at 400°C. The subsequent treatment at 500°C resulted in the site 'switch-off'. After the treatment at 400°C, a higher field was required for the same shift and FWHM, and the gradient of the shift with field was reduced. As considered above, these effects are consistent with several variations in the properties of the sample: i) the M-I interface band structure, ii) the conductivity of the dielectric, and iii) the electronic structure of the I-V interface region.

At the M-I interface, an increase in the barrier width would result in an increase in the voltage across the interface region to sustain a given tunnelling current density into the insulator. Similarly, if the degree of charge stored at the surface altered, then the field intensification could be reduced. A reduction in the conductivity of the bulk insulator would result in an increase in the potential needed for a given current density within the bulk. As discussed above, all these factors would result in an increase the gap field for a given emission current density from the site. It has been shown on niobium electrodes that diffusion effects are important to the distribution of emission sites [44], and furthermore, it is postulated within the hot electron model [8] that a favourable M-I interface region having a high degree of impurities is required at an emission site. Thus, these observations would most likely result from diffusion of impurities reducing the tunnelling current density in the sensitive M-I interface region and thereby causing an increase in the gap field required to sustain emission from the site. However, as this effect was not generally observed, and it is known that a wide variety of elements are present at emission sites [32,34], it is not possible to be more specific in the discussion of this observation.

4.4 Effects resulting from the localised transient heating of electrodes

The effects of bulk sample heating on site distributions over a time scale of several hours have previously been explained in terms of the diffusion of impurity materials between the bulk and surface of the electrode, and the consequent concentration of impurities at the surface to form particles [12,44]. In contrast, short term transient heating, over nanosecond timescales, would only influence the surface region to a depth of no more than a few microns [107]. Thus, such heating will only influence the electronic and structural properties of the impurity particle, and the associated interface region, rather than the electrode bulk. It therefore follows that such heating could be used as a complimentary diagnostic technique. It is also possible that an alternative electrode conditioning treatment could be developed based on the principles of this technique.

By the use of a high power pulsed laser, such as a NdYAG laser, which has a pulse width time of less than 10ns, it is possible to achieve the required conditions of fast, localised surface heating in order to investigate the effects of transient surface heating. Such lasers, having the capability to focus down to spot sizes of several microns (as limited by optical diffraction effects) can cause vaporisation of the surface and hence may also be useful as a probe to 'treat' local regions of an electrode surface.

4.4.1 Experimental procedure

The effect of varying the intensity of the incident laser radiation over a range corresponding to the induction of modest surface heating of several hundred degrees celsius to the vaporisation of a region of several tens of microns in depth was investigated using standard polished Cu electrodes. To achieve thermal dosing over this range, surface fluences of between 10^7 Wcm^{-2} to 10^9 Wcm^{-2} were required (see section 4.4.3.1). The experiments were performed by measuring the emission properties of electrodes before and after treatment, which included their total and site I-V characteristics, the site distributions and the spectra of individual sites.
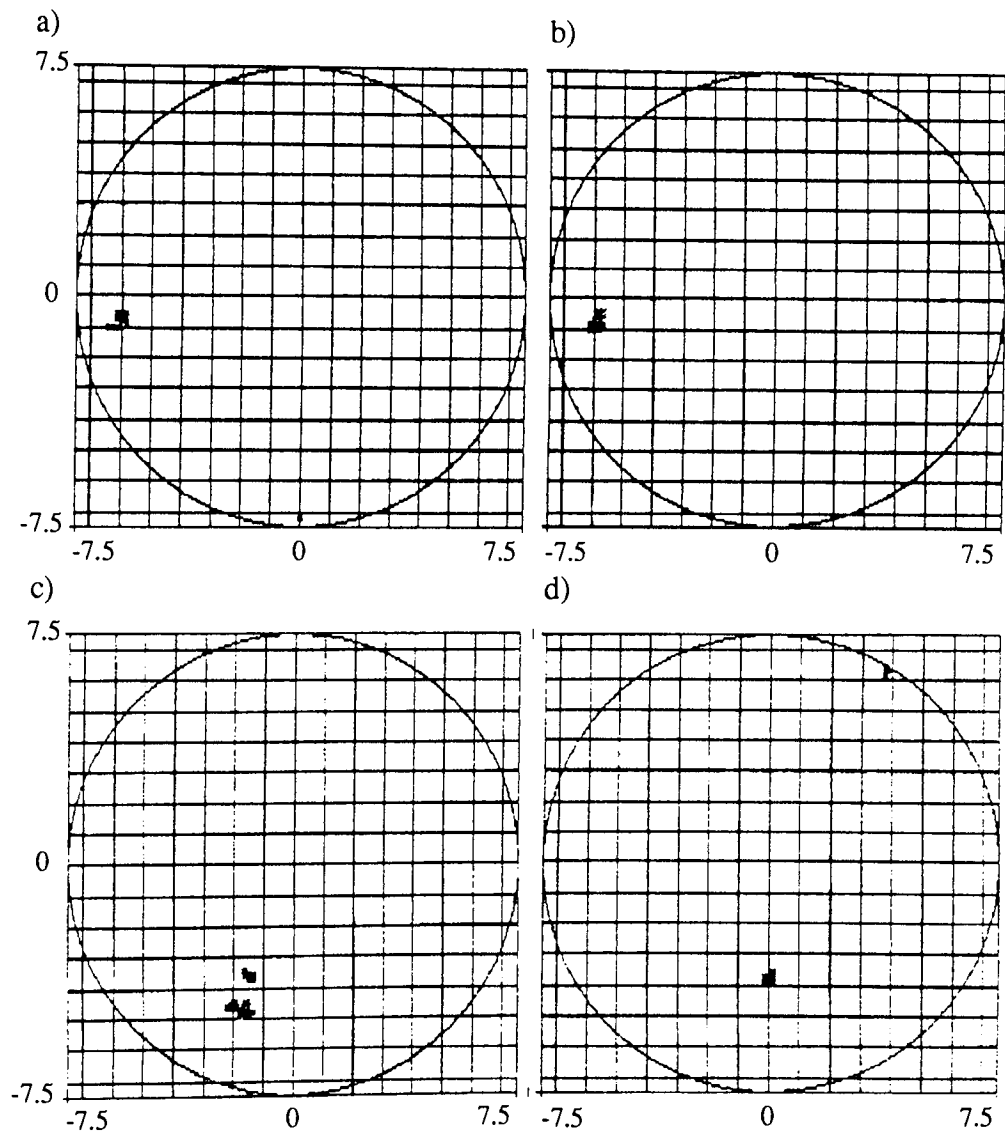
Figure 4.29 Variation in site distribution with laser dose: a) before and b) after dosing at 3×10^7Wcm^{-2} and c) before and d) after dosing at 4.5×10^8Wcm^{-2}

125

In order to perform the experiment, requiring as it does the application of a broad range of photon fluences to the electrode surface, a variety of methods were used to alter the beam intensity. These included variation of the beam energy by changing the flash tube voltage (range 40mJ-10mJ per pulse), the insertion of neutral density filters in the beam path (1% and 0.1% beam transmittance), and by moving the sample relative to the focal point of the beam in order to change the spot size (0.05-1mm). Combinations of these approaches thus enabled the power/unit area at the sample to be varied continuously over the full range required.

a)
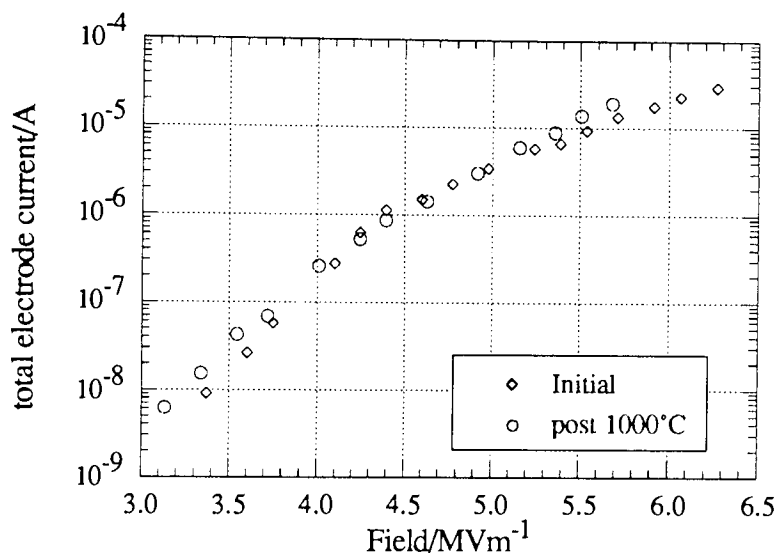
b)
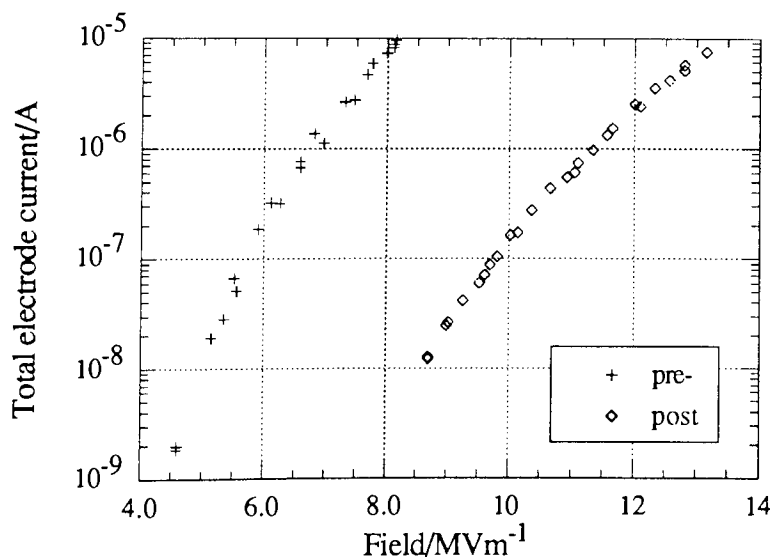
Figure 4.30 Electrode I-V characteristics after laser treatment at a) $3 \times 10^7 Wcm^{-2}$ and b) $4.5 \times 10^8 Wcm^{-2}$.

4.4.2 Experimental results

The experiments revealed that the observed effects could be divided into two ranges of incident flux which had a significant overlap region. At low dosing levels up to a threshold of $\sim 5 \times 10^7$ Wcm^{-2}, i.e. in the range of surface heating up to the point of partial melting, there was no effect upon the emission characteristics of electrodes. In contrast, the use of very high dosing levels ($\geq 2 \times 10^8$ Wcm^{-2}), which resulted in significant damage to the electrode surface (see for example, Fig. 4.36), had a significant effect upon the distribution of emission centres to cause both the destruction of existing sites and the stimulation of new sites. Generally however, the overall effect was to reduce the total electrode emissivity. In the region between these two extreme situations i.e. in the band between 5×10^7 and 2×10^8 Wcm^{-2}, the effect could not be well quantified since site distributions, and consequently I-V characteristics, altered unpredictably with treatment.

These results are summarised by the series of site maps shown in Fig. 4.29, which clearly show that the site distribution was unaffected until a dose of some 8×10^7Wcm^{-2} was applied. At this point the existing sites were suppressed. At higher dosing levels, it was seen that sites were erased, but alternative new sites were stimulated, although of lower emissivity.
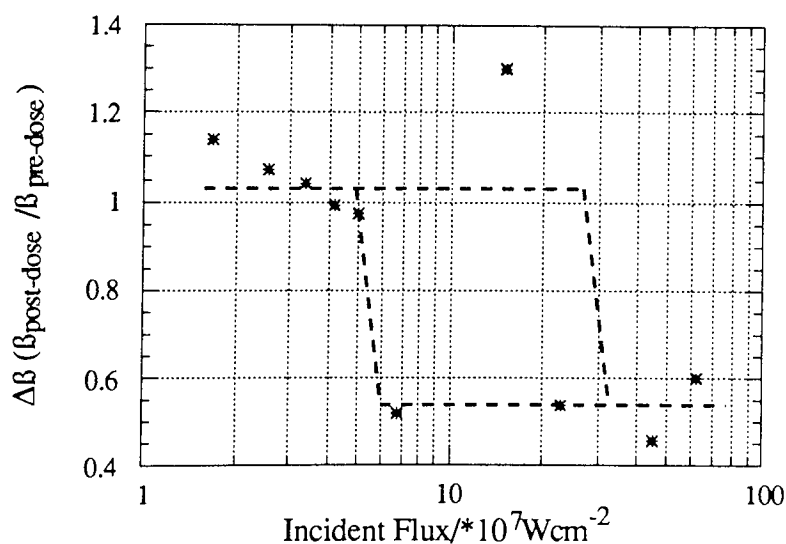
Figure 4.31 Graph showing the variation in electrode ß-factor after irradiating the surface at increasing fluences. The dose at which surface vaporisation begins is approximately 5×10^7Wcm^{-2}.

Thus, in the low dosing level range it was observed that the I-V characteristics were not significantly affected by the transient thermal loading, as may be seen from Fig. 4.30(a), for treatment of a sample at 2.8×10^7 Wcm^{-2}, corresponding to

surface heating of ~1000°C. In contrast, after treatment at 4.5×10^8 Wcm^{-2}, the emissivity of the sample is shown to be dramatically reduced, requiring a doubling of the gap field for the same electrode emission current (Fig. 4.30(b)). The variation in the overall electrode ß-factors with varying surface dose are summarised in Fig. 4.31 as the ratio of the pre- and post treatment ß-factors, and these results clearly show the threshold of the effect.

In the region below 5×10^7 Wcm^{-2} where only surface heating occured, without vaporisation of material, the spectral characteristics were not observed to be significantly affected by treatment. As may be seen from the spectral parameters plotted in Fig. 4.32, both the shift and FWHM show little effects. These data were obtained after heating an electrode to ~1000°C surface temperature.

a)

b)
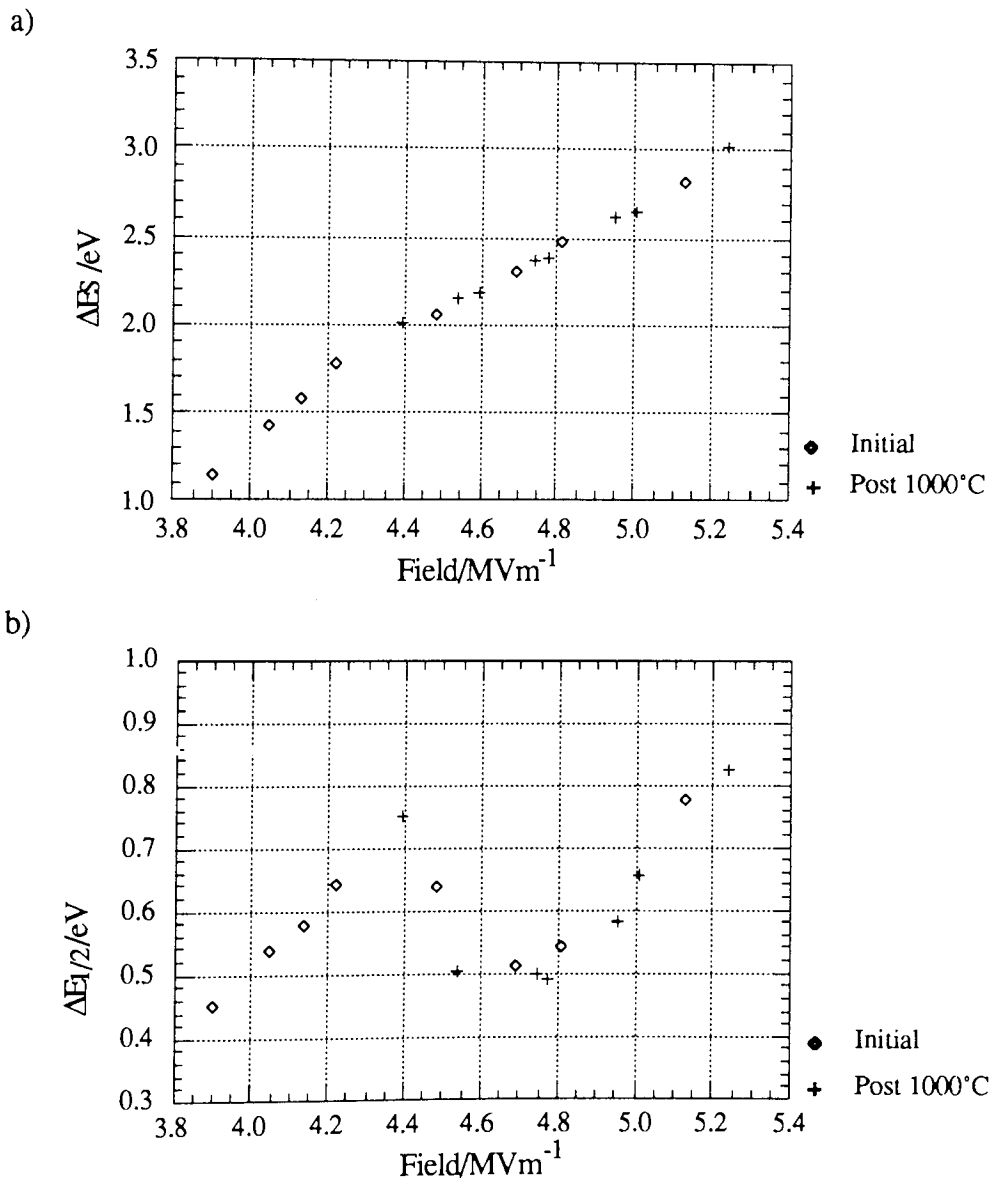
Figure 4.32 Effect of laser heating of electrode surface to ~1000°C, without material vaporisation, on the spectral characteristics of an emission site showing a)ΔE_S and b) $\Delta E_{1/2}$.

128

4.4.3 Discussion of transient surface heating effects

Before embarking on a full discussion of the results from these experiments it is first necessary to have some understanding of the laser beam/material interactions taking place. Subsequently, the effects of laser dosing on electrode I-V characteristics, site distributions and spectra will be explained in terms of a hot electron emission model.

4.4.3.1 Laser-material interaction

A simple model is presented here that enables the extent of sample heating of the sample to be calculated. The interaction is assumed to involve several stages when different factors play an important role in determining the temperature profile. Initially, heating of the material surface occurs as photons are absorbed according to an exponential power law of the form [108]

$$I = I_0 \exp(-\alpha x) \qquad\qquad 4.15$$

where I_0 is the incident beam intensity, x is distance into the surface and α is the absorbtion co-efficient, typically 10^5 cm^{-1} for metals [108]. The extent of heating then depends upon the optical penetration depth, the reflectivity, $\mathfrak{R}$, the themal diffusivity, κ, and the rate of energy absorbtion. It should also be noted that the

Aston University

Content has been removed for copyright reasons
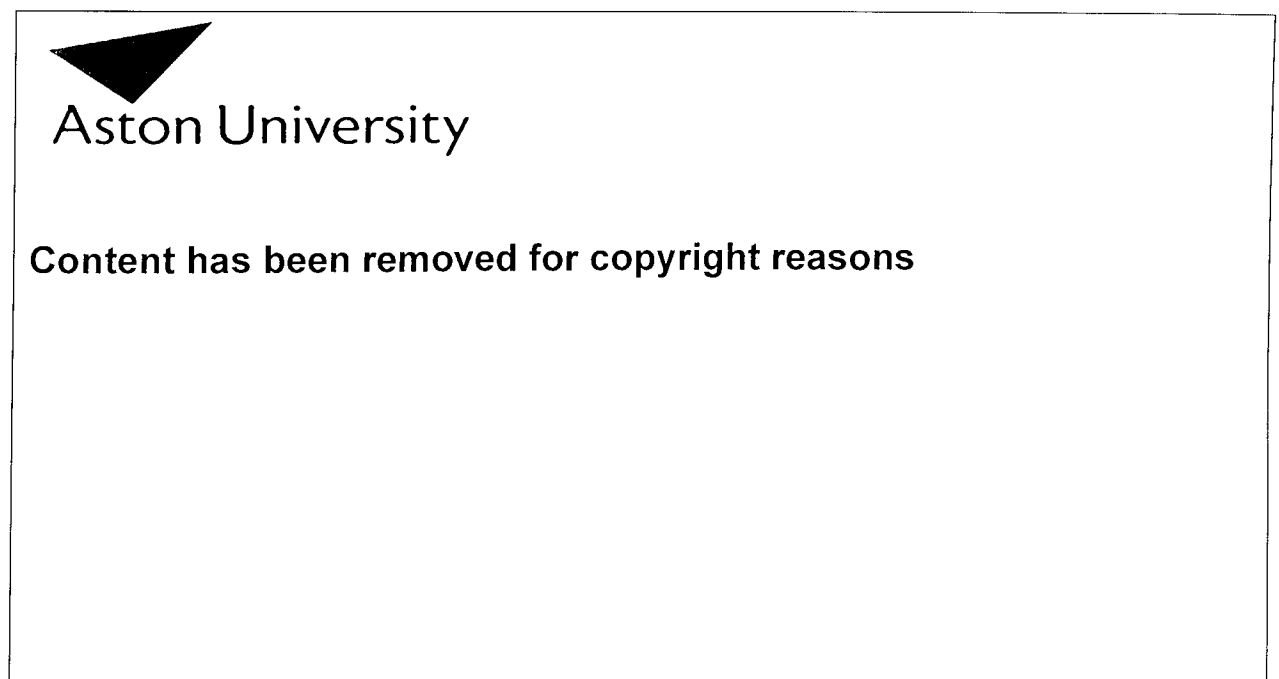
Figure 4.33 Schematic graph showing the variation in sample surface temperature with time whilst being irradiated with laser energy (from [107]).

electronic structure of a material is largely unimportant to the absorbtion process since the high electric fields present cause dielectric breakdown of insulating materials and hence the strong absorbtion of laser energy [108]. Once the melting temperature is reached, the latent heat of melting must be absorbed before any further heating may occur. Subsequently the temperature will again rise until the vaporisation temperature is attained, at which point the latent heat of vaporisation must be absorbed. These steps are illustrated in Fig. 4.33, which shows a schematic diagram of the temperature vs heat energy profile.

The situation is further complicated at higher dose levels since, once a molten pool of material has been formed, the radiation pressure of the beam can be great enough to force liquid out of the light path and cause cratering without significant vaporisation of material [109]. Once a significant quantity of material has been vaporised, the pressure of the vapour plume acting on the surface will also have the same effect on existing molten material. Furthermore, this vapour will become ionised to form a plasma above the surface, which will then strongly attenuate the laser flux at the material surface [108] via various photon interactions. Also, material removal may occur by evaporation from the molten pool, but this depends upon the vapour pressure of the particular compound present. The physical properties of the material itself also vary with temperature and thus the heating rates are affected by changes to the reflectance and thermal conductivity as heating occurs. All these processes are indicated schematically in Figure 4.34.

The temperature profile parallel to the sample surface is also affected by the energy distribution across the beam. The simplest case to consider is that for a beam of constant energy profile and infinite extent, when edge effects due to the flow of thermal energy parallel to the sample surface may be neglected. In reality, the beam has a gaussian energy distribution when the TEM_{00} mode is used (this mode enables the minimum spot size to be obtained) [81]. However, when the beam width is significantly greater than the heating penetration depth, the beam may be approximated to a uniform energy distribution. The heating penetration depth, D, is defined to be the depth at which the temperature has decayed to 37% of its surface value, and may be estimated from the equation [109]

$$D \sim \sqrt{(4 \kappa t)} \qquad\qquad 4.16$$

where t is the pulse duration and κ the thermal diffusivity. For copper, D is approximately $2 \mu m$ and is therefore generally much less than the beam diameter. Figure 4.35 indicates the variation in temperature with material depth at various times for the indicated Q-switched laser pulse which is similar to the output from the experimental laser.
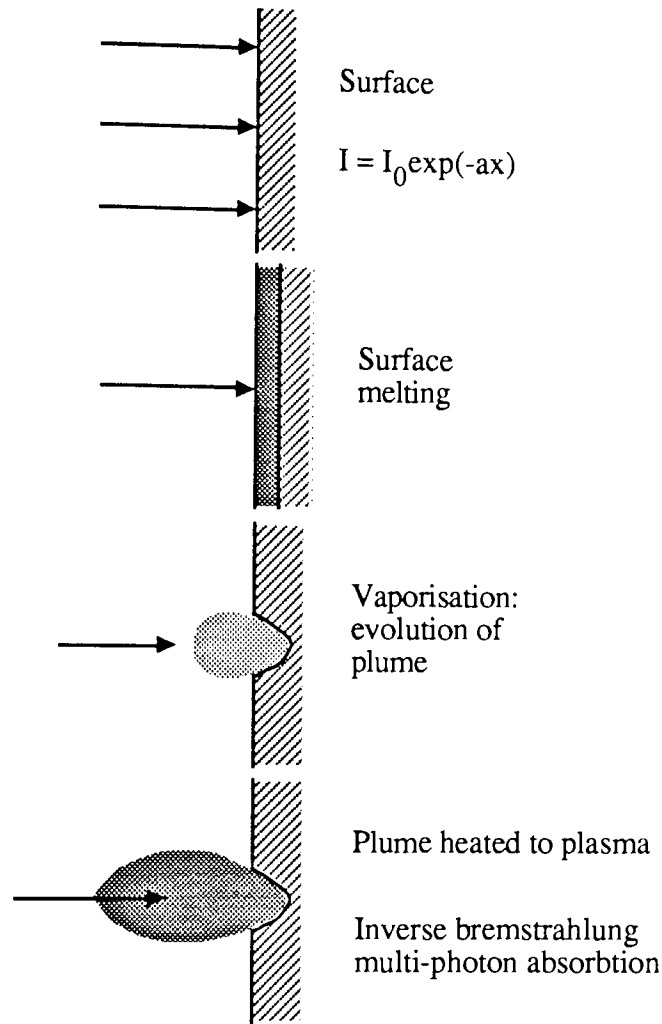
Figure 4.34 Schematic illustration of the physical processes occuring when a material surface is vaporised by a high power laser pulse.

For the case of surface heating below the melting temperature, the temperature-depth profile may be readily calculated by assuming that the beam has a uniform, infinite cross-sectional energy distribution [107] as

$$T(t) = \frac{2F_0}{K} \left[\frac{\kappa t}{\pi} \right]^{1/2}$$ 4.17

where K is the thermal conductivity and F_0 is the laser flux absorbed, which is related to the beam flux, F, as $F_0 = (1-\Re)F$. By application of this equation, the peak surface temperature for a beam energy of E in mJ, and a spot radius of r in cm, may be estimated from the relation

$$T_p \sim \frac{E}{100r^2}$$ 4.18

The situation becomes very complex once dose levels that result in melting and

vaporisation are attained, and computer models are required to predict the effects by numerical means. Such an analysis is beyond the scope of this thesis, and must therefore be considered in a qualitative fashion. It is possible to estimate the time before surface vaporisation begins to occur however, and for high flux densities, the latent heat of vaporisation is the most important factor since little heat conduction from the deposition area can occur under these conditions [107]. The time to vaporisation may be estimated from the equation

$$t_v = \frac{\pi}{4} \frac{K\rho c}{F^2} (T_v - T_0)^2 \qquad\qquad 4.19$$

where ρ is the material density and c is its specific heat capacity, and T_0 and T_v are the ambient and vaporisation temperatures respectively.
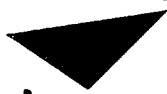
Figure 4.35 a) typical NdYAG Q-switched laser output pulse profile and b) associated sample heating in copper vs depth and time (from [107]).

4.4.3.2 Copper electrode damage

To calibrate the facility, measurements were undertaken on a copper electrode to find the co-ordinates of the optimum focus, and to assess the degree of damage caused to the electrode surface with varying beam diameter. For this intial study, the sample was irradiated with a series of single pulses, at full power, while the gap between the lens and sample surface was altered over a 5mm range in steps of $250\mu m$. The optics were calibrated by plotting the damaged surface diameter against the position co-ordinates of the sample, and this indicated that a minimum spot size of $25\mu m$ could be attained (Fig. 4.36).

As may clearly be seen from the sample micro-graphs, the laser is capable of causing significant vaporisation of the Cu surface over a small area. A closer examination of a single irradiation point reveals that quite complex processes are in operation. The micrograph of Fig. 4.37 shows the effect of irradiation near the position of the minimum spot diameter, and reveals a central region where the beam vaporised material to a depth of $\sim 50\mu m$ at a diameter of $\sim 45\mu m$, surrounded by a ring of splashed, melted copper of $\sim 150\mu m$ diameter. Bounding this area there is then a clearly defined 'crater wall' surrounded by undamaged electrode material, i.e. as shown schematically in Fig. 4.38.
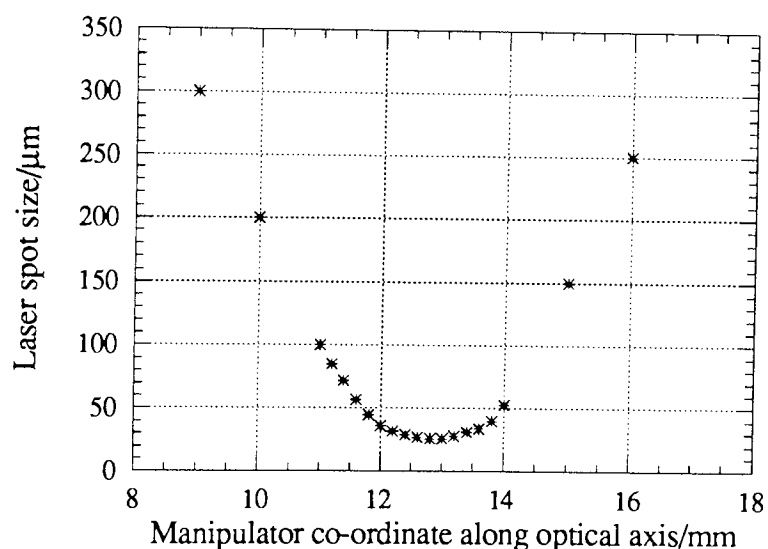
Figure 4.36 Variation in spot size of laser beam with position along the axis from the focussing lens.
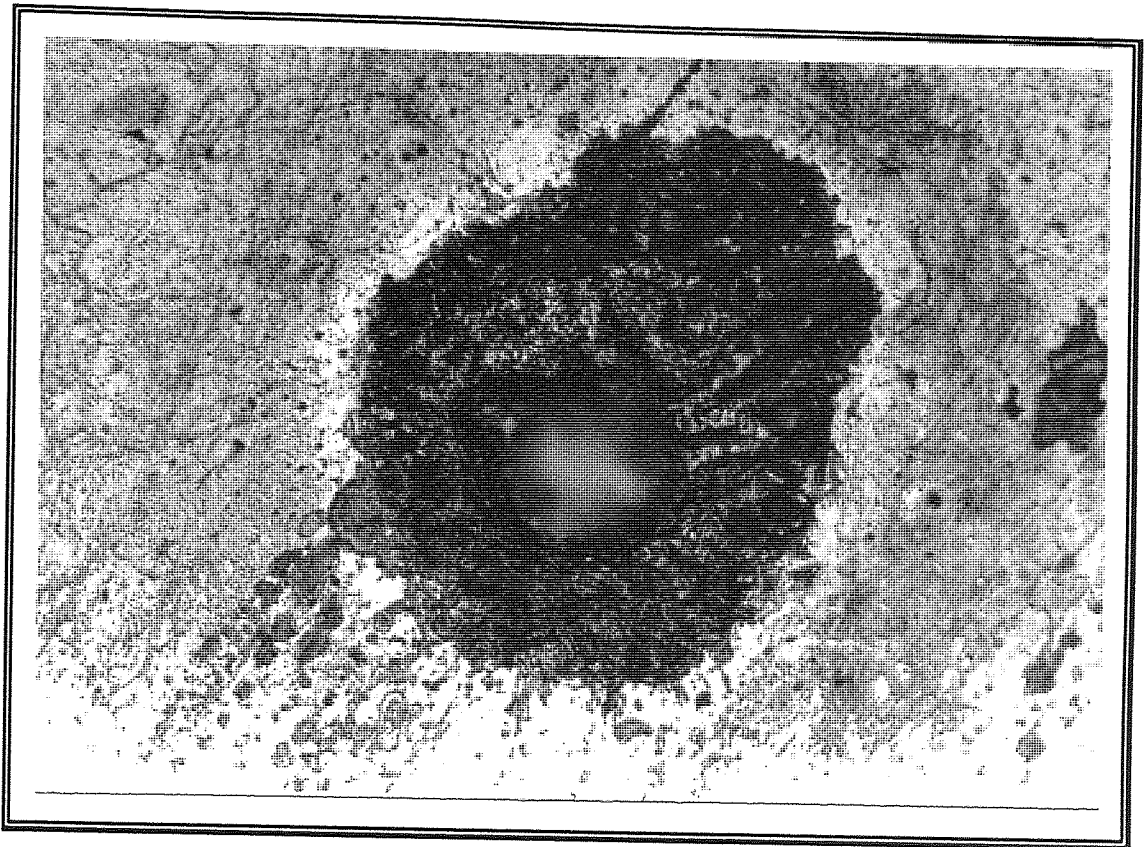
Figure 4.37 Micrograph of the surface damage caused to a copper electrode at the focal point of the lens system and an ouptut pulse energy of 40mJ (corresponding to a peak fluence of $5 \times 10^9 Wcm^{-2}$).
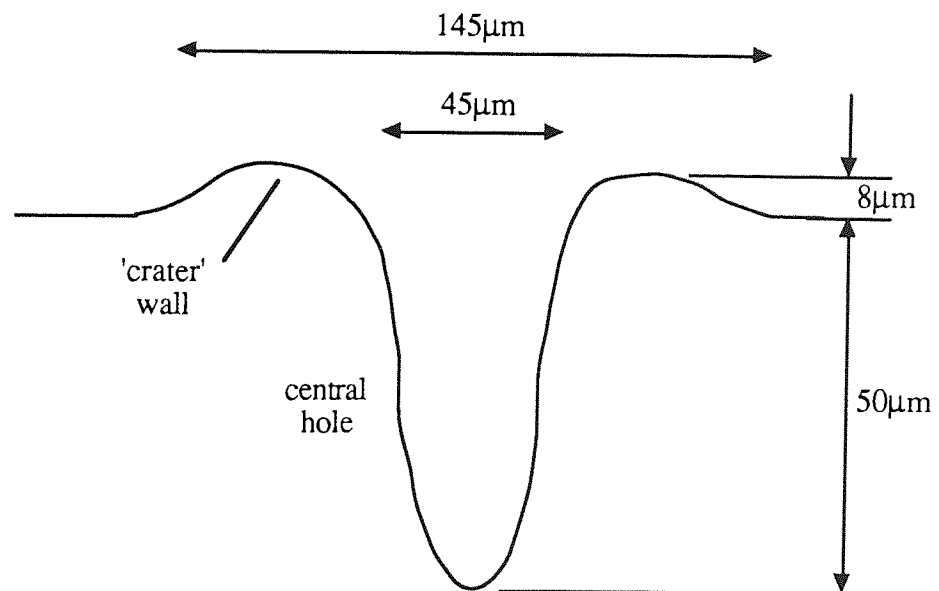
Figure 4.38 Schematic cross-section of the above vaporisation pit.

4.4.3.3 Variation in the site distribution with incident flux

Following from the discussion of photon/material interactions, material properties only tend to have a significant effect in the initial stages of irradiation i.e. before melting begins to occur. The depth of heating, maximum temperature attained, and degree of melting and vaporisation all depend upon the physical properties of the material being exposed to the radiation, but in general the impurity particles are significantly smaller than the characteristic heating depths, since they are typically $\leq 1 \mu m$.

In the initial heating stage, the main physical property influencing the amount of energy absorbed is the reflectivity of the material. Although this varies with temperature, copper is likely to have a higher reflectivity (~0.9 at room temperature [111]) than many dielectric materials and will therefore reflect more of the incident energy than the surface impurities during this stage. Furthermore, Cu also has a high thermal conductivity of $3.85 Wcm^{-2}K^{-1}$, which will be significantly greater than the contaminant particles would be expected to possess. Therfore, due to these two factors, surface impurity micro-structures will generally be heated more rapidly than the surrounding Cu surface, but to a lesser depth, and so melting processes are likely to occur at impurities before the bulk electrode surface begins to melt. It must be noted, however, that the reflectivity for all materials tends to a similar value once significant heating has occurred, as may be seen from the series of curves illustrated in Figure 4.39 [112]. Preferential melting, and then vaporisation, of many of the surface impurity particles is still probable since many dielectrics have lower thermodynamic constants than does Cu [113] (see Table 4.2). Thus, the experimental observation that there is a region of incident energy over which the transition in electrode emission properties occurs, at the onset of surface melting, is therefore likely to be related to these factors.

Temperature/°C	Gradient	Intercept/eV	R	ß-factor
25	0.50	-1.20	0.992	773
100	0.49	-1.10	0.982	752
200	0.43	-0.78	0.985	634
300	0.48	-0.85	0.994	732
400	0.69	-1.41	0.968	1186
500	1.23	-2.88	0.993	2557

Table 4.2 The thermal properties and estimated vaporisation times for a pulse of $1 \times 10^8 Wcm^{-2}$ of some elements.

Thus, one may begin to explain the observations of the changes in emission site distributions with photon flux, once the dose energy approaches 6×10^7 Wcm^{-2}, as existing surface impurity micro-structures will first suffer melting, and then at higher doses, vaporisation. Indeed, as discussed above, many such structures may well be vaporised before the surrounding Cu regions and partially shield the underlying surface due to plasma processes. This may well explain the destruction of existing sites by vaporisation of the source particle. It would, however, be expected that new sites would be generated by this process since removal of the surface layer will expose the underlying Cu substrate, and consequently, expose new impurity particles which may then become emission centres.

Evaporation of material may also be an additional important process. Under irradiation conditions corresponding to the threshold for vaporisation, the vapour pressure of the individual phases present will have an effect. This could then result in the 'thinning' of impurities such that emission sites were no-longer capable of emitting at the applied field levels, although it must be stressed that this idea is very speculative.

Figure 4.39 Illustration of the variation in material reflectivity vs irradiance flux from a Q-switched laser for: 1. teflon, 2. aluminium, 3. tin, 4. copper, 5. ebonite and 6. carbon (from [113]).

It must also be noted that due to the splashing of molten copper, the surface is left in an extremely rough state compared to the original polished finish. In this context, studies by Bayliss [42] found that a breakdown event, with consequent splashing of electrode material, resulted in an increase in the emissivity of electrodes. In contrast, the current study did not find such an effect, although splashing around the irradiated area may be clearly observed (see Fig. 4.37). Since the beam has a gaussian energy profile, the area where splashing occurs will also

have been irradiated, but at a far lower intensity than the central vaporised region. Therefore, some surface melting to a very limited depth may be occuring, resulting in the metal droplets being in intimate contact with the electrode substrate, and thus preventing the required blocking contact between the substrate and droplets [42]. Hence, these features are unlikely to become emitters below the field levels required to stimulate emission by purely geometric means.

The overall results on sample emissivity variations are similar to observations made by Bayliss [42] on the effect of argon-ion etching of a Cu electrode surface. In contrast to the present study however, it was found that after treatment, the emissivity of new sites created by etching was random, and could be greater or smaller. That process was explained in terms of the gradual removal of material to uncover new impurities in the electrode bulk. The present study showed a similar effect except that there was a general trend for the emissivity of an electrode to be reduced. Although this observation may not be explained from the present results, it is possible to consider several mechanisms that may have an effect.

The experiments on argon ion beam etching involved low rates of material removal without significant surface damage occuring whereas the laser dosing experiments resulted in serious surface damage, including bulk (on the micron scale) melting and vaporisation of material. The argon etching process would also involve the implantation of argon into the lattice which could affect the electronic properties of the interface and insulator bulk regions. In contrast, the transient laser heating of the surface layer would probably have a profound effect upon the impurity structures present. Melting and resolidification of the surface layer is very rapid, occuring on the micro-second timescale, and hence the chemical composition will be altered as the molten layer will be effectively quenched from a non-equilibrium state. Hence, impurities will not have time to precipitate out of the melt, as would occur under conditions of slower cooling in thermal equilibrium. There would also be insufficient time for a significant diffusion of impurities to occur, and hence the mechanisms discussed under bulk heating will be generally inapplicable to this regime. Thus the electronic structure of the M-I interface may also be modified by the processes occuring during transient heating which would influence the emissivity of the electrode after treatment.

CHAPTER 5 : UV TOPOGRAPHICAL IMAGING SYSTEM

5.1 Systems for the fundamental study of the emission process

In this first section, the requirement for, and implementation of, a system capable of generating high resolution maps of the sample surface in order to relate the position of an emission site to the associated impurity particle will be discussed.

5.1.1 Requirement for a surface/field imaging system

As discussed in chapter 2, the work of Cox [5,31], Latham and co-workers [6,8,32] and Niedermann *et al* [7,34] has shown field emission sites on broad area metallic electrodes to be associated with impurity micro-particulates, typically of dimensions in the range 0.1-10µm. As such structures appear bright in SEM images [6], they are believed to be either dielectric in nature, or insulated from the metallic electrode. They have been shown to be of varied elemental composition, containing foreign metals, metallic oxides and sulphides, sulphur, and frequently carbon [6,34]. These results have been obtained using anode tip scanning systems of increasing complexity contained within SEM's that incorporate microprobe analytical systems to identify the elemental composition of the impurity particles.
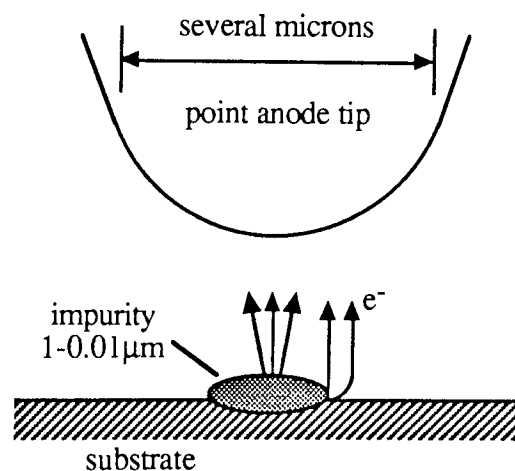
Figure 5.1 Schematic illustration of the site location resolution limit imposed by the point anode scanning technique.

The resolution of this method is limited both by the size of the metallic tip employed and the resolution of the SEM. Thus, it has only been possible to establish the association of an emission site with the impurity particle, but not the precise location of the emission relative to the sub-structure of the particle, as illustrated schematically in Fig. 5.1. In order to improve upon the fundamental understanding of the emission process, more detailed information is required relating the precise position of the electron emission to the topography of the micro-

structure, and hence to an emission model. Thus, an experimental system is required capable of imaging both the surface topography at high resolution and locating an emission site to better than 0.1μm, the lower bound to the typical micro-structure dimension [8]. In the first part of this chapter, the potential experimental approaches are considered in more detail. This will be followed by a description of the design and construction of a dedicated system developed around a photo-electron emission microscope.

5.1.2 Experimental Approaches

Several different approaches are available that could form the basis of an instrument capable of performing the required function, each having both advantages and disadvantages. Either an enhancement of the point anode scanning technique, as described by Cox [5], could be used, or alternatively, a system based on some form of emission microscopy could be employed.

The first approach, based around a point anode scanning technique [6] in conjunction with an SEM can image both the surface and located emission sites, but suffers from a resolution limit of several microns imposed by both the anode tip size and the microscope performance [6,34]. However, the resolution of the technique could be improved dramatically by using a scanning tunnelling electron microscope (STM) and this approach is being explored by Niedermann *et al* [114,115]. The technique offers the prospect of very high resolution surface imaging and emission site location on the scale of ångstroms. In the standard STM configuration, a tunnelling electron current flows from the tip to the sample surface when a bias voltage is applied to the tip, and thus a topographical surface map may be generated. By reversing the polarity of the bias voltage however, field emission may be stimulated from the sample and hence it is possible to locate emission sites. This technique should easily fulfill the criteria applying to resolution and will give a high degree of topographical information. The disadvantages include: a long scan time at an emission site in order to gather the data; an inability to image in 'real time'; and an extremely localised field at the scanning tip which may give rise to spurious field emission from topographical features in the site location mode.

In practice, a low resolution scan must first be made using the standard point anode technique in order to locate emission sites for further study at higher resolution, and to perform measurements on the individual site I-V characteristics [114]. For high resolution work, an anode with a finer tip is then rotated into place. At high resolution, an area of up to 50μm square may be scanned at a resolution limit of 10Å vertically and 20Å in the horizontal plane [115]. This scan must be repeated twice, firstly to map the surface topography and then a second time, with the opposite polarity applied to the tip, to precisely locate the emission sites. Thus,

it is not possible to observe the evolution of an emission site in real time using this technique. There are some indications that the scanning process may cause some localised surface damage, either from micro-breakdowns, or by actual contact between the tip and surface [115]. A small tip-sample gap spacing of the order of 500Å is typically employed, and this in conjunction with the tip diameter of some 1μm results in an extremely localised surface field which might excite field emission from purely geometrical features rather than from 'true' emission sites.

For the second approach, a variety of electron emission techniques are available: thermionic, photo and secondary emission. However, neither thermionic nor secondary emission techniques are practicable for this study. Thermionic emission requires extremely high sample temperatures which, as discussed in Chapter 4, strongly influence the emission process [12]. Secondary emission is impractical owing to the constraint of generating field emission from the sample under identical optical imaging conditions, and also from potential effects upon the emission process by particulate bombardment.

At Aston it was therefore decided to adopt a system based around a photo-emission microscope. An ultra-violet (UV) photon source is employed to generate photo-electrons which are then focussed through an electrostatic lens assembly. The potential resolution is limited by several factors including the electron-optical behaviour of the immersion objective, which extracts both field- and photo-emitted electrons, and the optical properties of the following lens elements. Existing photo-emission microscopes have been shown to have a potential operating resolution of the order of ~150Å [116]. By using an electrostatic lens assembly, the imaging properties depend solely upon the ratios of voltages between the different lens elements [74], and not on the absolute applied voltages. Thus, the magnitude of the cathode-anode gap voltage may be altered during an experiment in order to control the field emission current without affecting the optical properties of the imaging system.

The Aston approach therefore has the considerable advantage of producing a direct image of both the topography and field emitted electrons on a screen, thus greatly facilitating experimental interpretation. The imaging system is also very sensitive to surface orientation and composition, which, coupled with a small depth of field [117], gives a high contrast image. Furthermore, the system offers the possibility to perform dynamic studies of the emission process.

5.2 Electron optical design

In this section, the physics of the photo-emission process and of electron-optics will be discussed and their application to the design of the electron-optical column will be illustrated.

5.2.1 UV photon-material interaction

Photo-electric emission from solids is governed by the equation determined by Einstein [118] which related the maximum possible energy of an emitted electron with the wavelength of an incident photon

$$h\nu = E + \phi \qquad\qquad 5.1$$

where ν is the incident photon frequency, E the maximum kinetic energy of the emitted electron, and ϕ is the work function of the material.

An incident photon may ionise electrons in different energy levels so that under illumination with monochromatic photons, a polychromatic electron energy distribution results. UV photons only have sufficient energy to ionise the most weakly bound electrons in solids, generally only those occupying the conduction and valence bands. The core electrons are more tightly bound, and require photons in the X-ray region of the spectrum to ionise them.

Incident UV photons penetrate more deeply into solids than the photo-electron escape depth: for example the penetration depth in Cu is 40Å [119]. However, the excited electrons have only a short inelastic mean free path (IMFP), λ, before they suffer an inelastic collision to lose their energy [118]. The IMFP also depends upon the energy of the excited electron, and varies as shown by the graph of Fig. 5.2. At the low energy end, when E<5eV, the IMFP is dominated by electron-phonon interactions. Above this energy the scattering processes are dominated by electron-electon interactions. As may be seen, the IMFP is of the order of tens of ångstroms, and therefore only surface electrons are detected by photo-emission.
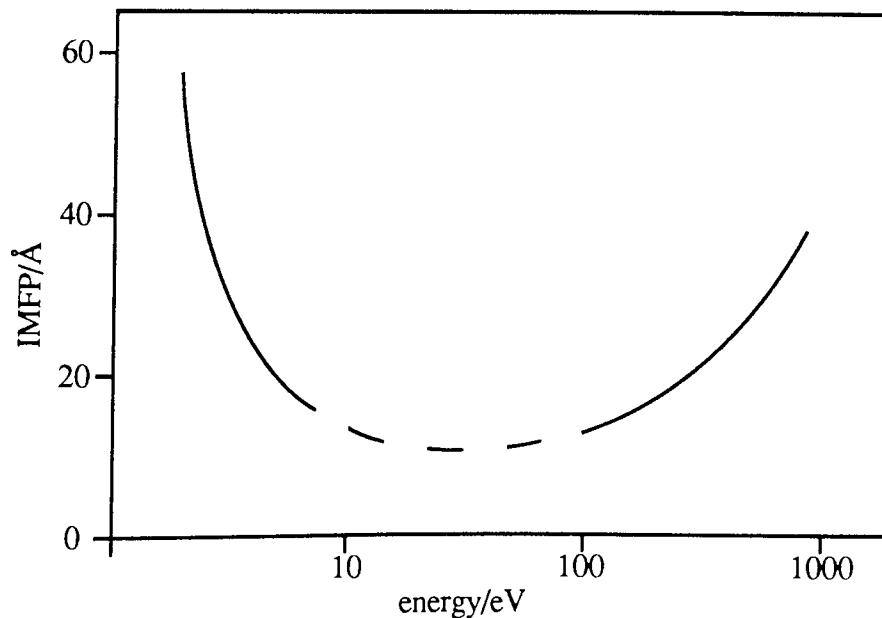
Figure 5.2 Graph of the inelastic mean free path (IMFP) vs electron energy.

For insulating or semi-conducting samples, surface charging effects can be important to the emission mechanism. There are two competing processes which tend to result in a dynamic equilibrium state: i) emission of electrons by photo-ionisation, and ii) neutralisation of charge by recombination of electrons from molecules in the vacuum system and leakage from the material bulk. These processes lead to the accumulation of a net positive charge on the surface which then reduces the emitted current since the photo-electrons then require more energy to escape from the surface. Furthermore, the emitted electrons do not emerge perpendicular to the surface of the solid but with a conical distribution; a factor that reduces the ultimate resolution of a photo-electron microscope as discussed in section 5.2.5.5.

5.2.2 Refractive index

Hamilton, over the years 1828-1837, developed the theoretical basis upon which the theory of electron optics is founded. The theory was developed from his association of the optical description of the path of a light ray through a refractive medium with the mechanical description of the motion of a mass through a potential field. By consideration of these fundamental principles, it is possible to show [120] that for the case of electron motion through a region of given electric potential a refractive index, N, may be defined as

$$N = \sqrt{V} \qquad\qquad 5.2$$

where V is the energy of the electron in eV. The zero of potential is defined to be zero when the electron momentum is zero. For full details the reader is referred to Klemperer and Barnett [120].

The definition of the zero point may sometimes require careful consideration. For the case of field emission, where the cathode is assumed to be at earth potential, the emitted electrons have an emission energy V_{em} which should actually be taken as the cathode potential. For thermionic emission, this is of the order of 0.25eV for tungsten cathodes, and in the case of photo-emission from a UV source, may be as high as tens of eV. For a source resting at earth potential, the refractive index at any point is then given by

$$N = \sqrt{(V_r + V_{em})} \qquad\qquad 5.3$$

where V_r is the voltage difference of the equipotential as measured against earth potential.

Considering the movement of an electron between two regions of different

electric potential, V_1 and V_2, Snell's Law may be shown to apply [120] giving the well known result

$$\frac{N_1}{N_2} = \frac{\sin\theta_1}{\sin\theta_2} = \frac{\sqrt{V_1}}{\sqrt{V_2}}$$

5.4

The advantage in defining a refractive index, rather than treating electron-optical problems in a kinematic fashion, becomes important when dealing with axially symmetric systems. Every electric or magnetic field of circular symmetry has the properties of a lens i.e. it can project an optical image. This then implies that with a knowledge of six points of the field, the cardinal points of the lens (c.f. light optics), the electron path external to the particular refracting field may be predicted i.e. in the 'object' and 'image' spaces. These cardinal points are the focal planes, the principal planes, and the nodal points.

It should be noted that there is a major difference between the majority of light-optical and electron-optical problems. Light rays are generally refracted by a finite series of refracting surfaces with a discontinuous variation in the refractive index. In electron-optical problems however, the refractive index varies continuously along the path of the electron and solutions to problems generally require the application of computer techniques.

A similar process may also be followed in order to derive a refractive index associated with magnetic fields. However, only electrostatic lenses were considered for the design since their optical properties depend solely upon the ratio of the applied lens voltages. This condition is necessary for the study of field emission sites owing to the variation of emission current with gap field. For further information, the interested reader is referred to standard texts on electron optics, such as Klemperer and Barnett [120] or Grivet [74].

5.2.3 Single aperture lens

Although in most cases the calculation of the electron-optical behaviour for a system must be performed using numerical or physical [74,120] techniques, the simplest case of an aperture in a plane diaphragm separating two planar conductors, as shown in Figure 5.3 may be derived mathematically [121]. It is important to note that this is the only type of lens which may behave with a diverging action [74]. Since a strong electric field exists between the anode and cathode, in order to extract electrons, the aperture in the anode behaves as this type of lens.

143
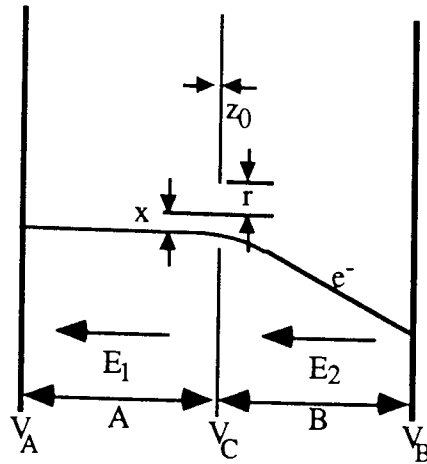
Figure 5.3 Electron-optical effect of a single aperture in a thin conducting sheet, C, between two plane conductors A and B.

By geometry, the electric fields on either side of the diaphragm are given by

$$E_1 = \frac{V_A - V_B}{A} \qquad E_2 = \frac{V_C - V_B}{B}$$

where V_A and V_B are the potentials of the two plane conductors, and V_C is the potential of the central diaphragm. A an B are the separations of the central diaphragm from the two external conductors. This system may be shown to behave as a lens of focal length, f, given by

$$f = \frac{4V_C}{E_1 - E_2} \qquad\qquad 5.5$$

This is the aperture lens formula of Davisson and Calbick [121], and applies to paraxial rays (x<<r) in a thin lens (z_0<<r). r should also be small in comparison with the dimensions of the arrangement of electrodes producing E_1 and E_2. It should be noted that for the case when $E_1 > E_2$, the focal length is negative and the aperture will behave as a diverging lens.

5.2.4 Multi electrode lenses

In the case of the previous lens, and certain other classes of lens, such as those consisting of two or more tubes, the lens operates with a different potential on the input and output which corresponds to the optical case of the lens being surrounded by media of different refractive indices. Lenses that consist of three diaphragms or tubes may be run with the two outer electrodes at the same potential. In this case, the lens will behave in a similar fashion to a thick symmetrical glass lens having media of the same refractive index either side.

144

In this situation, since the potentials on either side of the lens are the same, considerations of symmetry dictate that the two focal lengths, f and f', must be equal, and the two nodal points, K and K', must coincide with the principal planes. The electron velocity external to the lens is determined by V_0, the potential of the outer electrodes. Inside the lens, the electron is either accelerated or decelerated initially, but the overall action of the lens is always converging [74]. Short focal lengths are more readily obtained when applying a negative potential to the inner electrode ($V_i-V_0<0$) but the electron travels closer to the axis for a positive applied potential ($V_i-V_0>0$) [74].

For the particular case where the central electrode is held at the cathode potential, i.e. $V_i=0$, and the outer electrodes are held at the anode potential, so that only a single voltage is supplied to the lens system, it is generally termed a uni-voltage or uni-potential lens. Moreover, as the voltage ratio V_0/V_i is always infinite, the positions of the cardinal points become independent of the applied voltages, provided the electron energies are not sufficiently high for relativistic mass effects to become important.

The independence of the focal length from the applied voltage is of considerable technical importance since the lens becomes insensitive to voltage fluctuations. It is even possible to project a sharp image from a uni-potential lens operated from an a.c. supply [74]. For a three diaphragm type of lens (e.g. Fig. 5.5(a)), the focal length depends only on the aperture radii R_0 and R_i, the lens electrode spacings S, and the thicknesses T_0 and T_i of the diaphragms. Such lenses have been studied by many authors, including: Glaser [122], Vine [123], Read [124] and more recently Rempfer *et al* [125].

5.2.5 Lens aberrations

The ultimate resolution of an electron-optical system is not limited solely by its ultimate magnification, but also by the imaging imperfections due to both geometrical and electronic effects. These result in a point on the object being imaged not as a point, but as a disc, and hence for details to be observed their images must be of greater size than this disc diameter (c.f. the Rayleigh resolution criterion in diffraction limited optical systems). Both geometrical and electron energy effects are responsible for this image degradation.

Geometrical effects, such as misalignment of lens elements, either through displacement from the axis or tilting, and deviations of electrode profiles from true due to machining tolerances, all result in imperfections of the lens fields and thus image degradation. These geometrical effects can be classified into five types: spherical aberration, coma, astigmatism, field curvature and distortion.

Electron energy effects cause three further types of aberration. Non monochromatic electron energy distributions result in chromatic aberration as lenses tend to have slightly different imaging properties for particles of different energy. The mutual repulsion of electrons may result in space charge effects and the intrinsic wavelength associated with moving particles leads to diffraction of the electron beam.

5.2.5.1 Types of aberration

i) Spherical aberration results from a variation in focal length of a lens with the distance from the axis of incident ray bundles, as shown in Fig. 5.4(a). As may be seen, the best focus, where the diameter of the ray bundle is at a minimum, is achieved at a position away from the paraxial focal point. This 'best' image is termed the 'disc of least confusion'. The resolution of an optical system is then limited as features of the object that are imaged to a smaller size than the disc of least confusion in the image can not be resolved.

ii) Coma is an asymmetrical aberration for off axis object points resulting in a comet like appearance of an object point. This is best illustrated by Fig. 5.4(b), which shows that rays with a small angle of incidence to the equipotential (lens surface) will be focussed close to point F on the principal ray, whereas those with a large angle of incidence are brought to a focus at a different point. This effect is different to spherical aberration as it depends on the angle of incidence between the ray and lens, and not the off axis distance of the ray.

iii) Field curvature is the effect where the image lies not on a plane, but on a curved surface instead. This results in a ring of object points of equal radius from the central axis being in focus at one time, but points lying on a radius are not focussed except at the point of intersection with the ring (Fig. 5.4(c)). Astigmatism is due to rays in the sagittal and meridional planes having different focal points as shown in Fig. 5.4(d) i.e. assymmetry of the lens about the central axis.

iv) Distortion is caused by a variation of magnification with distance from the central axis. This results in a displacement of the image points from their true positions. It does not blur the image or decrease the resolution, but merely detracts from its accuracy. The effect is shown in Fig. 5.4(e), where, for image points pushed away from the axis pin-cushion distortion results, while for those deviated towards the axis the effect is known as barrel distortion.

v) Chromatic aberration results from a change in refractive index with electron energy. This causes a variation in focal point with electron energy similar to the effect of spherical aberration and hence, if the electron beam has an energy spread, the image will not be focussed to a point but a disc (c.f. Fig. 5.4(a)).

a)

paraxial focus

disc of least
confusion

b)

O

paraxial focus

c)

image plane

paraxial image plane

d)

secondary image

primary image

optical
axis

O

e) i) no distortion   ii) barrel distortion   iii) pin-cushion distortion
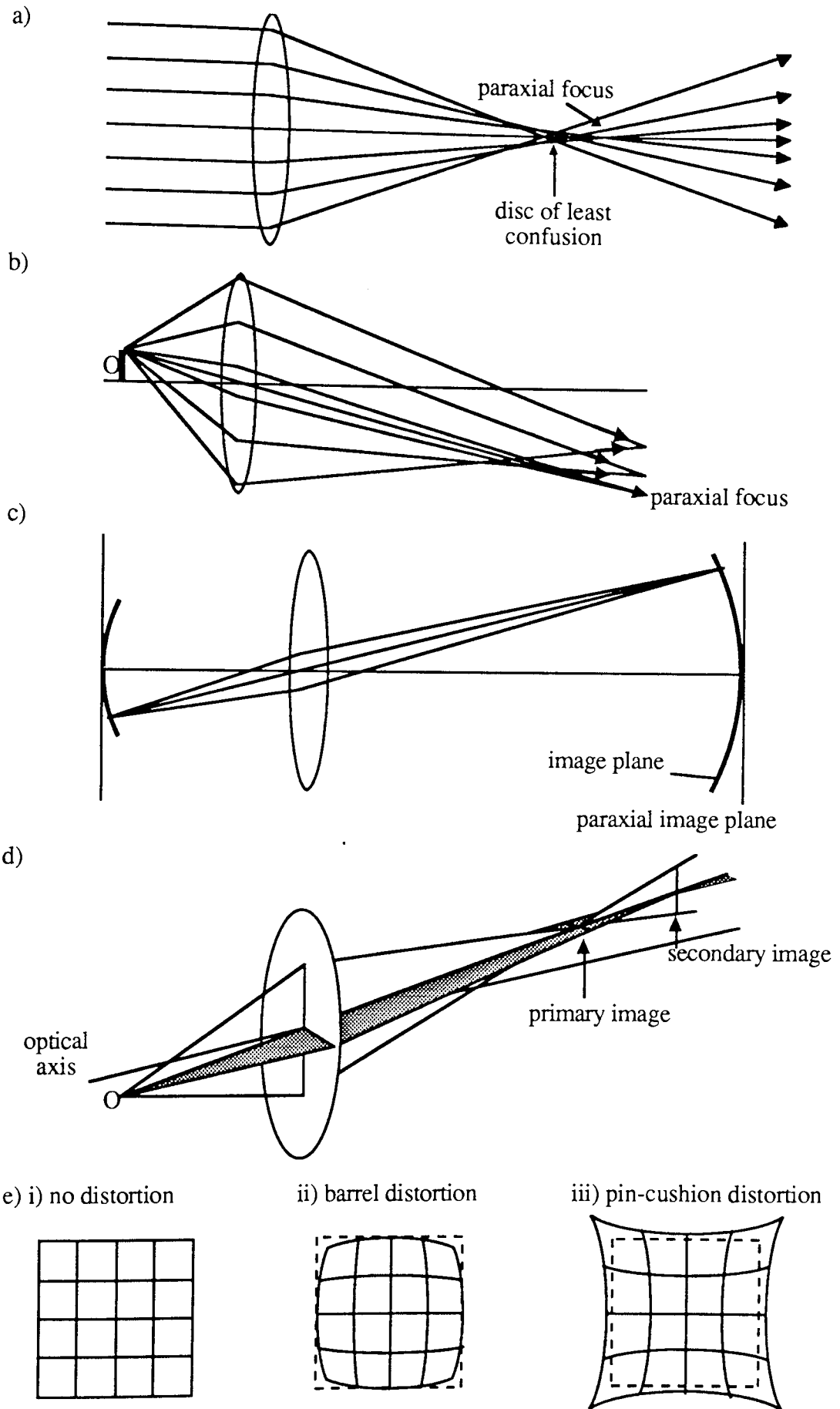
Figure 5.4 Illustrations of the effects of different types of lens aberration: a)
spherical aberration, b) coma, c) field curvature, d) astigmatism and e)
distortion.

147

vi) <u>Space charge effects</u>, where a bundle of electrons repel each other to cause degradation of the image only become important at high charge densities in excess of $1Acm^{-2}$ [126] and are not normally of importance for emission electron microscopes unless they use a pulsed laser to stimulate the emission.

The spherical and chromatic aberration coefficients intrinsic to the lens geometry employed for this project were known, and therefore the expected resolution of the instrument could be calculated, as is described in the following sections. It is also possible to calculate the effect on the resolution of electron diffraction by the lens apertures.

5.2.5.2 Definitions of the optical terminology

Figure 5.5(a) defines the parameters used to describe the dimensions of the unipotential lenses, where S is the separation between the outer and centre electrodes, D and t are the aperture and thickness of the central electrode respectively, and A is the aperture in the outer electrodes.
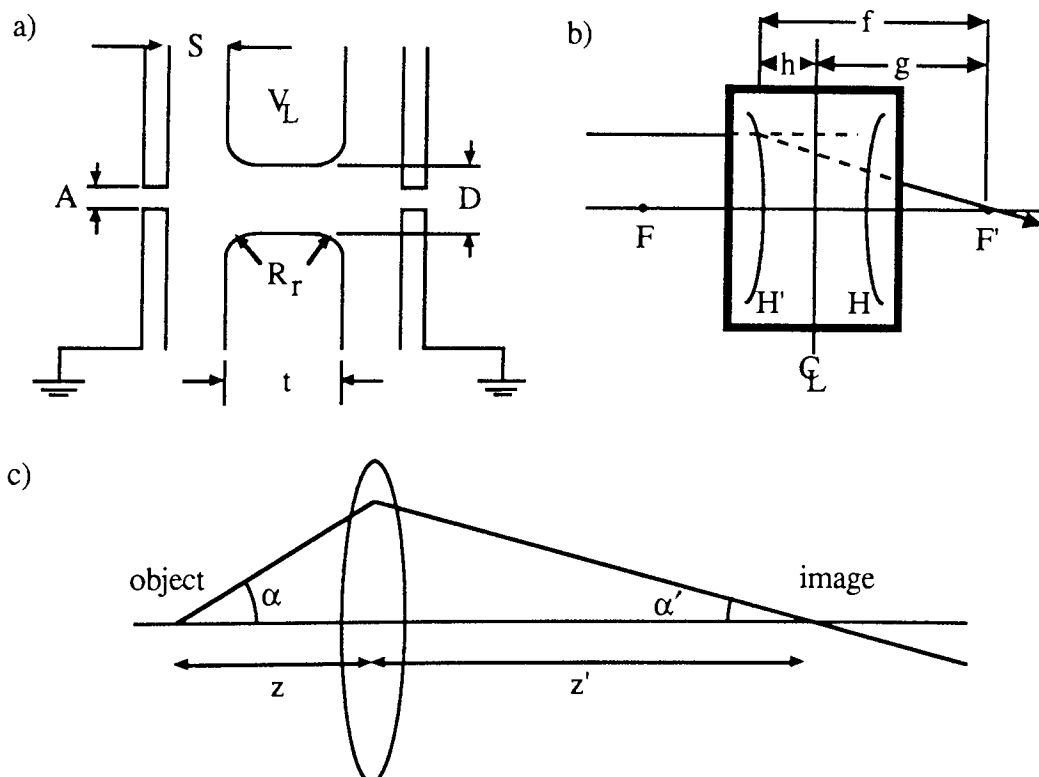
Figure 5.5 Diagrams illustrating the optical terminology employed in the following sections: a) the parameters specifing the dimensions of the uni-potential lenses, b) the parameters defining the optical behaviour of the lenses, and c) the definitions of the distances and angles for the optical system.

148

Figure 5.5(b) shows the definitions for the focal distance, g, and focal length, f, as related to the principal planes of the lens, H and H' (in the diagram these are shown as reversed, which is the case for the lenses used in this study) and the focal points F and F'. h is the distance between the centre-line of the lens and the principal planes. Figure 5.5(c) shows the principal definitions for an optical system where z and z' specify distances in object and image spaces, and α and α' respectively specify the angle the object and image rays subtend at the lens. The magnification, m, is positive for real images and is given by

$$m = \alpha/\alpha' = z'/z \qquad\qquad 5.6$$

5.2.5.3 Resolution limit due to spherical aberration

According to the terminology discussed above, the radius of the disc of least confusion for the case of spherical aberration is given by [125]

$$r_s' = \partial_s z'\alpha'/4 \qquad\qquad 5.7$$

where

$$\partial_s z' = [(1+m^2)S_g + 2mS_f](1+1/m)^2 f\alpha^2 \qquad\qquad 5.8$$

The terms S_f and S_g are the spherical aberration coefficients for the focal point and focal length respectively, and f is the focal length. The limit to resolution may be calculated by relating the diameter of the disc of least confusion to the size of a disc on the object which would be imaged to the same size. This is achieved by dividing Eq 5.7 by the magnification and substituting for α', as given in Eq 5.6, to give a resolution of

$$r_s = \left[\left(1 + \frac{1}{m^2}\right)S_g + \frac{2}{m}S_f\right](1+1/m)^2 f\alpha^3 \qquad\qquad 5.9$$

5.2.5.4 Resolution limit due to chromatic aberration

As with the case for spherical aberration, the size of the disc of least confusion due to chromatic aberration, r_c', is given by the equation [125]

$$r_c' = \partial_c z'\alpha'/4 \qquad\qquad 5.10$$

where

$$\partial_c z' = [(1+m^2)C_g + 2mC_f]f\alpha'\Delta V/V \qquad\qquad 5.11$$

149

$\Delta V/V$ is the fractional energy spread of the electrons, and C_f and C_g are the chromatic aberration coefficients for the focal point and length respectively.

By substitution of 4.6 and 4.11 into 4.10 the resolution may then be shown to be

$$r_c = \left[\left(1 + \frac{1}{m^2}\right) C_g + \frac{2}{m} C_f \right] f\alpha \frac{\Delta V}{V} \qquad 5.12$$

5.2.5.5 Aberrations of the accelerating field

Photo-emitted electrons may be emitted over a range of angles, α_e, up to 90° and then follow parabolic paths under acceleration by the gap field (Fig. 5.6). Following from the discussion of section 5.2.2, an aperture in a thin sheet of material, of small diameter compared to the accelerating gap, l, and with a zero-field region behind it, will behave as a diverging lens of focal length $f = -4l$. The tangents at the termination of the field space indicate the existence of a virtual sample image of unit magnification located at approximately 2l. By application of similar triangles to the velocity components of the emitted electrons, this may be shown to be

$$l^* = \upsilon_{ax} r_a / \upsilon_r \qquad 5.13$$

However, only axial acceleration occurs and therefore $u_r = \upsilon_r$ and u_r/r_a equals t_f, the time of flight. Also, the system may be assumed to cause uniform acceleration to the electrons and thus t_f may be shown to be

$$t_f = 2l/(u_{ax} + \upsilon_{ax}) \qquad 5.14$$

where u_{ax} is the axial component of the emission velocity. The true position of the apparent electron emission source due to the accelerating field is then

$$l^* = 2l/(1 + u_{ax}/\upsilon_{ax}) \qquad 5.15$$

Thus, since $u_{ax}/\upsilon_{ax} \ll 1$, this reduces to $l^* \approx 2l$.

By application of the thin lens formula with $u = l^*$ and $f = -4l$, the image of the emission point due to the accelerating field is the object for the rest of the optical system and may be shown to be a virtual image of magnification $2/3$ at position $-4/3l$.

By appropriate substitutions, equation 5.15 may be shown to be

$$l^* = 2l \left[1 - \left(\frac{V_e}{V_a}\right)^{1/2} \cos\alpha_e \right] \qquad 5.16$$

Figure 5.6 Diagrams illustrating the effect of the accelerating field on the optical behaviour of the cathode-anode gap. a) electrons may emerge over a range of angles, and are accelerated along parabolic paths, b) and therefore appear to originate from a point behind the cathode surface at approximately twice the gap spacing. c) if the aperture in the objective has a low field region behind it, then it will behave as a thin lens acting on the virtual image of the emission point. Therefore, the electrons appear from a point ~4/3 the gap spacing and magnified by 2/3 (from [117]).

thus showing that V_e, the emission energy, and α_e cause aberration by moving the apparent object position as

$$\partial_s l^* = 2l(V_e/V_a)^{1/2}[1-\cos\alpha_e] \tag{5.17}$$

The chromatic aberration is given by

$$\partial_c l^* = 2l\left[\left(\frac{V_e}{V_a}\right)^{1/2} - \left(\frac{V_e-\Delta V_e}{V_a}\right)^{1/2}\right]\cos\alpha_e \tag{5.18}$$

where ΔV_e is the spread of emission energies.

151

For a system with no aperture stop, these equations result in a disc of least confusion of [127]

$$r = 0.61 V_e / V_a$$

5.19

The angular aperture, α_e, of the emitted electrons is related to α_a by

$$\alpha_a = (V_e/V_a)^{1/2} \sin\alpha_e$$

5.20

and the angular aperture for rays entering the objective lens, $\alpha_1 = 1.5\alpha_a$ [117]. Therefore

$$\alpha_1 = 1.5(V_e/V_a)^{1/2} \sin\alpha_e$$

5.21

For small emission angles this then leads to a resolution of

$$r = 0.251(V_e/V_a)\alpha_e^3$$

5.22

5.2.5.6 Combined effect of chromatic and spherical aberrations

For the case of spherical aberration greater than chromatic aberration, the combined effect on the resolution may be calculated from the equation [125]

$$r' = \left[\frac{\partial_s z'}{4} + \frac{\partial_c z'}{3} \right] \alpha'$$

5.23

When the chromatic aberration dominates, the combined effect reduces to the equation for chromatic aberration alone i.e. Eq.5.12.

5.2.5.7 Diffraction effects

The diffraction error may be calculated from two well known formulae, i.e. the de Broglie wave equation [128], relating the wavelength λ of an electron to its energy E, and the formula for the radius, d, of the first diffraction minimum at a distance l from a circular aperture of radius r [81]. Respectively, these are

$$\lambda = hc/E$$

5.24

$$d = l\tan(1.22\lambda/r)$$

5.25

By utilising these two equations, and taking d as the resolution limit (viz the Rayleigh criterion), the diffraction effects through the lens apertures may be calculated and their effect upon overall system resolution determined.

5.3 Overall system design and layout

5.3.1 Experimental chamber

The experimental chamber is based around a VG pumping well incorporating an isolation valve to a liquid nitrogen trapped Edwards E02 oil diffusion pump and backed by an E2M8 rotary pump. For economic reasons, an existing chamber was utilised as its porting was suitable for the required application although it did place some constraints on the overall system design. In fact, it was the commitment to this chamber which determined the requirement that the electron-optical column had to be mounted horizontally rather than in the optimum vertical configuration [74].
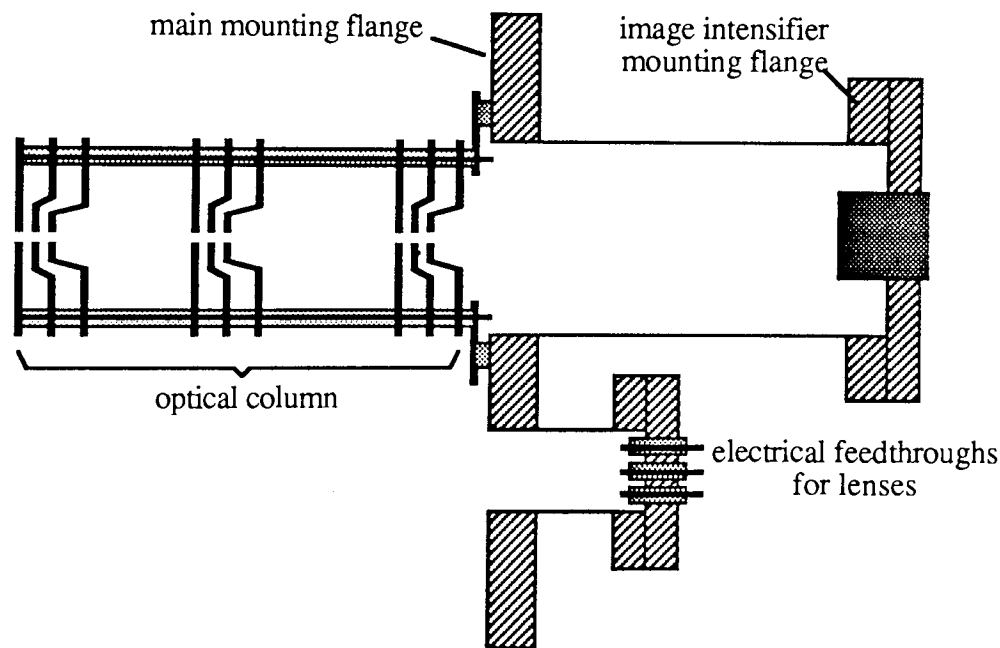
Figure 5.7 Schematic diagram of the demountable electron-optical column and detector assembly designed for the UV imaging system.

The entire electron-optical assembly was designed as a demountable unit (see Fig. 5.7). Thus, all the elements were mounted on a single custom built flange. This flange not only contained the mounting points for the electron lenses, but also the micro-channel plate image intensifier and all the necessary electrical feedthroughs to run the lenses. All the lens elements were constructed from electro-polished stainless steel and insulated by alumina tubing. Central metal rods were utilised to tension the entire assembly.

153
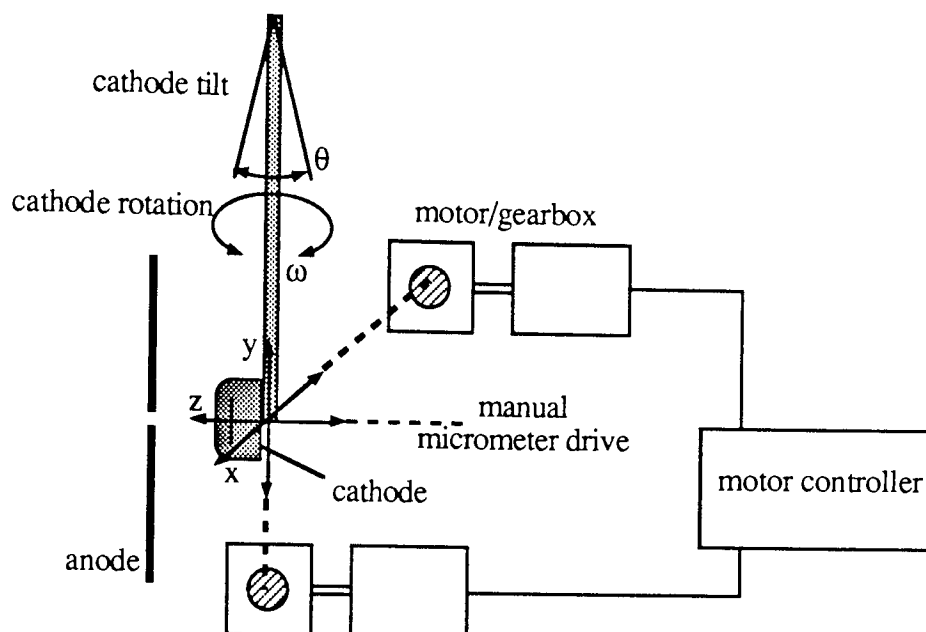
Figure 5.8 Sample manipulator movements for the translation and alignment of the sample stage plane-parallel to the anode.

Sample manipulation was achieved using a specimen holder mounted on an XYZ movement stage incorporating a rotational motion and a tilt assembly for the alignment of the specimen motion plane-parallel to the anode face (see Fig. 5.8). The two motions in the plane parallel to the anode are motorised, and there is an electronic controller that may be used to locate emission sites by the anode probe-hole technique [5] using a spiral scan pattern. Subsequent manual control over the sample movement is available for the axial alignment of individual sites for their study in greater detail. The motorised manipulation system is fully described elsewhere by Bayliss [42].

The UV source is mounted on a bellows assembly to enable the accurate alignment of the UV beam through the apertures in the objective lens stage (Fig. 5.9). Owing to the operational principle of the UV source, a differential pumping system is required. Thus, a rotary pump is used to maintain the correct operating pressure within the discharge chamber of the source, whilst an intermediate stage between the source and main experimental chamber is pumped by a liquid nitrogen trapped Edwards E04 oil-diffusion pump and backed by an E2M5 rotary pump. The intermediate chamber is required in order to maintain a pressure of better than 10^{-9} mBar within the main experimental chamber.
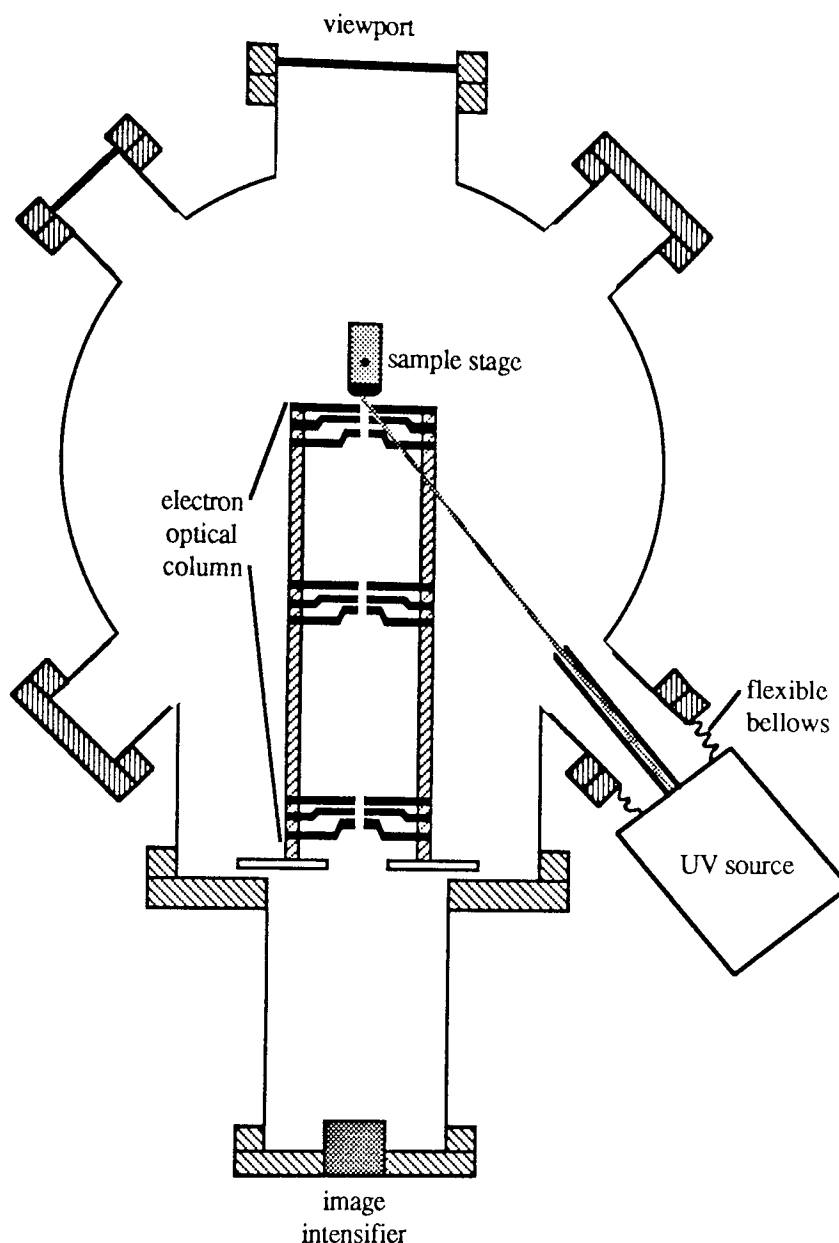
Figure 5.9 Schematic diagram of the layout of the experimental UHV chamber showing the electron-optical column, sample position and UV source adjustment bellows.

5.3.2 UV source

5.3.2.1 Design of UV source

The UV source is an in-vacuum type which operates using an electric arc through a low pressure gas (0.1 - 0.03 torr) to generate UV emission. The UV spectrum emitted depends upon the particular gas used, which in this case was chosen to be argon for its ready availability and low cost. By using a gas discharge, high energy UV photons may be generated to which materials available for window construction are opaque, hence the requirement for an 'in-vacuum' design.

The design of the source is shown schematically in Fig. 5.10 and consists of two stages. In order to control the arc chamber pressure, the gas is fed in via a needle valve. At the same time however, the chamber is also pumped to reduce gas escape into the main vacuum chamber. A glass window is mounted at the far end of this chamber to enable visual confirmation of an arc. A short quartz tube of 1mm diameter allows transmission of the UV photons, while reducing gas conductance to the next stage of pumping. The second pumping stage removes most of the gas streaming back from the first stage, and thus allows a low main chamber pressure to be maintained. A further quartz tube of ~150mm length is then used to achieve a high degree of output collimation, and further reduce gas conductance into the main vacuum chamber [129].
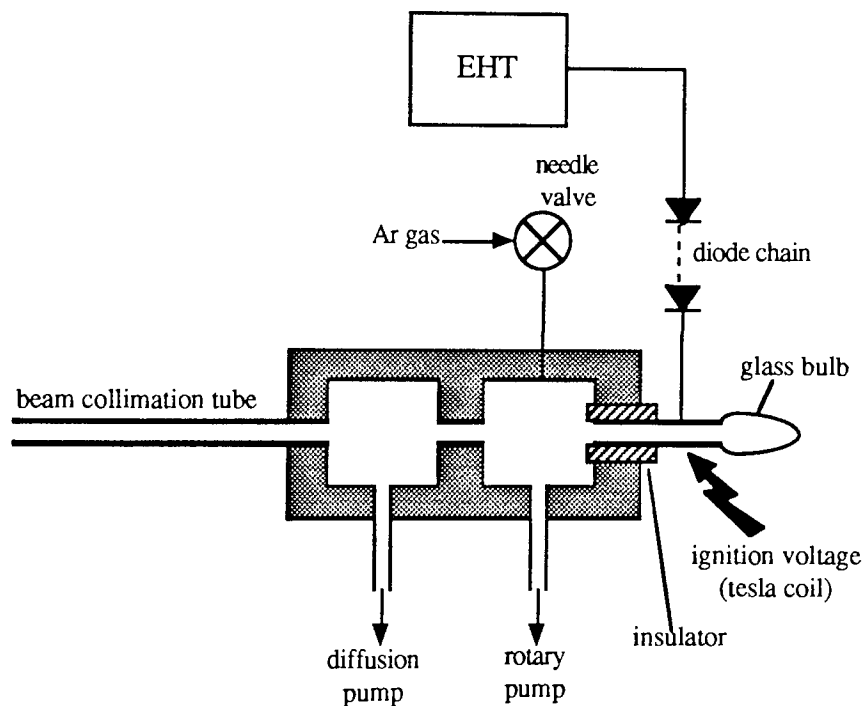
Fig 5.10 Schematic of the UV source and the gas and power supplies required for operation.

The UV output consists of a line spectrum excited by the electrical discharge. Table 5.1 shows some of the principal lines excited in the UV, and gives their relative intensities and photon energies [130].

The source is powered by a modified ionisation pump power supply enabling control of the discharge current and hence photo-emission current. The UV source is ignited by applying a potential of ~1000V, which is insufficient to 'switch-on' the arc across the gas, and then supplying an extra 'jolt' using a tesla coil to excite the discharge. The arc is self-sustaining after ignition. The power supply is protected from this additional voltage by a diode chain as shown in Fig. 5.10.

Table 5.1 Principle lines excited in the UV region of the spectrum by electrical discharge through Ar gas, indicating the intensity, wavelength and photon energy (from [130]).

5.3.2.2 Photo-emission current

Using the experimental arrangement shown in Fig. 5.11, the variation of photo-emission current from a standard cathode was measured with respect to the UV source arc current. In order to collect all the electrons emitted by the electrode, the anode was biased with a positive potential of several hundred volts. A Keithley 410BR electrometer was connected to the cathode to measure the emission current.
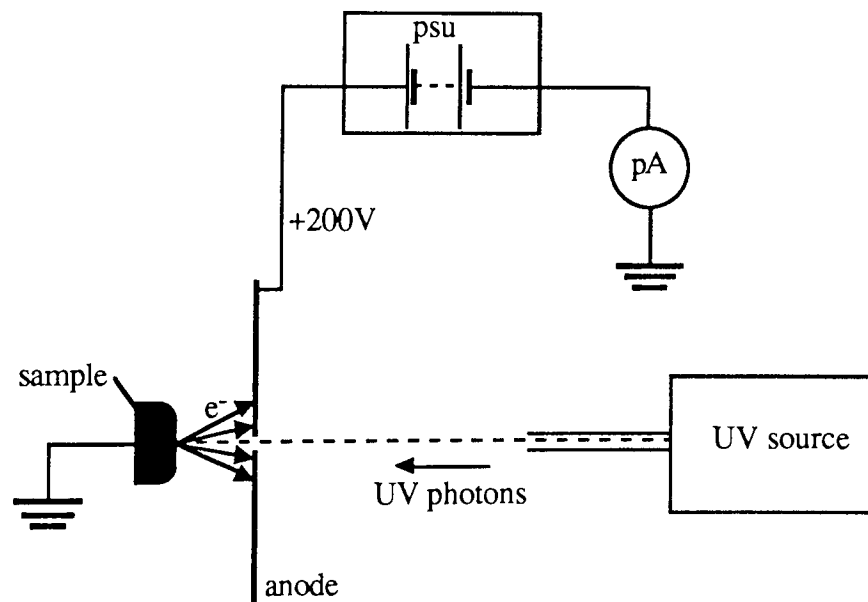
Figure 5.11 Illustration of the experimental arrangement used to measure the photo-electron current from a Cu electrode illuminated by the UV source.

This experiment showed that a photo-emission current of 1nA could be attained at low values of the source current. Further work was also undertaken to measure the variation of the photo-emission current with arc current which revealed that the photo-electron current varied linearly with source current (Fig. 5.12).

The photo-emission occured from a spot of 1mm diameter, and thus the emission current density was of the order of $10^{-7}Acm^{-2}$. Space-charge effects,

which become important to the optical behaviour of an electron lens system at current densities of $\geq 1 \mathrm{Acm^{-2}}$ [126] may therefore be neglected.
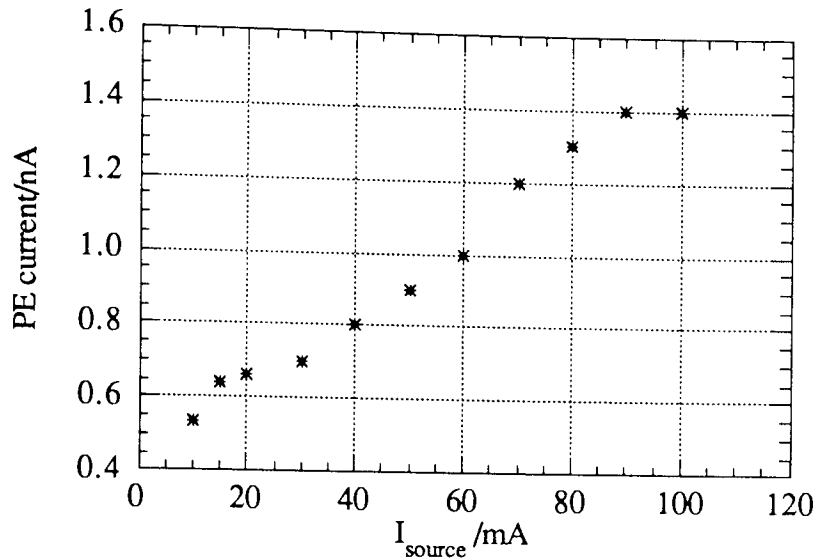
Figure 5.12 Photo-electron current vs UV source arc current measured from a standard Cu electrode at a collection voltage of 200V.

5.3.3 Electron-optical column

The electron-optical column is designed around three uni-potential lenses, with field-free spaces between the lenses. Each of the lenses consists of three stainless steel electro-polished electrodes manufactured to our design by VG Special Systems. These lenses are separated by tubular alumina spacers and the whole assembly is mounted on four alumina tubes which have central steel rods for rigid tensioning (Fig. 5.13).
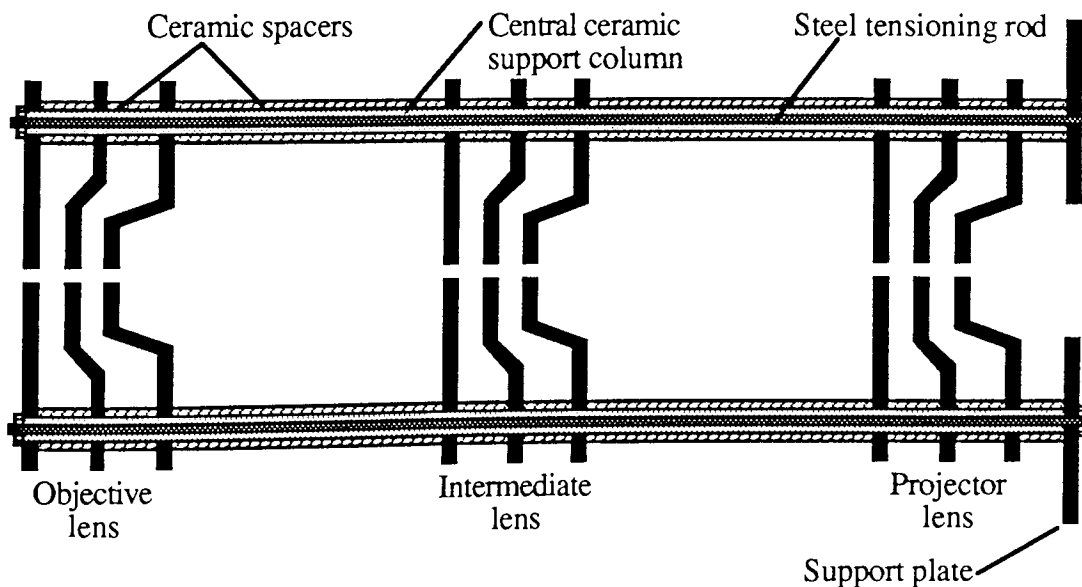
Figure 5.13 Illustration of the optical column assembly technique to provide rigid support for the lens elements.

5.3.3.1 Objective lens

The objective lens was designed to perform the functions of extraction and acceleration of the emitted electrons, and the primary magnification of the emission image. Furthermore, additional apertures had to be provided to enable the UV beam to illuminate the sample surface underneath the objective lens aperture whilst maintaining a sample-electrode spacing of ~1mm.

The lens, shown in cross-section in Fig. 5.14(a), is actually composed of two separate lenses: a standard uni-potential lens, and a single aperture lens built into the first electrode. The purpose of this arrangement is to produce an object for the rest of the electron-optical system at a well defined position.

Figure 5.14. Dimensions and spacings of the electrodes for a) the objective and b) the intermediate and projector lenses.

159

The single aperture lens approximates to the case described in section 5.2.2, with the cathode-anode gap field infront, and a zero field region behind the aperture. From the discussion of the behaviour of such a single aperture lens, a virtual image of the sample is formed at a distance of $4/3$ the cathode-anode gap, at a magnification of $2/3$, as shown by Fig 5.6. This virtual image is then the object for the uni-potential lens.

The uni-potential lens has the properties shown by the graphs of Fig. 5.15 and will therefore operate optimally on an image at the front face of the lens assembly. Thus, it will be capable of imaging a surface using any gap separation. The values of the various optical parameters for a voltage ratio of $V_L/V_C = 1$ are given in Table 5.2. In addition, the UV beam must be able to strike the sample surface in order to generate the photo-electrons. This requirement is achieved by the use of a series of apertures through the electrodes of the objective lens of decreasing diameter towards the cathode. These enable some flexibility in the positioning of the UV source whilst reducing the perturbation to the lens and accelerating fields.

Fine focussing is achieved by reducing the potential applied to the central electrode from that of the cathode towards ground. This has the effect of increasing the focal length of the lens and thus correcting for variations of the sample spacing. The variation of the focal point is shown by the graph of Fig. 5.15(a). These also show the spherical and chromatic aberration coefficients intrinsic to the lens design [124].

parameter	objective lens	intermediate/projection lenses
s	5.10	4.28
t	0.60	3.81
D	6.00	4.06
f	9.45	4.5
g	8.62	0.8
S_f	-20	-2.5
S_g	-20	-11
C_f	3.3	2.3
C_g	3.3	7.8

all values in mm

Table 5.2 Optical properties of the objective and intermediate/projection lenses for the same potential applied to the central electrode of the lens and the cathode i.e. $V_L/V_C=1$.
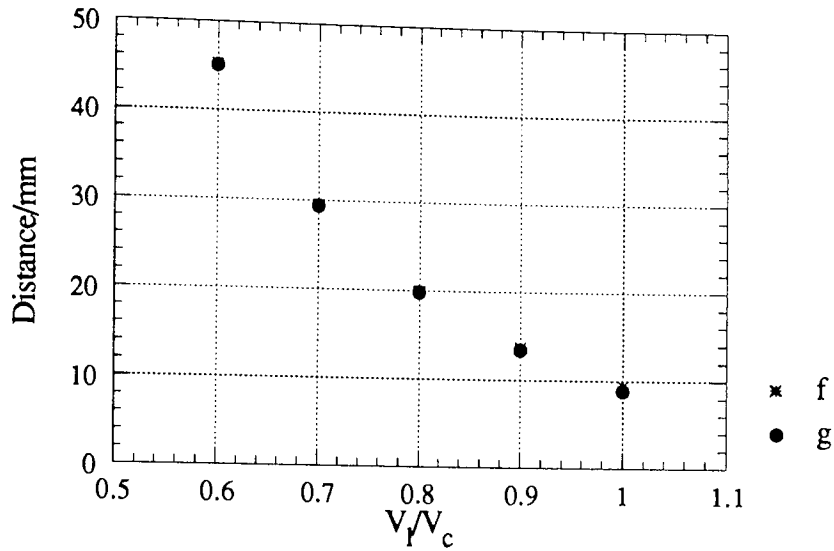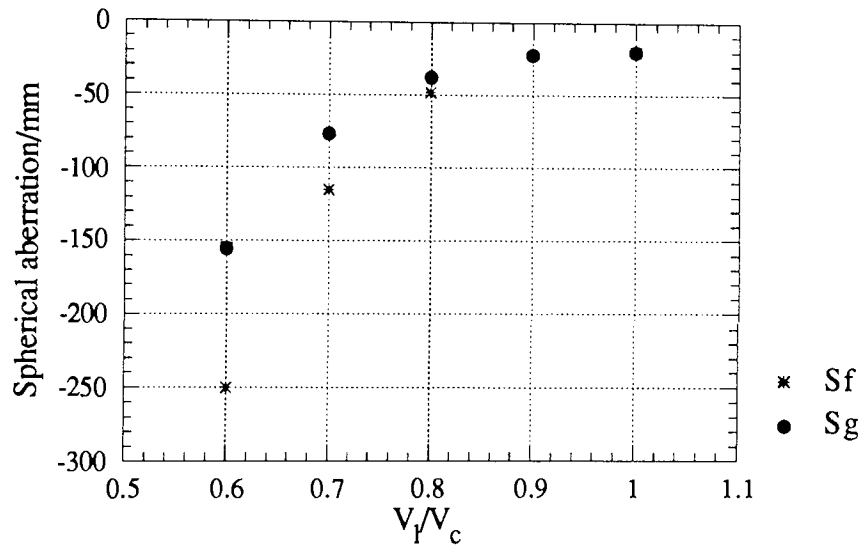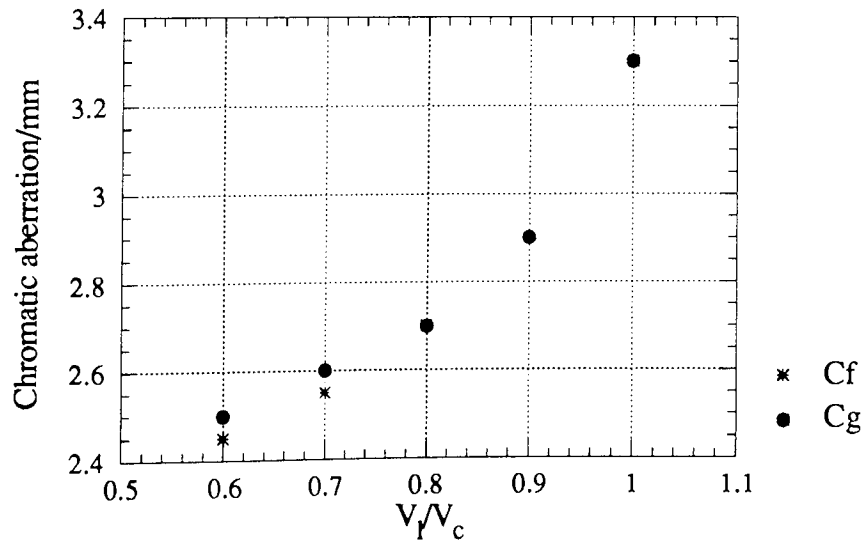
Figure 5.15 Graphs of the optical properties of the objective lens illustrating their dependence upon the ratio of the potentials applied to the centre electrode and to the cathode showing a) focal distances, b) spherical aberration co-efficients and c) chromatic aberration co-efficients.

a)

b)

c)
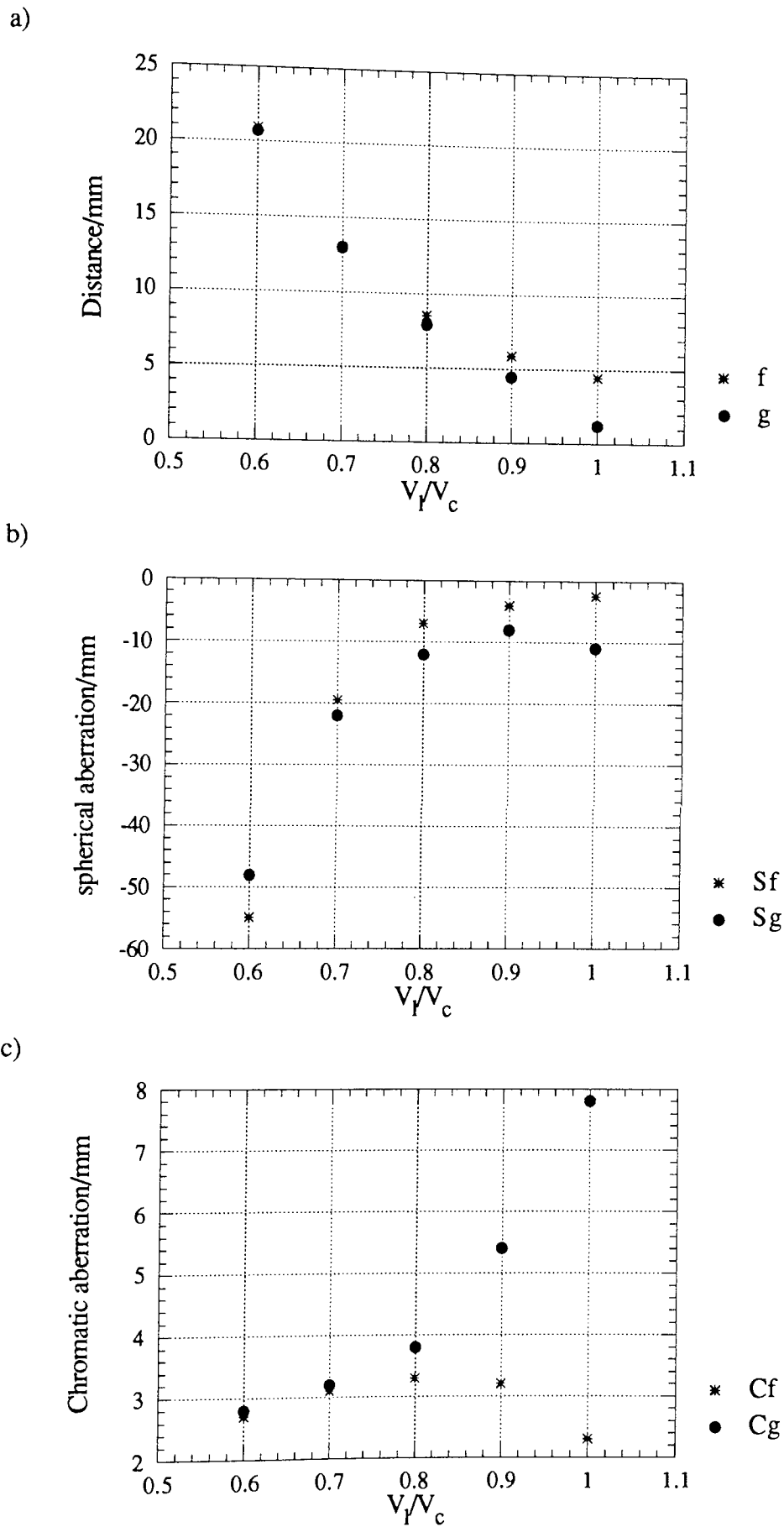
Figure 5.16 Graphs of the optical properties of the intermediate and projection lenses illustrating their dependence upon the ratio of the potentials applied to the centre electrode and to the cathode showing a) focal distances, b) spherical aberration co-efficients and c) chromatic aberration co-efficients.

5.3.3.2 Additional lens stages

The design of the following two lenses is identical, and taken directly from information supplied by the Oregon group of Griffiths [131]. Their design was optimised from the data of Rempfer *et al* [124] to perform the role of intermediate and projector lenses in their UV emission microscope [116], which is capable of a resolution of 150Å. The imaging properties and aberration coefficients of these lenses are shown in the graphs of Fig. 5.16. As may be seen from Table 5.2, they have a minimum focal length of 4.5mm, and a focal distance of 0.2mm i.e. the focal point is virtually at the centre-line of the electrode assembly. Fine focussing of these stages is accomplished in a similar manner to that employed for the objective lens, where a reduction in the potential of the centre electrode towards earth again results in an increase of the focal length.

5.3.3.3 Predicted electron-optical performance

The spacing of the lens elements is indicated in Fig. 5.17(a), however, since the uni-potential lenses behave as thick lenses with crossed principal planes the optical path is actually longer than the physical separations. For analytic purposes, this optical system is equivalent to the thin lens analogue shown in Fig. 5.17(b). In order to determine the approximate maximum magnification of this lens system, it will be assumed that the object for each lens is positioned at the paraxial focal point.
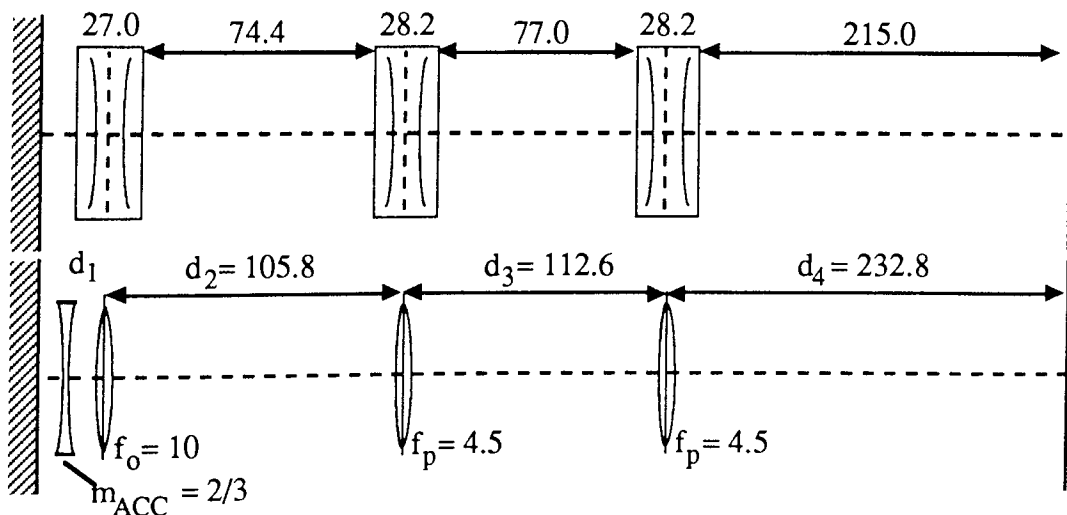
Figure 5.17a) physical dimensions of the optical column and b) the thin lens optical analogue of the optical column.

By geometrical optics, the magnification m of a lens is given by equation 5.6. Thus, by making the approximation that $z = f_n$, the focal length of the nth lens, and

$z' = d-f_{n+1}$, where d is the distance to the next lens and f_{n+1} is that lenses focal length, the overall system magnification may be estimated. This assumption is justified since the system is configured to maximise the magnification and therefore $z/f \ll 1$ whilst $z'/f \gg 1$. The overall magnification, m_T, is the multiplicand of the original accelerating field magnification, $m_{ACC}=2/3$, and the individual lens magnifications (i.e. the objective lens, m_{OBJ}, the intermediate lens, m_{INT}, and the projector lens, m_{PRO}) and is given by the equation

$$m_T = m_{ACC} * m_{OBJ} * m_{INT} * m_{PRO}$$

5.26

where

$$m_{OBJ} \approx \frac{d_2-f_p}{f_o} \; ; \; m_{INT} \approx \frac{d_3-f_p}{f_p} \; ; \; m_{PRO} \approx \frac{f_4}{f_p}$$

5.27

In this equation $d_{1..n}$, are the lens separations, and f_o and f_p are the focal lengths of the objective and intermediate/projector lenses respectively. Substitution of the values used for the given optical configuration, shown in Fig. 5.17(b), allows a maximum magnification of ~8500x to be estimated for the microscope.

5.3.3.4 System resolution

The overall imaging resolution of the system is governed by three principal factors: the intrinsic lens aberrations, the mechanics of the electron emission process, and the resolution of the micro-channel plate. The first factor may be estimated from the given lens data according to the priciples discussed in section 5.2.4., and is found to be ~1μm. The effect of the accelerating field requires an estimation of the emitted electron energy, V_e. This was taken to be in the region of 7eV by only considering the two principal Ar emission lines and subtracting the work function of copper. The accelerating field was found to limit the resolution of the optical system to ~2μm. Owing to other factors, including the accuracy of the electrode machining and alignment, it is only possible to estimate the resolution.

5.3.4 Imaging system

5.3.4.1 Micro-channel plate detector

Micro-channel plates are broad area devices that multiply electrons while maintaining the information contained in the spatial distribution of the incident electron flux. They are therefore used for the intensification of images, and find a wide range of applications in the fields of surveillance and night-time photography, as well as in particle detectors and photon counters.

Typically, a microchannel plate consists of a thin sheet of material of thickness
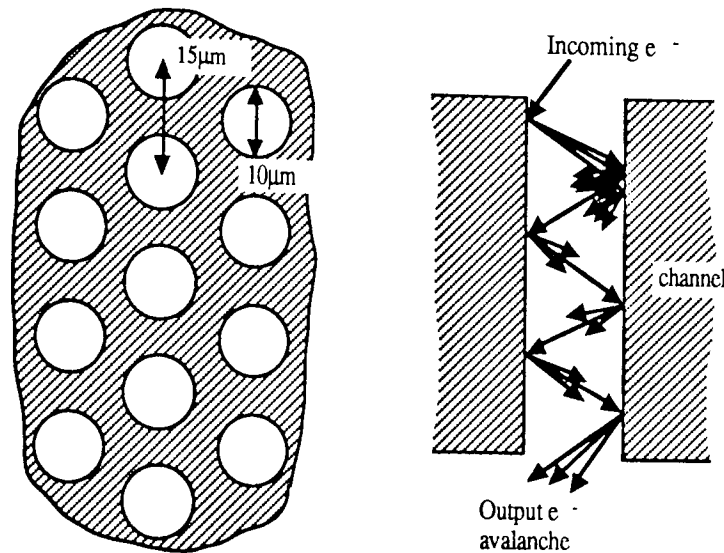
Figure 5.18 Schematic of a micro-channel plate illustrating a) the arrangement of multiplier channels and b) the electron multiplication within a channel.

<1mm which contains many channels arranged in a regular array, as shown in Fig. 5.18(a). Each of these channels behaves as an independent electron multiplier which thus enables the device to preserve the spatial information of an incoming signal [132]. In a typical device the channels have diameters of ~10μm and are spaced at approximately the same distance. An intensified image resolution of >30 line pairs/mm is therefore possible. This compares with a video monitor resolution of ~5 line pairs/mm.

Micro-channel plates operate in a similar fashion to the channeltron detector utilised in the electron energy spectrometer descibed in Chapter 3 [132]. A large potential is maintained between the two sides of the sheet so that an incoming particle, either an electron or an ion, will emit several secondary electrons on collision with the channel wall, which is coated in a low work function material (Fig. 5.18(b)). These electrons are then accelerated by the pd along the channel and collide with the wall further along the channel to cause the emission of further electrons. Thus, an avalanche of electrons is created at the output of the channel. Typically, multiplication factors of up to 10^4 to 10^5 may be obtained by applying several hundred volts across the channel plate.

The active material coating the micro-channel plate has a high impedance in order to limit the current flowing through each channel when a potential is applied across the device. This current is typically in the range of a few tens of micro-amps and is termed the strip current. It replaces the electrons emitted and thus limits the maximum output flux obtainable from the device. The device saturates when the gain multiplied by the incoming electron flux approaches the strip current. The current is evenly distributed between the channels, as each has a similar impedance, and therefore saturation will occur locally should the local incoming flux be too great, as may well happen for field emission electrons under high gain conditions. This will not be a problem though, since it is a highly localised region of the image, and will only affect current density measurements from image brightness.

5.3.4.2 Specification of the micro-channel plate detector

By experiment (see section 5.3.2.2) the UV source was found to be able to generate a photo-emission current of ~1nA or ~10^{10} electrons.s^{-1}, which was emitted from an area of ~1mm^2. The average flux observed in the image plane, ϕ_s, may then be calculated according to the equation

$$\phi_s = \frac{\pi}{4} \cdot \frac{d_s^2 \phi_e}{m^2}$$

5.28

Where d_s is the diameter of the screen, m is the magnification and ϕ_e is the photo-emitted electron flux.

Hence, with a magnification of 5000x at the required resolution of 0.05µm, i.e. corresponding to 0.5mm in the image plane, an average flux of just 10^2 electrons.s^{-1} per unit resolvable area would be observed. For this reason, it was decided to opt for a dual channel plate device, consisting of a pair of micro-channel plates stacked one on top of the other in order to obtain a higher gain of up to 10^7, albeit at the expense of a lower detector resolution of some 18 line pairs/mm at the screen [133]. Thus, for a feature to be resolvable on the screen, its magnified image must be greater than 56µm. At high magnifications, this will not limit the overall microscope image resolution since this criterion corresponds to 56nm in the object plane at a magnification of 1000x. The multiplication characteristics for the chosen device are shown in Fig. 5.19.
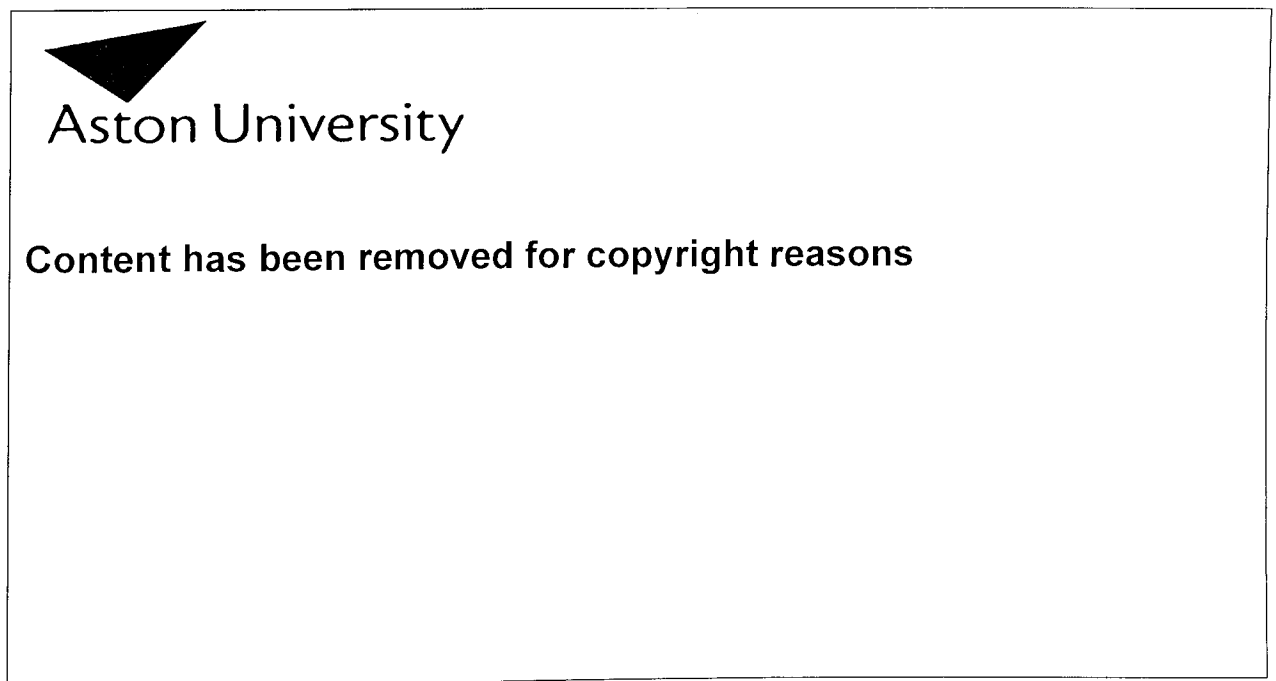
Figure 5.19 Multiplication characteristics of the chosen micro-channel plates indicating the relative performance of 1 and 2 plate devices (from [133])

An open face detector was employed i.e. there was no photo-emitting screen before the detector such as would be used for light intensification purposes. This maximises the efficiency of the multiplication of the incoming electron flux. The device had an active surface of 40mm diameter, and a strip current of 10-100μA.

Figure 5.20 Graph showing the efficiency of the mulit-channel plate intensifier against the incident electron energy (from [133])

5.3.4.3 Micro-channel plate drive electronics

As shown in Fig. 5.21, four separate voltage supplies are required to operate the device: one to the input side of the first detector, one to the intermediate connection point, one to the output of the second detector, and one to the phosphor screen. Typical operating values of 600 volts across each of the micro-channel plates and 3kV between the plates and the phosphor screen gave a multiplication factor of $\sim 10^4$x. All the inputs are isolated, so the input of the first plate could be held at earth potential thus leaving the space between the projector lens and intensifier field-free. All the feedthroughs were limited to a maximum of 5kV wrt earth.

A potential divider circuit, shown in Fig. 5.21, was designed to provide the correct voltages for the image intensifier from a single Brandenburg 0-5kV, 5mA HT power supply. This was designed to apply half the total output potential to the centre connection between the two plates. A separate HT power supply was used to drive the phosphor screen thus maintaining maximum flexibility.

5.4 System performance

Initial experiments aimed at assessing the performance of the system utilised TEM grids of known dimensions in order to provide a quantified image for determining the system magnification and resolution. These are not ideal objects however, since the sides, as well as front surface of the grid, are illuminated by the UV light. A non-uniform field also exists at the surface of the grid since the field
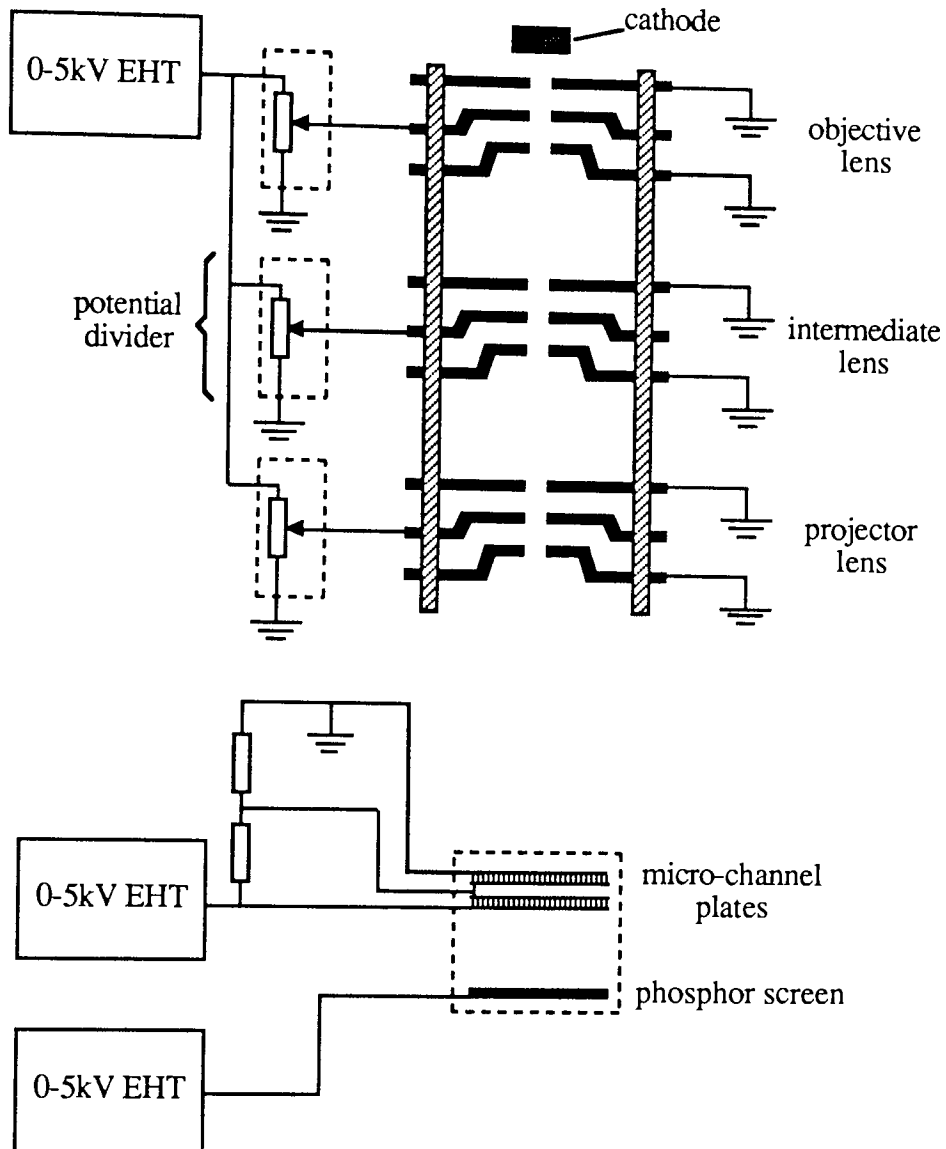
Figure 5.21 Schematic illustration of the micro-channel plate power supplies.
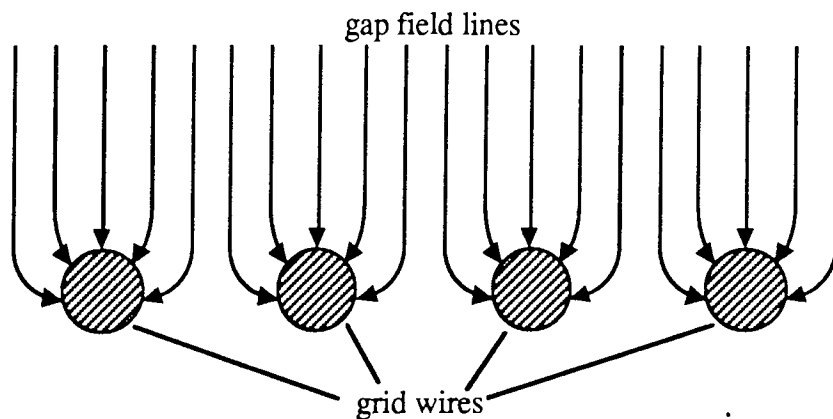
Figure 5.22 Schematic illustration of the field intensification at the surface of the TEM grids used for evaluating the UV imaging system performance.

penetrates the gaps in the grid, as indicated in Fig. 5.22. The system is therefore probably capable of attaining a superior resolution using an actual sample than is indicated from these sample grids.

The image of a grid having 2000 lines/inch is shown in Fig. 5.23, where this line density corresponds to a wire thickness of 3μm and a spacing of 12μm. The image of this grid is then displayed within a field of view of 40mm diameter hence the magnification is ~1000x. From this image the resolution may be estimated to be at least 1-2μm. At higher magnifications, further imperfections may be observed in the grid wires, and thus the overall system resolution is certainly approaching 1μm. Furthermore, the image maintains its 'squareness' and thus distortion of the image is negligible compared to the system resolution.

Mention must also be made of other problems that reduced the quality of the images. Most important, vibration of the sample relative to the optical column seriously limited the actual resolution, where the degree of the vibration was typically ~1-2μm, i.e. the same order as the resolution derived from the image of the TEM grid. This effect could be observed simply by looking at the image on the screen which could be seen to be vibrating by this degree.
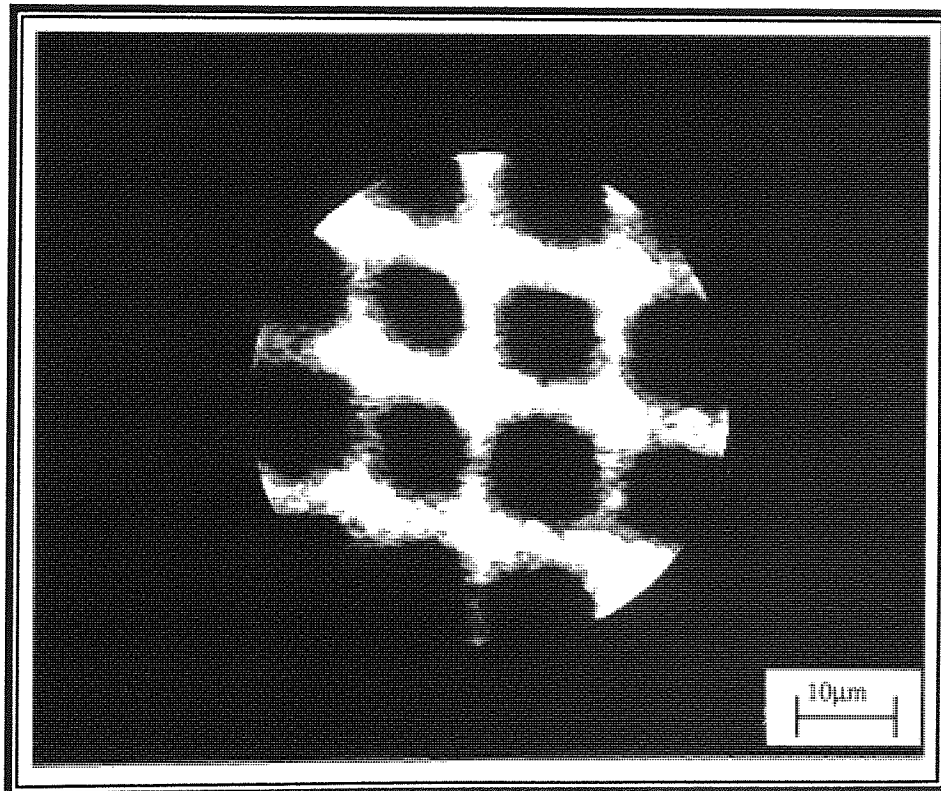
Figure 5.23 Photo-electron image of a 2000 line/inch TEM grid at a microscope magnification of 1000x.

5.4.1 Photo-emission studies of carbon emitters

As discussed in Chapter 2, carbon micro-structures have previously been found to provide very active low-field micro-emission [12,42,61]; and furthermore, the emission mechanisms involved for these structures are of considerable technological importance. Bayliss investigated natural sites resulting from breakdown events and showed that the emission was associated with small droplets of electrode material deposited on the ambient oxide surface layer of the electrode [42]. From his results he concluded that such emission sites have a metal-insulator-metal type of structure. Further work by Xu [53,68], using 'artificial' MIM sites, made by the deposition of carbon flakes on a substrate electrode indicated that several mechanisms might be involved in the emission processes of MIM sites. In particular, emission images from such sites frequently exhibited bright arc-like structures (see Fig. 2.22). From this evidence he hypothesised an emission mechanism based on coherent scattering occuring in the carbon flake. Such arc-like images are also often observed in natural sites and may therefore result from a similar mechanism.

Since it would be valuable to investigate the emission from such structures, it was decided to use this regime for a pilot study aimed at evaluating the performance of the new UV imaging system. The use of such sites offers the further advantage that emission readily occurs at relatively low field strengths, only requiring gap voltages in the region of a few kV. The technique also results in emission centres that may be readily located and identified from the surrounding electrode substrate material.

5.4.2 Site preparation technique

Pure graphitic carbon powder of particle size ~100μm was used to prepare the sample electrodes by the following method. The carbon powder was placed upon a glass slide, and could then be transferred to the electrode surface by the use of a tungsten tip wetted in methanol. When this dried, the remaining residue held the carbon particle to the electrode surface with sufficient strength to withstand both handling and the electrostatic forces developed on the particle by the electric field within the photo-electron microscope. To minimise contamination, the glass slide, tungsten tip and electrode were ultrasonically cleaned prior to the procedure.

5.4.3 Emission images from carbon emitters

Although detailed IV characteristics were not recorded for these samples, their emission characteristics were similar to those obtained in previous studies [42,61],
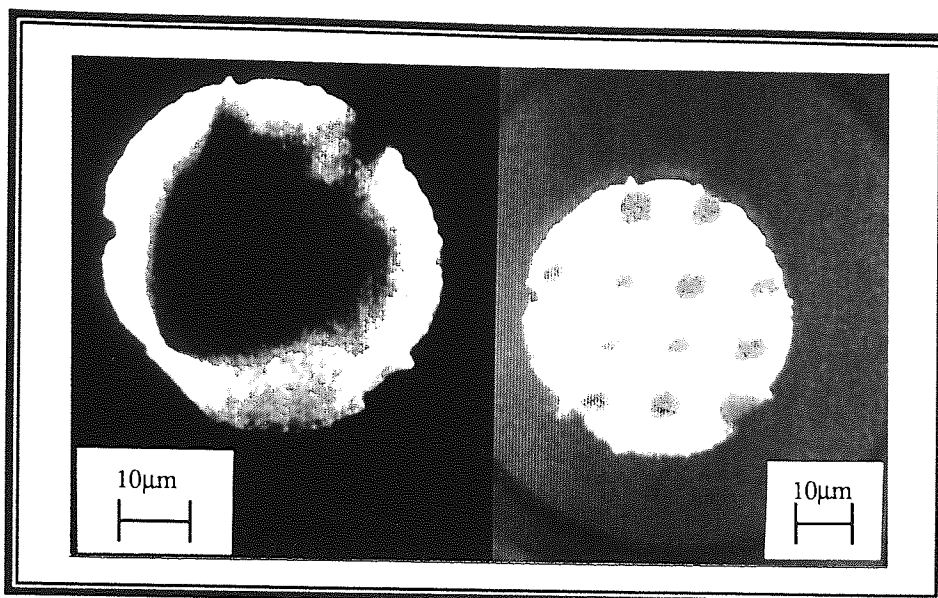
Figure 5.24 a) UV photo-electron image of a C particle and b) image of a 2000 lines/inch TEM grid imaged under low field conditions (these are digitally processed images).
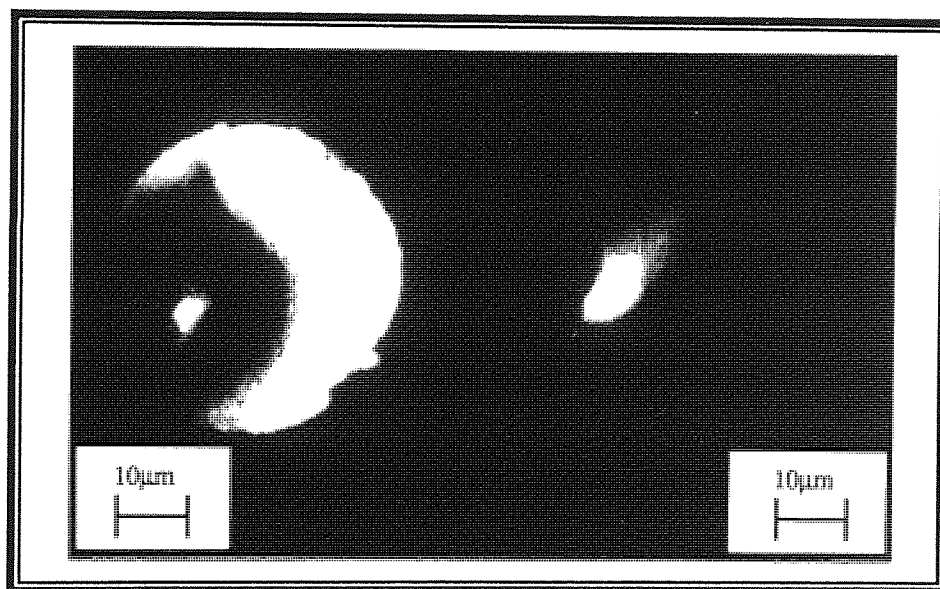
Figure 5.25 Digitally processed image of the C particle above showing a) combined photo/field electron image and b) field emission image with UV source switched off. These images were recorded under high field conditions.

i.e. emission was observed to 'switch-on' at low fields, and generate high emission currents of typically 5μA at 5MVm⁻¹ from the entire electrode. Thus, any photo-emission current will have no effect on the measured IV characteristics since it is smaller by several orders of magnitude.

Before emission was stimulated, the graphite particles were found to be significantly darker in the photo-electron images than the copper substrate (see Fig. 5.26), which is important since it is consistent with a 'blocking contact' existing between the substrate and carbon particle. In Fig. 5.24 a digitally processed image of a carbon particle is shown, with the image of a TEM grid at the same
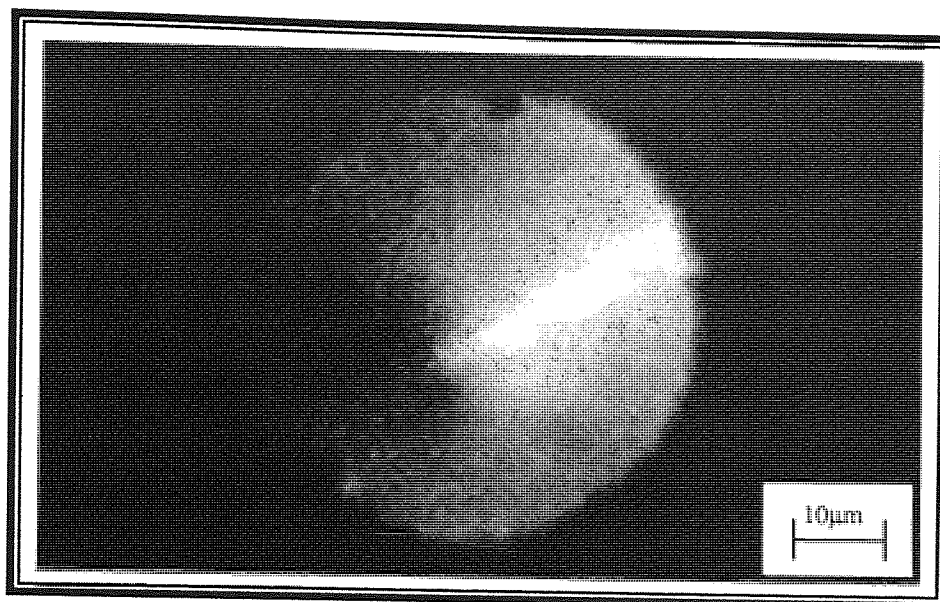
Figure 5.26 Image of a carbon particle showing field emission from the edge region of the particle as two 'jets' to the RHS of the field of view.

magnification for comparison. On stimulating field emission from the samples, the photo-emitted topographical image could still be observed simultaneously with the image of field-emitted electrons. These images reveal that the field-emitted electrons may indeed be observed. Typical examples are shown by Figs 5.25(a) and (b), which have a field of view of ~40μm, and were obtained with and without a simultaneous photo-electron image: These images show the field-emission image to be identical under the two imaging conditions and therefore indicate that the incident UV photons have little effect upon the field emission process.

The images of Fig. 5.25 clearly show emission occuring from the bulk region of the carbon particle. It was possible to obtain an image of emission occuring from the edge region (i.e. triple junction) of another carbon particle, which is shown in Fig. 5.26. Although this image is not as clear as those of Fig. 5.25, since it has not been digitally processed, two 'jets' of electrons may be seen to the right-hand side of ~20μm in length. The non-processed image of Fig. 5.26 also indicates the low intensity of emission from the sample which results in the poor quality and high level of noise present.

5.5 Discussion of UV photo/field emission microscope

5.5.1 Overall system performance

As discussed in section 5.3.3.4, the resolution expected from the imaging system is of the order of 2μm. In practice, as may be observed from the images of the TEM grid shown in Fig. 5.23, the actual resolution is of this order.

Furthermore, these grid images themselves suffer from some distortion owing to the field penetration between the grid wires which effectively broadens the image of the wire which would explain the difference between the measured grid wire/gap width ratio of 0.25, and that measured experimentally from the images of Fig. 5.23 of ~0.4. There are also a number of other potential reasons for the difference between the 'theoretical' and experimental resolution that may be commented upon since these conclusions have a relevance to improving the instrument performance.

Firstly, it will be recalled that for the purposes of these calculations, the resolution was assessed using the minimum radius of the ray bundle focused by the lens, i.e. the 'disc of least confusion'. However, this does not take account of the intensity distribution across the ray bundle and therefore does not necessarily represent the best focus. Indeed, the best focus is normally attained closer to the paraxial focus, for although the ray bundle is of greater diameter, the intensity distribution across the bundle has the form shown in Fig. 5.27 [117]. This clearly shows that most of the intensity is actually contained within a diameter of ~15% of the total ray bundle diameter, and hence, the outer portions, while contributing a low intensity halo, will not significantly affect the image.

Figure 5.27 Intensity distribution across caustic of ray bundle illustrating improved resolution (from [117]).

Secondly, the electron energy assumed for the calculation will probably be an over-estimate of the true value since 7eV represents the energy an electron emitted form the Fermi level would have, but many electrons from lower energy levels, and consequently smaller kinetic energy, would also be emitted with a distribution reflecting the emitting band structure. This would have the effect of reducing the aberration due to the accelerating field which depend linearly on the emission energy for a system with no aperture stop (see Eq. 5.19). The chromatic aberration

would also be reduced by this effect, although the effects of the accelerating field are the limiting cause of aberration within this system.

It is also possible that there may be differences in the resolution of the system for photo- and field-emitted electrons. This follows from the effect of electron emission energy on the initial aberration due to the accelerating field. Thus, from equation 5.19, the aberration induced by the accelerating field depends upon the electron emission energy relative to the zero of potential. The photo-emitted electrons are emitted over a wide energy range up to ~15eV, although principally at 7eV, whereas the field emitted electrons are generally emitted at just below the substrate metal Fermi level. They will therefore experience a different chromatic aberration and therefore the two images will not have the same 'best' focus.

Vibration is also a problem with the current system and may ultimately be responsible for limiting its resolution.

5.5.2 Possible design improvements

As indicated in the discussion above, several factors other than the intrinsic lens properties are likely to affect the ultimate resolution that may be obtained by the present system. It is therefore possible that the resolution of the system may be improved by making minor alterations to the overall design of the objective lens stage and UV excitation, since it is these stages that impose the principle limits on the resolution of the system.

Ideally, a UV source that produces photons of energy just sufficient to cause emission of electrons is required for UV photo-microscopy. With this condition satisfied, the resolution would be improved in two ways. Firstly the emitted electrons would only have very low energies and hence, from equation 5.19, the radius of the 'disc of least confusion' would be reduced. Secondly, the angular distribution of the emitted electrons would be reduced since they require the work function energy in the direction normal to the surface in order to escape. Thus, only electrons moving within a narrow range of angles normal to the surface would be able to escape. It is also advisable to minimise the electrode gap, but this must be balanced against the requirement to illuminate the sample surface with UV light. This factor therefore also influences the choice of objective lens focal length and dimensions. Furthermore, a more intense UV source would also be useful since the current source produces very few electrons.s^{-1} from each unit resolvable area thus resulting in noisy low contrast images. The optimum source satisfying both these conditions would be a CW laser operating in the near UV where special viewport materials would enable transmission of the beam into the UHV chamber, and a high intensity focussed spot could be obtained to illuminate the sample surface.

The objective lens is the other principal limit to the resolution since the object

for the following lens stages is the magnified image produced by the objective. Thus, by fine tuning of the objective lens design to reduce its aberration coefficients, and also minimising the gap, it should be possible to further enhance the resolution.

Another method of improving the resolution would be to use an aperture stop in the system. Such a stop would be required between the objective lens and the intermediate lens stages. From texts on electron-optical design [74,120], the optimum place for such a stop would be at the axial position of the image formed by the objective lens, such that only a small bundle of rays at the paraxial focus (and hence emitted with small angles) could be transmitted. From Fig. 5.28(a), it will be seen that it is possible to transmit just these low emission angle electrons since the others do not have their focus at the position of the stop, and so do not fall on the aperture. Unfortuantely, the focal plane of the intermediate lens is within the body of the lens, so it would not be possible to use this technique without redesigning the intermediate lens. The other alternative is to reduce the exit aperture from the objective lens, so that ray bundles at large angles would not be able to escape from the lens, thus limiting the angular aperture as indicated in Fig 5.28(b). Furthermore, since the lens is designed to operate with a field free external region, the size of the outer electrode aperture has little effect upon the optical properties of the lens [74].
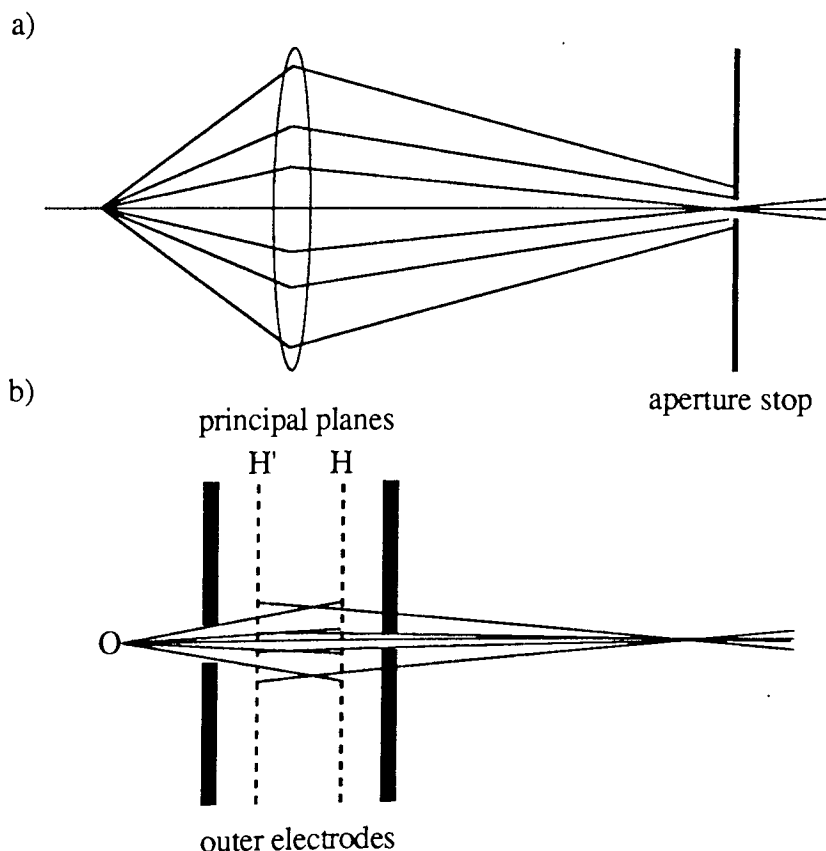
Figure 5.28 Reduction of input aperture by a) aperture stop and b) minimisation of lens outer electrode aperture.

Finally, it would also be possible to extend the operational functions available on the instrument. For example, the incorporation of a grid between the electron lenses and the micro-channel plate would potentially enable crude electron energy measurements to be undertaken. With a grid at the cathode potential, an additional bias voltage would enable the selection of an energy threshold below which electrons would not be passed. By sweeping the bias voltage, the flux detected would then depend upon the proportion of electrons with sufficient energy to be transmitted, c.f. the retarding potential analyser [20]. By the application of image processing techniques, the spatial electron energy distribution could then be determined, although probably to a poor resolution. This would not only provide information about the field-emitted electrons, but also the photo-electrons, and therefore about the surface they were emitted from, since the photo-emission spectrum is influenced by the band structure of the emitting surface [118]. However, such a technique would probably have a detrimental effect upon the imaging resolution when in operation.

5.5.3 Discussion of FIEE images from MIM carbon emitters

PE images obtained from MIM carbon emitters revealed that field induced electron emission, FIEE, could occur from both the particle edge or from the bulk. Furthermore, the images of the carbon particles were always found to be dark. These results will now be discussed in terms of the MIM model developed by Xu [53,61,68].

Consideration shall first be given to the implications of obtaining dark particle images. For an area of the emission image (PE or FE) to appear dark, there must be no significant electron emission occuring from that region. Thus, as the carbon particles appear to be dark under illumination from the UV source, they can not be emitting photo-electrons. This would therefore appear to imply that a blocking contact must exist between the particle and the substrate, i.e. satisfying a principal assumption of the MIM model. However, this could have some important implications towards the emission mechanism: initially, under illumination from the UV source, photo-electrons will be emitted until the particle has charged up to a potential preventing even electrons with the maximum possible emission energy to escape. In fact, with the noble gas argon used in the source, this will be at a potential of some 15V! Within the context of the model, it is assumed that FIEE is initiated by a breakdown event occuring in the insulator due to the intensification of the gap field resulting from the antenna effect on the carbon particle. Thus, for an applied gap field, E_g, of 5MVm^{-1}, and assuming a particle height, h, of ~100μm, the field across the ambient oxide layer, E_I of thickness d ~20Å would be $hE_g/d \approx 2.5 \times 10^5$MVm^{-1}. Should the particle charge up to some 15V however, the field

176

across the ambient oxide layer of ~20Å thickness will only be ~ $7.5 \times 10^3 MVm^{-1}$, which is significantly less than that generated by the gap field required to stimulate FIEE. Therefore, even observations performed using such high energy UV photons should have little effect upon the emission mechanism, although these data do not permit a quantitative assessment to be made.

Significantly, the image of the particle also remains dark even after FIEE has been stimulated. Indeed, as seen in Fig. 5.26, the images show a bright spot associated with the emission, against the dark particle which is on a light background of the substrate. It would be expected, however, that once FIEE has been stimulated, the conductive path existing between the particle and the substrate would provide a mechanism for replacing photo-emitted electrons, and hence the particle should become brighter in the field of view. From the photo-emission current measurements discussed in section 5.3.2.2, the current density is approximately $10^{-7} Acm^{-2}$, which would imply a total photo-emission current of ~10^{-11}A assuming the carbon particle is about 100μm square. A typical FIEE current is ~10^{-7}A however, which is many orders of magnitude greater than the photo-emission current. Therefore, it would be expected that the particle would lose any charging due to the photo-emission. Furthermore, should charging of the particle be occuring, there would be a reduction in the surface field at the particle which would tend to inhibit the emission of electrons. It is therefore unlikely that any charging is occuring and consequently the dark appearance of the particle must be due to a lower photo-emission cross-section at the UV source energy.

The image of the emission sites, at ~10μm, is also far larger than would be expected. Although it is not possible to explain this fully, several factors may be considered. Firstly, the image may well be out of focus as the system is focussed on the substrate surface. Secondly, space-charge effects could be playing an important role in the observed site images: the current density from an emitter of area one square micron would typically be $J \geq 10 Acm^{-2}$, which is significantly greater than the threshold of $1 Acm^{-2}$ at which space-charge effects become important [126]. Field intensification at the point of emission would also tend to enlarge the emission site image since the electrons tend to follow the field lines as they are accelerated from the sample surface, and these will curve into any region of enhanced surface field (c.f. Fig. 4.25).

Previous images observed from carbon sites have shown evidence of both sites that consist of diffuse spots and arc-like structures [61,68]. Similar images have also been observed from some 'natural' emission sites [42]. These data have been interpreted in terms of coherent scattering occuring in the top conducting layer [53]. The evidence from this present study is insufficient to comment extensively on the emission models since no arc-like images were actually observed. The site images did show evidence of emission occuring both from the bulk of particles and

at their edges however.

The observation of emission from the edge of a particle may tentatively be explained in terms of diffraction however. The appearance of the 'jets' from the side of a particle would be consistent with this model since the emission appears to be parallel to the substrate surface and does not overlap the upper surface of the particle. These effects could, however, be produced by distortion of the gap field due to the presence of the particle. Additionally, it may be possible that the emission is occuring from an area occluded by the bulk of the particle, i.e. the particle has a curved underside.

It is difficult to see how the emission site observed near the centre of a particle could be explained in terms of the MIM coherent scattering model [53], and is more consistent with either the antenna or hot electron emission models. It is reasonable to assume that this emission is occuring from a region experiencing a geometrical field enhancement, since it would be expected that the centre of the particle would be the highest point. Unfortunately, since the images of the carbon particles were of such low contrast, it was not possible to make any correlations between the particle topography and the emission site.

5.5.4 Potential future applications of the combined UV photo/field emission microscope

The photo/field-emission microscope has shown itself capable of generating simulataneous FIEE and photo-emission images of samples. Currently however, its imaging performance lies at the lower end of the range for useful work on 'natural' emission sites, which are typically sub-micron in size. Improvements in the resolution and image brightness by the various methods discussed above would increase the scope of potential applications for the system.

With an improvement in resolution, the system could be used for the study of 'natural' emission sites, to locate the emission relative to the topography of the emitting particle. Studies on the effects of bulk heating, as discussed in the preceeding chapter, could also be performed to determine whether diffusion between the bulk and surface of the electrode was responsible for the observed site distribution effects of bulk heating.

Should it prove possible to implement some form of energy analysis, the use of sophisticated image processing techniques would enable 2-D electron energy distributions to be mapped. Such maps would not only provide information about the field-emitted electrons, but could also conceivably give further information about the emitting particle itself, since the electronic band structure affects the energy spectrum of the photo-emitted electrons (c.f. UPS [118]).

CHAPTER 6 CONCLUSIONS

Two dedicated experimental systems for the fundamental study of field induced electron emission processes on broad area planar cathodes have been described. A novel UV imaging system has been described and the early findings of a study into the position of emission sites on contaminant particles have been presented. The extensive redesign of an electron spectrometer system has been undertaken, and utilised to study various aspects of the emission mechanism. These studies have investigated the effects of coating electrodes with thin dielectric films and the thermal stimulation of emission sites, by both bulk and surface heating techniques. In this chapter a summary will be presented of the performance characteristics of these two experimental systems, the principal experimental findings that have emerged and the conclusions that have been inferred from these findings. This will include a brief assessment of the technological implications arising from the studies, and suggestions for further developmental work and experimental studies.

6.1 Spectrometer system

Major improvements have been made to a high resolution UHV electron spectrometer system to improve operator control and enable greater experimental flexibility. These innovations have included the design and construction of:

i) a new vacuum chamber including a separate pre-chamber for specimen insertion and treatment.
ii) an improved specimen manipulation and transport system with a sample stage incorporating a heating element for studies of thermal effects.
iii) a computer control and data acquisition system thus enabling the application of more powerful analysis techniques to experimental results and offering the possibility of theoretical curve fitting to experimental data.
iv) the interfacing of a pulsed laser system enabling studies on localised surface heating effects to be performed.

These innovations have improved the flexibility of the system, opening the possibility of performing mathematical manipulations to the data such as smoothing, integration and theoretical curve fitting. The present software will need further modifications and some re-writing. While it allows adequate control of the experimental system, its use under operating conditions has shown the need for further modifications. The present analysis facilities are somewhat limited since the peak-fitting routine for determining the spectral shift and peak height is estimated

from a quadratic function fitted to the peak region. The FWHM is then estimated by taking width values at the half-height points, which may result in an under estimate of the 'true' value if the spectrum is noisy. Curve fitting routines for the data would require significant work since several parameters must be fitted to log and exponential functions. This is due to the large number of variable parameters required to accurately fit the spectral curves within the context of the hot electron model [8]. Therefore, it was not possible to produce such fits for the experimental spectra obtained during the present investigation. Such software would also create the possibility of analysing overlapping multi-peaked spectra observed from sub sites within a single emission centre.

The addition of a transparent anode imaging facility [89] to the main experimental chamber would provide a significant improvement to the analytical capabilities of the system by enabling visual study of site distributions in real time, and the coarse location of individual sites for subsequent detailed analysis using the spectrometer. The pre-chamber has the porting facilities to enable sample treatments such as ion beam etching and gas conditioning to be performed. A further transparent imaging anode could be advantageously incorporated in this chamber for the screening and monitoring of samples during surface treatment experiments. The present sample heating stage is also limited to a sample temperature range of ambient-600°C, and could profitably be redesigned to extend its temperature range to both higher and lower temperatures.

6.2 UV imaging system

A new type of surface analysis facility has been developed for dynamic studies of field emission sites. It is based upon the principle of superimposing a field emission image, and a photo-electron image of the associated micro-topography of the electrode in the vicinity of an emission site.

The design and operation of an imaging system based on the principle of combined photo- and field-emission has been demonstrated. The experimental system has been demonstrated to be capable of topographical imaging of a surface in the UV photo-emission mode with a resolution approaching 1μm and a magnification approaching 10000x. Furthermore, it has been shown that field emission may be stimulated, emission sites located, and that the field emission and UV topographical images may be viewed simultaneously in real time.

From an analysis of the electron optical behaviour of the photo-electron imaging system, it has been shown that the resolution obtained under operating conditions is better than expected, and that there are several alternative routes by which the performance of the system may be improved. In particular, it should be possible to improve the resolution significantly by the incorporation of aperture

stops, a redesign of the objective lens system and the use of a lower photon energy UV source.

Studies of combined photo/field-stimulated emission images from carbon emission sites on an OFHC copper electrode have shown that electrons are emitted from microscopic locations at the edges of particles and also from their bulk. Edge sites are consistent with a coherent scattering model discussed by Xu and Latham [53,61], while those from the bulk region are broadly consistent with the hot electron model [8] in which a channel has been formed in the bulk of the particle. Both of these results are consistent with previous observations of the emission images and spectra from such carbon sites by Bayliss [42] and Xu [61].

The technique has been demonstrated to work in principle, although improvements to the performance of the system will be required in order to exploit the microscope fully. For example, the current resolution limits the application of the system to the study of 'natural' sites, as they typically involve micron to sub-micron sized impurity particles. The system would also enable the study of sites at very low emission currents owing to the high sensitivity of the image intensifier. Image processing techniques may be applied to improve the contrast within images and also to study the spatial current density distributions across emission sites and topographical images. This development would open up the possibility of studying current density fluctuations across an emission site, and the variation of total emission current with time. With the incorporation of a sample heating stage, the photo/field imaging system would be ideal for the study of the effects of sample temperature on the emission process. The system could also be applied to the study of cold cathode electron sources.

6.3 Dielectric-coated cathodes

This study showed that the coating of a metal electrode with a thin layer of dielectric LB film (100-500Å) had the surprising effect of enhancing electron emission from the electrode i.e. increasing the density of emission sites and lowering the surface field required to switch-on sites. Electron spectroscopy measurements revealed that the emission was characteristic of microscopic conducting filaments having been formed within the dielectric medium or of hot electron emission processes. Thus, individual sites revealed field dependent shifts below the substrate Fermi level ≥ 0.8eV, and broad symmetric energy distributions of ≥ 0.5eV. Furthermore, these data revealed evidence of an oscillatory behaviour associated with field. There was apparently no correlation between any of the measured parameters and individual film thicknesses.

This study revealed many similarities in the properties of LB film coated cathodes and MIM devices based on an LB insulating layer [91,92]. In contrast to

the MIM devices, it was not possible to determine if a metallic conduction process was involved i.e. whether the conducting filaments were metallic or non-metallic in nature. Assuming that the filaments were formed within an idealised planar metal-LB film structure, the spectral shift data of section 4.2.3.2, showed that a field enhancement of 10-100x was required within the dielectric medium at the position of an emission site. From this evidence it was shown how the field enhancement and hence emission mechanism could potentially be influenced or stimulated by various factors including: particulate contamination, induced charging at the bulk or interface regions, or the formation of metallic filaments by electromigration.

Whilst the physical basis of the emission mechanism is still unclear, there is a clear technological advance from this study. The use of thin dielectric coatings is thus to be avoided in applications for high voltage insulation, since these coatings have a degrading effect on the performance of an electrode by reducing the field at which significant field emission, or leakage, occurs across a HV electrode gap. It is well known [134,135] however that thick dielectric coatings ($\geq 1\mu m$) can have the opposite effect of improving HV performance and it is therefore suggested that future work should study a wider range of thicknesses, up to a few microns, especially in the area where the crossover from enhancement to suppression occurs.

Alternatively, other studies [45,85] have shown that the coatings give rise to high stability, high current emission sites and, as such, could be of potential practical application to high brightness cold cathode field emission sources. Such applications would require the ability to 'write' emission sites at particular locations in the dielectric film coating, and this aspect of the work will clearly require further investigation. Should the emission be stimulated by sub-micron particulate contamination, then it may be possible to develop a doping technique to achieve the required degree of control for commercial development of electron sources.

6.4 Bulk heating of electrodes

An investigation has been made on the effects of bulk heating on the emission process in the temperature range from ambient to 570°C. These studies were performed under conditions of both zero- and high-applied field, and investigated the effects of bulk heating on site distributions, electrode and site I-V characteristics, and the spectral characteristics.

The investigation showed that, for OFHC copper electrodes, there was no observable effect upon the emission processes under zero field conditions. Thus, the site distribution, I-V characteristics, and spectral features showed no more than the random fluctuations associated with emission from 'natural' sites.

For the case of bulk heating under a high-applied field the observations were markedly different. The site distribution was found to be drastically altered

once the temperature exceeded ~300°C. It was found that existing sites were extinguished while new sites were stimulated: furthermore, the overall number of sites was also found to increase. On cooling back to ambient temperature, it was also found that some of the original sites began to emit again, while a proportion of those that were stimulated during the thermal treatment switched off. Although it was only possible to speculate upon the physical basis of these findings, they were discussed in terms of possible insulator band structures. By consideration of the energy levels of the electron donors and traps, the observations were shown to be consistent with the hot electron emission model of Bayliss and Latham [8].

From a study of the J-V characteristics of individual sites, it was shown that as the temperature was raised there was a significant increase in the current density for a given applied field. Furthermore, the rate of increase was also found to increase with temperature, which resulted in a reduction of the applied field by a factor of 2 from ambient to 500°C for the same emission current density. This behaviour could not be discussed in a fully quantitative fashion since the current density data was not calibrated; however, it was shown to be consistent with the hot electron model [8]. In fact, it was shown that the findings could be explained in terms of an increase in the surface ß-factor with temperture due to variations in the insulator conductivity and charge distribution with temperature.

The overall emissivity of the electrode was also found to increase significantly as the bulk temperature was increased. This behaviour was readily explained in terms of the increase in the total number of emission sites coupled with the increased site emissivity. Interestingly, it was found that the emissivity was still significantly increased after cooling back to ambient temperature; however, this could be explained as a consequence of the rise in the number of observed emission sites that followed the thermal processing.

The energy spectra showed several interesting features as the bulk temperature was increased, including a decrease in both the absolute peak shift and the rate of increase of the shift, and an increase in both the FWHM and its rate of increase with applied field. These findings were again shown to be consistent with an increase in the surface ß-factor resulting from the electronic effects of bulk heating, and were therefore consistent with the hot electron model [8].

Thus, further experimental information has been presented that supports a non-metallic emission process from localised emission sites on broad area copper electrodes. The observations have also been shown to be consistent with the hot electron model of Bayliss and Latham [8], and that they result from changes that occur in the conductivity and charge distribution within the insulator under the influence of bulk heating. It has been shown that an increase occurs in the surface field intensification during bulk heating with an applied field, and that this factor is principally responsible for the experimental observations.

These results suggest that further investigation is required into the effects of bulk heating, particularly under high applied field conditions. Of most interest would be an extension of the temperature range for the investigation of possible impurity diffusion effects. It would also be desirable to determine whether such effects occur with different emission regimes, for example the MIM regime based on added carbon particles. Finally, electrodes of different materials should be studied in order to confirm the findings discussed in this thesis: such results should be similar if the effects are due to the intrinsic emission mechanism.

6.5 Localised heating of electrodes

The effect of localised transient thermal processing has also been investigated. This study involved the design and development of a pulsed laser system for the localised heating of the electrode surface on the scale of a few microns. Characterisation of the system revealed that the minimum area experiencing significant heating was of the order of ~40μm diameter. Sufficient energy was available to vaporise the surface layer to a depth of ~50μm across this diameter, or to melt the electrode across a diameter of 0.5mm.

Studies aimed at investigating the effect of varying the incident flux showed that, within the incident energy range for melting the surface without inducing vaporisation, namely $\leq 5 \times 10^7 Wcm^{-2}$, there was little effect upon the emission site distribution or the electrode emissivity. The surface finish of the electrode did, however, suffer significant damage above this range due to the flow of melted substrate material. At higher incident fluxes of $>10^8 Wcm^{-2}$, when extensive damage could be caused on the electrode surface, it was observed that the emission site distribution was altered by each successive surface treatment and that there was a general decrease in the overall emissivity of the electrode. It must be noted however, that this level of dosing was accompanied by a significant 'roughening' of the surface which could, in principle, provide numerous field enhancing topographical features. Although it was not possible to determine whether the new emission centres were associated with topographical features generated by the thermal treatment, indirect evidence suggests that this is unlikely since they displayed the same characteristic features of a non-metallic emission process exhibited by sites on untreated electrodes. In the boundary region between these two surface dosing ranges random behaviour was observed: sometimes the site distribution was altered, while on other occasions there was no apparent effect.

The above findings were discussed in terms of the material-photon interactions that occcur during the heating process. It was shown that there was no effect on the site distribution, or I-V characteristics, until the incident dose exceeded the level necessary to cause some vaporisation of the surface. The extension of this

study to dosing solely at emission site locations may well be of significant technological interest, as such a process would potentially allow the controlled destruction of sites without the introduction of new sites. Studies are also required to determine the effect of the surface damage introduced by the beam at the high incident fluences required to vaporise the surface, in association with a more detailed study of the effect of varying dose levels on a precisely targeted site.

6.6 Technological overview

The experimental studies undertaken during the course of the research programme described in this thesis are of considerable technical importance. Thus, the findings have a bearing on both the suppression of parasitic 'cold' electron emission from HV electrodes, and the utilisation of the emission process in the development of cold cathode electron sources.

In this latter context, the enhancement of emission by coating electrodes with thin dielectric films shows potential promise as the basis for developing a cold cathode electron source that avoids the requirement of UHV conditions and the extremely high fields required by conventional field emission tips, while enjoying the same advantages of high source brightness, such as the LaB_6 sources currently employed in electron microscopes [137]. However, an improved understanding of the basic emission mechanism will be required before this application can be fully exploited. If, for example, it were possible to 'write-in' the position(s) of the emission sites on suitably prepared 'virgin' electrodes, such a technique would find potential application to micro-valve arrays for radiation hard electronics or displays [138].

Previous studies investigating the effects of bulk heating on the emission process have tended to concentrate on thermal processing under zero field conditions over long time scales. Work on Nb electrodes [12,44] has shown that the diffusion of impurities between the substrate bulk and surface can play an important role. The current study has revealed that additional processes occur under emission conditions. Indeed, heating under high-field conditions stimulates the formation of emission sites and enhances the emissivity of indivual emission sites. Thus, these results imply that care should be taken during device design to avoid the heating of electrodes. For example, these results would suggest that high voltage electrodes in space-power systems should be protected from direct solar illumination, which can lead to surface temperatures of many hundreds of degrees celsius.

Localised transient thermal treatment using a pulsed laser shows promise as an alternative electrode conditioning technique. Although only an initial study was performed, it was shown that a reduction in electrode emissivity could be obtained.

Therefore, this process is clearly of interest as it would enable the treatment of electrodes to be performed locally on individual emission sites without affecting the surrounding electrode material.

REFERENCES

1. Latham R.V.,"High voltage insulation: the physical basis", Academic Press, London, 1981.

2. Noer R.J., "Electron field emission from broad area electrodes", Appl. Phys. A(Germany), **A28**, No1, 1-24, 1982.

3. Millikan R.A. and Sawyer R.A., "Extreme ultra-violet spectra of hot sparks in high vacua", Phys. Rev., **12**, 167-170, 1918.

4. Fowler R.H. and Nordheim L., "Electric emission in intense electric fields", Proc. Roy. Soc., **A119**, 173-81, 1928.

5. Cox B.M., "The nature of field emission sites", J. Phys. D, **8**, 2065-2073, 1975.

6. Athwal C.S. and Latham R.V., "A micro-point probe technique for identifying field emitting sites on broad area high voltage electrodes", Proc. IX-DEIV, Physica, **104C**, 46-49, 1981.

7. Niedermann Ph., Sankarraman N. and Fischer Ø., Proc. 2nd Workshop on RF Superconductivity, Geneva, Switzerland, ed. H. Lengeler, 583-596, 1984.

8. Bayliss K.H. and Latham R.V., "An analysis of field-induced hot-electron emission from metal-insulator microstructures on broad-area high-voltage electrodes", Proc. Roy. Soc., London, **A403**, 285-311, 1986.

9. Bajic S. and Latham R.V., "Enhanced cold cathode emission using composite resin-carbon coatings", J. Phys. D, **21**, 200-204, 1988.

10. Latham R.V. and Archer A.D., "Characterisation of individual micro-emission centres distributed in planar arrays", Inst. Phys. Conf. Ser., **99**, section 6, 153-164, 1989.

11. Bajic S., Cade N.A., Archer A.D. and Latham R.V., "Stimulated cold-cathode emission from metal electrodes coated with Langmuir-Blodgett multilayers", Inst. Phys. Conf. Ser., **99**, section 3, 57-60, 1989.

12. Niedermann Ph., Sankarraman N., Noer R.J. and Fischer Ø., "Field emission from broad area niobium cathodes: effects of high temperature treatment", J. Appl. Phys., **59**, 892-901, 1986

13. Padamsee H., Gendreau K., Harting W., Kichgessner J., Moffat D., Noer R., Rubin D.L., Sears J. and Shu Q.S., "Does UHV annealing above 1100°C as a final surface treatment reduce field emission loading in superconducting cavities", 1988 Linear Acc. Conf. Proc., Newport News, VA, USA, 377-379, 1988.

14. Millikan R.A. and Lauritsen C.C., "Relations of field-currents to thermionic-currents", Proc. Nat. Acad. Sci., **14**, 45-49, 1928.

15. Boyle W.S., Kisliuk P., Germer L.H., "Electrical breakdown in high vacuum", J. Appl. Phys., **26**, 720-725, 1955.

16. Little R.P. and Smith S.T., "Field enhancing projections produced by the application of an electric field", J. Appl. Phys., **36**, 1502-1504, 1965.

17. Tomasche H.E. and Alpert D., "Role of sub-micron projections in electrical breakdowns", J. Vac. Sci. Tech., **4**, 192-198, 1967.

18. Schottky W., "Cold and hot electron discharges", Physik. Z., **14**, 63, 1923.

19. Good R.H. and Muller E.W., "Handbuck der physik", Springer-Verlag, Berlin, **21**, 176-231, 1956.

20. Van Oostrum A.G.J., "Validity of the Fowler-Nordheim model for field electron emission", Philips Res. Reports, Suppl. No. 1, 1966.

21. Gadzuk L.W. and Plummer C.W., "Field emission energy distribution (FEED)", Rev. Mod. Phys., **45**, 487-548, 1973.

22. Young R.D., "Theoretical total energy distribution of field emitted electrons", Phys. Rev., **113**, 110-114, 1959.

23. Modinos A., "Field, thermionic and secondary emission spectroscopy", Plenum Press, New York and London, 1984.

24. Murphy E.L. and Good R.H., "Thermionic emission, field emission and the transition region", Phys. Rev., **102**, 1464-1473, 1956.

25. Christof S.G., "General theory of electron emission from metals", Phys. Stat. Sol., **17**, 11-26, 1966.

26. Ermich W., "Influence of slow electron impact upon gases adsorbed on tungsten, investigated by means of a field electron microscope", Philips Res. Reports, **20**, 94-105, 1965.

27. Duke C.B. and Alferieff M.E., "Field emission through atoms adsorbed on metal surfaces", J. Chem. Phys., **46**, 923-937, 1967.

28. Plummer E.W. and Young R.D., "Field emission studies of electronic energy levels of adsorbed atoms", Phys. Rev. B, **1**, 2088-2109, 1970.

29. Cox B.M., CEGB Laboratory Note R/M/N, 1021, 1979.

30. Hurley R.E., "Electrical phenomena occuring at the surface of electrically stressed metal cathodes: III current-voltage characteristics of electro-luminescent (k spot) regions on broad area cathodes", J. Phys. D, **13**, 1121-1128, 1980.

31. Cox B.M. and Wort D.E.J., "Mapping field emission from surfaces", Vacuum, **22**, 453-455, 1972.

32. Athwal C.S. and Latham R.V., "The effect of the applied field on the energy spectra of electrons field-emitted from microscopic sites on broad area copper electrodes", Proc. IX-DEIV, Physica, **104C**, 189-195, 1981.

33. Athwal C.S. and Latham R.V., "Switching and other non-linear phenomena associated with pre-breakdown electron emission currents", J. Phys. D, **17**, 1029-1043, 1984.

34. Niedermann Ph., "Experiments on enhanced field emission", PhD Thesis, Geneva University, Switzerland, 1986.

35. Hurley R.E. and Dooley P.J., "Electro-luminescence produced by high electric fields at the surface of copper electrodes", J. Phys. D, 10, L195-L201, 1977.

36. Hurley R.E. and Dooley P.J., Vacuum, 28, 147-149, 1978.

37. Klyarfell B.N. and Pokrovskaya-Soboleva A.S., "Arc discharge in vacuum with high tension arcing", Sov. Phys., 15, 149-152, 1970.

38. Alfrey G.F. and Taylor J.B., "The mechanism of electro-luminescence of zinc sulphide", Brit. J. Appl. Phys., 6, supp. 4, S44-S49, 1955.

39. Hurley R.E., "Electrical phenomena occuring at the surface of electrically stressed metal cathodes: II identification of electro-luminescent (k spot) radiation with electron emission on broad area cathodes", J. Phys. D, 12, 2247-2252, 1979.

40. Allen N.K. and Latham R.V., "The energy spectra of high ß electron emission sites on broad area copper electrodes", J. Phys. D, 11, L55-L57, 1978.

41. Bayliss K.H. and Latham R.V., "The spatial distribution and spectral characteristics of field induced electron emission sites on broad area high-voltage electrodes", Vacuum, 35, 211-217, 1985.

42. Bayliss K.H., "The physical origin of pre-breakdown electron emission from broad-area high voltage electrodes", PhD Thesis, Aston University, UK, 1984.

43. Athwal C.S., Bayliss K.H., Calder R. and Latham R.V., "Field induced electron emission from artificially produced carbon sites on broad area copper and niobium electrodes", IEEE Trans., Plasma Sci., PS-13, 226, 1985.

44. Noer R.J., Niedermann Ph., Sankarramann N. and Fischer Ø., "Electron field emission from intentionally introduced particles on extended niobium surfaces", J. Appl. Phys., 59, 3851, 1986.

45. Bajic S., "'Non-metallic' cold-cathode electron emission from composite metal-insulator microstructures", PhD Thesis, Aston University, UK, 1988.

46. Hurley R.E., "Electrical phenomena occuring at the surface of electrically stressed metal cathodes: I electro-luminescnce and breakdown phenomena with medium gap spacings (2-8mm)", J. Phys. D, 12, 2229-2245, 1978.

47. Ovshinsky S.R., "Reversible electrical switching phenomena in disordered structures", Phys. Rev. Lett., 21, 1450-1453, 1968.

48. Dearnaley G., Stoneham A.M. and Morgan D.V., "Electrical phenomena in amorphous oxide films", Rep. Prog. Phys., 33, 1129-1191, 1970.

49. Adler D., Henisch H.K. and Mott N.F., "The mechanism of threshold switching in amorphous alloys", Rev. Mod. Phys., 50, 209-20, 1978.

50. Hickmott T.W., "Electro-luminescence and conduction in Nb-Nb$_2$O$_5$-Au diodes", J. Appl. Phys., 37, 4380-4388, 1966.

51. Halbritter J., "Dynamically enhanced electron emission and discharges at contaminated surfaces", Appl. Phys. A(Germany), **A39**, 49-57, 1986.

52. Fischetti M.V., Dimaria D.J., Brorson S.D., Theis T.N. and Kirtley J.R., "Theory of high field electron transport in silicon dioxide", Phys. Rev. B, **311**, 8124-8142, 1985.

53. Xu N.S. and Latham R.V., "Coherently scattered hot electrons emitted from MIM graphite micro-structures deposited on broad area vacuum insulated high-voltage electrodes", J. Phys. D, **19**, 477-82, 1986.

54. Allen N.K., "The energy analysis of electrons emitted from localised sites on extended area high voltage electrodes", PhD Thesis, Aston University, UK, 1979.

55. Athwal C.S., "An investigation into the nature of field emission electron sites on broad area metallic electrodes", PhD Thesis, Aston University, UK, 1981.

56. Latham R.V., "The origin of pre-breakdown electron emission from vacuum insulated HV electrodes", Vacuum, **32**, 137-140, 1982.

57. Halbritter J., "Enhanced electron emission and its reduction by electron and ion impact", IEEE Trans. Electr. Insul., **EI-18**, 204, 1983.

58. Mott N.F., "Conduction in non-crystalline systems XI: the on-state of the threshold switch", Phil. Mag., **32**, 159-171, 1975.

59. Simmons J.G. and Verderber R.R., "New conduction and reversible memory phenomena in thin insualting films", Proc. Roy. Soc. London, **A301**, 77-102, 1967.

60. Simmons J.G., "Incorporation of electric field penetration of the electrodes in the theory of electron tunnelling through a dielectric layer", Brit. J. of Appl. Phys., **18**, 269-275, 1967.

61. Xu N.S., "Field induced hot electron emission from composite metal-insulator-metal microstructures", PhD Thesis, Aston University, UK, 1986.

62. Simmons J.G., "Transition from electrode limited to bulk-limited conductive processes in metal-insulator-metal systems", Phys. Rev., **166**, No. 3, 912-920, 1968.

63. Latham R.V. and Mousa M.S., "Hot electron emission from composite metal-insulator micropoint cathodes", J. Phys. D, **19**, 699-713, 1986.

64. Halbritter J., private communication, 1985.

65. Verderber R.R. and Simmons J.G., "A hot electron, cold cathode, emitter", The Radio and Electronic Engineer, **33**, 347-351, 1967.

66. Simmons J.G. and Verderber R.R., "Observations on coherent electron scattering in thin film cold cathodes", Appl. Phys. Lett., **10**, 197- 199, 1967.

67. Simmons J.G., Verderber R.R., Lytollis J. and Lomax R., "Coherent scattering of hot electrons in gold films", Phys. Rev. Lett., **17**, 13, 675-677, 1966.

68. Xu N.S. and Latham R.V., "Field induced hot electron emission (FIHEE) from MIM microstructures", J. de Physique, colloque C2, **47**, 67-72, 1986.

69. Xu N.S. and Latham R.V., J. de Physique, colloque C2, **47**, 95-99, 1986.

70. Purcell E.M., "The focussing of charged particles by a spherical condenser", Phys. Rev., **54**, 818-26, 1938.

71. Kuyatt C.E. and Plummer E.W., "Field emission deflection energy analyzer", Rev. Sci. Inst., **43**, 108-11, 1972.

72. Braun E., Forbes R.G., Pearson J., Pelmore J.M. and Latham R.V., "An advanced field electron emission spectrometer", J. Phys. E, **11**, 222-8,1978.

73. Heddle D.W.O. Keesing R.G.W. and Kurega J.M., "High resolution studies of electron excitation in the 4S states of helium and the energy scale", Proc. Roy. Soc. London, **A334**, 135-47, 1973.

74. Grivet P., "Electron optics", Pergamon Press, Oxford, 1969.

75. Pelmore J.M., "High resolution hemispherical analyser for field emission spectroscopy", SRC contract report no. 1, Dept of physics, University of Aston, 1975.

76. Young R.D., Kuyatt C.E., "Resolution determination of field emission energy analysers", Rev. Sci. Inst., **39**, 1477-80, 1968.

77. Muller E.W., Field desorption", Phys. Rev., **102**, 618-624, 1956.

78. Young R.D. and Muller E.W., "Experimental measurement of the total-energy distribution of field-emitted electrons", Phys. Rev., **113**, 115-20, 1959.

79. Bogart T.F., "Electronic devices and circuits", Merrill Publishing Co., Columbus, 1986.

80. Savitzky A. and Golay M.J.E., "Smoothing and differentiation of data by simplified least squares procedures", Anal. Chem., **36**, 1627-39, 1967.

81. Hecht E. and Zajac A., "Optics", Addison-Wesley, Reading Mass., 1974.

82. Self S.A., "Focussing of spherical Gaussian beams", Appl. Optics, **21**, 658-61, 1983.

83. Veale G., Girling I.R. and Peterson I.R., "A comparison of deposition, epitaxy and crystallinity in Langmuir-Blodgett films of fatty acids", Thin Solid Films, **127**, 293, 1985.

84. Mousa M.S., PhD thesis, Aston University, UK, 1984.

85. Cade N.A., Cross G.H., Lee R.A., Bajic S. and Latham R.V., "Field-induced electron emission through Langmuir-Blodgett multilayers", J. Phys. D, **21**, 148-153, 1988.

86. Barnes W.L. and Sambles J.R., "Optical constants of 22-tricosenoic acid multi-layers", Thin Solid Films, **143**, 237, 1986.

87. Long Range Group, GEC Hirst Research Centre, East Lane, Wembley, Midds, HA9 7PP UK.

88. Peterson I.R., "Optical observation of monomer Langmuir-Blodgett film structure", Thin Solid Films, **116**, 357, 1984.

89. Bajic S. and Latham R.V., "The spatial and temporal behaviour of electron emission sites during He conditioning", IEEE trans., **EI-23**, no. 1, 27-32, 1988.

90. Less K.J. and Wilson E.G., "Intrinsic photo-conduction and photo-emission in polyethylene", J. Phys. C, **6**, 3110, 1973.

91. Couch N.R., Movaghar B. and Girling I.R., "Electromigration failure in filaments through Langmuir-Blodgett films", Solid State Commun., **59**, 7, 1986.

92. Couch N.R., Montgomery C.M. and Jones R., "Metallic conduction through Langmuir-Blodgett films", Thin Solid Films, **135**, 173, 1986.

93. Yankelvitch Y.B., "The thin film metal-insulator-metal system used as a non-heated source of electrons", Vacuum, **30**, 97-107, 1979.

94. Mott N.F. and Davies E.A., "Electronic processes in non-crystalline materials", Clarendon Press, Oxford, 1979.

95. Chopra K.L., "Thin Film Phenomena", McGraw-Hill Inc, NY, 1969.

96. Kittel C., "Introduction to solid state physics (5th edition)" , Wiley, NY, 1976.

97. Bajic S., Abbot A.M. and Latham R.V., "The influence of gap voltage, temperature and gas species on the 'gas conditioning' of high voltage electrodes", IEEE Trans. Elect. Insul., **EI-24**, 8-12, 1989.

98. Bajic S. and Latham R.V., "A new perspective on the gas conditioning of high-voltage vacuum-insulated electrodes", J. Phys. D, **21**, 943-950, 1988.

99. Ridley B.K., "Quantum theory of semiconductors", Clarendon Press, Oxford, 1982.

100. Woratschek B., Ertl G., Kuppers J. and Sesselman W., "Evidence for a quantum size effect of the conduction electrons during oxidation of Cs", Phys. Rev. Lett., **57**, 1484-1487, 1986.

101. Duffin W.J., "Electricity and magnetism" (3rd edition), McGraw-Hill, London, 1980

102. Boer K.W., "Survey of semiconductor physics", Van Nostrand Rheinhold, NY, 1990.

103. Hibbert D.B. and Goodman A., Int. J. Electron, **59**, 701, 1988.

104. Tagawa M., Takenobu S., Ohmae N. and Umeno M., "Field stimulated exoelectron emission from 99.9999% pure aluminium", Appl. Phys. Lett., **53**, 626-7, 1988.

105. Xu N.S. and Latham R.V., "Thermal and photo-assisted hot electron emission from MIM micro-structures", J. de Physique, Colloque C2, **47**, 73-77, 1986.

106. Renner C., Niedermann Ph. and Fischer Ø., "Enhanced field emission investigation of aluminium", Post Deadline Suppl., Proc. 8th Symp. DEIV, IEEE, Paris, 1988.

107. Ready J.F., "Effects of high power laser radiation", Academic Press, 1971.

108. Cheung J. and Horwitz J., "Pulsed laser deposition: history and laser-target interactions", MRS Bulletin, **XVII**, 2, 30-36, 1992

109. Ready J.F., "Industrial aplication of lasers", Academic Press, NY, 1978.

110. Ready J.F., "Effects due to absorbtion of laser radiation", J. Appl. Phys., **36**, 462-468, 1965.

111. "Handbook of Chemistry and Physics", the Chemical and Rubber Company, Cleveland.

112. Basov N.G., Boiko V.A., Krokhin, O.N., Semenov O.G. and Sklizkov G.V., "Reduction of reflection coefficient for intense laser radiation on solid surfaces", Sov. Phys.-Tech. Phys., **13**, 1581-1582, 1969.

114. Niedermann Ph., Renner Ch., Kent A.D. and Fischer Ø., "Study of field emitting micro-structures using a scanning tunnelling microscope", J. Vac. Sci. Technol. A, **8**, 594-597, 1990.

115. Emch R., Niedermann Ph., Descouts P. and Fischer Ø., "A scanning tunnelling microscope combined with a scanning field-emission microscope", J. Vac. Sci. Technol. A, **6**, 379-385, 1988.

116. Griffith O.H. Rempfer G.F. and Lesch G.H., "A high vacuum photo-electron microscope for the study of biological specimens", SEM, **2**, 123-30, 1981.

117. Griffith O.H. and Rempfer G.F., "Photoelectron microscopy", SEM, **8**, 257-337, 1987.

118. "Handbook of X-ray and ultraviolet photo-electron spectroscopy", Ed. Briggs D., Heyden, London, 1979.

119. American Institute of Physics Handbook

120. Klemperer O. and Barnett M.E., "Electron optics" (3rd edition), Cambridge University Press, 1971.

121. Davisson C.J. and Calbick C.J., "Electron lenses", Phys Rev, **42**, 580, 1932.

122. Glaser W. and Schiske P., "Rigorous calculation of a typical electrostatic unipotential lens", Optik, **11**, 423-443, 1954.

123. Vine J., "Numerical investigation of a range of unipotential electron lenses", Brit. J. Appl. Phys., **11**, 408-411, 1960.

124. Read F.H., "Accurate calculations of double aperture electrostatic immersion lenses", J. Sci. Instr., **2**, 165-169, 1969.

125. Rempfer G.F., "Unipotential electrostatic lenses: paraxial properties and aberrations of the focal point", J. Appl. Phys., **57**, 2385-2401, 1985.

126. Massey G.M., Jones M.D. and Plummer B.P., "Space-charge aberrations in the photo-electron microscope", J. Appl. Phys., **52**, 3780-86, 1981.

127. Langmuir D.B., "Theoretical limitations of cathode ray tubes", Proc. Inst. Radio Engineers, **25**, 977-91, 1937.

128. Beiser A., "Concepts of modern physics", McGraw Hill, 1981.

129. Technical data sheet, Vacuum Science Workshop, Manchester.

130. Baker A.D. and Betteridge D., "Photo-electron spectroscopy", Pergamon Press, Oxford, 1972.

131. Orlov , Private communication, 1989.

132. Kleinknecht K., "Detectors for particle radiation", Cambridge University Press, 1986.

133. Instrument Technology Ltd, UHV compatible micro-channel plate detectors data sheet, St. Leonards on Sea, East Sussex, TN38, 9NS, UK.

134. Rohrbach F., Proc. I-IHVV, 393-429, 1964.

135. Germain C., Jeannerot L., Rohrbach F., Simon D. and Tinquely R., Proc. II-IHVV, 279-91, 1966.

136. Latham R.V., Bayliss K.H. and Cox B.M., "Spatially correlated breakdown events initiated by field electron emission in vacuum and high pressure SF_6", J. Phys. D, **19**, 219-31, 1986.

137. Siegel B.M and Beaman D.R., "Physical aspects of electron microscopy and microbeam analysis", Wiley, NY, 1975.

138. Holland C.E., Spindt C.A., Brodie I., Mooney J.B. and Westerberg E.R., "Spindt cold-cathode vacuum fluorescent display", (SRI International, USA), Eurodisplay '87, London, September 1987.

57

Stimulated cold-cathode emission from metal electrodes coated with Langmuir–Blodgett multilayers

S. Bajic, N.A. Cade[*], A.D. Archer and R.V. Latham
Dept. of Electronic Engineering and Applied Physics
Aston University, Birmingham, B4 7ET, UK.

PUBLICATIONS

Characterization of individual micro-emission centres distributed in planar arrays

R.V.Latham and A.D.Archer

Department of Electronic Engineering and Applied Physics
Aston University, Birmingham B4 7ET, U.K.

Aston University

Content has been removed for copyright reasons